

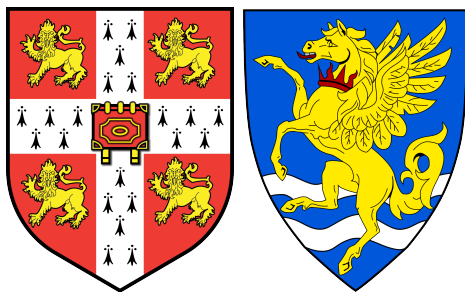
LIAM COATMAN

BLACK HOLE MASSES AND OUTFLOWS IN HIGH
REDSHIFT QUASARS

A DISSERTATION SUBMITTED TO THE
UNIVERSITY OF CAMBRIDGE FOR THE DEGREE
OF DOCTOR OF PHILOSOPHY

BLACK HOLE MASSES AND OUTFLOWS IN HIGH REDSHIFT
QUASARS

LIAM COATMAN
UNIVERSITY OF CAMBRIDGE
INSTITUTE OF ASTRONOMY
ROBINSON COLLEGE
SUBMITTED TO THE BOARD OF GRADUATE STUDIES APRIL 2017
UNDER THE SUPERVISION OF
PROF. PAUL C. HEWETT
DR. MANDA BANERJI



Liam Coatman: *Black hole masses and outflows in high redshift quasars*,
An Homage to The Elements of Typographic Style, © September 2015

Ohana means family.
Family means nobody gets left behind, or forgotten.
— Lilo & Stitch

Dedicated to the loving memory of Rudolf Miede.

1939 – 2005

ABSTRACT

Short summary of the contents in English...a great guide by Kent Beck how to write good abstracts can be found here:

<https://plg.uwaterloo.ca/~migod/research/beck00PSLA.html>

ZUSAMMENFASSUNG

Kurze Zusammenfassung des Inhaltes in deutscher Sprache...

ACKNOWLEDGMENTS

Put your acknowledgments here.

CONTENTS

1	INTRODUCTION	1
1.1	The AGN-Host Galaxy Connection	1
1.2	Measuring Black Hole Masses	1
1.2.1	Reverberation Mapping	2
1.2.2	Single-Epoch Virial Estimates	2
1.3	Orientation-Based Unification Models	3
1.4	Evolutionary Models	5
1.5	Interesting Sub-Populations	6
1.5.1	Red and Reddened Quasars	6
1.5.2	Broad Absorption Line Quasars	7
1.5.3	Hot-Dust-Poor Quasars	7
1.5.4	Type II Quasars	8
1.6	Spectral Energy Distributions	8
2	A NEAR-INFRARED SPECTROSCOPIC DATABASE OF HIGH-REDSHIFT QUASARS	11
2.1	Introduction	11
2.2	Sample Selection for LIRIS/NTT Program	14
2.3	C _{IV} blueshifts in the quasar population	15
2.3.1	Quasar systemic redshifts	15
2.3.2	C _{IV} emission line blueshift measurements	18
2.3.3	Sample selection - C _{IV} properties	19
2.3.4	Relation to virial BH mass estimates	19
2.4	Observations	21
2.5	Emission line measurements	24
2.5.1	C _{IV}	24
2.5.2	H α	27
2.5.3	Comparison of H α and H β profiles	27
2.5.4	Emission line parameters	28
2.5.5	Emission line parameter uncertainties	32
2.6	Results	34
2.6.1	Characterising the emission-line profiles	35
2.6.2	Computing BH mass estimates	38
2.6.3	C _{IV} -derived BH masses at low C _{IV} blueshift	38
2.6.4	C _{IV} -derived BH masses at high C _{IV} blueshift	39
2.6.5	Population trends with C _{IV} blueshift	42
2.7	Discussion	43
2.7.1	Biases in single-epoch C _{IV} -based BH-mass estimates	43
2.7.2	Possible systematic trends in H α BH-mass estimates	45
2.7.3	Accretion-rate trends in the quasar population	47

2.7.4	The BAL parent population	48
2.7.5	The frequency of quasars with high accretion rates	48
2.8	Conclusions	49
3	BLACK HOLE MASSES	51
3.1	Introduction	51
3.2	Quasar Sample	53
3.2.1	Near-infrared observations	54
3.2.2	Optical observations	59
3.3	Spectral Measurements	59
3.3.1	CIV	61
3.3.2	H α	62
3.3.3	H β and [O III]	62
3.3.4	Fitting procedure	63
3.3.5	Spectra removed from sample	63
3.3.6	Emission-line parameter uncertainties	66
3.3.7	Contemporaneity of spectra	67
3.3.8	Quasar monochromatic luminosity	67
3.4	An empirical correction to C IV-based virial BH-mass estimates	69
3.4.1	H α /H β FWHM comparison	69
3.4.2	Measuring the quasar systemic redshift	73
3.4.3	Balmer/C IV line widths as a function of C IV-blueshift	74
3.4.4	C IV based virial BH mass estimates	76
3.5	Practical application of the C IV-based correction to virial BH-mass estimates	79
3.5.1	Recipe for unbiased C IV based BH masses	79
3.5.2	Systematic trends in residuals	80
3.5.3	Effectiveness of the C IV blueshift based correction to BH masses	82
3.5.4	Comparison to previous prescriptions	86
3.6	Conclusions	88
3.7	Comparison to Shen	89
4	NARROW LINE REGION PROPERTIES	91
4.1	Introduction	91
4.2	Quasar Sample	92
4.3	Parameteric Model Fits	94
4.3.1	Derived Parameters	95
4.3.2	Other flags	105
4.4	ICA Component Fits	105
4.5	Measuring the quasar systemic redshift	105
4.5.1	H α	105
4.5.2	ICA	106
4.5.3	Parameter uncertainties and upper limits	107

4.5.4	Absolute flux calibration of spectra and continuum luminosities	107
4.6	Results from ICA fits	108
4.7	Luminosity/redshift-evolution of [O III] properties	108
4.8	Equivalent width	109
4.8.1	OIII outflows	111
4.8.2	[O III] and C IV outflows are linked	112
4.9	Eigenvector one correlations	114
4.10	Signal to noise tests	115
4.11	Broad Absorption Line Quasars	115
4.12	Discussion	115
4.12.1	Type II quasars	115
5	SECOND YEAR REPORT	117
5.1	Introduction	117
5.2	Future Work	118
6	HOT DUST	119
6.1	Data	119
6.2	Surveys	119
6.2.1	The Sloan Digital Sky Survey	119
6.2.2	UKIDSS Large Area Survey	121
6.2.3	WISE All-WISE Survey	122
6.3	Completeness of Photometry	123
6.4	SED Model	125
6.5	Model Components	125
6.5.1	Accretion Disk	125
6.5.2	Hot Dust	126
6.5.3	Emission Lines	126
6.5.4	Host Galaxy	127
6.5.5	Lyman- α Forest Absorption	129
6.5.6	Lyman-Limit Systems	130
6.5.7	Dust Extinction	130
6.6	Converting Spectrum into Observed SED	131
6.7	Results From Fit	133
6.8	Fitting Procedure	133
6.8.1	The ‘Standard’ SED Model	133
6.8.2	Discussion of Fit	134
6.9	Reddened Quasars	137
6.9.1	Colour Selection	138
6.9.2	Model Fitting	140
6.9.3	MCMC Fitting	141
6.9.4	Acquiring Near-IR Spectroscopy	142
6.10	Hot Dust	144
6.10.1	Defining Sample	146
6.10.2	Flux Correction	147
6.11	Results From Blackbody Fit	148

6.12	Conclusions and Future Work	149
6.13	Draft Paper	151
6.14	Introduction	151
6.15	Data	152
6.16	UV Spectra Parameters	153
6.17	Model Description	153
6.17.1	Sample	155
6.18	Results	155
6.19	Hot Dust	155
6.19.1	Low-z Results	158
6.20	Results From Blackbody Fit	158
6.20.1	Results 1: β_{NIR} , T_{BB} , $R_{\text{UV/NIR}}$	158
6.20.2	Results 2: Redshift	159
6.20.3	Results 3: Luminosity	159
6.20.4	Results 4: Eddington Ratio/ Black Hole Mass	159
6.20.5	CIV Emission Line Properties	159
6.20.6	Reddening	159
6.20.7	BALs	159
6.20.8	RL/RQ	166
6.21	WHT Telescope Proposal	166
6.22	NTT Proposal	171
6.23	Future Work	173
7	CONCLUSIONS / FUTURE WORK	177
	BIBLIOGRAPHY	193

LIST OF FIGURES

- Figure 1 Illustration of the physical structure of an AGN in a simple orientation-based unification model. From Urry and Padovani, (1995). 3
- Figure 2 Median SEDs for radio-loud and radio-quiet quasars from Shang et al., (2011). 8
- Figure 3 Rest-frame EW versus blueshift of the broad C_{IV}-emission line for 32,157 SDSS DR7 quasars at $1.6 < z < 3.0$ (grey) and our sample (orange). Panel (a) uses C_{IV} line parameters from Shen et al., (2011) and SDSS pipeline systemic redshifts. Panels (b) and (c) use systemic redshifts from Hewett and Wild, (2010) and Allen & Hewett (2016, in preparation) respectively, and C_{IV} line measurements described in Sec. 2.3.2. In regions of high point-density, contours show equally-spaced lines of constant probability density generated using a Gaussian kernel-density estimator. The three rectangles in panel (b) show the regions of parameter space used to generate the composite spectra shown in Fig. 4. 16
- Figure 4 Composite spectra of the C_{IV}-emission line as a function of C_{IV} blueshift for SDSS DR7 quasars. The quasars contributing to each composite are indicated in Fig. 23b. Virtually the entire C_{IV}-profile appears to shift blueward and the change in line shape is not simply an enhancement of flux in the blue wing of a still identifiable symmetric component. In order of increasing C_{IV} blueshift, the composite spectra have FWHM 4870, 5610, and 6770 km s⁻¹ and EW 33.1, 31.6, and 28.8 Å. 20
- Figure 5 LIRIS spectrum of SDSSJ1246+0426. The gap between the H and K bands ($\sim 5500\text{--}6300\text{ \AA}$) has been greyed-out. 23

- Figure 6 2nd-order Gauss-Hermite (GH) polynomial and 3-component Gaussian fit to the C IV-emission line of SDSSJ0858+0152, which is the most blueshifted in our sample. We derive line parameters from the GH polynomial fit; using the Gaussian model changes the FWHM, line dispersion, and blueshift by -250, -150, and 500 km s^{-1} respectively. For the C IV lines of all other quasars in our sample the GH polynomial and Gaussian models provide equally good fits. [26](#)
- Figure 7 The H α and H β emission line regions in the median composite spectrum, shown as function of the velocity shift from the respective predicted line peak wavelengths. The line fluxes have been scaled in order for the profile shapes to be readily compared. The H α and H β line profiles are very similar, which suggests a tight correlation between the H α and H β line widths. Quasar narrow-line emission from O III $\lambda 5008.2$ is visible but, overall, the O III $\lambda\lambda 4960, 5008$ emission is relatively weak in these spectra. [28](#)
- Figure 8 C IV (SDSS/BOSS) and H α (LIRIS) emission lines and best-fitting model. Δv is the velocity shift from the line rest-frame transition wavelength, with the systemic redshift defined using the centroid of the fit to H α . Objects are presented in order of increasing C IV blueshift relative to the H α centroid. Below each fit we plot the data-model residuals, scaled by the errors on the fluxes. [30](#)
- Figure 8 *Continued* [31](#)
- Figure 9 The FWHM, dispersion (σ) and shape (FWHM/ σ) of C IV and H α as a function of the C IV blueshift. The vertical line demarcates the ‘high’ and ‘low’ C IV blueshift regimes discussed in the text. At high blueshift it is clear that BH masses estimated from the C IV FWHM (as is typically done at the redshifts considered) will be significantly larger than those estimated from the H α FWHM. [35](#)

- Figure 10 Comparison of the C IV line profiles of SDSSJ₁₂₃₆₊₁₁₂₉ and SDSSJ₁₅₂₅₊₀₄₂₆. Notwithstanding the essentially identical dispersion values, the emission-line velocity fields differ dramatically and, therefore, the dispersion values cannot be measuring accurately the virial-induced velocity spread of the C IV emission in both quasars. 37
- Figure 11 Comparison of virial BH mass estimates based on the C IV FWHM (*top*) and dispersion σ (*bottom*) and H α FWHM as a function of the C IV blueshift. The horizontal line indicates agreement between C IV and H α BH masses, and the vertical line demarcates the ‘high’ and ‘low’ C IV blueshift regimes discussed in the text. The BH masses of quasars with moderate C IV blueshifts are underestimated when using the C IV FWHM, while the masses of quasars with large blueshifts are severely overestimated. This situation cannot be corrected by changing the exponent on the FWHM (e.g. Rafiee and Hall, 2011; Park et al., 2013) or the overall scaling in standard virial BH mass relations. 40
- Figure 12 H α -derived Eddington ratio versus C IV blueshift. At blueshift $\gtrsim 2000 \text{ km s}^{-1}$ all quasars have high accretion rates ($L/L_{\text{Edd}} \simeq 1$). This is in agreement with Kratzer and Richards, (2015), but in contrast to what one would derive from naive use of C IV-based BH mass scaling relations. 42
- Figure 13 Comparison of BH mass estimates derived from the FWHM of C IV and H α as a function of the C IV blueshift (*black circles*), and after applying corrections to the C IV-derived mass based on the line shape (*blue triangles*; Denney, 2012) and the peak flux ratio of the Si IV+O IV blend relative to C IV (*red squares*; Runnoe et al., 2013a). While the shape-based correction improves the consistency between BH mass estimates in the low-blueshift population, only the Si IV+O IV/C IV peak flux-based correction is effective at high blueshifts (although a weak systematic remains). 45

- Figure 14 The ranges in redshift and luminosity covered by our sample, relative to the redshift-luminosity distribution of the SDSS DR7 quasar catalogue. In regions of high point-density, contours show equally-spaced lines of constant probability density generated using a Gaussian kernel-density estimator. For the SDSS sample we use Hewett and Wild, (2010) redshifts and bolometric luminosities measured by Shen et al., (2011). For the quasars in this paper the redshift is defined using the peak of the H α /H β emission and the luminosity is measured in the continuum at 1350Å and converted to a bolometric quantity using the same conversion factor employed by Shen et al., (2011). 55
- Figure 15 Model fits to continuum-subtracted H α , H β , and C IV emission in six quasars, chosen to represent the range of S/N (indicated in the figure and given per 150km s $^{-1}$ pixel in the continuum) and line shapes present in the catalogue. The data is shown in grey, the best-fitting parametric model in black, and the individual model components in orange. The centroid of the broad H α emission is used to set the redshift, and Δv is the velocity shift from the line rest-frame transition wavelength. Below each fit we plot the data minus model residuals, scaled by the errors on the fluxes. 65
- Figure 16 The redshift and luminosity distributions of the spectra removed from our H α /C IV (a, b) and H β /C IV (c, d) samples. 66
- Figure 17 Comparison of H α and H β FWHM measurements for 99 quasars. The solid line is our best-fitting power-law model, and the blue-shaded region shows the 2- σ uncertainties on the model parameters. The dashed line is the relation found by Greene and Ho, (2005) using a sample of $z < 0.35$ SDSS AGN. 70
- Figure 18 One- and two-dimensional projections of the MCMC sampling of the posterior distribution from the fit in Fig. 17. α is the power-law index, 10^β is the normalisation, and σ_I is the intrinsic scatter. In the two-dimensional projections, 1- and 2- σ contours are shown. 72

- Figure 19 C_{IV} FWHM relative to H α FWHM (a) and H β FWHM (b), and C_{IV} based BH mass (BHM) compared to H α based mass (c) and H β based mass (d), all as a function of the C_{IV} blueshift. The black line is our best-fit linear model, and the shaded region shows the 2- σ uncertainties on the slope and intercept. The H α FWHM have been scaled to match the H β FWHM using Eq. 5. 75
- Figure 20 One- and two-dimensional projections of the MCMC sample of the posterior distribution for a linear fit to the FWHM C_{IV}/H α ratio as a function of the C_{IV} blueshift. In the two-dimensional projections we show 1- and 2- σ contours. The posterior distribution for the linear fit to the FWHM C_{IV}/H β ratio, which we do not show, has a very similar appearance. 77
- Figure 21 The distribution of the orthogonal displacement of each data point from the best-fitting linear relationship in the fit to FWHM(C_{IV})/FWHM(H α) as a function of the C_{IV} blueshift (blue histogram). The black curve is a Normal distribution with a width equal to the intrinsic scatter in the population inferred from the fit. The two distributions are well-matched, which demonstrates that our model is a good representation of the data and the measurement errors on the data points are small relative to the intrinsic scatter. 78
- Figure 22 Same as Fig. 19a, with the marker colour representing the H α FWHM. At fixed C_{IV} blueshift, there is a clear H α FWHM dependent systematic in the model residuals. 82

- Figure 23** Rest-frame EW versus blueshift of the broad C_{IV}-emission line for 32,157 SDSS DR7 quasars at $1.6 < z < 3.0$ (*grey*) and our sample (*blue*). For the SDSS quasars, the systemic redshifts used to calculate the blueshifts are from Hewett and Wild, (2010) and C_{IV} emission properties are described in Paper I. In regions of high point-density, contours show equally-spaced lines of constant probability density generated using a Gaussian kernel-density estimator. Our sample has very good coverage; the shift to high blueshifts is a result of the high luminosity of our sample in relation to the SDSS sample and the correlation between luminosity and blueshift. 83
- Figure 24** Comparison of the C_{IV}- and H α -based BH masses before (a) and after (b) applying the C_{IV} blueshift-based correction to the C_{IV} FWHM. The density of the plotted points (estimated using a Gaussian kernel density estimator) is represented by the colour. The correction to the C_{IV} BH masses decreases the scatter by from 0.4 to 0.2 dex. 84
- Figure 25** Comparison of the C_{IV} and H α line dispersion, σ . The density of the plotted points (estimated using a Gaussian kernel density estimator) is represented by the colour. Estimating a reliable BH mass from the C_{IV} FWHM and blueshift line is substantially more effective than using the C_{IV} line dispersion with, or without, the line blueshift. The C_{IV} dispersion values are larger than the corresponding H α measurements by a factor of 1.4 on average, which is consistent with reverberation mapping measurements (Vestergaard and Peterson, 2006). 85
- Figure 26** Comparison of BH mass estimates derived from C_{IV} and H α as a function of the C_{IV} blueshift. Corrections to the C_{IV}-based masses have been applied based on the shape (FWHM/ σ) of the C_{IV} emission line (a; Denney, 2012), the peak flux ratio of the Si_{IV}+O_{IV} blend relative to C_{IV} (b; Runnoe et al., 2013a), by significantly reducing the dependence of the derived BH mass on the C_{IV} velocity-width (c; Park et al., 2013), and based on the C_{IV} blueshift (d; this paper). 87

- Figure 27 Demonstration of the effectiveness of our line parameter estimation scheme via a comparison of (a) the H β FWHM with Shen, (2016), (b) the H β FWHM with Shen and Liu, (2012), and (c) the C IV FWHM with Shen et al., (2011). 90
- Figure 28 The ranges in redshift and luminosity covered by our sample, relative to the redshift-luminosity distribution of the SDSS DR7 quasar catalogue with measured [O III] line properties (Shen et al., 2011). The gaps in our sample coverage at $z \sim 1.8$ and $z \sim 3$ are due to the near-infrared transmission windows. In regions of high point-density, contours show equally-spaced lines of constant probability density generated using a Gaussian kernel-density estimator. 92
- Figure 29 Multi-component Gaussian fits to the continuum-subtracted H β /[O III] emission in 16 quasars, chosen to be the representative of the wide range of [O III] line widths we measure in our sample. The data is shown in grey, the best-fitting parametric model in black, and the individual model components in orange. The broad H β centroid is used to measure the systemic redshift, and Δv is the velocity shift from the line rest-frame transition wavelength for H β . Below each fit we plot the data minus model residuals, scaled by the errors on the fluxes. **Resample model at higher resolution.** 96
- Figure 30 The relative weight in each of the six positive ICA components for the high-luminosity (blue) and low luminosity samples (grey). In the high-luminosity sample Fe II emission is stronger (component w_1). The core [O III] emission is weaker (components w_4, w_5) but the strength of the blueshifted wing is the same (w_6). 97

- Figure 31 The relative weight in the three ICA components corresponding to [O III] emission (*left*) and the relative weight of the component most closely related to blueshifted [O III] emission relative to all three [O III] components (*right*). [O III] emission is weaker in the high-luminosity sample, but the relative contribution but the fractional contribution from the blueshifted component to the total [O III] emission is higher. Hence [O III] is weaker, broader, and more asymmetric in the high-luminosity sample. See Zakkamska discussion. 98
- Figure 32 Comparison of [O III] velocity-widths in the high and low luminosity samples using the ICA component fits. If keep this need to explain in text how w_{80} is calculated from ICA component fits. 98
- Figure 33 Black solid line is the median from the ICA fits to the high-luminosity sample. Black dashed line shows the median from the low-luminosity sample. The six positive ICA components are also shown. 99
- Figure 34 [O III] strength decreases as the C IV blueshift increases, I run in to problems comparing the C IV blueshift to the [O III] blueshift / velocity-width. See similar thing if I use [O III] EQW instead. Need to fix y ticks. Only showing the core components here. The C IV blueshift is now measured relative to the NIR ICA redshift. I think this is trend is mostly being driven by the Eigenvector 1 correlations: as the blueshift increases the Fe II strength increases and the [O III] strength decreases. Doesn't appear to be driven by the luminosity. Is this tighter than EV1 trend shown with Fe/OIII strength by other authors? 100
- Figure 35 I think there is a trend here but at high blueshifts the OIII is undetected / very low S/N. Need to determine when we can believe OIII parameters. Why at low CIV blueshift is there a much bigger dynamic range than in [O III] blueshifts in Fig. 13. Is it just because we have more objects? 101
- Figure 36 Comparison of median [O III] profiles from ICA fits for low- and high-luminosity samples. 102

Figure 37	ICA median weights as a function of the CIV blueshift. 103
Figure 38	Example where poorly subtracting the iron can be confused with [O III]. 103
Figure 39	104
Figure 40	Redshift comparisons. Lots have been excluded from Ha/Hb so need to look at flags greater than one. What is the big peak? 105
Figure 41	The [O III] velocity-width, characterised by w_{80} , as a function of the [O III] luminosity and the quasar redshift. The color of each hexagon denotes the mean w_{80} for the objects in that luminosity-redshift bin. We have supplemented our sample with low- z objects from Zakamska and Greene, (2014) and medium ($z \sim 1.5$) redshift objects from Harrison et al., (2016). If I keep this plot make sure its clear which points belong to which sample. 108
Figure 42	The [O III] EW as a function of the quasar bolometric luminosity for the sample presented in this paper (blue circles) and the low- z SDSS sample (grey points and contours). Upper limits are denoted by the downward arrows. 110
Figure 43	The distributions of and correlations between a subset of the non-parameteric measures we made of the best-fitting [O III] models. 111
Figure 44	The relation between the blueshifts of C IV and [O III]. Equivalent to Fig 8. We use the H β peak in this figure, which I think is responsible for some of the trend. However, we do see a correlation (albeit noisier) using the NIR ICA redshifts. Not a sensible to use the [O III] redshifts, since these become much more unreliable at the high C IV blueshift end (when [O III] is weaker: figure 7. Note that we are using v_{10} for the [O III] position and v_{50} for the C IV position. We can't use v_{50} for [O III] because sometimes we are using a single Gaussian, especially if the [O III] is weaker and we miss the broad component. Need to remake this plot / don't use at all because I don't believe some of the Gaussian fits to [O III], especially at high C IV blueshifts when [O III] is weak and Fe II is strong.) Only objects where fit with two components. 113
Figure 45	114

- Figure 46 The [O III] EQW as a function of the H β FWHM and the optical Fe II strength (EQW Fe II/ EQW H β). [115](#)
- Figure 47 The distribution of w_{80} and v_{10} for the 19 BALs are compared to the distribution for the non-BALs. These look rubbish. Cumulative distributions instead? [116](#)
- Figure 48 Black-body temperature plotted (from *left* to *right*) as a function of the ultra-violet luminosity, the black-hole mass and the Eddington ratio. [117](#)
- Figure 49 *Left:* Ratio of $\text{FWHM}_{\text{CIV}}^2$ and $\text{FWHM}_{\text{H}_\alpha}^2$ plotted as a function of the CIV blue-shift. *Right:* $\text{FWHM}_{\text{H}_\alpha}^2$ plotted as function of CIV equivalent width. Note how at high blue-shifts CIV-based BH masses will be overestimated, and how, at low CIV equivalent width, the H α -based BH masses are systematically lower for the quasars with blue-shifted CIV. [118](#)
- Figure 50 Histograms comparing the DR7Q and DR10Q catalogues: *Top:* Redshift distribution; *Middle:* Distribution of apparent i-band magnitudes; *Bottom:* Distribution of absolute i-band magnitudes **missing this.** [121](#)
- Figure 51 *Top:* Fraction of objects which were matched to DR7Q catalogue with WISE and UKIDSS photometry ($\text{SNR} > 5$) as a function of minimum i-band magnitude of the sample (*coloured lines*). Total number of objects in DR7Q catalogue as function of minimum i-band magnitude (*black dashed line*). Primary quasar colour selection minimum i magnitude (*grey line*). *Bottom:* Fraction of objects which were matched to DR10Q catalogue with WISE and UKIDSS photometry ($\text{SNR} > 5$) as a function of minimum g-band magnitude of sample (*coloured lines*). Total number of objects in DR10Q catalogue as function of minimum g-band magnitude (*black dashed line*). Primary quasar colour selection minimum g magnitude (*grey line*). [124](#)
- Figure 52 Model spectrum at $z = 1$, showing the contributions to the total flux from the blue power-law slope, red power-law slope, blackbody and host galaxy. The locations of the most prominent emission lines in the spectrum are also indicated. [125](#)

- Figure 53 Model spectrum at three different redshifts (each arbitrarily scaled), and throughput functions for SDSS, UKIDSS and WISE band-passes (scaled so that the peak transmission is equal to one.) The dashed line indicates the slope of the AB magnitude system zero point. [131](#)
- Figure 54 Colours of median SED (*black circles*), individual objects (*grey points*), best-fitting uncorrected model (*black line*) and best-fitting corrected model (*red line*) as a function of redshift. [136](#)
- Figure 55 Residuals from fit to DR7Q-matched catalogue as a function of rest-frame wavelength. [137](#)
- Figure 56 $i - K$ colours of DR10Q-matched catalogue quasars as a function of redshift z (*grey points*). $i - K$ colours of ‘standard’ SED model as a function of redshift z with dust reddening $E(B-V)=0.0$, 0.1 , and 0.2 (*black lines*). [139](#)
- Figure 57 SDSS spectra of two quasars with red $i - K$ colours relative to our unreddened SED model. Whereas the optical spectrum of SDSS J_{150019.64+082643.6} suggests it may be a genuinely dust-reddened quasar, the red colour of SDSS J_{0240000.6+010317.0} is probably due to strong H α emission in the K band-pass. [139](#)
- Figure 58 Dust reddening $E(B-V)$ and emission line equivalent width distributions from SED fitting. [140](#)
- Figure 59 Fraction of quasars in 3,117 object sample which are best fit by models with emission line equivalent width scaling parameter < 0.01 as a function of redshift. [141](#)
- Figure 60 Posterior plots from MCMC fit to SDSS J_{121956.49-011907.8}. [143](#)
- Figure 61 $W1 - W2$ colours of DR7 sample as a function of redshift, up to $z = 1.8$. Above a certain density threshold points are represented by a density plot. On top we plot our standard model, with a blackbody temperature varying from 1000 - 1600 K (*top figure*) and a blackbody normalisation between 0 and 0.5 (*bottom figure*). [145](#)

Figure 62

Top: Residuals from fitting the overall normalisation of the SED as a function of wavelength in the quasar rest frame. The different lines correspond to 101-point running medians for the H, K, W1 and W2 band-passes, and have been colour-coded to indicate the redshift for which the given quasar rest frame wavelength corresponds to the un-redshifted effective wavelength of the band-pass. The black line is a cubic interpolation of a 801-point running-median through all residuals, irrespective of the band-pass used. The red dashed line marks the wavelength of the Pa α emission line. *Bottom:* The spectral model before and after the flux correction (see main text). [147](#)

Figure 63

Blackbody temperature from fit against redshift before correction (grey circles). Black line is running median through blackbody temperatures before correction, blue line is running median after correction. [149](#)

Figure 64

Model spectrum at $z = 1$, showing the contributions to the total flux from the blue power-law slope, red power-law slope, blackbody and host galaxy. The locations of the most prominent emission lines in the spectrum are also indicated. [153](#)

Figure 65

$i - K$ vs z . Demonstrates how sample was defined. The grey points show, as a function of redshift, the $i - K$ colours of all DR7Q quasars which are not classified as broad-absorption line quasars by Shen et al. and i magnitude > 19.1 . The black line shows the $i - K$ colour of our standard, unreddened SED model as a function of redshift. The red and blue lines show the $i - K$ colours of our SED model with dust reddening $E(B-V) = 0.075$ and $E(B-V) = -0.075$ respectively. A significant amount of this reddening can be attributed to intrinsics variations in the UV power-law slopes of the individual quasars, which is why we allow a negative reddening. However, there is a clear ‘red tail’ to the colour distribution which can be explained by dust reddening at the redshift of the quasar. We defined two samples, at low ($0.5 < z < 1.5$) and high ($2 < z < 2.7$) redshift, which are shown in the figure. [155](#)

Figure 66 W1 – W2 colours of DR7 sample as a function of redshift, up to $z = 1.8$. Above a certain density threshold points are represented by a density plot. On top we plot our standard model, with a blackbody temperature varying from 1000 - 1600 K (*top figure*) and a blackbody normalisation between 0 and 0.5 (*bottom figure*). Around $z = 1.5$ the model no longer appears to be a very good fit to the data, which I suppose is just the fact that the blackbody is turning over, whereas in the data the flux keeps increasing (additional contributions from cooler components.) Add ticks to top of top panel. Think about how useful these plots really are. In top plot I'm changing the temperature, which is changing the normalisation (Lum IR). This is effectively same as bottom plot, except here I'm keeping the shape the same, just moving it up and down. Even if this is fine these plots are probably a bit misleading as they are (need to be clear normalisation will also be changing in the top plot. [156](#)

Figure 67 [159](#)

Figure 68 Need to somehow show the uncertainty in the parameters and demonstrate how the spread is real and not just due to the uncertainties in the photometry. [159](#)

Figure 69 [160](#)

Figure 70 Colour-bar might not be accurate for each subfigure. CIV blueshift also positively correlated with Eddington Ratio. [161](#)

- Figure 71 Plot of the near-IR/ultra violet luminosity ratio ($R_{\text{NIR/UV}}$) against the NIR power-law slope for the low- z sample. The NIR lumionsity is measured by integrating the best-fit model spectrum (with a black body component) in the rest-frame of the quasar between 0.2 and 1 μm . The NIR power-law slope is fit between 1 and 2.4 μm (although the exact wavelength region being fit depends on the redshift of the quasar; see somewhere else). This allows us to extend our investigation to high- z , where we are unable to constrain both the temperature and normalisation of the black-body component, but can constrain the slope of a single power-law. Included the second plot because I want to emphasise that the density of points is not constant - i.e. if you measure a certain value for beta, say 0.6, it's much more likely to be around (1200,0.2) than it is, say, (1100,0.3). Must be some way of quantifying this. [162](#)
- Figure 72 fgh [163](#)
- Figure 73 IR/UV luminosity ratio versus black hole mass (Shen et al.) for high- z sample. Fairly strong negative correlation. We believe that this is just a manifestation of the fact that at high redshift the blackhole masses are derived from CIV. We already know that the FWHM of CIV has a positive correlation with the hot dust abundance, and large CIV FWHM leads to larger black hole mass estimates. This explains the apparent correlation between the IR/UV ratio and the black hole mass. Eddington ratio measures the luminosity relative to the Eddington luminosity. Higher blackhole mass estimates will lead to lower Eddington ratios, which is why the Eddington ratio appears to decrease with increasing IR/UV ratio. [163](#)
- Figure 74 Now using same high-redshift sample as Figure 8 (with cut on beta uncertainty). I'm only plotting where I have a miniumum of two objects per bin, which is probably not acceptable. Clear non-virial component to CIV line - caveat about CIV based black hole masses. [164](#)

- Figure 75 Plot E(B-V) versus β . Just fit $E(B-V) < 1$ micron and $z > 1$ to avoid galaxy contribution. No cuts made to sample. No correlation/weak negative. [164](#)
- Figure 76 High-z only since very few BALs in low-z sample. β on x-axis. BALs clearly have bigger NIR slopes, so I would expect to also see β increase with $E(B-V)$, which I don't. [165](#)
- Figure 77 Weak negative correlation for core-dominated sources and weak positive correlation for lobe-dominated sources. [165](#)
- Figure 78 Radio-loud objects appear to have less hot dust on average. Statistically at least, the "radio-loud" objects are thought to have high black-hole masses and there is some form of radio-mode feedback (jet related) which is very different from the much more common (almost certainly wider opening-angle) outflow objects with large CIV-blueshifts. [166](#)
- Figure 79 Figure 1: The rest-frame equivalent width of the CIV line plotted against a measure of its blueshift, for 1,464 SDSS DR7 quasars. The red circles represent hot-dust ($T \approx 1200$ K) rich quasars which have the steepest near-infrared slopes (measured by fitting single power-law beyond 1 μm in the quasar rest-frame). The blue triangles represent quasars that are hot dust poor (i.e. have the shallowest near-infrared slopes). Quasars with the most extreme outflow signatures (in box C) are hot-dust rich. The measure of the CIV-emission blueshift is obtained from the wavelength of the centroid of the emission line relative to the predicted location for emission at the systemic velocity of each quasar. Systemic redshifts are obtained from Hewett and Wild (2010). [170](#)
- Figure 80 Rest-frame model quasar spectra for the hot-dust rich and hot-dust poor subsamples, corresponding to $\beta_{\text{NIR}} = 0.85$ and $\beta_{\text{NIR}} = -0.09$ respectively. Circles are observed fluxes for individual objects in the WISE W₁, W₂, and W₃ bands, transformed to the rest frame of the quasar. [170](#)

Figure 81

Rest-frame equivalent width and blueshift of the C₄ line for 7,115 SDSS DR7 quasars. The colours of the hexagons denote the median hot dust ($T \simeq 1200$ K) abundance for all quasars at a given equivalent width and blueshift. The hot dust abundance is parameterised by fitting a single power-law with slope β_{NIR} beyond 1 μm in the quasar rest-frame. Quasars with the most extreme outflow signatures (in region C) are predominantly hot-dust rich. The C₄ emission line blueshift is obtained from the wavelength of the centroid of the emission line relative to the predicted location for emission at the systemic velocity of each quasar. Systemic redshifts are obtained from Hewett and Wild (2010). [173](#)

Figure 82

Representative rest-frame model spectra for the most hot-dust rich and hot-dust poor quasars in our SDSS sample, with error bars indicating the range of WISE W₁, W₂, and W₃ magnitudes for the objects in these subsamples, transformed to the rest frame of the quasar. Grey lines show the W₁, W₂, and W₃ fluxes for our sample of highly reddened quasars. [174](#)

Figure 83

Black-body temperature plotted (from *left* to *right*) as a function of the ultra-violet luminosity, the black-hole mass and the Eddington ratio. [174](#)

LIST OF TABLES

Table 1

Summary of near-infrared spectroscopic observations with LIRIS. [22](#)

Table 2

Summary of the fitting regions and the parameters of the models used to fit the C_{IV} and H α emission lines. [25](#)

Table 3

Summary of emission line properties derived from parametric model fits to H α and C_{IV}. [29](#)

Table 4

Monochromatic continuum luminosities used to derive bolometric luminosities and BH masses. [33](#)

Table 5	The numbers of quasars with reliable H α and H β line measurements, the spectrographs and telescopes used to obtain the near-infrared spectra, and the instrumental configurations. 56
Table 6	The format of the table containing the emission line properties from our parametric model fits. The table is available in machine-readable form in the online journal. 64
Table 7	The number of spectra removed from our sample by the cuts described in Section 3.3.5 . 64
Table 8	The fractional error on the corrected BH mass as a function of C IV blueshift for different uncertainties in the quasar systemic redshift. 80
Table 9	The numbers of quasars with [O III] line measurements and the spectrographs and telescopes used to obtain the near-infrared spectra. Further details on the instrumental configurations are given in paper I. Check numbers. 93
Table 10	Approximate physical origin of the ICA components. 95
Table 11	Vega to AB magnitude conversion factors for UKIDSS (Hewett et al., 2006) and WISE (Cutri et al., 2013) photometry. 122
Table 12	Best-fitting parameters from fit to DR7Q-matched sample. 134

LISTINGS

ACRONYMS

INTRODUCTION

1.1 THE AGN-HOST GALAXY CONNECTION

Super-massive black holes (BHs) are found at the centres of most nearby massive galaxies and the BH mass and mass of the host galaxy spheroid are strongly correlated (Ferrarese and Merritt, 2000; Gebhardt et al., 2000; Kormendy and Ho, 2013). Although any underlying causal mechanism(s) responsible for the correlation is yet to be conclusively identified, there is considerable observational and theoretical support for models that involve BH-fuelling, outflows and a ‘feedback’ relationship (e.g. King and Pounds, 2015). The number density of quasars, which evolves strongly with redshift, peaks at redshifts $2 \lesssim z \lesssim 3$ (e.g. Brandt and Hasinger, 2005; Richards et al., 2006b) and the most massive ($M_{\text{BH}} \gtrsim 10^9 M_{\odot}$) present-day BHs experienced much of their growth during this epoch. The star formation rate, which closely follows the cosmological evolution of the quasar luminosity function, also peaks during this epoch (e.g. Boyle and Terlevich, 1998). Quantifying the growth-rate of massive BHs at $2 \lesssim z \lesssim 3$ would therefore help significantly in understanding the role quasars play in galaxy evolution.

There is now considerable observational and theoretical support for models of galaxy formation that involve black hole-fuelling, outflows and a ‘feedback’ relationship between active black holes and star formation in the host galaxy. Super-massive black holes accreted most of their mass and galaxies formed most of their stars at redshifts $z \gtrsim 2$ (e.g. Madau & Dickinson 2014 for star formation; find quasar reference.) During this key cosmological epoch star formation is believed to be suppressed by the energy output from the quasar, establishing the tight relationship between BH mass and host galaxy spheroid mass observed in the local Universe (e.g. Kormendy & Ho 2013).

1.2 MEASURING BLACK HOLE MASSES

The goal of better understanding the relationship between super-massive BH accretion and star formation has led to much work focussing on the properties of quasars and active galactic nuclei at these redshifts. Accurate BH mass estimates for quasars are essential in these studies. Furthermore, as one of just two fundamental quantities describing a black hole on astrophysical scales, the mass is of crucial importance

to virtually all areas of quasar science, including the evolution and phenomenology of quasars, and accretion physics.

1.2.1 Reverberation Mapping

Reliable estimates of BH masses are a prerequisite for investigating the relationship between BHs and their host galaxies. If the line-emitting clouds in the broad line region (BLR) are assumed to be virialized and moving in a potential dominated by the central BH, then the BH mass is simply a product of the BLR size and the square of the virial velocity. The reverberation-mapping technique uses the time lag between variations in the continuum emission and correlated variations in the broad line emission to measure the typical size of the BLR (Peterson, 1993; Peterson, 2014). The full width at half maximum (FWHM) or dispersion (σ ; derived from the second moment) velocity of the prominent broad emission line of H β (4862.7Å)¹ is used as an indicator of the virial velocity, with extensions to other low-ionization emission lines such as H α (6564.6Å) and Mg II $\lambda\lambda$ 2796.4,2803.5 (e.g. Vestergaard, 2002; McLure and Jarvis, 2002; Wu et al., 2004; Kollmeier et al., 2006; Onken and Kollmeier, 2008; Wang et al., 2009; Rafiee and Hall, 2011). Extensive reverberation mapping campaigns have provided accurate BH masses for \sim 50 active galactic nuclei (AGN) at relatively low redshifts and of modest luminosity (e.g. Kaspi et al., 2000; Kaspi et al., 2007; Peterson et al., 2004; Bentz et al., 2009; Denney et al., 2010). [See galaxies talk for a few more details]

1.2.2 Single-Epoch Virial Estimates

Reverberation mapping campaigns have also revealed a tight relationship between the radius of the BLR and the quasar optical (or ultraviolet) luminosity (the R – L relation; e.g. Kaspi et al., 2000; Kaspi et al., 2007). This relation provides a much less expensive method of measuring the BLR radius, and large-scale studies of AGN and quasar demographics have thus become possible through the calibration of single-epoch virial-mass estimators using the reverberation-derived BH masses (e.g. Greene and Ho, 2005; Vestergaard and Peterson, 2006; Vestergaard and Osmer, 2009; Shen et al., 2011; Shen and Liu, 2012; Trakhtenbrot and Netzer, 2012). The uncertainties in reverberation mapped BH masses are estimated to be \sim 0.4 dex (e.g. Peterson, 2010), and the uncertainties in virial masses are similar (e.g. Vestergaard and Peterson, 2006). Since the structure and geometry of the BLR is unknown, a virial coefficient f is introduced to transform the observed line-of-sight velocity inferred from the line width in to a virial velocity. This simplification accounts for a significant part of the uncertainty in virial BH masses (in addition to, for example, describ-

¹ Vacuum wavelengths are employed throughout the thesis.

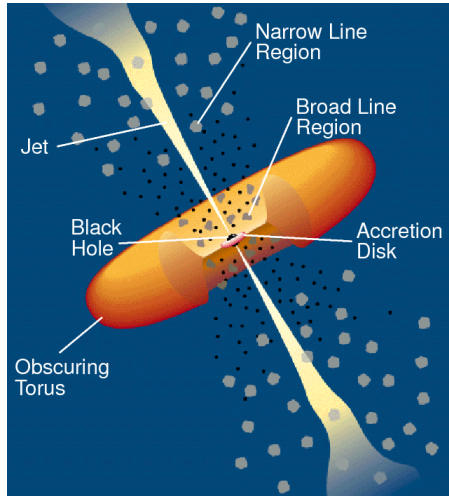


Figure 1: Illustration of the physical structure of an AGN in a simple orientation-based unification model. From Urry and Padovani, (1995).

ing the BLR with a single radius R and scatter in the $R - L$ relation; Shen, 2013). Furthermore, if the BLR is anisotropic (for example, in a flattened disk; e.g. Jarvis and McLure, 2006) then the line width will be orientation-dependent (e.g. Runnoe et al., 2013b; Shen and Ho, 2014; Brotherton et al., 2015).

For example, single epoch estimates have been used to calculate black hole masses in the highest redshift quasars to study the growth of SMBHs. This figure shows a compilation of SE mass estimates for quasars over a wide redshift range from different studies. These studies show that massive, 10^9 BHs are probably already in place by $z \sim 7$, when the age of the Universe is less than 1 Gyr. This places strong constraints on BH growth models. Single epoch masses have also been used to study the distribution of quasars in the BH mass-luminosity plane, which conveys important information about the accretion process of these active black holes (e.g. Kollmeier et al. 2016). Redshift evolution of BH-bulge scaling relations (e.g. Bennert et al. 2011). Clustering (Shen & Ho 2014; Timins et al.?).

An *active galactic nucleus*, or AGN, is an energetic, non-stellar phenomena in the central region of a galaxy. AGN are powered by the accretion of gas, primarily through an accretion disk, onto a central *super-massive black hole* (SMBH) of mass $10^{6-9} M_{\odot}$ (Lynden-Bell, 1969). With bolometric luminosities in the range 10^{44-48} ergs $^{-1}$, they are the most luminous persistent sources of radiation in the Universe.

1.3 ORIENTATION-BASED UNIFICATION MODELS

AGNs are divided into numerous classes and sub-classes based on their observational properties. AGN unification models (Antonucci,

(1993; Urry and Padovani, 1995) attempt to explain the diversity in their observational properties using as few physical parameters as possible. In many unification models the optical and radio luminosities are considered to be intrinsic parameters. Variations in the radio luminosity explains the difference between the 15 – 20% of AGN which are *radio-loud* (i.e. have radio to optical flux ratios $\gtrsim 10$) and the remainder which are *radio-quiet*. The optical luminosity explains, for example, the difference between low-luminosity *Seyfert Galaxies* and high-luminosity *quasars*². In a typical quasar the optical emission may be brighter than the combined emission from all of the stars in the host galaxy by a factor of 100 or more. The large brightness contrast between the nucleus and the host galaxy makes the host galaxy difficult to detect, and the quasar is observed as an unresolved stellar-like object³.

Unification models attempt to explain all further observational differences as being apparent differences due to *orientation* effects. The basic physical structure of an AGN in this model is illustrated in Figure 1. Material is pulled towards the SMBH at the centre and sheds angular momentum through viscous and turbulent processes in an accretion disk, which radiates primarily at ultraviolet (UV) to soft-X-ray wavelengths. Strong optical and UV emission lines are produced in photo-ionised gas clouds moving rapidly in close proximity to the SMBH. The doppler-broadened emission line widths imply gas cloud velocities of thousands of km s^{-1} in this *broad-emission line*. Further out are dusty, molecular clouds, the geometry of which is often modelled as a torus co-planar with the accretion disk. Along some lines of sight from the observer to the accretion disk / broad line region the dusty torus obscures the UV/optical radiation. In this case, an observer would see a weak UV/optical continua and no broad emission lines and classify the AGN as being *Type II*. On the other hand, if the line of sight is unobscured by the dusty torus then a broad emission line component would be observable in the spectrum and the AGN would be classified as being *Type I*. Further away from the central black hole and beyond the dusty torus are slower moving clouds of gas which are photo-ionised by the continuum emission from the accretion disk and produce forbidden emission lines of narrower widths (typically hundreds of km s^{-1}). Outflows of energetic particles occur along the poles of the accretion disk and form collimated radio-emitting jets and in some cases giant radio-emitting lobes. A strong, relativistically beamed component with large variations in brightness on very short timescales (e.g. $\Delta m \gtrsim 0.1$ and $\Delta t \lesssim 1$

² The term ‘quasar’ is sometimes reserved for radio-loud objects and ‘quasi-stellar object’, or ‘QSO’, for radio-quiet objects. Here, ‘quasar’ is used to refer to all luminous AGN.

³ The name ‘quasar’ is shortened from ‘quasi-stellar radio source’, since quasars were originally discovered as optical point-source counterparts to a newly discovered population of radio sources.

day) is observed and a source with these properties is classified as a *blazar*.

While an orientation-based unification scheme such as this is somewhat successful at explaining many of the observational properties of AGNs, other factors such as the host galaxy morphology and gas/-dust content may also be important (Peterson, 1997). It is also doubtful whether the geometry of the dusty torus is the same in all AGNs, and the fraction of obscured quasars has been shown to decrease with increasing nuclear luminosity (Lawrence, 1991). As we will now discuss, quasars might play an important role in a broader cosmological context, affecting the formation and evolution of the galaxies, groups, and clusters in which they reside. In this scenario of galaxy/quasar co-evolution the quasar is expected to transition from a highly active obscured phase to an unobscured phase as it clears out the dust surrounding it. If this picture is true then we should expect to find variations in the observational properties of the quasar and host galaxy as the system transitions through the different stages of its evolution.

1.4 EVOLUTIONARY MODELS

A number of observations link the growth and evolution of quasars to the growth and evolution of galaxies. These include the following:

1. SMBHs appear to be a ubiquitous feature at the centres of all massive galaxies (e.g. Kormendy and Ho, 2013).
2. SMBH masses are proportional to the mass/velocity dispersion of their host spheroid (the $M - \sigma$ relation; Ferrarese and Merritt, 2000; Gebhardt et al., 2000).
3. The cosmological evolution of the star formation rate and the quasar luminosity function are very similar (e.g. Wall et al., 2005).
4. Cosmological simulations of galaxy formation and evolution require feedback from SMBH growth in order to reproduce the galaxy luminosity function (Kauffmann and Haehnelt, 2000).

These observations suggest that all galaxies may have gone through a ‘quasar phase’ during which the SMBH accretes most of its mass and the stellar-bulge forms most of its stars. This evolutionary phase could be triggered by a major merger or by instabilities in the galactic disc or bulge. In a galaxy merger large amounts of gas can shed sufficient angular momentum to settle into dense clouds and form stars or be funnelled to the centre of the galaxy to grow the existing SMBH. The large amounts of gas and dust funnelled inward to the galactic nucleus is predicted to obscure the quasar until the dust is

cleared out either by quasar-driven or stellar-driven processes. An unobscured quasar then emerges, and is active until all of the available material has been accreted (Hopkins et al., 2006; Narayanan et al., 2010). The feedback processes involved are also thought to be responsible for shutting down star formation in the galactic bulge (Silk and Rees, 1998) and establishing the $M - \sigma$ relation.

Such scenarios have been invoked to explain the presence of buried AGN seen in ultra-luminous infra-red galaxies (ULIRGs; Sanders et al., 1988), a high fraction of which also show evidence of merging and interaction. However, the full picture is likely to be more complicated. Although there is evidence that mergers dominate at high luminosities (Treister et al., 2012), stochastic accretion may be more important at low luminosities (e.g. Hopkins and Hernquist, 2006).

Luminous unreddened quasars show few signs of interaction (e.g. Dunlop et al., 2003) which, if the quasar-galaxy co-evolution model is true, suggests that indications of an interaction disappear during a transitional phase. Quasars in this transitional phase would be highly reddened, as the dust enshrouding the nucleus will not have been fully cleared, but not completely obscured. A population of quasars with these properties may therefore represent a link between ULIRGs and unobscured quasars.

1.5 INTERESTING SUB-POPULATIONS

1.5.1 Red and Reddened Quasars

Magnitude limited optical surveys of quasars are biased against selecting red and reddened quasars. Richards et al., (2003) studied a large sample of optically selected Sloan Digital Sky Survey (SDSS; York et al., 2000) quasars and showed the mean reddening to be $E(B - V) = 0.03$ at the redshift of the quasar. They estimated that $\sim 15\%$ of the population was missing from the survey due to dust extinction. The missing fraction, and it's dependence on luminosity and redshift, could help to determine whether the reddened population is best explained in the context of orientation-based unification models with non-spherical geometry or as an evolutionary stage in a quasars lifetime.

Populations of heavily dust-reddened quasars have been identified using radio surveys (e.g. Glikman et al., 2012), by using the 'K-band excess' in the spectra of quasars relative to stars (Maddox et al., 2012), and using near-IR colour selection (Banerji et al., 2012; Banerji et al., 2013). Recently, Ross et al., (2014) identified a small sample of very red SDSS quasars based on their extreme IR to optical luminosity ratios. It is yet to be determined whether these extreme objects are simply the tail of a population dominated by less reddened quasars, or whether the distribution is bi-modal with reddening. A

population of quasars with intermediate amounts of dust reddening ($0.1 \lesssim E(B-V) \lesssim 0.5$) would help to address this question.

1.5.2 Broad Absorption Line Quasars

Broad absorption line quasars (BALQSOs) are a sub-population of quasars exhibiting blue-shifted absorption troughs broader than $2000\text{km}\text{s}^{-1}$ (Weymann et al., 1991) which are unambiguously associated with AGN-driven out-flowing gas. As well as showing high rates of mergers, an anomalously large fraction of heavily reddened objects exhibit broad blue-shifted absorption troughs in their spectra (Urrutia et al., 2009; Glikman et al., 2012). This observation suggests that the BAL phenomenon may be related to a ‘blow-out’ phase of a quasar’s lifetime as it transitions from a dusty, obscured object to a luminous blue quasar, at the same time quenching star formation. Since outflows are believed to be fundamental to AGN feedback, a better understanding of their properties could shed light on the outflow phenomenon. Alternatively, whether a quasar is observed to have broad absorption lines could depend only on the orientation of the observer in relation to an intrinsically anisotropic system.

1.5.3 Hot-Dust-Poor Quasars

The near-IR emission from AGN is generally explained by thermal emission from dust grains at the edge of the dusty torus closest to the accretion disk. The dust is heated to its sublimation temperature (1300–2000K Barvainis, 1992) by emission from the accretion disc. However, Hao et al., (2010) reported that 6% (at $z \lesssim 2$) to 20% (at $2 \lesssim z \lesssim 3.5$) of the quasars in the X-ray selected XMM-COSMOS Type 1 AGN sample (Brusa et al., 2010) have an unusually small amount of hot dust emission, despite having normal accretion disc spectra. They infer a torus covering factor of $\sim 2\%$ to 30% for these ‘hot dust poor’ (HDP) quasars, well below the $\sim 75\%$ predicted by unified models (e.g. Krolik and Begelman, 1988). Hao et al., (2011) found that HDP quasars were just as common in the Richards et al., (2006a) Spitzer/S-DSS sample ($8.7\% \pm 2.2\%$) and the Elvis et al., (1994) Palomar-Green-quasar-dominated sample ($9.5\% \pm 5.0\%$). Either the hot dust is destroyed (dynamically or by radiation), or the dust is not centred on the SMBH, which could happen during a major merger (e.g. Blecha et al., 2011). Alternatively, misaligned accretion disks, which will result from discrete isotropic accretion events (Volonteri, Sikora, and Lasota, 2007), will lead to a wider range of covering factors (Lawrence and Elvis, 2010).

At higher redshifts, Jiang et al., (2010) found two HDP quasars in a sample of 21 at $z \sim 6$. They find that at $z \sim 6$ the hot dust abundance is roughly proportional to the black hole mass, indicating that the

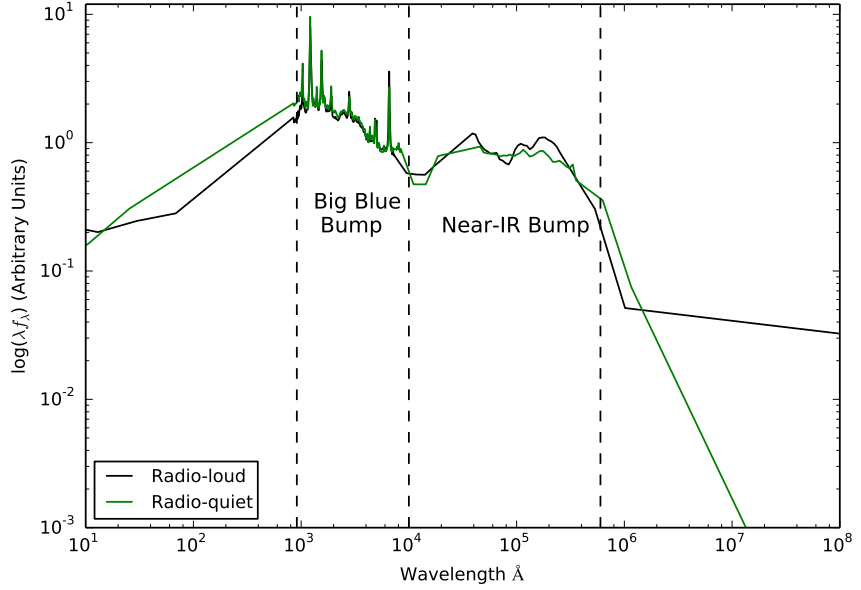


Figure 2: Median SEDs for radio-loud and radio-quiet quasars from Shang et al., (2011).

two grow at about the same rate. The two HDP quasars also have the smallest SMBH masses, and may be too young to have formed a significant amount of hot dust.

1.5.4 Type II Quasars

As well as lacking a broad-line spectral component, Type II AGN tend to have high IR to optical light ratios, hard X-ray spectra, and be strongly polarised, consistent with dusty torus based unification schemes. The detection of unobscured continuum emission that is scattered and polarised by dust above the torus has confirmed the orientation-based unification of Type I and Type II Seyfert Galaxies. Their higher luminosity analogues, Type II quasars, have been much more difficult to detect and study. It is possible that the orientation-based Type I/II unification scheme may break down at high-luminosities, and that instead all quasars could pass through a Type II phase before the obscuring dust is cleared out by the quasar-driven outflows and a Type I quasar emerges.

1.6 SPECTRAL ENERGY DISTRIBUTIONS

AGNs emit strongly over many decades in frequency of the electromagnetic spectrum and the energy emitted as a function of frequency is described by a *spectral energy distribution* (SED). As we will describe below, the broad features in the SED originate from processes which

occur in different regions of the AGN. In the preceding sections, we have described how some interesting sub-populations of AGNs might relate to the broader population in the context of orientation-based unification schemes and evolutionary schemes. Comparing SEDs of different sub-populations can help to shed light on these relationships and the physical processes which drive them. Possible correlations between the SED shape and luminosity, redshift, and other properties of the AGN such as black hole mass and Eddington ratio can also constrain models of AGN structure and evolution.

Since the physical processes involved are generally understood only qualitatively, almost all AGN SED templates are empirical. The empirical template of Elvis et al., (1994), constructed using photometric observations from the radio to the hard X-rays of 29 radio-quiet and 18 radio-loud Type I quasars, is still the most commonly cited, despite many additions and updates (e.g. Polletta et al., 2000; Kuraszkiewicz et al., 2003; Risaliti and Elvis, 2004; Richards et al., 2006a; Polletta et al., 2007; Lusso et al., 2010; Shang et al., 2011; Marchese et al., 2012; Trichas et al., 2012). In Figure 2 we show the median spectrum from the radio-loud and radio-quiet samples of Shang et al. (2011). Shortward of the radio region, the radio-loud and radio-quiet spectra are almost indistinguishable.

A large amount of energy is emitted in the UV/optical region shortward of $\sim 4000\text{\AA}$: the *Big Blue Bump*. In the X-ray region, the *soft X-ray excess* may be the high-energy end of this feature. The Big Blue Bump is generally attributed to thermal emission from the accretion disk. In Type II AGNs, the continuum emission from the accretion disk is obscured, and so the Big Blue Bump in the SED of a Type II AGN would be less prominent than is seen in Figure 2.

The feature at wavelengths long-ward of $\sim 1\mu\text{m}$ is the *IR Bump*, and is generally attributed to thermal emission from dust at a wide range of temperatures ($\sim 50 - 1000$ K). The amount, geometry, ionisation and optical depth of absorbing dust and gas and its inclination determines the shape of the IR Bump and the absorption of the optical/UV continua. The relative strengths of the IR Bump and the Big Blue Bump are generally comparable, although they do vary from object to object. In particular, for the HDP objects we described above the IR Bump appears to be missing entirely. The minimum between the two peaks is at $\sim 1\mu\text{m}$, which reflects the sublimation of dust at $T \gtrsim 2000$ K (Sanders et al., 1989).

Emission in the hard X-ray region of the spectrum is believed to be due to Compton up-scattering of accretion disk photons by hot electrons forming a corona in the vicinity of the disk (e.g. Sunyaev and Titarchuk, 1980). The radio emission, which originates from synchrotron emission in relativistic jets, contributes very little to the total energy output. However, the mechanical energy provided by the jets

is an important component of AGN feedback models (e.g. Fabian, 2012).

Many parameters might be expected to affect the shape of the AGN SED (e.g. the black hole mass, the accretion rate, the physical properties of the accretion disk, the properties of the absorbing dust) and many of these properties might be expected to change as the quasar evolves (e.g. as dust is expelled from the nuclear regions). Given this, it is perhaps surprising that many authors have found no significant dependence of the mean SED on properties such as redshift, bolometric luminosity, SMBH mass, or accretion rate (e.g. Elvis et al., 2012; Hao et al., 2013) and that quasars up to redshift 7 have been shown to have similar UV spectra to low redshift quasars (e.g. Mortlock et al., 2011).

A NEAR-INFRARED SPECTROSCOPIC DATABASE OF HIGH-REDSHIFT QUASARS

Black-hole masses are crucial to understanding the physics of the connection between quasars and their host galaxies and measuring cosmic black hole-growth. At high redshift, $z \gtrsim 2.1$, black hole masses are normally derived using the velocity-width of the C IV $\lambda\lambda 1548, 1550$ broad emission line, based on the assumption that the observed velocity-widths arise from virial-induced motions. In many quasars, the C IV-emission line exhibits significant blue asymmetries ('blueshifts') with the line centroid displaced by up to thousands of km s^{-1} to the blue. These blueshifts almost certainly signal the presence of strong outflows, most likely originating in a disc wind. We have obtained near-infrared spectra, including the H α $\lambda 6565$ emission line, for 19 luminous ($L_{\text{Bol}} = 46.5 - 47.5 \text{ erg s}^{-1}$) Sloan Digital Sky Survey quasars, at redshifts $2 < z < 2.7$, with C IV emission lines spanning the full-range of blueshifts present in the population. A strong correlation between C IV-velocity width and blueshift is found and, at large blueshifts, $> 2000 \text{ km s}^{-1}$, the velocity-widths appear to be dominated by non-virial motions. Black-hole masses, based on the full width at half maximum of the C IV-emission line, can be overestimated by a factor of five at large blueshifts. A larger sample of quasar spectra with both C IV and H β , or H α , emission lines will allow quantitative corrections to C IV-based black-hole masses as a function of blueshift to be derived. We find that quasars with large C IV blueshifts possess high Eddington luminosity ratios and that the fraction of high-blueshift quasars in a flux-limited sample is enhanced by a factor of approximately four relative to a sample limited by black hole mass.

2.1 INTRODUCTION

At redshifts of $z \gtrsim 2.0$ the low-ionization hydrogen and Mg II emission lines are no longer present in the optical spectra of quasars and it is necessary to employ an emission line in the rest-frame ultraviolet. The strong C IV $\lambda\lambda 1548.2, 1550.8$ emission doublet is visible in the optical spectra of quasars to redshifts of $z \sim 5$ and C IV-derived BH masses have become the standard (e.g. Vestergaard and Peterson, 2006; Park et al., 2013) for both individual quasars and in studies of quasar population demographics.

The luminosities of quasars at redshifts $z \gtrsim 2$ are much greater than the majority of AGN at lower redshifts for which reverberation mapping results are available. Therefore, the reliability of the existing

calibration involving C IV FWHM velocity measurements and ultraviolet luminosity is not established definitively when extrapolating to high-redshifts and luminosities. While some authors have found good agreement between BH mass-estimates based on C IV and H β (e.g. Vestergaard and Peterson, 2006; Assef et al., 2011; Tilton and Shull, 2013), others have questioned the consistency (e.g. Baskin and Laor, 2005a; Trakhtenbrot and Netzer, 2012; Shen and Liu, 2012).

Denney, (2012) presented evidence that the interpretation of the FWHM velocity of the C IV-emission being due primarily to virial motions within the quasar BLR requires care. Specifically, both a low-velocity core component and a blue excess to the C IV-emission, both of which do not reverberate, can be present and Denney, (2012) proposes that a contribution from an accretion disc wind or from a more distant narrow emission line region is important.

Certainly, in contrast to the hydrogen Balmer lines and Mg II, the C IV emission line in quasar spectra exhibits a broad range of line shapes, including significant asymmetry, with shifts of the line-centroid to the blue ('blueshifts') of up to several thousand km s $^{-1}$ (Richards et al., 2002; Baskin and Laor, 2005a; Sulentic et al., 2006). Shen and Liu, (2012) found, using a sample of 60 luminous quasars, that the scatter between the FWHM of C IV and H β was correlated with the blueshift of C IV relative to H β . Shen et al., (2008) found a similar result by comparing C IV with Mg II for quasars from SDSS DR5. The blueshifting of C IV is usually interpreted as evidence for strong outflows (e.g. Sulentic et al., 2007; Richards et al., 2011) which, most likely, result from the presence of a radiation line-driven accretion-disc wind (e.g. Konigl and Kartje, 1994; Murray et al., 1995; Proga, Stone, and Kallman, 2000; Everett, 2005; Gallagher et al., 2015). In this picture, the non-virial wind component makes a significant contribution to the observed C IV-emission FWHM in quasars with large C IV blueshifts ('wind-dominated quasars') and hence increases the inferred BH masses. A primary goal of this chapter is to present the full range of C IV-emission line blueshifts present among high-luminosity quasars at redshifts $z \sim 2.5$ and investigate potential systematic trends in the derived C IV-based BH masses as a function of blueshift.

Changes in the C IV blueshift and equivalent width are correlated with changes in the velocity widths and strengths of other optical and ultra-violet emission lines. In the spectra of lower-redshift AGN, the FWHM of the broad H β emission line and the relative strengths of optical Fe II and H β have been identified as the features responsible for the largest variance in the population. These parameters form part of 'Eigenvector 1' (EV1), the first eigenvector in a principal component analysis which originated from the work of Boroson and Green, (1992). The underlying driver behind EV1 is thought to be the Eddington ratio (e.g. Sulentic et al., 2000; Shen and Ho, 2014). Sulentic et al., (2000) proposed a two-population model to classify AGN by

their EV1 properties. In this scheme AGN with $\text{FWHM}(\text{H}\beta) < 4000 \text{ km s}^{-1}$ and $\text{FWHM}(\text{H}\beta) > 4000 \text{ km s}^{-1}$ are classified as population A and B objects respectively, although there is a continuous distribution of parameter values across this divide. Sulentic et al., (2007) added a measure of the C IV asymmetry to EV1, and found a strong association between blue-asymmetry and their population A quasars.

Denney, (2012) found the level of contamination in single-epoch spectra from non-reverberating gas to be correlated with the shape (FWHM/σ) of the C IV profile. Runnoe et al., (2013a) found the scatter between the C IV and H β line widths to be correlated with the continuum-subtracted peak flux ratio of the ultraviolet emission-line blend of Si IV+O IV (at 1400 Å) to that of C IV. Both authors used these correlations to propose empirical corrections to the C IV line width which can improve the consistency between C IV and H β -based virial BH mass estimates. In fact, the shape, peak flux relative to the 1400 Å blend, and blueshift of C IV all correlate with one another and with other parameters in EV1. Therefore, EV1 provides a useful context for understanding systematic trends in C IV velocity widths, and hence virial BH masses.

Currently, the number of reverberation mapped quasars is both small (~50 quasars; Park et al., 2013) and, as highlighted by Richards et al., (2011), includes a restricted range of the C IV emission line shapes seen in the quasar population. In particular, the reverberation mapped objects generally possess high C IV equivalent widths and low C IV-blueshifts. Nevertheless, the derived scaling relations based on the reverberation-mapped sample are regularly applied to the quasar population with low C IV EWs and/or large C IV-blueshifts, where any non-virial outflow-related contribution to the dynamics is significant. Much more complete coverage of the C IV-emission properties within the population of luminous quasars will come from the new SDSS-IV reverberation mapping project (Shen et al., 2015) but, for now, additional direct comparison of C IV-emission and low-ionization emission-line properties in the same quasars offers a way forward.

Near-infrared spectra, including the H α emission line, for a sample of 19 quasars, at redshifts $2.0 < z < 2.7$, have been obtained to complement existing SDSS optical spectra covering the C IV emission line. The 19 quasars were chosen to include a broad range of C IV line blueshifts. Our aim is to directly test the reliability of C IV-based BH mass estimates at high redshift for objects with a diverse range of C IV-line shapes. In particular, we will investigate potential systematic effects on the C IV-emission based BH masses for quasars with large, $\gtrsim 1200 \text{ km s}^{-1}$, C IV blueshifts, using the properties of the H α emission line to provide BH-mass estimates for the objects unbiased by non-virial contributions to the emission-line profile. Examining higher redshifts, our work complements other studies which

attempt to improve the reliability of BH mass estimates which use the C IV line (e.g. Runnoe et al., 2013a; Denney, 2012). However, the range of C IV blueshifts in our sample is significantly more extended, which will allow us to study systematic biases in C IV-based virial BH masses more directly, i.e. as a function of the C IV blueshift. Established relations to derive BH masses from emission-line properties are employed but an advantage of our approach is that C IV and H α can be directly compared as a function of C IV-emission line shape.

Throughout this thesis we adopt a Λ CDM cosmology with $h_0 = 0.71$, $\Omega_M = 0.27$, and $\Omega_\Lambda = 0.73$. All wavelengths and equivalent width measurements are given in the quasar rest-frame, and all emission line wavelengths are given as measured in vacuum.

2.2 SAMPLE SELECTION FOR LIRIS / NTT PROGRAM

The parent sample for our investigation is the spectroscopic quasar catalogue of the Sloan Digital Sky Survey (SDSS; York et al., 2000) Seventh Data Release (DR7; Schneider et al., 2010). The SDSS DR7 catalogue contains moderate resolution $\sim 3800 - 9180\text{\AA}$ spectra for 105,783 quasars. Shen et al., (2011) have compiled a catalogue of properties for the SDSS DR7 quasars including, at $z > 1.5$, measurements of the broad C IV $\lambda\lambda 1548.2, 1550.8$ emission line. Our aim is to explore the relationship between the H α and C IV emission-line properties over the full dynamic range in C IV-emission shapes, with particular emphasis on quasars possessing large C IV-blueshifts (see Section 2.3). The sample was restricted to objects with redshifts $2.14 < z < 2.51$ (7,258 quasars), to ensure that the H β and H α emission lines fall within the H- and K-bands respectively, allowing us to observe both simultaneously with the appropriate grism configuration. Given the limited number of quasars for which near-infrared spectra could be obtained, the quasar sample was further restricted to objects that are radio-quiet (5,980 quasars), show no evidence of broad absorption lines (BALs) in their spectra (5,299 quasars), and are free from significant dust extinction. We removed radio-loud objects from our sample using the same radio-loud classification as Shen et al., (2011), and BAL quasars using the classifications of both Shen et al., (2011) and Allen et al., (2011). The removal of quasars with significant dust extinction was achieved by identifying quasars with $i - K$ colours redder than a parametric spectral energy distributions (SED) model + SMC-like extinction curve with $E(B - V) = 0.05$ (see Maddox et al., 2012). The K-magnitude was taken from the UKIRT Infrared Deep Sky Survey (UKIDSS; Lawrence et al., 2007) Large Area Survey (ULAS). The requirement to be in the ULAS footprint and have reliable K band photometry reduced our sample of possible targets to 1,683, and the $E(B - V)$ cut left 1,204 in our sample. Finally, a flux-limit of $K < 18.5$

(AB) was applied to ensure that spectra of sufficient signal-to-noise ratio (S/N) could be obtained (412 quasars).

We were able to obtain new infra-red spectra for 19 quasars from this sample of 412 possible targets (Section 2.4). The quasars included in this sub-sample were selected to have C IV-emission shapes which span the full range observed in the population. Reliably quantifying the distribution of C IV-emission shapes has been made possible thanks to redshift-determination algorithms (Hewett and Wild, 2010, Allen & Hewett 2016, in preparation) which are independent of the C IV-emission shape. Calculation of the C IV emission line parameters is described in detail in the next section.

2.3 C IV BLUESHIFTS IN THE QUASAR POPULATION

Recognition that the C IV emission line in quasars can exhibit significant asymmetric structure, with an excess of flux to the blue of the predicted rest-frame transition wavelength, extends back to Gaskell, (1982). Significant progress in understanding the relationship between changes in C IV-emission shape and quasar properties has come about through studies in which near-infrared spectra of the hydrogen Balmer lines have been obtained. Such studies typically involve samples of modest size and the location of the Balmer lines provides a reliable estimate of the quasar systemic redshifts; recent examples include Shen and Liu, (2012) and Marziani et al., (2016). In Section 2.5 we adopt the same approach to estimate systemic redshifts for the quasar sample presented here with near-infrared spectra. However, improvements in the estimation of systemic redshifts from ultraviolet quasar spectra means that it is now possible to quantify the distribution of C IV-blueshifts in the observed quasar population as a whole.

2.3.1 Quasar systemic redshifts

Historically, the parametrisation of the C IV emission-line properties for quasars in large surveys has not proved straightforward because the C IV emission line has itself been used in the determination of the quasar redshifts. The SDSS provided the first catalogue of tens of thousands of redshift $z > 1.6$ quasars with spectra of adequate velocity resolution and S/N that effective statistical studies of the rest-frame ultraviolet emission-line properties, including line-shape, have proved possible.

The comprehensive compilation of quasar properties for the SDSS DR7 quasars by Shen et al., (2011) provides a natural starting point for population studies. In Fig. 23a we plot the C IV-blueshift versus C IV-emission equivalent width (EW) using the SDSS pipeline redshifts and the blueshifts calculated by Shen et al., (2011). The grey points show all SDSS DR7 quasars for which measurements exist and the or-

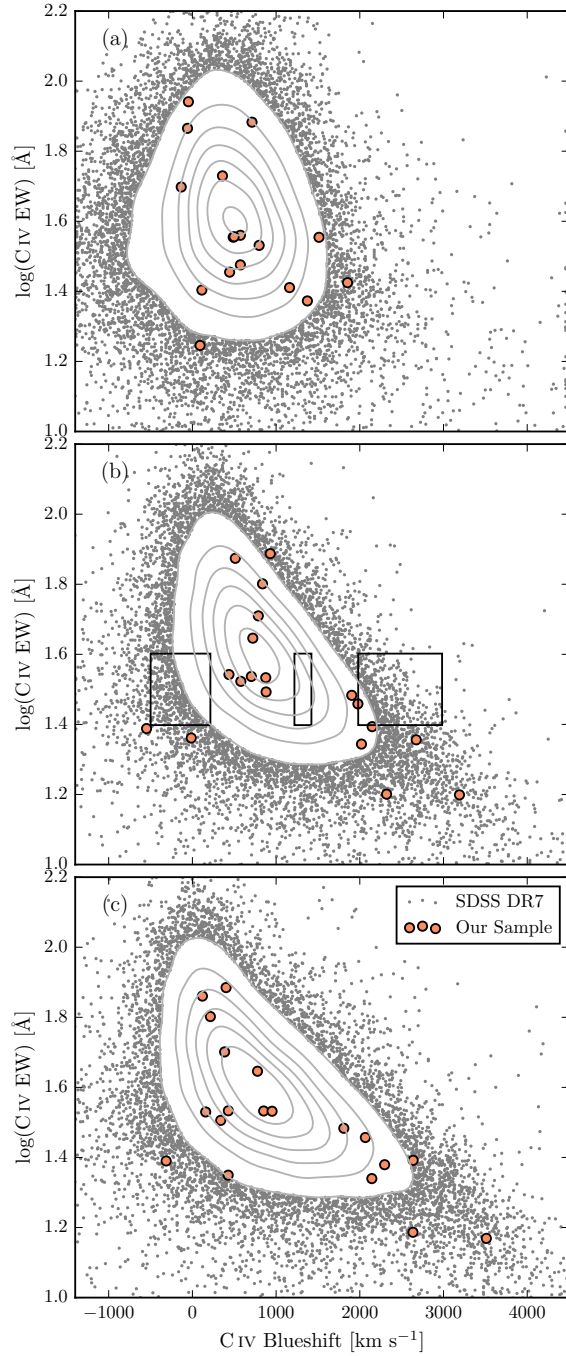


Figure 3: Rest-frame EW versus blueshift of the broad C IV-emission line for 32,157 SDSS DR7 quasars at $1.6 < z < 3.0$ (grey) and our sample (orange). Panel (a) uses C IV line parameters from Shen et al., (2011) and SDSS pipeline systemic redshifts. Panels (b) and (c) use systemic redshifts from Hewett and Wild, (2010) and Allen & Hewett (2016, in preparation) respectively, and C IV line measurements described in Sec. 2.3.2. In regions of high point-density, contours show equally-spaced lines of constant probability density generated using a Gaussian kernel-density estimator. The three rectangles in panel (b) show the regions of parameter space used to generate the composite spectra shown in Fig. 4.

ange circles show the 19 quasars with near-infrared spectra presented in this paper. A strong trend in the blueshift values as a function of line EW is not evident in Fig. 23; structure in the parameter space is being masked because the C IV emission line is itself being used in the determination of the quasar redshifts.

The redshift-determination scheme of Hewett and Wild, (2010) provided much improved redshifts, not least because the redshift estimates for the majority of quasars were derived using emission-lines other than the C IV-line itself. Figure 23b shows SDSS DR7 quasars in the same C IV parameter space as Figure 23a, but now using Hewett and Wild, (2010) redshifts. The improved redshift estimates are predominantly responsible for the differences seen in Fig. 23a and b; the appearance in Fig. 23b of the extension to high blueshift for quasars with low C IV EW is particularly evident.

The large systematic variation in the C IV emission-line profile within the population is evident from figures 11 and 12 of Richards et al., (2011). The plots and analysis in Richards et al., (2011) employ the quasar redshifts from Hewett and Wild, (2010) but, as is evident from the figures, the systematic variation in the C IV shape is correlated with changes in the quasar SEDs, including the strengths of the Si III λ 1892 and C III λ 1908 emission lines in the rest-frame ultraviolet. As a consequence, the redshifts from Hewett and Wild, (2010) still suffer from systematic errors that are correlated with the shape, and particularly the blueshift, of the C IV emission line. The nature of the systematic variations in the quasar ultraviolet SEDs are such that for quasars with close-to symmetric C IV profiles and line centroids close to the systemic redshift, the Hewett and Wild, (2010) redshifts result in C IV blueshifts that are overestimated by a few hundred km s^{-1} , whereas, for quasars with strong blue-asymmetric C IV profiles and line centroids displaced significantly to the blue of the systemic redshift, the C IV blueshifts are underestimated by, in the most extreme cases, up to 1200 km s^{-1} .

Figure 23c shows the C IV emission line parameters calculated using a new redshift-estimation algorithm (Allen & Hewett 2016, in preparation) that takes account of the quasar SED variations, producing redshifts independent of the large systematic shape changes seen in the C IV emission line. The low-ionization emission lines visible in the rest-frame ultraviolet (over wavelengths from Mg II $\lambda\lambda$ 2796,2803 down to the O I λ 1304+Si II λ 1307 blend) using the new redshift-algorithm are located at rest-frame wavelengths in excellent agreement with the systemic redshift defined using the rest-frame narrow-line optical O III $\lambda\lambda$ 4960,5008 and broad-line H β and H α .

The systematic trends seen in Fig. 23b, in particular the extension to high blueshift at low C IV EW, become more apparent in Fig. 23c, as expected from consideration of the known SED-related errors in the

redshifts from Hewett and Wild, (2010). A population of quasars with only modest blueshifts and low EW is also apparently still present.

2.3.2 C IV emission line blueshift measurements

The differences in the distribution of C IV emission line properties seen in the three panels of Fig. 23 are due primarily to the change in the systemic redshift estimates. It is also necessary, however, to obtain a measure of the C IV emission line ‘location’ in order to calculate the blueshifts. When working with moderately-sized samples, parametric fits to the emission-line profile may be undertaken using careful mask-definition to minimise the effect of absorption features on the profiles used for the parametrization, and this is the approach we follow below in Section 2.5. Effective analysis of the tens of thousands of spectra from SDSS DR7, and now DR12, however, requires a more robust scheme to determine a C IV-blueshift estimate that is not very sensitive to the range of S/N among the spectra or the presence of narrow absorption systems within the C IV-emission profile. Shen et al., (2011) provide a discussion (their section 3) of the factors that effect the measurement of broad emission lines in quasar spectra of modest S/N. Their careful analysis of the C IV emission properties employed the results of parametric fits of three Gaussians to the spectra. Our own experiments in quantifying the C IV emission properties of SDSS spectra showed that a simple non-parametric measure of the C IV emission location reduced the number of outliers significantly. Visual inspection of spectra demonstrated that the improvement is due primarily to the identification of, and interpolation over, associated and outflow absorption systems, which forms part of the non-parametric measurement scheme.

We therefore chose to use a non-parametric scheme to measure the blueshift of the C IV line, which we will now describe. A continuum is first defined as a power-law of wavelength, $f(\lambda) \propto \lambda^{-\alpha}$, with the slope, α , determined using the median¹ values of the flux in two continuum windows at 1445–1465 and 1700–1705Å (the same wavelengths as adopted by Shen et al., (2011)). The C IV emission line is taken to lie within the wavelength interval 1500–1600Å, a recipe that is commonly adopted (e.g. Shen et al., 2011; Denney et al., 2013). To reduce the impact of narrow absorption systems on the emission-line profile a ‘pseudo continuum’ is defined by applying a 41-pixel median filter to the quasar spectrum. Pixels within the C IV profile that lie more than 2σ below the pseudo-continuum are deemed to be affected by absorption and added to an ‘absorber’-mask. Two pixels on either side of each such pixel are also included in the mask. For each masked

¹ The median is used to improve the robustness of the continuum estimate from the relatively small wavelength intervals.

pixel, the flux values in the spectrum are replaced by values from the pseudo-continuum.

The wavelength that bisects the cumulative total line flux, λ_{half} , is recorded and the blueshift (in km s^{-1}) defined as $c \times (1549.48 - \lambda_{\text{half}}) / 1549.48$ where c is the velocity of light and 1549.48\AA is the rest-frame wavelength for the C IV doublet². Positive blueshift values indicate an excess of emitting material moving towards the observer and hence outflowing from the quasar. Hewett and Wild, (2010) redshifts are used to define the quasar rest-frame.

2.3.3 Sample selection - C IV properties

The primary aim of the paper is to investigate the potential systematic effects on the C IV-emission based BH masses for quasars with large, $\gtrsim 1200\text{km s}^{-1}$, C IV blueshifts, using the properties of the H α emission line to provide BH-mass estimates for the objects unbiased by non-virial contributions to the emission-line profile. The orange symbols in Fig. 23 show the C IV parameters of our quasar targets for which near-infrared spectra of adequate S/N were obtained. These quasars were selected using our non-parametric blueshift measures (based on the Hewett and Wild, (2010) redshifts). The sample of 19 quasars spans the full dynamic range in C IV-parameters based on the Hewett and Wild, (2010) systemic redshifts and the coverage is in fact even more complete when using the forthcoming SED-independent redshifts from Allen & Hewett (2016, in preparation). As is evident from the sparsity of quasars with large C IV blueshifts when the SDSS pipeline systemic redshifts are used (Fig. 23a), improvements in the estimation of systemic redshifts from ultraviolet spectra have been a crucial factor in allowing us to reliably select a sample of quasars with a range of C IV blueshifts. In subsequent sections we re-derive the systemic redshifts and C IV blueshifts for this sample using parametric fits to the H α and C IV emission (the former from our-near infrared observations). Thus, while the systematic trends in BH masses inferred from measurements of the C IV emission line depend on the distribution of C IV emission line properties within the quasar population, the results of our analysis of the H α and C IV emission line properties are independent of the redshifts used to produce the panels in Fig. 23.

2.3.4 Relation to virial BH mass estimates

In general, researchers studying quasar demographics at high-redshift adopt estimates of BH masses based on the width of C IV-emission,

² The adopted C IV rest-frame wavelength assumes an optically thick BLR, in which case the contribution from each component is equal. Adopting a 2:1 ratio (appropriate for an optically thin BLR) changes the blueshifts by $\sim 80\text{km s}^{-1}$.

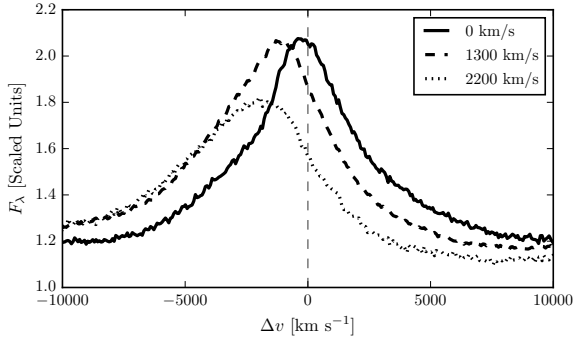


Figure 4: Composite spectra of the C IV-emission line as a function of C IV blueshift for SDSS DR7 quasars. The quasars contributing to each composite are indicated in Fig. 23b. Virtually the entire C IV-profile appears to shift blueward and the change in line shape is not simply an enhancement of flux in the blue wing of a still identifiable symmetric component. In order of increasing C IV blueshift, the composite spectra have FWHM $4870, 5610$, and 6770 km s^{-1} and EW $33.1, 31.6$, and 28.8 \AA .

without reference to the blueshift of the C IV-emission (e.g. Vestergaard, 2004; Kollmeier et al., 2006; Gavignaud et al., 2008; Vestergaard et al., 2008; Vestergaard and Osmer, 2009; Kelly et al., 2010; Kelly and Shen, 2013). The systemic redshift is often assumed to be given by the peak of the C IV emission, regardless of whether there is evidence that the line is shifted or not. Figure 4 shows the shape of the C IV-emission in composite spectra constructed from SDSS DR7 quasars with $\text{EW}(\text{C IV})=25\text{-}40\text{\AA}$, as a function of C IV blueshift. Quasars classified as BALs, or possessing strong associated absorbers have been excluded, and the composite-spectra shown are derived using an arithmetic mean of a minimum of 200 spectra at each blueshift. The blueshifts and EWs of the quasars contributing to each of the composites are indicated by the boxes in Fig. 23b. The profiles show how, at large values of blueshift ($\gtrsim 2000 \text{ km s}^{-1}$) the C IV-profile is displaced to the blue by amounts comparable to the FWHM of the profile.

A possible origin of the blueshifts is the presence of a disc-wind (see Gallagher et al., 2015; Higginbottom and Proga, 2015, for recent papers) but, irrespective of the physical origin of the high-blueshift C IV-profiles, measures of the emission-line ‘width’ do not relate simply to virialized motions of the emitting gas under the gravitational influence of the BH. On the other hand, Denney et al., (2013) point out that any radiatively driven wind will have a velocity comparable to the escape velocity, i.e. approximately twice the virial velocity. Even if dominated by an outflow component, the C IV line width might therefore still be expected to relate to the BH mass.

2.4 OBSERVATIONS

Near-infrared spectra were obtained with the Long-slit Intermediate Resolution Infrared Spectrograph (LIRIS) mounted on the 4.2m William Herschel Telescope (WHT) at the Observatorio del Roque de los Muchachos (La Palma, Spain). Observations took place over four non-contiguous nights from 2015 March 31 to April 4. Approximately one night was lost due to poor weather and a further half-night was affected by poor transparency due to cloud. A one arc-second slit-width was employed and the LIRIS H + K low-resolution grism was selected, which covers the spectral ranges 1.53–1.79 μm and 2.07–2.44 μm with a dispersion of 9.7 $\text{\AA}/\text{pixel}$. The spatial scale of the instrument is 0.25 arcsec/pixel. Observations were divided into 60 s sub-exposures and performed in an ABBA nodding pattern, with the object placed at two positions along the slit 12 arcsec apart. Bright Ao-5V stars were observed at similar air-masses to the targets in order to provide both telluric absorption corrections and a flux calibration of the quasar spectra.

The raw LIRIS data frames incorporate a known ‘pixel shift’ which was first removed from all frames using the LIRIS data reduction package LIRISDR. Subsequent data reduction was undertaken with standard IRAF³ procedures. The flat-field images, which were taken at the beginning of each night via illumination of the dome, were averaged and normalised to remove any wavelength-dependent signature. Each individual two-dimensional spectrum was then flat-field corrected. Consecutive AB and BA pairs of two-dimensional spectra were subtracted to remove the sky background. All the subtracted AB/BA-pairs for a target were then averaged to give the final two-dimensional spectrum.

The size of the one-dimensional spectrum extraction windows, in the slit direction, varied from 6–10 pixels. To increase the S/N, optimal variance-weighted extraction with sigma clipping was employed. For the fainter objects in our sample we were unable to trace the spectrum across the dispersion axis reliably and the trace from a telluric standard-star observation, observed at a similar air mass and time, was used instead. The wavelength calibration, using argon and xenon lamp exposures, resulted in root mean square errors in the range 1.01–1.71 \AA , with a mean of 1.47 \AA . The telluric standard star observations were reduced using the same steps described above. The stellar continuum was divided out of the standard star spectrum, which was then divided into the quasar spectrum to remove telluric absorption features. The spectral type and magnitude of the standard star were used to flux calibrate the quasar spectrum both in a relative and

³ IRAF is distributed by the National Optical Astronomy Observatory, which is operated by the Association of Universities for Research in Astronomy (AURA) under a cooperative agreement with the National Science Foundation.

Table 1: Summary of near-infrared spectroscopic observations with LIRIS.

SDSS Name	SDSS DR	z^a	i_{SDSS}	UTC Date	$T_{\text{exp}} (\text{s})$	$S/\text{N}(\text{CIV})^b$	$S/\text{N}(\text{H}\beta)^b$	$S/\text{N}(\text{H}\alpha)^b$
073813.19+271038.1	DR12	2.4508	18.80	2015-04-01	720	29.13	17.27	10.0
074352.61+245743.6	DR12	2.1659	19.09	2015-04-04	2160	8.64	18.68	11.43
080651.54+245526.3	DR12	2.1594	18.91	2015-04-01	1200	10.37	6.04	3.91
085437.59+031734.8	DR7	2.2504	18.41	2015-03-31	2520	26.58	5.82	3.09
085856.00+015219.4	DR12	2.1675	17.62	2015-04-04	1800	66.16	24.37	12.71
110454.73+095714.8	DR12	2.4238	19.12	2015-04-03	1440	19.41	10.75	7.81
123611.21+112921.6	DR12	2.1527	18.53	2015-04-04	1680	35.24	21.3	11.51
124602.04+042658.4	DR12	2.4473	18.49	2015-04-01	960	35.34	8.1	5.73
130618.60+151017.9	DR12	2.4020	19.00	2015-04-05	840	29.83	8.91	5.13
131749.78+080616.2	DR12	2.3791	19.04	2015-04-05	2880	19.25	5.6	3.32
132948.73+324124.4	DR12	2.1684	18.40	2015-04-01	2520	32.58	10.4	6.96
133646.87+144334.2	DR7	2.1422	18.84	2015-04-01	1200	15.2	23.82	16.34
133916.88+151507.6	DR12	2.3157	18.52	2015-04-03	2880	20.52	5.79	3.28
140047.45+120504.6	DR12	2.1722	18.29	2015-04-02	840	36.64	9.83	5.68
152529.17+292813.2	DR12	2.3605	17.52	2015-04-04	1440	80.55	2.17	1.5
153027.37+062330.8	DR12	2.2198	18.62	2015-04-04	1800	29.9	21.01	12.58
153848.64+023341.1	DR12	2.2419	17.56	2015-04-01	2520	64.82	5.63	3.56
161842.44+234131.7	DR7	2.2824	18.49	2015-04-04	1320	23.37	11.1	6.43
163456.15+301437.8	DR12	2.4901	18.29	2015-04-01	1920	36.06	9.44	8.63

^a From Hewett and Wild, (2010).^b Measured in the continuum and quoted per resolution element.

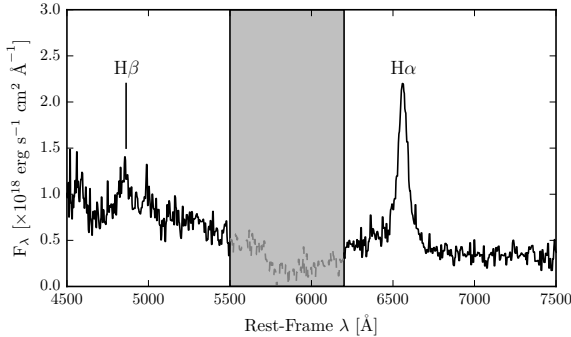


Figure 5: LIRIS spectrum of SDSSJ1246+0426. The gap between the H and K bands ($\sim 5500\text{--}6300\text{\AA}$) has been greyed-out.

absolute sense. Variable atmospheric conditions combined with the narrow slit width resulted in a significant level of uncertainty in the absolute flux calibration for the quasar observations. The use of the UKIDSS broadband magnitudes (H and K) to normalise the spectra results in a significantly improved calibration.

Spectra with sufficient S/N for analysis of the $\text{H}\alpha$ emission line properties were obtained for a total of 19 quasars. Sixteen of the 19 quasars have been re-observed in the Sloan Digital Sky Survey-III: Baryon Oscillation Spectroscopic Survey (SDSS-III/BOSS; Dawson et al., 2013) and the spectra are available in the SDSS DR12 quasar catalogue (Pâris et al., 2017). As the BOSS-spectra have higher S/N compared to those in DR7, we have used the BOSS spectra when available. A typical reduced LIRIS spectrum is shown in Fig. 5. A log of the observations, the quasar positions, magnitudes and redshifts, along with the S/N achieved for the $\text{H}\beta$, $\text{H}\alpha$ and $\text{C}\,\text{IV}$ emission line regions (the last from the optical SDSS/BOSS spectra) are listed in Table 1. The S/N, which is given per resolution element, was measured in the continuum in the region around the emission lines. The full SDSS name is given in Table 1; in the subsequent tables and text we will refer to objects using an abbreviated name of the form SDSSJHHMM+DDMM.

Although the S/N is similar in the continuum regions adjacent to the $\text{H}\alpha$ and $\text{H}\beta$ emission lines, in practice the much lower EW of $\text{H}\beta$ compared to $\text{H}\alpha$ meant that both parametric and non-parametric characterisation of the emission-line parameters did not produce results that could be used in this investigation. The individual $\text{H}\beta$ profiles were thus not employed, although a composite spectrum of the $\text{H}\beta$ region is used below.

2.5 EMISSION LINE MEASUREMENTS

Virial BH mass estimators are calibrated using either the FWHM or dispersion (σ ; derived from the second-moment velocity) of a broad emission line (e.g. Vestergaard and Peterson, 2006; Park et al., 2013). Complications which are encountered when measuring line widths include how to model the ‘continuum’ flux, where to define the limits of the line emission, and how to deal with absorption. All of these issues are exacerbated when working with low S/N data (see Denney et al., 2013, for a discussion). In Section 2.3.2 we measured the blueshift of C IV for tens of thousands of SDSS DR7 quasar spectra. This allowed us to quantify the distribution of C IV blueshift values and hence select a subset for near-infrared observations which have C IV blueshifts spanning the full range of this distribution (Fig. 23). A non-parametric scheme was employed because, in comparison to recipes involving the fitting of multiple Gaussian (or other parametric) profiles, it was found to be more robust and less sensitive to the range of S/N among the spectra and to the presence of narrow absorption systems within the C IV-emission profile. In this section we will use a different approach, and measure the line properties by fitting a parametric model to the data. When working with a small number of spectra, it is possible to use careful mask-definition to minimise the effect of absorption features on the profiles used for the parametrization. The purpose of the model fits is purely to best represent the intrinsic line profile, and no physical meaning is attached to the individual model components. We will now describe the parametric model and fitting procedure used for each emission line. The models were fit using a standard variance-weighted least squares minimisation procedure employing the Levenberg-Marquardt algorithm. Prior to the fit, the spectra were visually inspected and regions significantly affected by absorption were masked and excluded.

2.5.1 C IV

We first measure and subtract the local continuum emission, by fitting a power-law to two windows on either side of the line emission, as described in Section 2.3.2. For a small number of objects, absorption features, or artefacts, in the spectrum necessitated modest adjustments to the window extents, which are specified in Table 2. The continuum-subtracted spectra are then transformed from wavelength units into units of velocity relative to the rest-frame line-transition wavelength for the C IV doublet (1549.48 Å, assuming equal contributions from both components). The parametric model is ordinarily fit within the same 1500–1600 Å window used in Section 2.3.2, which corresponds to approximately $\pm 10\,000 \text{ km s}^{-1}$ from the rest-frame transition wavelength. The line-window was extended if significant

Table 2: Summary of the fitting regions and the parameters of the models used to fit the C IV and H α emission lines.

Name	Fitting Region [km s $^{-1}$]			Continuum Region[Å]			GH Order	Gaussians	χ^2_v
	C IV	H α	C IV	H α	C IV	H α			
0738+2710	-9570,9770	-7530,10740	1445-1465,	1700-1705	6000-6250,	6800-7000	6	2	0.66 1.0
0743+2457	-9570,9770	-7530,10740	1445-1465,	1700-1705	6004-6210,	6800-7000	2	2	0.84 1.0
0806+2455	-9570,9770	-9219,10759	1445-1465,	1700-1705	6000-6250,	6800-7000	3	1	0.87 0.83
0854+0317	-9570,9770	-7530,10740	1445-1465,	1700-1705	5989-6135,	6800-7000	3	2	0.91 0.85
0858+0152	-20000,7400	-7530,10740	1423-1428,	1700-1705	6000-6200,	6800-7000	2	2	0.94 0.96
1104+0957	-9570,9770	-7530,10740	1445-1465,	1700-1705	6000-6250,	6801-6845	6	2	0.68 0.95
1236+1129	-15363,7650	-8904,10590	1445-1465,	1700-1705	6063-6210,	6800-7000	3	2	0.84 0.89
1246+0426	-9570,9770	-7530,10740	1445-1465,	1700-1705	6000-6250,	6799-6906	4	2	0.66 0.83
1306+1510	-13000,7800	-7530,10740	1445-1465,	1700-1705	6000-6250,	6800-7000	2	3	0.73 0.18
1317+0806	-9198,9755	-7530,10740	1445-1465,	1700-1705	6000-6250,	6800-7000	2	1	0.78 2.16
1329+3241	-12000,9000	-7605,7406	1445-1461,	1700-1705	6000-6250,	6800-7000	3	2	0.61 0.84
1336+1443	-14000,10000	-10131,10674	1445-1465,	1700-1705	6000-6250,	6800-7000	3	2	0.87 1.51
1339+1515	-12000,11000	-7530,10740	1445-1465,	1700-1705	6046-6250,	6800-7000	4	1	0.69 0.14
1400+1205	-15000,10000	-2000,10815	1445-1465,	1700-1705	6000-6250,	6800-7000	6	2	0.82 0.2
1525+2928	-9570,9770	-7586,8080	1459-1466,	1700-1705	6055-6251,	6800-7000	4	1	0.49 0.39
1530+0623	-12000,10000	-7530,10740	1445-1465,	1700-1705	6127-6186,	6800-7000	4	3	0.84 1.14
1538+0233	-13500,9000	-7530,10740	1450-1465,	1700-1705	6000-6250,	6855-7002	4	2	0.61 0.82
1618+2341	-9190,9770	-7530,10740	1445-1465,	1689-1697	6000-6250,	6800-7000	4	2	1.16 0.93
1634+3014	-9570,9770	-8400,8500	1445-1465,	1700-1705	6000-6250,	6736-6779	3	2	0.59 0.22

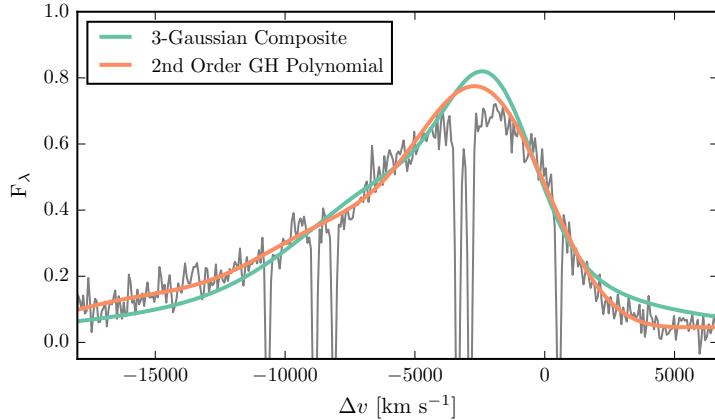


Figure 6: 2nd-order Gauss-Hermite (GH) polynomial and 3-component Gaussian fit to the C_{IV}-emission line of SDSSJ0858+0152, which is the most blueshifted in our sample. We derive line parameters from the GH polynomial fit; using the Gaussian model changes the FWHM, line dispersion, and blueshift by -250, -150, and 500 km s⁻¹ respectively. For the C_{IV} lines of all other quasars in our sample the GH polynomial and Gaussian models provide equally good fits.

flux in the profile was present blueward of the short wavelength limit. The adopted line-fitting windows, in units of velocity from the rest-frame transition wavelength, are given in Table 2.

To fit the C_{IV} profile we employed Gauss-Hermite (GH) polynomials, using the normalisation of van der Marel and Franx, (1993) and the functional forms of Cappellari et al., (2002). We allowed up to six components in the GH polynomial model, but in many cases a lower order was sufficient; the polynomial order used for each line is given in Table 2. It is also a common practice to fit the C_{IV} emission profile with two or three Gaussian components (e.g. Shen et al., 2011). We opted to use a GH-polynomial model primarily because it provided a significantly better fit to the most blueshifted and asymmetric C_{IV} line (in SDSSJ0858+0152). Figure 6 shows how a model with three Gaussian components underestimates the flux in the blue wing and overestimates the flux in the red wing of the line profile. Using the Gaussian model rather than the GH polynomial changes the FWHM, line dispersion, and blueshift by -3, -3, and 10 per cent respectively. We have highlighted SDSSJ0858+0152 because, of all the objects in our sample, the choice of model leads to the largest change in C_{IV} line parameters. Even in this case, however, the differences are modest.

For every other C_{IV} line in our sample we found only marginal differences in our best-fit line parameters when, rather than using a GH polynomial model, the C_{IV} emission was fit using a composite model of up to three Gaussians. Our best-fit parameters are also in good

agreement with Shen et al., (2011), who employ a multi-Gaussian parametrization⁴. The scatter between the Shen et al., (2011) results and our own is 0.1 dex about the one-to-one relation and, as expected, is larger for lines with smaller EWs.

2.5.2 $H\alpha$

We employ the same continuum subtraction and fitting method as for CIV, with the continuum and fitting windows as given in Table 2. We adopt a rest-frame transition wavelength of 6564.89 Å to transform wavelengths into equivalent Doppler velocities. We used a simple model with up to three broad Gaussian components to fit the H α emission line. We opted against parametrizing the H α line using a GH polynomial because the extra degrees of freedom in this model did not improve the quality of the fits⁵. Upon inspection of the residuals from the fit, we also found no evidence that additional model components for narrow H α , N IIλλ6548,6584 and S IIλλ6717,6731 were required. Furthermore, narrow O IIIλλ4960,5008 emission is relatively weak in these spectra.

The sole exception is the H α line in the spectrum of SDSSJ0738+2710. In addition to having the narrowest H α line, this spectra also has the strongest narrow O III component (EW = 63 Å), which suggests that a contribution from the narrow-line region might be important. Introducing a single Gaussian for the narrow emission, while retaining a double Gaussian for the broad emission, the FWHM of the broad component increases to 3400 km s⁻¹ (compared to 1580 km s⁻¹ without the narrow component). For consistency, the parameters quoted in Table 3 are from the model with no narrow component. However, because the properties derived from the emission line width (the BH mass and the mass-normalised accretion rate) are strongly biased by the probable contribution from the narrow-line region, SDSSJ0738+2710 is excluded from the analysis in Section 2.6.

2.5.3 Comparison of H α and H β profiles

Virial BH mass estimators are typically based on the width of H β . However, the H α and H β emission is believed to originate from the same gas and the transformation between the emission-line velocity widths is expected to be well defined. Greene and Ho, (2005), using

⁴ The Shen et al., (2011) parameters are derived from the SDSS DR7 spectra, whereas 16 out of 19 of our fits are to higher S/N BOSS DR12 spectra.

⁵ The emission line parameters and subsequent analysis do not depend on whether line parameters from multiple-Gaussian or GH-polynomial model fits are used.

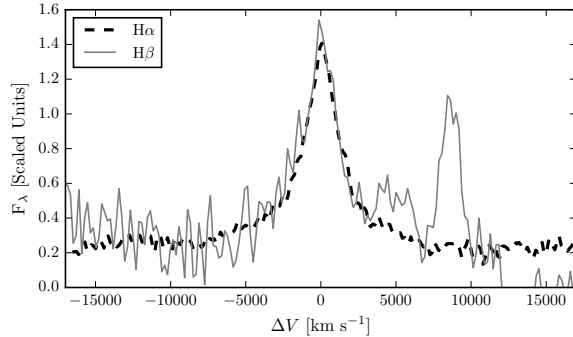


Figure 7: The H α and H β emission line regions in the median composite spectrum, shown as function of the velocity shift from the respective predicted line peak wavelengths. The line fluxes have been scaled in order for the profile shapes to be readily compared. The H α and H β line profiles are very similar, which suggests a tight correlation between the H α and H β line widths. Quasar narrow-line emission from O $_{\text{III}}\lambda 5008.2$ is visible but, overall, the O $_{\text{III}}\lambda\lambda 4960, 5008$ emission is relatively weak in these spectra.

a sample of 162 quasars with high S/N SDSS spectra, established the following relation between the H α and H β FWHM:

$$\text{FWHM}(\text{H}\beta) = (1.07 \pm 0.07) \times 10^3 \left(\frac{\text{FWHM}(\text{H}\alpha)}{10^3 \text{ km s}^{-1}} \right)^{(1.03 \pm 0.03)} \quad (1)$$

Greene and Ho, (2005) found the root-mean-square scatter about this relation to be ~ 0.1 dex. We do not have a sufficient number of robust H β line measurements to test this relation directly. However, we are in the process of acquiring a much larger sample of quasars with near-infrared spectra covering H α and H β at similar redshifts and luminosities to the sample presented here. The H α and H β line widths of this sample are in excellent agreement with the Greene and Ho, (2005) relation. To indirectly test the H α /H β line width relation for the sample presented here, we first constructed mean composite spectra in the H α and H β emission line regions to increase the S/N. The individual rest-frame spectra (defined using the wavelength of the H α centroid) were interpolated on to a common wavelength grid. The spectra were then normalised using the continuum flux under the line centre, which was found by linearly interpolating between two emission-line free windows on either side of the line. Figure 7 shows the composite H α and H β line regions overlaid and, as expected, the line profiles are closely matched.

2.5.4 Emission line parameters

In Fig. 8 we show our best-fitting models overlaid on the observed flux in the spectral regions around C $_{\text{IV}}$ and H α . The spectra are pre-

Table 3: Summary of emission line properties derived from parametric model fits to H α and C $_{\text{IV}}$.

Name	z (H α)	Blueshift		FWHM		σ [km s $^{-1}$]	C $_{\text{IV}}$	H α	C $_{\text{IV}}$	H α	C $_{\text{IV}}$	H α	EW [Å]	
		C $_{\text{IV}}$ [km s $^{-1}$]	C $_{\text{IV}}$ [km s $^{-1}$]	FWHM [km s $^{-1}$]	H α									
0738+2710	2.4396	50 ± 21	2255 ± 42	1503 ± 95	2916 ± 42	1789 ± 95	54 ± 2	532 ± 43	3904 ± 511	33 ± 4	351 ± 23	3904 ± 511	33 ± 4	
0743+2457	2.1662	692 ± 210	5924 ± 536	6036 ± 511	3801 ± 536	1724 ± 403	51 ± 4	488 ± 56	3146 ± 522	24 ± 2	617 ± 90	3146 ± 522	24 ± 2	
0806+2455	2.1542	389 ± 115	3435 ± 267	4059 ± 403	3387 ± 267	2723 ± 334	70 ± 3	441 ± 72	3155 ± 80	28 ± 1	622 ± 23	3155 ± 80	28 ± 1	
0854+0317	2.2475	-403 ± 134	3940 ± 354	4436 ± 522	3448 ± 354	3259 ± 112	3259 ± 112	3277 ± 131	4168 ± 271	28 ± 1	631 ± 29	3259 ± 112	3277 ± 131	
0858+0152	2.1692	4354 ± 82	8412 ± 384	3155 ± 80	5298 ± 384	2543 ± 472	48 ± 1	536 ± 77	3091 ± 88	2543 ± 472	48 ± 1	3091 ± 88	2543 ± 472	
1104+0957	2.4217	-299 ± 55	3590 ± 112	3307 ± 334	3259 ± 112	3277 ± 334	70 ± 3	441 ± 72	4168 ± 271	3277 ± 131	28 ± 1	631 ± 29	3259 ± 112	3277 ± 131
1236+1129	2.1559	2828 ± 99	7540 ± 271	3152 ± 131	3259 ± 112	3277 ± 334	70 ± 3	441 ± 72	3091 ± 88	2543 ± 472	48 ± 1	3091 ± 88	2543 ± 472	
1246+0426	2.4393	325 ± 145	4126 ± 88	4268 ± 472	3901 ± 88	2145 ± 330	3905 ± 158	2145 ± 330	3819 ± 491	3033 ± 946	33 ± 2	349 ± 52	3819 ± 491	3033 ± 946
1306+1510	2.3989	2043 ± 84	6660 ± 158	2626 ± 330	3905 ± 158	3227 ± 67	3227 ± 67	3227 ± 67	3675 ± 182	3033 ± 946	33 ± 2	374 ± 67	3675 ± 182	3227 ± 67
1317+0806	2.3748	437 ± 289	5256 ± 182	7188 ± 946	3675 ± 182	3350 ± 410	3905 ± 158	3350 ± 410	3819 ± 491	3033 ± 946	33 ± 2	374 ± 67	3819 ± 491	3033 ± 946
1329+3241	2.1637	652 ± 113	4528 ± 491	4908 ± 410	3819 ± 491	3227 ± 67	3227 ± 67	3227 ± 67	3675 ± 182	3033 ± 946	33 ± 2	374 ± 67	3675 ± 182	3227 ± 67
1336+1443	2.1466	3668 ± 345	8780 ± 1003	2954 ± 67	3772 ± 1003	3627 ± 1072	4501 ± 935	3627 ± 1072	4092 ± 302	3103 ± 227	44 ± 2	500 ± 98	4092 ± 302	3103 ± 227
1339+1515	2.3207	133 ± 184	3865 ± 935	8816 ± 1072	4501 ± 935	2696 ± 1915	4303 ± 128	2696 ± 1915	4092 ± 302	2664 ± 145	25 ± 1	642 ± 55	4092 ± 302	2696 ± 1915
1400+1205	2.1672	2492 ± 107	7590 ± 290	3231 ± 227	4363 ± 290	3103 ± 227	3103 ± 227	3103 ± 227	4215 ± 253	2415 ± 253	25 ± 1	458 ± 186	4215 ± 253	2415 ± 253
1525+2928	2.3572	612 ± 536	5697 ± 128	6360 ± 1915	4303 ± 128	2664 ± 145	4092 ± 302	2664 ± 145	4092 ± 302	2664 ± 145	26 ± 1	499 ± 28	4092 ± 302	2664 ± 145
1530+0623	2.2169	1471 ± 108	5397 ± 302	3073 ± 145	4092 ± 302	3103 ± 227	3103 ± 227	3103 ± 227	4215 ± 253	2415 ± 253	25 ± 1	465 ± 75	4215 ± 253	2415 ± 253
1538+0233	2.2420	2018 ± 80	5567 ± 100	2892 ± 253	3596 ± 100	2359 ± 175	3312 ± 161	2359 ± 175	34 ± 2	425 ± 39	34 ± 2	425 ± 39	34 ± 2	2359 ± 175
1618+2341	2.2755	42 ± 53	2516 ± 161	2669 ± 175	3312 ± 161	3236 ± 900	4566 ± 745	3236 ± 900	4566 ± 745	3236 ± 900	26 ± 1	327 ± 65	3236 ± 900	3236 ± 900
1634+3014	2.5018	1509 ± 223	6835 ± 745	6210 ± 900	4566 ± 745	3236 ± 900	4566 ± 745	3236 ± 900	4566 ± 745	3236 ± 900	26 ± 1	327 ± 65	3236 ± 900	3236 ± 900

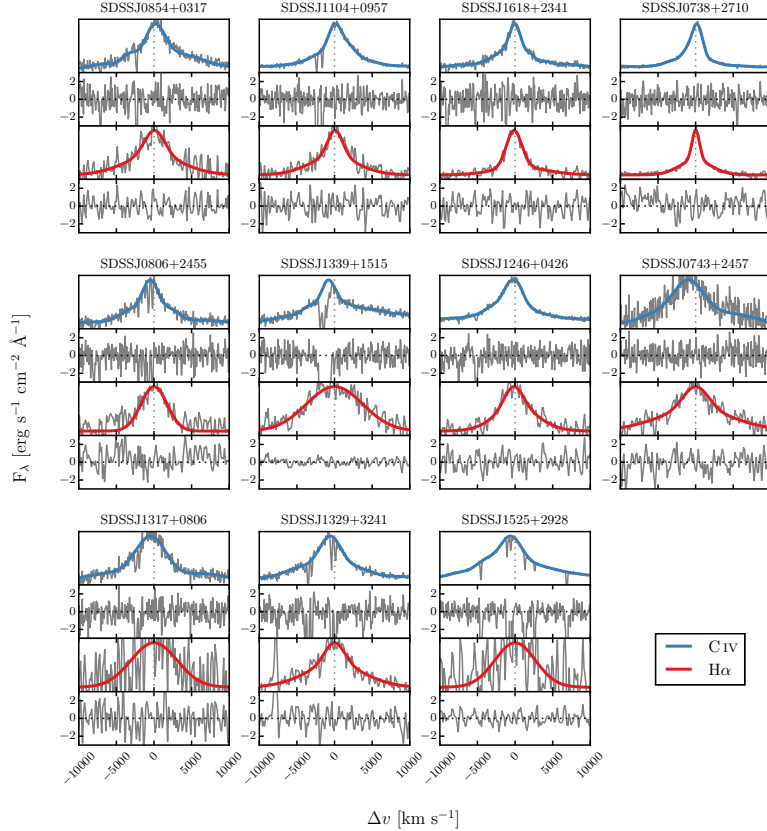
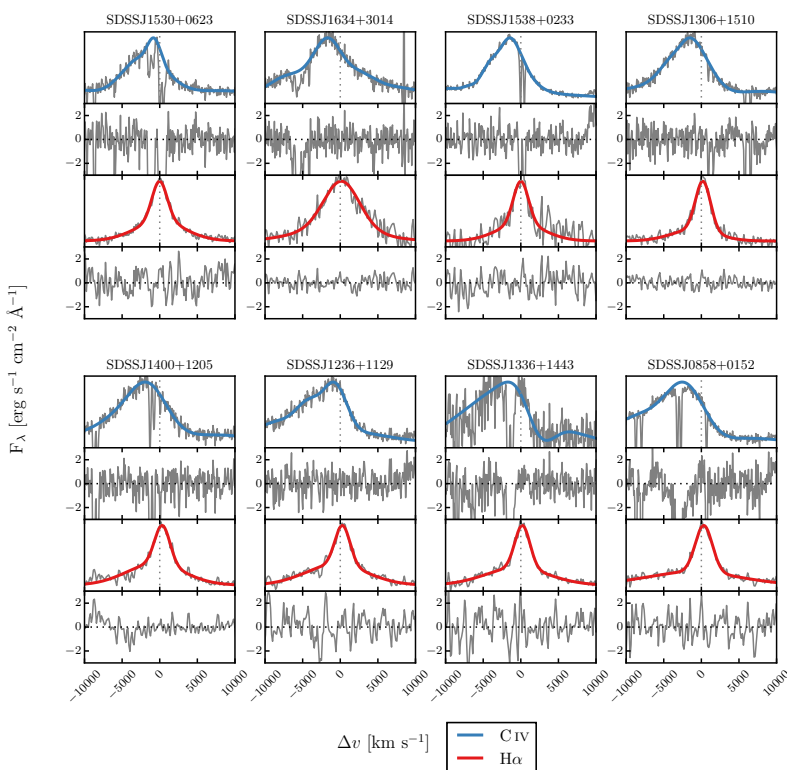


Figure 8: CIV (SDSS/BOSS) and H α (LIRIS) emission lines and best-fitting model. Δv is the velocity shift from the line rest-frame transition wavelength, with the systemic redshift defined using the centroid of the fit to H α . Objects are presented in order of increasing CIV blueshift relative to the H α centroid. Below each fit we plot the data-model residuals, scaled by the errors on the fluxes.

Figure 8: *Continued*

sented in order of increasing C_{IV} blueshift. The Doppler velocities have been shifted so that the H α emission line centroid is at 0 km s⁻¹. The y-axes of the data-minus-model residual plots have deliberately been scaled by the spectrum flux errors. The model fits are generally very good with only minimal systematic residuals. The only significant features seen in the residual C_{IV} spectra correspond to the location of narrow absorption lines which were excluded in the fitting procedure. The continuum windows for a number of the H α lines extend close to the edges of the K-band and uncertainties in the flux calibration, and hence continuum level, are almost certainly responsible for the low-amplitude, large-scale, systematic residuals seen in a number of objects (e.g. SDSSJ 0806+3455, 0858+0152, 1400+1205, 1538+0233). The amplitudes are, however, small and redefining the continuum levels to eliminate the residuals has only a very small effect on the line-profile parameters used in the analysis.

The systemic redshift (defined using the H α peak), the C_{IV} blueshift, the line FWHM, dispersion, and EW of H α and C_{IV} are all given in Table 3. Both the FWHM and the dispersion (σ) have been corrected for instrumental broadening by subtracting the FWHM resolution (152 and 477 km s⁻¹ for SDSS/BOSS and LIRIS respectively) in quadrature⁶.

Our definition of the C_{IV} blueshift differs slightly in two ways from the values plotted for the quasar population in Fig. 23. Firstly, we use the peak of our parametric model fit to the H α line to define the quasar systemic-redshift⁷. Secondly, the centre of the C_{IV} line is now defined as the wavelength that bisects the cumulative total flux of our best-fit GH-polynomial model rather than of the data.

The monochromatic luminosity of the continuum at 1350 and 5100 Å, which are used to calculate virial BH mass estimates, are given in Table 4. The luminosity at 1350 Å was taken from the spectral fits of Shen et al., (2011). The quasar rest-frame continuum at 5100 Å often lies at the edge, or beyond, the wavelength coverage of the LIRIS spectra. Monochromatic 5100 Å luminosities were therefore calculated from the fit of our parametric quasar model (described in Maddox et al., (2012)) to the UKIDSS H- broadband magnitude for each quasar. The model fits to the quasars are excellent, with residuals in SDSS and UKIDSS passbands under 10 per cent.

2.5.5 Emission line parameter uncertainties

The 1σ error bars calculated from the covariance matrix in least-squares minimisation will underestimate the true uncertainties on the line

⁶ For the dispersion we first divide the FWHM resolution by 2.35, which assumes that the line profile is Gaussian.

⁷ The H α -derived redshifts are very closely in agreement with those from the forthcoming Allen & Hewett redshifts, which are plotted in Fig. 23c.

Table 4: Monochromatic continuum luminosities used to derive bolometric luminosities and BH masses.

Name	Log L_λ [erg s $^{-1}$]	
	1350Å	5100Å
0738+2710	46.43 ± 0.02	46.14 ± 0.01
0743+2457	46.07 ± 0.02	45.93 ± 0.02
0806+2455	46.09 ± 0.01	45.95 ± 0.02
0854+0317	46.28 ± 0.01	46.27 ± 0.01
0858+0152	46.82 ± 0.00	46.37 ± 0.01
1104+0957	46.11 ± 0.03	45.92 ± 0.02
1236+1129	46.45 ± 0.01	46.01 ± 0.01
1246+0426	46.46 ± 0.01	46.13 ± 0.01
1306+1510	46.35 ± 0.01	46.00 ± 0.02
1317+0806	46.31 ± 0.01	46.02 ± 0.01
1329+3241	46.35 ± 0.01	46.08 ± 0.02
1336+1443	45.84 ± 0.02	45.95 ± 0.01
1339+1515	46.42 ± 0.01	45.97 ± 0.01
1400+1205	46.45 ± 0.01	46.05 ± 0.01
1525+2928	46.84 ± 0.01	46.50 ± 0.01
1530+0623	46.26 ± 0.01	45.97 ± 0.01
1538+0233	46.94 ± 0.00	46.51 ± 0.01
1618+2341	46.59 ± 0.01	46.10 ± 0.01
1634+3014	46.66 ± 0.01	46.16 ± 0.01

parameters, since they do not account for systematic errors such as the significant uncertainty introduced in the continuum subtraction procedure. To calculate more realistic uncertainties on our fitted variables we employed a Monte Carlo approach. Artificial spectra were synthesised, with the flux at each wavelength drawn from a Normal distribution (mean equal to the measured flux and standard deviation equal to the known error). Our emission-line fitting recipe was then implemented on five thousand artificial spectra. Our parameter uncertainties are defined as the standard deviation of the best-fitting parameter values from these five thousand realisations. The uncertainty on the monochromatic continuum luminosity at 5100 Å was estimated via a very similar method – using the error on the UKIDSS H-band magnitude to run a number of realisations of our SED-fitting routine. The uncertainties on all derived quantities, such as the BH mass, are propagated through by assuming that the uncertainties are uncorrelated and independent.

Because of its sensitivity to the flux in the wings of the line profile, care must be taken to define an appropriate range over which to measure the line dispersion. This is particularly true of Lorentzian-like profiles with extended wings. In spectra of only moderate S/N the line limits are difficult to determine unambiguously, which introduces an extra degree of uncertainty in line dispersion measurements. In common with previous work (e.g. Vestergaard and Peterson, 2006), by default, the dispersion was calculated within $\pm 10\,000 \text{ km s}^{-1}$ of the line centre, but this was extended when appropriate to avoid excluding a significant amount of line flux.

2.6 RESULTS

A fundamental assumption on which single-epoch virial BH-mass estimates are based is that the widths of the broad emission lines are directly related to the virial motions of the emitting clouds moving in the gravitational potential of the central BH. However, the C IV line profiles of the quasars in our sample with the largest C IV blueshifts indicate that non-virial motions, very likely due to outflows, are having a significant effect on the observed C IV emission velocity profile (e.g. Gaskell, 1982; Baskin and Laor, 2005a; Sulentic et al., 2007; Richards et al., 2011; Wang et al., 2013). As shown in Fig. 4, at fixed emission-line EW, virtually the entire C IV-profile appears to shift blueward and the change in line shape is not simply an enhancement of flux in the blue wing of a still identifiable symmetric component. While gravity almost certainly plays a key role, determining the escape velocity for out-flowing material for example, it is clear that the virial assumption, on which single-epoch BH-mass measurements are predicated, is not straightforwardly applicable for the C IV-emission line in quasars exhibiting large blueshifts.

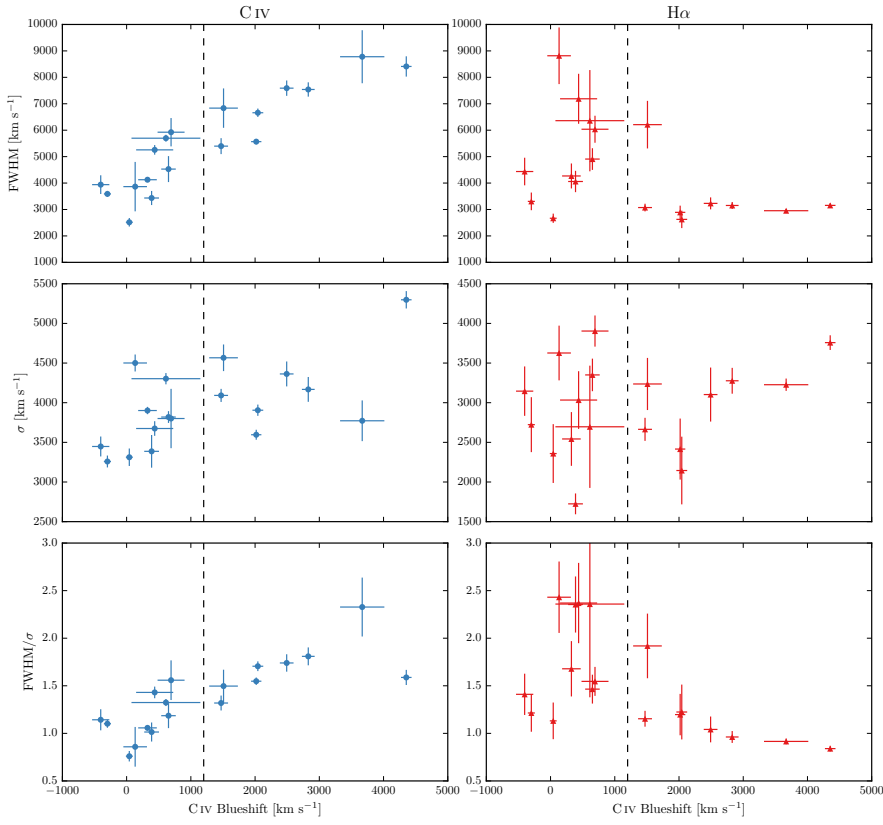


Figure 9: The FWHM, dispersion (σ) and shape (FWHM/ σ) of CIV and H α as a function of the CIV blueshift. The vertical line demarcates the ‘high’ and ‘low’ CIV blueshift regimes discussed in the text. At high blueshift it is clear that BH masses estimated from the CIV FWHM (as is typically done at the redshifts considered) will be significantly larger than those estimated from the H α FWHM.

The main aim of this paper is to investigate potential systematic trends in CIV-based single-epoch virial BH masses as a function of the CIV blueshift. Calibrations using H β (and therefore also H α) are generally accepted to be the most reliable, since most reverberation mapping employs the H β line and the R – L relation has been established using H β . Therefore, we will test the reliability of the CIV-based estimates by comparing CIV line profiles to H α profiles in the same quasars.

2.6.1 Characterising the emission-line profiles

There has been a considerable degree of attention paid to the effectiveness of different velocity-width measures of the CIV-emission; specifically, the line FWHM and the dispersion, σ , derived from the second-moment velocity (e.g. Assef et al., 2011; Denney et al., 2013). The FWHM and line dispersion trace different parts of the broad line velocity field, with the FWHM relatively more sensitive to any low-

velocity core present and the line dispersion relatively more sensitive to the high velocity wings. The shape of the line can be characterised by the ratio FWHM/σ . $\text{FWHM}/\sigma \simeq 2.35$ for a Gaussian profile, while $\text{FWHM}/\sigma \simeq 1$ for a peakier Lorentzian profile⁸. In practice, the line dispersion is almost certainly a more robust velocity indicator when the assumptions underlying the virial-origin of the emission-line velocity width are true and the spectral S/N and resolution are adequate. This was demonstrated by Denney et al., (2013) for a sample of quasars possessing a significantly smaller range in C IV-blueshift than investigated here.

In reality, however, as highlighted by Denney, (2012), contributions to the C IV-emission line profile from gas where virial motions do not dominate can be significant. Looking to the future, the results of the new reverberation-mapping projects (Shen et al., 2015; King et al., 2015) will show what fraction of the C IV-emission line, as a function of velocity, does reverberate for quasars with an extended range of C IV-emission shapes. The derivation of quantitative corrections to transform velocity-width measures from single-epoch to reverberation-only line profiles should then be possible.

As such information is not yet available, there is a strong rationale for investigating whether the systematic changes in the C IV-emission line profile can be used to improve the single-epoch BH-mass estimates derived using the C IV line. In the left panels of Fig. 9 we show how the C IV FWHM, line dispersion, σ , and line shape, FWHM/σ , vary as a function of the blueshift. The C IV FWHM is correlated with the blueshift, with the median FWHM of quasars with the largest blueshifts a factor of 2-3 higher than quasars with only moderate blueshifts. The dispersion, however, does not show a similarly strong systematic variation.

Without knowledge of the C IV-blueshifts, the dynamic range present in the FWHM and line dispersion measurements accords with the expectations from the study of Denney et al., (2013); the factor of $\simeq 4$ spread in the FWHM measurements indicating greater sensitivity to the emission-line profile shape than is the case for the dispersion, which varies by a factor of only $\simeq 2$. Adopting a value of 1200 km s^{-1} to define ‘low’ and ‘high’ blueshift, the median C IV-emission dispersion for the low and high-blueshift samples differ by only 10 per cent. It follows, therefore, that while the dispersion provides a relatively line-profile independent measure of the velocity width for quasars where the underlying assumption regarding the virial-origin of the velocity width applies, quasars where the assumption is not true can be assigned apparently normal velocity-widths and hence potentially incorrect BH-masses.

⁸ Strictly $\text{FWHM}/\sigma \rightarrow 0$ for a Lorentzian profile, but values close to unity are typical when the dispersion is calculated over a velocity range, $\simeq \pm 10000 \text{ km s}^{-1}$, used to parametrize broad emission lines in quasar spectra.

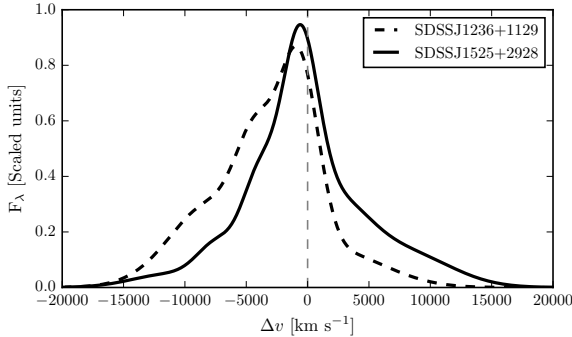


Figure 10: Comparison of the C IV line profiles of SDSSJ1236+1129 and SDSSJ1525+0426. Notwithstanding the essentially identical dispersion values, the emission-line velocity fields differ dramatically and, therefore, the dispersion values cannot be measuring accurately the virial-induced velocity spread of the C IV emission in both quasars.

To emphasise this point, in Fig. 10 we overlay the C IV line profiles of SDSSJ1236+1129 and SDSSJ1525+2928, whose dispersions (Table 3) are indistinguishable (4168 ± 271 and $4303 \pm 128 \text{ km s}^{-1}$ respectively). Notwithstanding the very similar dispersion values, the emission-line velocity fields differ dramatically and, therefore, the dispersion values cannot be measuring accurately the virial-induced velocity spread of the C IV emission in both quasars.

The analysis here, building on earlier work (including Shen and Liu, 2012; Sulentic et al., 2007), confirms a link between C IV emission-line shape and blueshift, raising the prospect of developing a blueshift-dependent correction to single-epoch BH-mass estimates based on the C IV line. Expressed in another way, we are interested in testing if the significant systematic change in line shape as a function of C IV blueshift can be used to provide improved single-epoch BH-masses from the C IV emission line. The tightness of the correlation we observe between the C IV FWHM and blueshift implies that such an approach may be more effective than using the C IV emission-line velocity dispersion without reference to blueshifts. A further practical advantage is that, given the typical S/N of current survey-quality spectra, virial BH mass estimates for high-redshift quasars are usually based on the FWHM rather than the dispersion (e.g. Shen et al., 2011), which, being strongly affected by the continuum placement, is often found to be difficult to measure robustly (e.g. Mejía-Restrepo et al., 2016). As a first step towards the goal, below (Sec. 2.6.5) we investigate the apparent systematic trends in the H α FWHM and line shape as a function of C IV blueshift (shown in the right of Fig. 9).

2.6.2 Computing BH mass estimates

Single-epoch virial BH mass estimates normally take the form

$$M_{\text{BH}} = 10^a \left(\frac{\Delta V}{1000 \text{ km s}^{-1}} \right)^b \left[\frac{L_\lambda}{10^{44} \text{ erg s}^{-1}} \right]^c \quad (2)$$

where ΔV is a measure of the line width (from either the FWHM or dispersion), L_λ is the monochromatic continuum luminosity at wavelength λ , and a , b , and c are coefficients, determined via calibration against a sample of AGN with reverberation-mapping BH mass estimates. Several calibrations have been derived using different lines (e.g. H β , Mg II, C IV) and different measures of the line width (FWHM or dispersion) (e.g. Vestergaard, 2002; McLure and Jarvis, 2002; Vestergaard and Peterson, 2006; McGill et al., 2008; Wang et al., 2009; Rafiee and Hall, 2011; Park et al., 2013).

Reverberation mapping measurements of nearby AGN have revealed the BLR to be stratified, with high-ionisation lines, including C IV, emitted closer to the BH than low-ionisation lines, including H α and H β (e.g. Onken and Peterson, 2002). Vestergaard and Peterson, (2006) found that the C IV-emitting region is at approximately half the radius of the H β /H α emitting region. Given the $\Delta V \propto R_{\text{BLR}}^{-0.5}$ virial relation, this leads to the prediction that the C IV line widths should be $\simeq 1.4$ times broader than H α for a given BH mass. More recently, Denney, (2012) found that there is a significant contribution from gas at larger radii to the C IV emission line, enhancing the profile at lower-velocity and leading to smaller FWHM or dispersion values. The ratio of the line widths is therefore predicted to be lower than the factor of $\simeq 1.4$.

An alternate virial BH-mass calibration is proposed by Park et al., (2013), using an improved sample of AGN with reverberation mapped masses. A major difference from the calibration of Vestergaard and Peterson, (2006) is that Park et al., (2013), recognising the poor correlation sometimes observed between the C IV and H β FWHM, allow the exponent on the velocity width (b in Eq. 2) to vary. Calibrating Eq. 2 against reverberation BH masses, they find a best-fit value of $b = 0.56$, which is much less than the $b = 2.0$ in the strict virial regime. As a result, the derived BH masses are much less sensitive to the C IV-emission line properties. By contrast our approach is to investigate whether a more complete parametrization of the C IV-emission profile can be used to improve BH-mass estimates based on the conventional virial relation, with $b = 2.0$.

2.6.3 C IV-derived BH masses at low C IV blueshift

The H α and C IV FWHM (dispersion) of the 10 quasars with C IV blueshifts $< 1200 \text{ km s}^{-1}$ are linearly correlated, as expected if the

dynamics of the BLR clouds are dominated by virial motions. The median C_{IV}/H_α FWHM (dispersion) ratio is 0.91 (1.22) with standard deviation 0.17 (0.28). Thus, the dispersion-based comparison results in a median C_{IV}/H_α consistent with the value of $\simeq 1.4$ from assuming a virial origin for the emission but with a relatively large standard deviation. As predicted in Section 2.6.2, the FWHM-based comparison results in a systematically lower median C_{IV}/H_α. However, the correlation between the C_{IV} and H_α FWHMs is significantly tighter, lending support to the proposal that corrections to BH-mass estimates based on the C_{IV} emission line properties may be possible.

Virial BH masses were calculated using the widely adopted Vestergaard and Peterson, (2006) calibrations. The Vestergaard and Peterson, (2006) C_{IV} FWHM calibration uses the monochromatic continuum luminosity at 1350 Å to predict the BLR radius and corresponds to ($a = 6.66$, $b = 2$, $c = 0.53$) in Eq. 2. The calibration coefficient $a = 6.73$ in their equivalent dispersion-based relation. For the H_β calibration, Vestergaard and Peterson, (2006) use the monochromatic continuum luminosity at 5100 Å and calibration coefficients corresponding to ($a = 6.91$, $b = 2$, $c = 0.5$). BH masses are computed using the line and continuum properties given in Tables 3 and 4, and we convert our H_α emission-line velocity-width measures to predicted H_β widths using Eq. 1.

As a direct consequence of the empirically small C_{IV}/H_α FWHM ratio, the C_{IV}-derived BH mass estimates are systematically lower than the corresponding H_α-derived masses when the blueshift is small. This can be seen in Fig 11, where for every quasar with a C_{IV} blueshift $< 1200 \text{ km s}^{-1}$ (i.e. to the left of the dashed line), the C_{IV}-derived BH mass is smaller than the corresponding H_α-derived mass. The median fractional difference between the two estimates is 0.60.

For the 10 quasars with low C_{IV} blueshifts, we looked for correlations of the C_{IV}/H_α FWHM ratio with other spectral properties. We found marginal evidence for an anti-correlation with the H_α FWHM (Spearman coefficient 0.58 with p-value 0.08). Among the quasars with H_α FWHM $> 4000 \text{ km s}^{-1}$ we found the mean C_{IV}/H_α FWHM ratio to be 0.83, compared to 1.01 for the quasars with H_α FWHM $< 4000 \text{ km s}^{-1}$. Similar trends have been observed at low- z ; in a sample of Boroson and Green, (1992) quasars, Baskin and Laor, (2005a) found the C_{IV} line to be broader than H_β when the H_β FWHM $< 4000 \text{ km s}^{-1}$ and narrower when the H_β FWHM $> 4000 \text{ km s}^{-1}$.

2.6.4 C_{IV}-derived BH masses at high C_{IV} blueshift

In Section 2.6.1 we have shown that the C_{IV} emission at large C_{IV}-blueshift is not dominated by virial-induced motions due to the BH. The empirically derived increase in the C_{IV} emission FWHM with

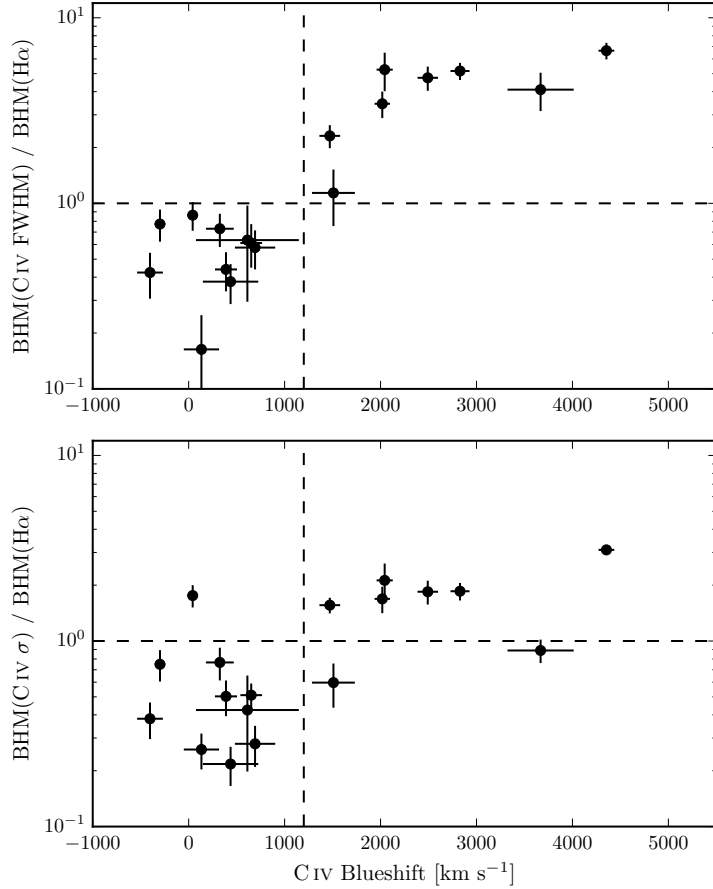


Figure 11: Comparison of virial BH mass estimates based on the C IV FWHM (top) and dispersion σ (bottom) and H α FWHM as a function of the C IV blueshift. The horizontal line indicates agreement between C IV and H α BH masses, and the vertical line demarcates the ‘high’ and ‘low’ C IV blueshift regimes discussed in the text. The BH masses of quasars with moderate C IV blueshifts are underestimated when using the C IV FWHM, while the masses of quasars with large blueshifts are severely overestimated. This situation cannot be corrected by changing the exponent on the FWHM (e.g. Rafiee and Hall, 2011; Park et al., 2013) or the overall scaling in standard virial BH mass relations.

blueshift leads directly to an overestimate of BH-mass if the trend with blueshift is not taken into account. The availability of the H α -spectra for the sample allows the quantification of the bias in inferred BH-mass under the assumption that the H α emission line provides a reliable BH mass.

Figure 11 shows the ratio of the C IV- and H α -FWHM derived BH masses as a function of the C IV blueshift. We see that for quasars with C IV blueshifts $> 2000 \text{ km s}^{-1}$, the C IV-based masses overestimate the H α -based masses by as much as a factor of ~ 5 .

The existence of a trend in the C IV-dispersion values with C IV blueshift is evident from inspection of the bottom left panel of Fig. 9 but the systematic trend relative to the spread at fixed blueshift is significantly smaller than when using C IV FWHM. Similarly, Fig. 11 shows, at most, only a weak increase in the ratio of C IV- and H α -derived masses. Without knowledge of the C IV blueshifts the distribution of C IV- and H α -dispersion based BH masses could be taken to be reassuring. Including the C IV-blueshift information, however, demonstrates that any such interpretation is inherently flawed because the origin of the C IV emission velocity width is not due to virial-motions for a significant range of C IV blueshift. To reiterate the point made above (Sec. 2.6.1), we believe that using a greater knowledge of the line profile (i.e. both the FWHM and blueshift) is a better motivated (and more practical) approach to obtaining more reliable virial BH mass estimates from the C IV line.

The number of objects in our sample is small but an important factor contributing to the significant correlation evident in the FWHM version of Fig. 11 is a change in the emission-line shape of H α as the C IV-blueshift increases. By comparing the distributions of the H α FWHM and dispersion as a function of C IV-blueshift (shown in the right-panels of Fig. 9), there is a trend for the H α lines to become peakier (with FWHM/ σ approaching unity) as the C IV blueshift increases. Whether the size of the true systematic bias in BH masses inferred from C IV-emission FWHM is as large as shown in Fig. 11 will depend on the future parametrization of the reverberation-component present in H β (and H α) profiles for quasars with high luminosities and large C IV blueshifts.

In summary, Fig. 11 illustrates the extent to which key derived physical parameters, including the BH mass and L/L_{Edd}, could be systematically in error when C IV-FWHM measures are used without incorporating the information from the C IV blueshifts. Other authors have proposed empirical corrections to C IV-based BH masses based on similar systematic trends seen in the C IV line shape (Denney, 2012) and the continuum-subtracted peak flux ratio of the ultraviolet emission-line blend of Si IV+O IV (at 1400 Å) to that of C IV (Runnoe et al., 2013a). In Section 2.7.1 we apply these corrections the quasars

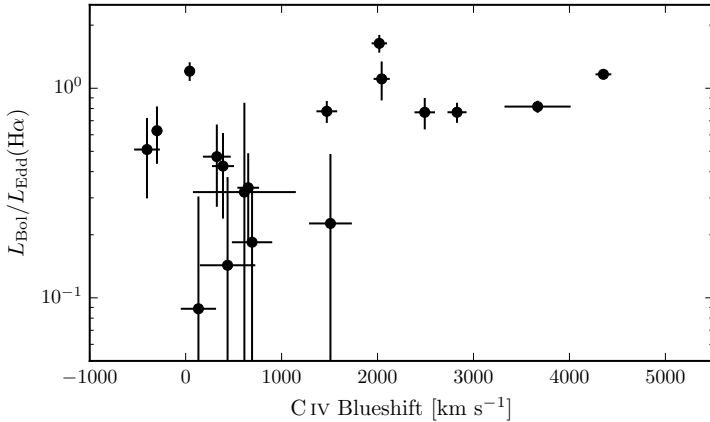


Figure 12: H α -derived Eddington ratio versus C IV blueshift. At blueshift $\gtrsim 2000 \text{ km s}^{-1}$ all quasars have high accretion rates ($L/L_{\text{Edd}} \simeq 1$). This is in agreement with Kratzer and Richards, (2015), but in contrast to what one would derive from naive use of C IV-based BH mass scaling relations.

in our sample, and discuss the effect they have on the systematic bias seen in Fig. 11.

2.6.5 Population trends with C IV blueshift

Even with the caveat regarding the small sample size, the differences in the H α emission-profile as a function of C IV-blueshift (Fig. 8) appear to be systematic. At C IV-blueshift $< 1200 \text{ km s}^{-1}$, the H α FWHM range is $\simeq 2700 - 8800 \text{ km s}^{-1}$, with mean $\simeq 5200 \text{ km s}^{-1}$. However, amongst the six quasars with C IV-blueshift $> 2000 \text{ km s}^{-1}$, the mean H α FWHM = 3000 km s^{-1} , with a scatter of just 200 km s^{-1} . The apparent trend of peakier H α -emission, with FWHM/ σ close to unity, at large C IV-blueshift is enhanced by the modest increase in H α EW with blueshift (Table 3). Amongst the low-C IV-blueshift population there are in addition quasars with broader and more Gaussian-like H α line profiles, with FWHM/ $\sigma \simeq 2$.

The change in the H α emission-line profiles as a function of C IV-blueshift means that the H α -FWHM derived BH masses at high-blueshift are smaller than the sample mean. We transformed the observed luminosity into a mass-normalised accretion rate (Eddington ratio). To convert the monochromatic luminosity, which is observed, in to a bolometric luminosity we use the bolometric correction factor given by Richards et al., (2006a) ($L_{\text{bol}} = 9.26L_{5100}$). Although there is evidence that the bolometric correction factor is a function of the luminosity, as well as of other parameters including the C IV blueshift (Krawczyk et al., 2013), the differences are small over the parameter

range covered by our sample, and for simplicity we adopt a constant factor.

The results, shown in Fig. 12, show that at large blueshifts quasars are accreting at around their Eddington limits (Fig. 12). The converse is, however, not true, i.e. not all quasars with high Eddington ratios possess large C IV blueshifts (see Baskin and Laor, 2005a).

2.7 DISCUSSION

2.7.1 Biases in single-epoch C IV-based BH-mass estimates

The C IV line profiles of the quasars with the largest C IV blueshifts (in the bottom right of Fig. 23) demonstrate that non-virial motions are having a significant effect on the C IV BLR dynamics. At fixed emission-line EW, almost the entire C IV-profile appears to shift blue-ward and the change in line shape is not simply an enhancement of flux in the blue wing of a symmetric component. It is clear that the virial assumption, on which single-epoch BH-mass measurements are predicated, is not straightforwardly applicable for the C IV-emission line in quasars exhibiting large blueshifts.

Quantitatively, the C IV-shape change is most apparent from the FWHM values, which are strongly correlated with the C IV-blueshift. This trend has previously been identified, by comparison with Mg II at lower-redshifts (Shen et al., 2008; Shen et al., 2011) and H β at higher redshifts (Shen and Liu, 2012). We find that virial BH mass estimates based on the C IV FWHM will overestimate the true mass by a factor of ~ 5 for objects exhibiting the largest C IV blueshifts.

In contrast, the C IV line dispersion does not show a similarly strong dependence on the blueshift. This is a result of the shape of the C IV line profile being dependent on the blueshift; the low-blueshift profiles are peakier ($\text{FWHM}/\sigma \simeq 1$) than the high-blueshift profiles ($\text{FWHM}/\sigma \simeq 2$). Denney, (2012) found the level of contamination in single-epoch spectra from non-reverberating gas to be correlated with the shape (FWHM/σ) of the C IV profile. Their investigation was based on a sample of reverberation mapped quasars, which have a narrow range of C IV-emission line shapes, including the absence of any objects with large C IV blueshifts. The FWHM/σ -based correction to the C IV FWHM proposed by Denney, (2012) increases the inferred BH masses by ~ 0.2 dex at the low end of our C IV blueshift distribution, thereby reducing part of the systematic trend in the BH mass (Fig. 13). However, it is not applicable at the high C IV blueshift end, where velocity widths are likely dominated by non-virial motions. Based on the typical line shape of C IV in these high-blueshift quasars ($\text{FWHM}/\sigma \simeq 2$), the Denney, (2012) correction decreases the predicted BH masses by ~ 0.3 dex, which has only a moderate decreasing effect on the strong systematic (Fig. 13).

While the C_{IV}-line dispersion is largely independent of the blueshift, it does not follow that dispersion-based BH-mass estimates are correct, because the underlying assumption regarding the virial-origin of the C_{IV} emission profile breaks down at large blueshifts. Furthermore, given the difficulty in obtaining reliable dispersion measurements from survey-quality spectra with limited S/N (e.g. Mej  a-Restrepo et al., 2016), virial BH-mass estimates for existing large samples of high-redshift quasars are usually based on the FWHM (e.g. Shen et al., 2011). Our work therefore suggests that a viable recipe for obtaining more reliable BH mass estimates for large numbers of quasars at high redshift is to measure both the FWHM and the blueshift, which together can be used to derive a FWHM corrected for the non-virial contribution.

Although we do not have enough quasars in our sample to derive a reliable quantitative correction to BH-masses as a function of C_{IV} blueshift, we are assembling a large sample of quasar spectra with coverage of both C_{IV} and H β /H α in order to empirically validate such a correction. Both Runnoe et al., (2013a) and Shen and Liu, (2012) considered a similar approach, but concluded that a low-ionisation broad line (e.g. Mg II), or features from the quasar NLR, are required to determine the systemic redshift and hence the C_{IV} blueshift. Empirical tests of the reliability of the improved Hewett and Wild, (2010) redshifts for the SDSS DR7 quasars (Shen et al., 2016) and the availability of the largely SED-independent principal component analysis redshifts for DR10 and DR12 (P  ris et al., 2014; P  ris et al., 2017) already allow meaningful corrections to BH-mass estimates for quasars exhibiting large C_{IV}-blueshifts. Our intention is, however, to determine a definitive correction formula using the redshifts from Allen & Hewett (2016, in preparation) for both DR7 and DR12.

Given the difficulty of measuring reliable C_{IV} blueshifts, Runnoe et al., (2013a) opted instead to use the continuum-subtracted peak flux ratio of the ultraviolet emission-line blend of Si_{IV}+O_{IV} (at 1400 Å) to that of C_{IV} to correct for non-virial contributions to the C_{IV} velocity width. This parameter was chosen because it showed the strongest correlation with the FWHM C_{IV}/H β residuals, as well as with the strengths of optical O_{III} and Fe II. The strengths of optical O_{III} and Fe II, being parameters in EV1, are also correlated with the C_{IV} blueshift (Sulentic et al., 2007). As the C_{IV} blueshift increases the EW decreases systematically (Fig. 23). The Si_{IV}+O_{IV} emission-line blend, however, shows significantly less systematic variation. Therefore, while the Runnoe et al., (2013a) Si_{IV}+O_{IV}-based correction is effective in practice, the C_{IV} blueshift measurement provides a more direct measure of the non-virial contributions to the C_{IV} velocity width.

In our sample, we find the 1400 Å/C_{IV} peak flux ratio to be strongly correlated to the C_{IV} blueshift (the Spearman coefficient for the correlation is 0.82, p-value 2E-5). As such, the correction to C_{IV}-based virial

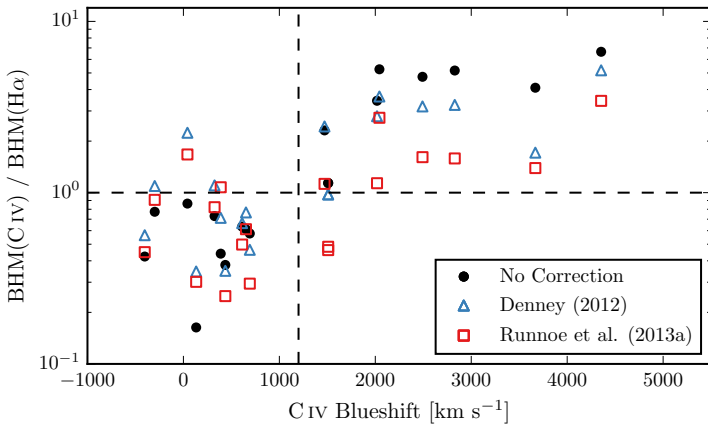


Figure 13: Comparison of BH mass estimates derived from the FWHM of C IV and H α as a function of the C IV blueshift (black circles), and after applying corrections to the C IV-derived mass based on the line shape (blue triangles; Denney, 2012) and the peak flux ratio of the Si IV+O IV blend relative to C IV (red squares; Runnoe et al., 2013a). While the shape-based correction improves the consistency between BH mass estimates in the low-blueshift population, only the Si IV+O IV/C IV peak flux-based correction is effective at high blueshifts (although a weak systematic remains).

masses proposed by Runnoe et al., (2013a, their equation 3) removes a large part of the systematic in the H α /C IV FWHM residuals with the C IV blueshift (Fig. 13); the median C IV/H α FWHM ratio at large C IV blueshifts ($>1200\text{ km s}^{-1}$) is reduced from 4.5 to 1.5. However, at low ($<1200\text{ km s}^{-1}$) C IV blueshifts, the trend for C IV to predict lower BH masses persists, and the scatter between the C IV- and H α -based masses increases by a factor of two. In accordance with our expectations, we find the FWHM C IV/H α residuals to be more tightly correlated to the C IV blueshift (Spearman coefficient 0.82, p-value 3E-5) than to the 1400 Å/C IV peak flux ratio (Spearman coefficient 0.72, p-value 7E-4).

2.7.2 Possible systematic trends in H α BH-mass estimates

In Section 2.6.5, we found that the quasars with large C IV blueshifts have systematically narrower H α FWHM (Fig. 9). Using the standard virial BH mass calibrations this implies that the high C IV blueshift population have high accretion rates ($L/L_{\text{Edd}} \simeq 1$; Fig. 12). This interpretation requires some caution since the emission-line shape (characterized by the value of FWHM/σ) of H α is also changing as a function of the C IV blueshift (Fig. 9). At low C IV blueshifts there are a range of shapes, but all of the quasars exhibiting large C IV blueshifts have peaky H α profiles with $\text{FWHM}/\sigma \simeq 1$. This raises the question of whether the H α FWHM is a reliable proxy for the virial-induced

velocity dispersion for the full range of H α line shapes we have in our sample.

When calibrating the virial-product to masses derived independently using the BH mass – stellar velocity dispersion ($M_{\odot} - \sigma$) relation, Collin et al., (2006) find that the scaling factor, f , is a factor ~ 2 larger for their Population '1' sources (with $\text{FWHM}/\sigma < 2.35$ and essentially equivalent to population A of Sulentic and co-workers and to the high-blueshift quasars here) than for their Population 2 (with $\text{FWHM}/\sigma > 2.35$). For single-epoch BH-mass estimates, assuming a constant value of f , as is normally done (e.g. Vestergaard and Peterson, 2006), means that Population 1 masses will be underestimated and Population 2 will be overestimated. In the context of this result from Collin et al., (2006), our high-blueshift objects all possess peaky H α -lines and, while our quasar sample probes much higher luminosities and masses, the true BH-masses may also be underestimated. Adopting such an interpretation, the amplitude of the trend seen in Fig. 11 might not be so pronounced.

As mentioned in Section 2.1 and discussed in Richards et al., (2011), quasars with current reverberation mapping measurements have a restricted range of C IV-line shapes. There are currently very few reverberation-mapping measurements of quasars with large C IV blueshifts but the results of the large on-going statistical reverberation mapping projects (e.g. Shen et al., 2015) for luminous quasars at high-redshift will go some way to establishing whether the quasar broad line regions producing Balmer emission look the same for objects with very different C IV-emission blueshifts.

Although the EV1-trends (Sulentic et al., 2000; Shen and Ho, 2014) are most likely driven by the accretion rate, orientation may also have a role to play in determining the observed properties of the BLR. Shen and Ho, (2014) argue that a large part of the scatter observed in the H β FWHM relates not to a spread in BH masses, but rather to the orientation of the BLR relative to the line-of-sight. For this to be true, the BLR would need to be in a flattened disc-like geometry, in which case the observed line width would increase with the inclination of the disc relative to the line of sight. Brotherton, Singh, and Runnoe, (2015) found that the core-dominance of radio-loud quasars, which is believed to be a reliable proxy for orientation, at least in a statistical sense, is significantly correlated with the H β FWHM and hence with the BH-mass estimates. This raises the question of whether the narrow H α emission lines observed in the quasars with the largest C IV blueshifts could be an orientation effect. However, there is no evidence that the C IV blueshift is dependent on the orientation (inferred from the radio core-dominance; Richards et al., 2011; Runnoe et al., 2014). Furthermore, Leighly, (2004) showed that the He II $\lambda 1640$ emission-line properties of quasars with large C IV blueshifts are more consistent with differences in the SED rather than differences in the

orientation. Collin et al., (2006) showed that orientation effects were also sub-dominant to the Eddington ratio in determining the shape of the H β line and the H α line shape trend we observe is consistent with the finding of Marziani et al., (2003) that the H β emission profiles of high/low Eddington ratio low-z quasars and type 1 Seyfert nuclei are well fit by Lorentzian and double Gaussian profiles respectively. Overall, therefore, orientation does not appear to be the dominant effect in determining the C IV blueshift and correlated changes in the H α line profile.

2.7.3 Accretion-rate trends in the quasar population

The blueshifting of C IV is usually interpreted as evidence for strong outflows resulting from the presence of a radiation-driven accretion-disc wind. Richards et al., (2002) found that quasars with large C IV blueshifts have weak He II. This is evidence for weak soft X-ray continuum emission (Leighly, 2004), which would allow a strong line-driven wind to form. The strength of such a wind is predicted to be related to the quasar far-ultraviolet SED, which, in turn, could be related to the mass-accretion rate. This picture is therefore consistent with our finding that the quasars with large C IV blueshifts have high accretion rates.

All of the objects in our sample which exhibit large C IV blueshifts would be classified as population A in the Sulentic et al., (2000) scheme based on the H α FWHM (see Section ??). Our results therefore support the idea of the Sulentic et al., (2000) A/B division being driven by the Eddington ratio, with population A sources possessing higher accretion rates. However, we also observe a number of quasars which have high Eddington ratios but do not have line profiles suggestive of strong outflows in the C IV BLR. This suggests that a high accretion rate is a necessary but not sufficient condition for the existence of outflows (Baskin and Laor, 2005a).

The two-dimensional nature of the C IV emission line parametrization and the apparent anti-correlation between C IV EW and C IV blueshift suggests that the quasar population exhibits a continuum of properties. As such, more accurate C IV blueshift measurements for SDSS-quasars should allow an improved mapping between the C IV-emission properties and key physical parameters of the quasars. This includes improving our understanding of the origin of quasars with exceptionally weak, blueshifted C IV emission (weak emission line quasars; Luo et al., 2015) which could be exotic versions of wind-dominated quasars (Plotkin et al., 2015).

2.7.4 *The BAL parent population*

Classical high-ionization BAL (HiBAL) quasars are also predominantly Population A objects in the scheme of Sulentic et al., (2000). There are no HiBAL quasars in our sample by design (Section ??) but it is generally accepted that quasars which show high-ionisation BALs are likely to be radiating with relatively high L/L_{Edd} (e.g. Zhang et al., 2014). We therefore propose that the subset of the quasar population that exhibits large C IV-emission blueshifts, with high-EW and narrow-H α emission lines, may be directly related to the HiBAL quasar population – perhaps even the ‘parent’ population (Richards, 2006). A prediction of such a linkage is that near-infrared observations of the rest-frame optical spectra of HiBAL quasars will show strong, relatively narrow, Balmer emission lines, very similar to those of the quasars with high C IV-blueshifts presented in this paper (see Runnoe et al., 2013b, for such a study).

2.7.5 *The frequency of quasars with high accretion rates*

Quantifying the frequency of quasars producing outflows as a function of key parameters, e.g. quasar luminosity, BH-mass, redshift,... will be important to constrain models of quasar-galaxy evolution. At fixed BH mass, the intrinsic and the observed fraction of quasars exhibiting properties that depend on the Eddington ratio can differ significantly. As an illustration, we consider the implications for the intrinsic fraction of quasars possessing large C IV blueshifts given the observed numbers in the $m_i < 19.1$ flux-limited sub-sample of the SDSS DR7 quasar catalogue, from which our quasar sample is effectively drawn (Section ??). In order to estimate the size of the selection effect, we considered the detection probability for a much-simplified quasar population. We assume that all quasars with C IV blueshifts $> 1200 \text{ km s}^{-1}$ have enhanced accretion rates relative to the ‘normal’ population (with C IV blueshifts $< 1200 \text{ km s}^{-1}$). If the accretion rate of the high-blueshift population is double the rate of the low-blueshift population (which is true in an average sense – see Fig. 12), then the high-blueshift population will be brighter by $\simeq 0.75$ magnitude. Under the assumption that the BH mass distribution is independent of the C IV blueshift, the high-blueshift population will then be over-represented in a flux-limited sample. To estimate the size of the bias, we need to know how many more quasars, at redshifts $2 < z < 2.5$, there are with $m_i < 19.1 + 0.75 = 19.85$ relative to $m_i < 19.1$. This is the fraction of the population which, as a consequence of having enhanced accretion rates, are boosted above the survey flux limit. The main colour-selected SDSS DR7 quasar catalogue extends only

to $m_i = 19.1$ and, assuming the luminosity function is continuous⁹ we thus use the number counts at $m_i < 19.1$ and $m_i < 18.35$, which differ by a factor of $\simeq 4$.

At redshifts $2 < z < 2.5$, there are 3,834 quasars with C IV blueshifts $< 1200 \text{ km s}^{-1}$ and 2,484 with blueshifts $> 1200 \text{ km s}^{-1}$ in the SDSS DR7 $m_i < 19.1$ quasar sample, a ratio of $\sim 2:1$. The above calculation, although much idealised, suggests that the intrinsic fraction of high-blueshift quasars is a factor of four smaller than in the flux-limited sample (i.e. ~ 15 per cent of the ultraviolet-selected non-BAL quasar population).

2.8 CONCLUSIONS

We have presented an analysis of biases in C IV-derived virial BH masses of high-luminosity ($L_{\text{bol}} \sim 47 \text{ erg s}^{-1}$) quasars at redshifts ~ 2.5 from the Sloan Digital Sky Survey. Many authors have reported a large scatter between C IV- and H α /H β -based masses, and part of this scatter has been shown to correlate with the C IV blueshift (Shen and Liu, 2012). The blueshifting of C IV is usually interpreted as evidence for strong outflows which, most likely, result from the presence of a radiation line-driven accretion-disc wind. Our study is the first to examine this bias systematically across the full range of C IV-emission line blueshifts observed in the SDSS sample. In particular, we have used rest-frame optical spectra of 19 quasars in the redshift range $2 < z < 2.7$ to directly compare C IV and H α emission properties as a function of the C IV blueshift. We reach the following conclusions:

- A strong correlation between C IV-velocity width and blueshift is found and at large blueshifts, $> 2000 \text{ km s}^{-1}$, the velocity-widths are dominated by non-virial motions. This suggests that the assumption that velocity-widths arise from virial-induced motions, on which single-epoch BH-mass measurements are predicated, is not straightforwardly applicable to these high-blueshift quasars.
- We use the H α emission line to provide BH-mass estimates that are unbiased by non-virial contributions to the velocity width. We find that the C IV-based BH masses of quasars with low C IV blueshifts are systematically underestimated (by a factor of ~ 1.7) whereas the masses of quasars with large blueshifts are severely overestimated (by a factor of ~ 5).
- We find a systematic change in the shape of the H α line profile as a function of the C IV blueshift. Specifically, the H α line profiles of the quasars with high C IV blueshifts are all ‘peaky’ with FWHM/ σ close to unity.

⁹ The luminosity function and number-counts vary only smoothly (e.g. Ross et al., 2013) for the magnitude and redshift range used here.

- We suggest that the high C IV blueshift quasars are high Eddington-ratio objects that are inherently rare (comprising $\sim 15\%$ of the UV-selected sample), but are being boosted in number by a factor of ~ 4 in the flux-limited SDSS sample.

With a relatively small sample of 19 quasars we have been able to uncover systematic trends in the C IV and H α emission line shapes as a function of the C IV blueshift. This confirms the prospect of developing a blueshift-dependent correction to C IV-based single-epoch BH-mass estimates using a larger samples of luminous quasars with both rest-frame UV and rest-frame optical spectroscopy. We are currently in the process of assembling such a sample, which will contain ~ 300 luminous quasars, 80 per cent at redshifts $z \geq 2$. A new SED-independent redshift-estimation algorithm (Allen & Hewett 2016, in preparation) makes it possible to quantify the distribution of C IV-blueshifts in the observed quasar population as a whole, thereby allowing us to make empirical corrections to C IV-based BH-masses for all luminous, high-redshift SDSS/BOSS quasars.

3

BLACK HOLE MASSES

The C_{IV} $\lambda\lambda 1498,1501$ broad emission line is visible in optical spectra to redshifts exceeding $z \sim 5$. C_{IV} has long been known to exhibit significant displacements to the blue and these ‘blueshifts’ almost certainly signal the presence of strong outflows. As a consequence, single-epoch virial black hole (BH) mass estimates derived from C_{IV} velocity-widths are known to be systematically biased compared to masses from the hydrogen Balmer lines. Using a large sample of 230 high-luminosity ($L_{\text{Bol}} = 10^{45.5} - 10^{48}$ erg s $^{-1}$), redshift $1.5 < z < 4.0$ quasars with both C_{IV} and Balmer line spectra, we have quantified the bias in C_{IV} BH masses as a function of the C_{IV} blueshift. C_{IV} BH masses are shown to be a factor of five larger than the corresponding Balmer-line masses at C_{IV} blueshifts of 3000 km s $^{-1}$ and are over-estimated by almost an order of magnitude at the most extreme blueshifts, $\gtrsim 5000$ km s $^{-1}$. Using the monotonically increasing relationship between the C_{IV} blueshift and the mass ratio BH(C_{IV})/BH(H α) we derive an empirical correction to all C_{IV} BH-masses. The scatter between the corrected C_{IV} masses and the Balmer masses is 0.24 dex at low C_{IV} blueshifts (~ 0 km s $^{-1}$) and just 0.10 dex at high blueshifts (~ 3000 km s $^{-1}$), compared to 0.40 dex before the correction. The correction depends only on the C_{IV} line properties - i.e. full-width at half maximum and blueshift - and can therefore be applied to all quasars where C_{IV} emission line properties have been measured, enabling the derivation of un-biased virial BH mass estimates for the majority of high-luminosity, high-redshift, spectroscopically confirmed quasars in the literature.

3.1 INTRODUCTION

The goal of better understanding the origin of the correlation between the masses of super-massive black holes (BHs) and the masses of host-galaxy spheroids has led to much work focussing on the properties of quasars and active galactic nuclei (AGN) at relatively high redshifts, $z \gtrsim 2$. Extensive reverberation-mapping campaigns (e.g. Kaspi et al., 2000; Kaspi et al., 2007; Peterson et al., 2004; Bentz et al., 2009; Denney et al., 2010) have been used to calibrate single-epoch virial-mass estimates which use the velocity widths of the hydrogen Balmer emission lines and the nuclear continuum luminosity to provide reliable BH masses (e.g. Greene and Ho, 2005; Vestergaard and Peterson, 2006; Vestergaard and Osmer, 2009; Shen et al., 2011; Shen and Liu, 2012; Trakhtenbrot and Netzer, 2012). Single-epoch virial BH mass

estimates using $H\beta$ are possible up to redshifts $z \sim 0.7$, and the technique has been extended to redshifts $z \sim 1.9$ via the calibration of the broad $Mg\,\mathrm{II}\lambda\lambda2796,2803$ emission line (McLure and Jarvis, 2002; Onken and Kollmeier, 2008; Wang et al., 2009; Rafiee and Hall, 2011). At redshifts $z \gtrsim 2$, however, ground-based statistical studies of the quasar population generally have no access to the rest-frame optical and near-ultraviolet spectral regions.

Attention has thus been drawn to the properties of the $C\,\mathrm{IV}\lambda\lambda1498,1501$ emission line, which is both relatively strong in the majority of quasars and visible in modern ‘optical’ spectra, such as those provided by the Sloan Digital Sky Surveys, to redshifts exceeding $z \sim 5$. In contrast to a number of low-ionisation emission lines, such as $Mg\,\mathrm{II}$, the $C\,\mathrm{IV}$ emission has long been known to exhibit significant displacements to the blue (Gaskell, 1982) and more recent work (e.g. Sulentic, Marziani, and Dultzin-Hacyan, 2000; Richards et al., 2011) has established that the extent of ‘blueshifts’ in the $C\,\mathrm{IV}$ emission correlates with a number of properties of quasar spectral energy distributions (SEDs). While the physical origin of the blueshifted emission has not been established there is a consensus that the associated gas is not tracing virial-induced velocities, that should allow a BH-mass estimate to be derived. A favoured interpretation associates the blueshifted emission with out-flowing material (see Netzer, 2015, for a recent review), reaching velocities significantly larger than virial-induced velocities associated with the BH (e.g. Sulentic et al., 2007; Richards et al., 2011). Certainly, excess emission-line flux in the blue wing of the $C\,\mathrm{IV}$ emission increases commonly employed measures of the line-width, notably the full-width at half maximum (FWHM) and the line dispersion (σ). As a consequence, BH-masses derived from $C\,\mathrm{IV}$ emission line velocity-widths are known to be systematically biased compared to masses from the Balmer lines (e.g. Shen et al., 2008; Shen and Liu, 2012; Coatman et al., 2016).

In recent literature, attempts have been made to minimise the influence of the systematic non-virial contribution to the $C\,\mathrm{IV}$ emission on estimates of the BH mass. Strategies include (i) significantly reducing the dependence of the derived masses on the emission-line velocity width (e.g. from the V^2 dependence predicted assuming a virialized broad line region to just $V^{0.56}$ in Park et al. 2013; see also Shen and Liu 2012), (ii) adopting a measure of emission-line velocity-width that is relatively insensitive to changes in the core of the emission-line profile (e.g. Denney et al., 2013) and (iii) estimating the amplitude of the non-virial contribution to the $C\,\mathrm{IV}$ emission-line via comparison with other ultraviolet emission lines (e.g. $Si\,\mathrm{IV}+O\,\mathrm{IV}\lambda1400$ in Runnoe et al. 2013a and Brotherton et al. 2015). The increased number of high-quality spectra of quasars where information on both the Balmer lines in the rest-frame optical and $C\,\mathrm{IV}$ in the ultraviolet is available enables a rather different approach. Specifically, to investigate whether, using

the properties of the C_{IV} emission line itself, it is possible to reduce, or even remove, the systematic bias in the BH-mass estimates.

In this paper we analyse the spectra of 230 high-luminosity ($10^{45.5} - 10^{48}$ erg s⁻¹), redshift $1.5 < z < 4.0$ quasars for which spectra of the hydrogen Balmer emission lines and the C_{IV} emission line exist. A direct comparison of the emission-line velocity widths is therefore possible, allowing us to determine a highly effective empirical correction to the C_{IV} emission line velocity width as a function of the C_{IV} emission line blueshift.

The paper is structured as follows. Section 2 presents the extensive set of near-infrared spectra that, combined with optical spectra of the quasar ultraviolet rest-frame, provides our spectroscopic catalogue. The scheme adopted to calculate emission-line parameters, which draws heavily on the methodology of Shen et al., (2011), Shen and Liu, (2012) and Shen, (2016), is described in Section 3. The observational results, where the emission-line properties of the Balmer lines and the C_{IV} emission are compared and a quantitative relationship derived, are included as Section 4. Then, in Section 5, the practical application of the new BH-mass estimation formula and the extent of remaining uncertainties are discussed, and our scheme is compared to others presented in the literature. Finally, we summarise the main points of the paper and highlight forthcoming improvements to systemic redshift estimates for quasars that should improve the accuracy of BH-masses from rest-frame ultraviolet quasar spectra even further. Throughout this paper we adopt a Λ CDM cosmology with $h_0 = 0.71$, $\Omega_M = 0.27$, and $\Omega_\Lambda = 0.73$. Vacuum wavelengths are used for both rest-frame ultraviolet and optical features. Unless otherwise stated, optical (i.e. SDSS) magnitudes are given in the AB system and infrared magnitudes in the Vega system, following the conventions of the original surveys.

3.2 QUASAR SAMPLE

The aim of this work is to measure empirically the systematic bias in C_{IV}-based virial BH mass estimates for high- z quasars as a function of the C_{IV} emission-line blueshift. The basis for the C_{IV} blueshift based correction is a large sample of quasars where it is possible to make a direct comparison of the C_{IV} line-width with the line-width of the low-ionisation Balmer lines H α and H β , which are believed to provide reliable proxies for the virial velocity. Such an approach has not been possible hitherto as spectra that cover both the observed-frame optical (where the redshifted C_{IV} appears) and near-infrared (where H β and H α lie) are required.

We have compiled a sample of 307 quasars at redshifts $1.5 < z < 4$ with both optical and near-infrared spectra to enable such a comparison to be performed. Reliable emission line properties were measured

for 230 quasars (Section 3.3.5), with 164 possessing H α line measurements and 144 H β line measurements. The sample is considerably larger than previous studies of the rest-frame optical spectra of high- z quasars (e.g. Shen and Liu, 2012). As we demonstrate in Section 3.5.3, the quasars have C IV blueshifts of up to $\sim 5000 \text{ km s}^{-1}$, and span the full range observed in the population. Part of this data set has been taken from the literature, but a substantial fraction is presented here for the first time. The infrared spectra were acquired using several different telescope and spectrograph combinations and the contributions from each telescope/spectrograph, along with the instrumental configurations, are summarised in Table 9. We have sub-divided our sample into two overlapping groups: quasars with reliable H α line measurements (the ‘H α sample’) and quasars with reliable H β measurements (the ‘H β sample’).

In Fig. 28 we show the luminosities and redshifts of the quasar sample relative to the redshift-luminosity distribution for the Sloan Digital Sky Survey (SDSS; York et al., 2000) Seventh Data Release (DR7; Schneider et al., 2010). Our sample spans a redshift range $1.5 < z < 4.0$ and a bolometric luminosity range $10^{45.5} - 10^{48} \text{ erg s}^{-1}$. Spectra were obtained within one or more of the JHK pass-bands and the gaps in our sample coverage at $z \sim 1.8$ and $z \sim 3$ are due to the presence of atmospheric absorption. Obtaining near-infrared spectra of adequate resolution and signal-to-noise ratio (S/N) of even moderately bright quasars remains resource intensive. As a consequence, at fixed redshift, the luminosities of the quasars are brighter than the average luminosity of the SDSS sample, although the dynamic range in luminosity is a full 1.5 decades.

Below, we present the key elements of the observations of the six quasar sub-samples that make up the full 230-quasar catalogue.

3.2.1 Near-infrared observations

3.2.1.1 Coatman et al. (2016) Quasars

Coatman et al., (2016) (hereafter Paper I) observed objects drawn from the SDSS DR7 quasar catalogue. Quasars were selected to i) have redshifts $2.14 < z < 2.51$, ii) be radio-quiet, iii) show no evidence of broad absorption lines (BALs) affecting the C IV emission line, iv) be free from significant dust extinction and v) possess C IV-emission shapes spanning the full range in the population. Near-infrared spectra, including the H α line, were obtained with the Long-slit Intermediate Resolution Infrared Spectrograph (LIRIS; Manchado et al., 1998) mounted on the 4.2 m William Herschel Telescope (WHT) at the Observatorio del Roque de los Muchachos (La Palma, Spain). The

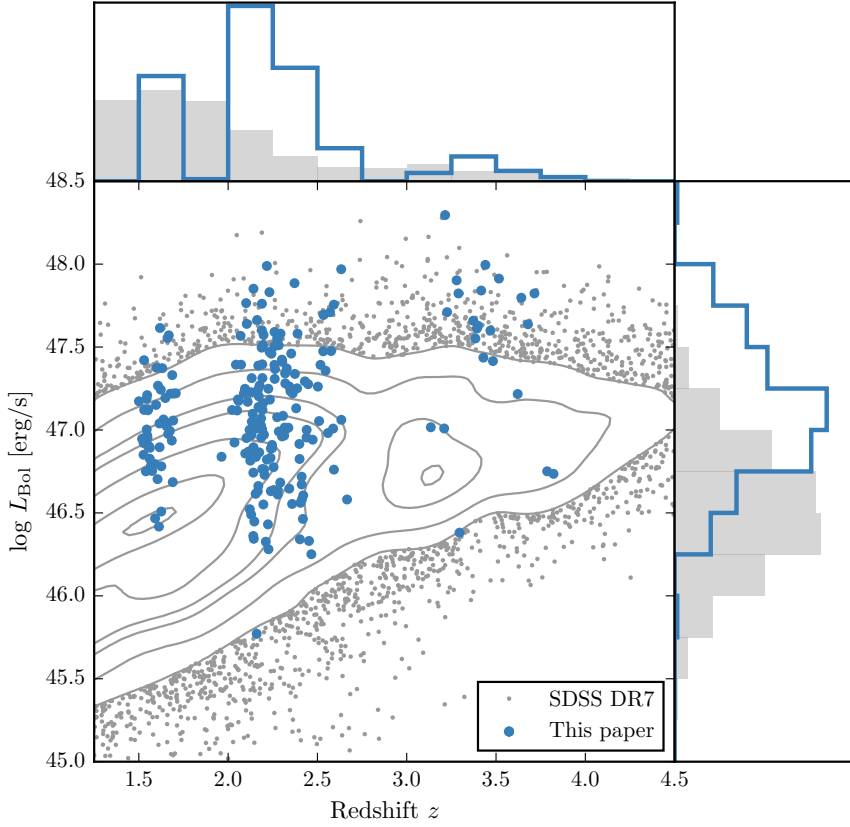


Figure 14: The ranges in redshift and luminosity covered by our sample, relative to the redshift-luminosity distribution of the SDSS DR7 quasar catalogue. In regions of high point-density, contours show equally-spaced lines of constant probability density generated using a Gaussian kernel-density estimator. For the SDSS sample we use Hewett and Wild, (2010) redshifts and bolometric luminosities measured by Shen et al., (2011). For the quasars in this paper the redshift is defined using the peak of the H α /H β emission and the luminosity is measured in the continuum at 1350Å and converted to a bolometric quantity using the same conversion factor employed by Shen et al., (2011).

Table 5: The numbers of quasars with reliable H α and H β line measurements, the spectrographs and telescopes used to obtain the near-infrared spectra, and the instrumental configurations.

Spectrograph	Telescope	Resolving power $\lambda/\Delta\lambda$	Wavelength coverage μm	Slit width arcsec	E
FIRE	MAGELLAN	6000	0.80-2.50	0.6	
GNIRS	GEMINI-N	5400	0.85-2.50	0.3-0.45	
ISAAC	VLT	5100	1.40-1.82	0.6	
LIRIS	WHT	945	1.39-2.42	1.0	
NIRI	GEMINI-N	520-825	1.43-1.96	0.47-0.75	
SINFONI	VLT	2000-3000	1.10-2.45 ^a		
SOFI	NTT	1000-2000	1.53-2.52 ^b	0.6	
TRIPLESPEC	ARC-3.5m	2500-3500	0.95-2.46	1.1-1.5	
TRIPLESPEC	P200	2500-2700	1.00-2.40	1.0	
XSHOOTER	VLT	4350-7450	0.30-2.50	0.5-1.6	
Total					

^a J, H or K filters were employed to ensure coverage of the H β -[O III] spectral region.

^b Both the low resolution red grism and the medium resolution grism, with K and H filters, were employed.

spectra were reduced using standard IRAF¹ packages, as described in Paper I. We have selected 15 quasars with the highest S/N H α spectra from the original sample of 19 (see Section 3.3.5) and the observational properties of these quasars are summarised in Table ??.

3.2.1.2 *Shen & Liu (2012) and Shen (2016) Quasars*

Shen, (2016) and Shen and Liu, (2012) obtained near-infrared spectroscopy for a sample of 74 luminous, $1.5 < z < 3.5$ quasars selected from the SDSS DR7 quasar catalogue. Targets had to possess good optical spectra covering the C IV line and have redshifts $z \sim 1.5, 2.1$, and 3.3 to ensure that the H β -[O III] region was covered in one of the near-infrared JHK bands. Thirty-eight of the quasars were observed with TripleSpec (Wilson et al., 2004) on the Astrophysics Research Consortium (ARC) 3.5 m telescope, and 36 with the Folded-port InfraRed Echellette (FIRE; Simcoe et al., 2010) on the 6.5 m Magellan-Baade telescope. The reduction of the spectra is described in Shen, (2016) and Shen and Liu, (2012). The 57 quasars for which we were able to measure reliable emission line properties (Section 3.3.5) are summarised in Table ??.

¹ IRAF is distributed by the National Optical Astronomy Observatory, which is operated by the Association of Universities for Research in Astronomy (AURA) under a cooperative agreement with the National Science Foundation.

3.2.1.3 Quasar Pairs

Twenty per cent of our catalogue was observed as part of an ongoing effort to identify quasar pairs at very close projected separations (Quasars Probing Quasars² (QPQ); Hennawi et al., 2006a; Hennawi et al., 2010). The primary science driver of this work is to study the circum-galactic medium of the foreground quasars in absorption (Hennawi et al., 2006b). Very accurate systemic redshift measurements are a requirement and a large amount of effort has gone into obtaining near-infrared spectra which cover low-ionisation broad lines or features from the quasar narrow line region (Prochaska and Hennawi, 2009; Lau, Prochaska, and Hennawi, 2015; Hennawi et al., 2015). From the QPQ data set we identified 46 quasars with good-quality near-infrared spectra covering the H α and/or H β lines and SDSS and/or BOSS spectra covering the C IV line. Twenty-two quasars were observed with the Gemini Near-Infrared Spectrograph (GNIRS; Elias et al., 2006) on the 8.1 m Gemini North telescope, 4 using the Infrared Spectrometer And Array Camera (ISAAC; Moorwood et al., 1998) on the European Southern Observatory (ESO) Very Large Telescope (VLT), 11 with the Near InfraRed Imager and Spectrometer (NIRI; Hodapp et al., 2003) also on Gemini North and 9 with XSHOOTER (Vernet et al., 2011), again, on the VLT. The broad wavelength coverage of XSHOOTER means that the spectra cover the region from C IV to H α at the redshifts targeted. The XSHOOTER spectra have higher S/N and resolution than the SDSS/BOSS spectra in the rest-frame ultraviolet and therefore the XSHOOTER spectra are used by default to measure the C IV emission.

The XSHOOTER spectra were reduced with a custom software package developed by George Becker (for details, see Lau, Prochaska, and Hennawi, 2015). The remaining data was processed with algorithms in the LowRedux³ package (see Prochaska and Hennawi, 2009).

The 46 quasars for which we were able to measure reliable emission line properties are summarised in Table ??.

3.2.1.4 VLT SINFONI Quasars

We performed a search of the ESO archive for high- z quasars observed with the SINFONI integral field spectrograph (Eisenhauer et al., 2003; Bonnet et al., 2004) at VLT/UT4. We found 37 quasars with redshifts $1.5 < z < 3.7$ which have H and/or K SINFONI spectroscopy, covering the H β and H α lines respectively, where good optical spectroscopy covering C IV is also available. Thirty of the quasars are from a large programme led by L. Wisotzki (programme 083.B-0456(A)) to study the mass function and Eddington ratios of active BHs at redshifts $z \sim 2$ drawn from the Hamburg/ESO survey (Wisotzki et al.,

² www.ucolick.org/~xavier/QPQ/Quasars_Probing_Quasars

³ www.ucolick.org/~xavier/LowRedux

2000). The Hamburg/ESO optical spectra have a typical $\sim 400 \text{ km s}^{-1}$ spectral resolution and $S/N \gtrsim 10$ per pixel. A further seven SINFONI spectra are from a programme led by J. D. Kurk (programme 090.B-0674(B)) to obtain reliable BH mass estimates from $\text{H}\alpha/\text{H}\beta$ for a sample of radio-loud/radio-quiet SDSS quasars.

The SINFONI spectra were reduced using the package EASYSINF⁴. The package, which is based on the ESO-SINFONI pipeline, is described in Williams et al., (2016).

The 25 quasars for which we were able to measure reliable emission line properties are summarised in Table ??.

3.2.1.5 ESO NTT SOFI Quasars

Twelve per cent of the quasar catalogue derives from a large programme (programme 187.A-0645; PI: J. Hennawi) to combine near-infrared spectra from SOFI (Moorwood, Cuby, and Lidman, 1998) on the 3.6 m New Technology Telescope (NTT) with archival high-resolution optical spectra from the UV-Visual Echelle Spectrograph (UVES; Dekker et al., 2000) at VLT/UT2 and the High Resolution Echelle Spectrometer (HIRES; Vogt et al., 1994) at Keck to construct a legacy database of bright, high-redshift ($2 < z < 4$) quasars with both rest-frame optical spectra, covering the $\text{H}\beta\text{-}[\text{O III}]$ complex, and high-resolution rest-frame ultraviolet spectra. The main science goal is to obtain precise systemic redshifts which are crucial for the study of absorption line systems. The SOFI spectra were reduced using a custom data reduction pipeline using algorithms in the LowRedux package.

Eighteen quasars have been targeted as part of the SDSS/BOSS spectroscopic quasar surveys. In addition, 13 reduced and fluxed UVES spectra have been made available to us by A. Dall'Aglio (a description of the reduction procedure is contained in Dall'Aglio, Wisotzki, and Worseck, (2008)). The sample is larger (~ 100 quasars) but reduced UVES spectra providing rest-frame ultra-violet coverage of C IV are not yet available for the remainder. The spectral resolution of the UVES observations is very high ($R \sim 40\,000$) and the S/N of the spectra re-binned to a resolution of $\simeq 2000$ is $S/N \simeq 300$. The 28 quasars for which we were able to measure reliable emission line properties are summarised in Table ??.

Over five nights from 2015 August 31 to September 4 we obtained near-infrared SOFI spectra for a further 26 quasars (programme 095.B-0644(A); PI: L. Coatman). These quasars were selected from the SDSS DR7 quasar catalogue using criteria very similar to those described in Paper I (see Section 3.2.1.1). In particular, we selected quasars with large C IV blueshifts to improve the statistics in this region of the C IV emission-line parameter space. The 27 quasars for which we were

⁴ www.mrao.cam.ac.uk/~rw480/easysinf

able to measure reliable emission line properties are summarised in Table ??.

3.2.1.6 *P200 TripleSpec Quasars*

A further 36 quasars in our catalogue are bright SDSS quasars which were observed with the TRIPLESPEC spectrograph on the Palomar 200-inch Hale telescope (P200). The objects were observed with the same science goals as the SOFI NTT large programme. The spectra were reduced using a custom pipeline, again using algorithms in the LowRedux package. The 32 quasars for which we were able to measure reliable emission line properties are summarised in Table ??.

3.2.2 *Optical observations*

In the previous sections, we described the infrared spectra of the 230 quasars making up our full spectroscopic catalogue. We will now describe the companion optical spectra, which provide coverage of the C IV emission.

Optical SDSS DR7 spectra are employed for 70 quasars in the full catalogue. The SDSS DR7 spectra are moderate resolution ($R \simeq 2000$) and S/N ($S/N \simeq 20$) and cover the observed-frame wavelength interval $\sim 3800 - 9180 \text{ \AA}$. Many of the quasars in the SDSS DR7 catalogue have been re-observed as part of the Sloan Digital Sky Survey-III: Baryon Oscillation Spectroscopic Survey (SDSS-III/BOSS; Dawson et al., 2013). As the BOSS-spectra typically have higher S/N than the SDSS DR7 spectra, we have used the BOSS spectra when available (126 quasars). We also use high-resolution optical spectra taken with VLT/UVES (11 quasars) and VLT/XSHOOTER (8 quasars), and Hamburg/ESO spectra for a further 15 quasars.

In summary, we have assembled a sample of 230 luminous, high- z quasars with optical and near-infrared spectra. This will allow us to directly compare virial BH mass estimates based on the C IV line-width with estimates based on the line-widths of the low-ionisation Balmer lines H α and H β .

3.3 SPECTRAL MEASUREMENTS

Conventionally, single-epoch virial estimates of the BH mass are a function of the line-of-sight velocity width of a broad emission line and the quasar luminosity. The velocity width is a proxy for the virial velocity in the broad line region (BLR) and, as revealed in reverberation-mapping studies, the luminosity is a proxy for the typical size of the BLR (the R – L relation; e.g. Kaspi et al., 2000; Kaspi et al., 2007). Most reverberation mapping campaigns have employed H β time-lags and velocity widths, but the line-widths of H α and

$\text{Mg II}\lambda 2800$ have been shown to yield consistent BH masses (e.g. McLure and Jarvis, 2002; Greene and Ho, 2005; Onken and Kollmeier, 2008; Shen et al., 2008; Wang et al., 2009; Rafiee and Hall, 2011; Mejía-Restrepo et al., 2016). In Section 3.4.1 we verify that this is the case for the 99 quasars in our sample with measurements of both $\text{H}\alpha$ and $\text{H}\beta$ lines.

At redshifts $z > 2.2$, where the hydrogen Balmer lines and Mg II are no longer accessible in many optical spectra, the $\text{C IV}\lambda 1550$ emission doublet has routinely been used to provide estimates of the virial velocity (e.g. Shen et al., 2011). As has long been recognised (Gaskell, 1982; Tytler and Fan, 1992) the C IV emission line in many quasars includes contributions from gas that does not straightforwardly relate to virial motions within a stable BLR. A number of studies (e.g. Shen et al., 2008; Richards et al., 2011) have shown that the amplitude of the systematic shift of the C IV emission to shorter wavelengths (relative to the systemic velocity) is strongly correlated with the properties of the emission-lines and the overall spectral energy distributions (SEDs).

In our work, a robust measure of the C IV emission-line ‘blueshift’ provides the basis for the corrected C IV velocity-width measurements, and hence BH masses. The effectiveness of the scheme is validated via a direct comparison of the C IV velocity-widths to the Balmer emission velocity-widths in the same quasars. Our process is as follows. First, an accurate measure of the quasar’s systemic redshift is required, for which we adopt the centre of the Balmer emission, where the centre, λ_{half} , is the wavelength that bisects the cumulative total flux. Balmer emission centroids are available for all quasars in the catalogue but we verify that the measure is relatively unbiased through a comparison of the centroids to the wavelengths of the peak of the narrow $[\text{O III}]\lambda\lambda 4960, 5008$ doublet for the subset of spectra where both are available. Second, the blueshift of the C IV emission line is determined. Again, we adopt the line centroid to provide a robust measure of the C IV emission blueshift. The blueshift (in km s^{-1}) is defined as $c \times (1549.48 - \lambda_{\text{half}}) / 1549.48$ where c is the velocity of light and 1549.48 \AA is the rest-frame wavelength for the C IV doublet, assuming equal contribution from both components. Positive blueshift values indicate an excess of emitting material moving towards the observer and hence out-flowing from the quasar.

Emission-line velocity widths are derived from the full-width-at-half-maximum (FWHM) of the lines but we also compute the line dispersion (calculated from the flux-weighted second moment of the velocity distribution) as some authors have claimed this provides a better estimate of the virial velocity (Denney et al., 2013).

To minimise the impact of the finite S/N of the quasar spectra and the presence of absorption features superposed on the broad emission lines we first fit a parametric model to the continuum and the

emission lines. The purpose of the parametric fits is, however, simply to provide higher S/N representations of the emission features. The particular form of the model parametrizations is not important and the fits are used only to provide robust line parameters, such as the centroid λ_{half} , and FWHM, which are measured non-parameterically from the best-fitting model. The models used and the fitting procedure are described below. The issues involved in deriving parameters for broad emission lines from spectra of modest S/N – for example, subtraction of narrow line emission, subtraction of Fe II emission – have been covered comprehensively by other authors (e.g. Shen et al., 2011; Shen and Liu, 2012; Denney et al., 2013; Shen, 2016) and, as far as possible, we follow standard procedures described in the literature.

3.3.1 C IV

The parametrization of the C IV emission line is identical to the one described in Paper I. We first define a power-law continuum, $f(\lambda) \propto \lambda^{-\alpha}$, with the slope, α , determined using the median values of the flux in two continuum windows at 1445–1465 and 1700–1705 Å. The continuum emission is subtracted from the spectra, which is then transformed from wavelength units into units of velocity relative to the rest-frame line-transition wavelength for the C IV doublet (1549.98 Å, assuming equal contributions from both components). The parametric model is ordinarily fit within the wavelength interval 1500–1600 Å (corresponding to approximately $\pm 10\,000 \text{ km s}^{-1}$ from the rest-frame transition wavelength), a recipe that is commonly adopted (e.g. Denney et al., 2013). The line-window was extended if more than 5 per cent of the total flux in the profile was present blueward of the short wavelength limit. Narrow absorption features, which are frequently found superimposed on C IV emission (see, for example, the C IV profile of J0942+3523 in Fig. 15), were masked out during the fit.

The C IV emission was fit with sixth-order Gauss-Hermite (GH) polynomials, using the normalisation of van der Marel and Franx, (1993) and the functional forms of Cappellari et al., (2002). We allowed up to six components, but in many cases a lower order was sufficient (40 and 45 per cent were fit with second- and fourth-order GH polynomials respectively). GH polynomials were chosen because they are flexible enough to model the often very asymmetric C IV line profile. The flip-side of this flexibility, however, is that the model has a tendency to over-fit when spectra possess low S/N. The fits were therefore carefully checked visually and the number of components reduced if over-fitting was evident.

In Paper I we found that using the commonly employed three-Gaussian component model, rather than the GH polynomials, resulted in only marginal differences in the line parameters. Our best-fit parameters are also in good agreement with Shen et al., (2011), who em-

ploy a multi-Gaussian parametrization. In the Appendix we demonstrate that the mean difference between our FWHM measurements and the measurements of Shen et al., (2011) is just 200km s^{-1} for the quasars common to both samples, which is much too small to have any significant effect on our results.

3.3.2 $H\alpha$

A power-law continuum is fit using two continuum windows at 6000–6250 and 6800–7000 Å. The continuum-subtracted flux is then fit in the wavelength interval 6400–6800 Å. We adopt a rest-frame transition wavelength of 6564.89 Å to transform wavelengths into equivalent Doppler velocities. The broad component of $H\alpha$ is fit using one or two Gaussians, constrained to have a minimum FWHM of 1200km s^{-1} . When two Gaussians are used, the velocity centroids are constrained to be the same.

The emission-line profiles of both $H\beta$ and $H\alpha$ frequently include a significant narrow component from the physically more extended narrow line region (NLR). Additional Gaussian components were included in our parametric model to fit the narrow component of $H\alpha$ as well as $[\text{N II}]\lambda\lambda 6548, 6584$ and $[\text{S II}]\lambda\lambda 6717, 6731$. This resulted in a better fit to the observed flux in 50 per cent of cases. We impose a 1200km s^{-1} upper limit on the FWHM of all narrow lines and the amplitudes of all components must be non-negative. The relative flux ratio of the two $[\text{N II}]$ components is also fixed at the expected value of 2.96. In 70 per cent of the spectra the $[\text{O III}]\lambda\lambda 4960, 5008$ doublet is detected at moderate S/N in the $H\beta$ region. In these cases the peak of the $[\text{O III}]$ is used to fix the velocity offsets and the FWHMs of the narrow line components in the $H\alpha$ region. For spectra where the $[\text{O III}]$ doublet does not constrain the velocity and FWHM accurately, the narrow emission in the $H\alpha$ and $H\beta$ regions are fitted independently but, for each region, the individual narrow-line velocity offsets and the FWHMs are constrained to be identical. In these objects the narrow line contribution is generally weak, and so does not have a large effect on the line parameters we measure for the broad component.

The model described above is very similar to the one described in Shen, (2016), Shen and Liu, (2012) and Shen et al., (2011), the only major difference being that we do not fit the $H\alpha$ and $H\beta$ emission regions simultaneously. In Appendix 3.7, we compare our $H\alpha$ line measurements for the subset of our sample taken from Shen, (2016) and Shen and Liu, (2012), and find a scatter of just 0.07 dex.

3.3.3 $H\beta$ and $[\text{O III}]$

Emission from optical Fe II is generally strong in the vicinity of $H\beta$. We therefore fit a combination of a power-law continuum and an

optical Fe II template – taken from Boroson and Green, (1992) – to two windows at 4435–4700 and 5100–5535 Å. The Fe II template is convolved with a Gaussian, and the width of this Gaussian, along with the normalisation and velocity offset of the Fe II template, are free variables in the pseudo-continuum fit. We use the same model to fit the broad and narrow components of H β as was used with H α . Each line in the [O III] doublet is fit with two Gaussians, to model both the systemic and any outflow contributions. The peak flux ratio of the [O III] 4960 Å and 5008 Å lines is fixed at 1:3. As for the fit to the narrow lines in the spectral region around H α , the width and velocity offsets of all the narrow components are set to be equal, and an upper limit of 1200 km s $^{-1}$ is placed on the FWHM.

3.3.4 Fitting procedure

Model parameters were derived using a standard variance-weighted least-squares minimisation procedure employing the Levenberg-Marquardt algorithm. Prior to the fit, the spectra were inspected visually and regions significantly affected by absorption or of low S/N were masked out.

In Fig. 15 we present our parametric fits to the C IV, H α and H β emission lines in a handful of quasars, which have been chosen to illustrate the range of spectrum S/N and line shapes in the sample. The mean reduced chi-squared values in our H α , H β and C IV fits are 1.69, 1.62, and 1.77 respectively and, in general, there are no strong features observable in the spectrum minus model residuals. Table 6 includes the line parameters of our best-fitting model for each line. The reported line-width measures are corrected for instrumental broadening by subtracting the resolution of the spectrograph in quadrature. The spectrograph resolutions, which we estimate from the line widths in the observed sky spectra, range from 25 km s $^{-1}$ for XSHOOTER to 477 km s $^{-1}$ for the low-resolution LIRIS grism and are therefore small relative to the quasar broad line widths.

3.3.5 Spectra removed from sample

Through visual inspection we flagged and discarded the spectra of quasars for which reliable emission line parameters could not be obtained.

First, we flagged emission lines in spectra that possessed insufficient S/N. A single minimum S/N threshold was not entirely effective and, instead, spectra were flagged when it was judged conservatively that no meaningful constraints could be placed on the velocity centroid and/or width of the emission-line.

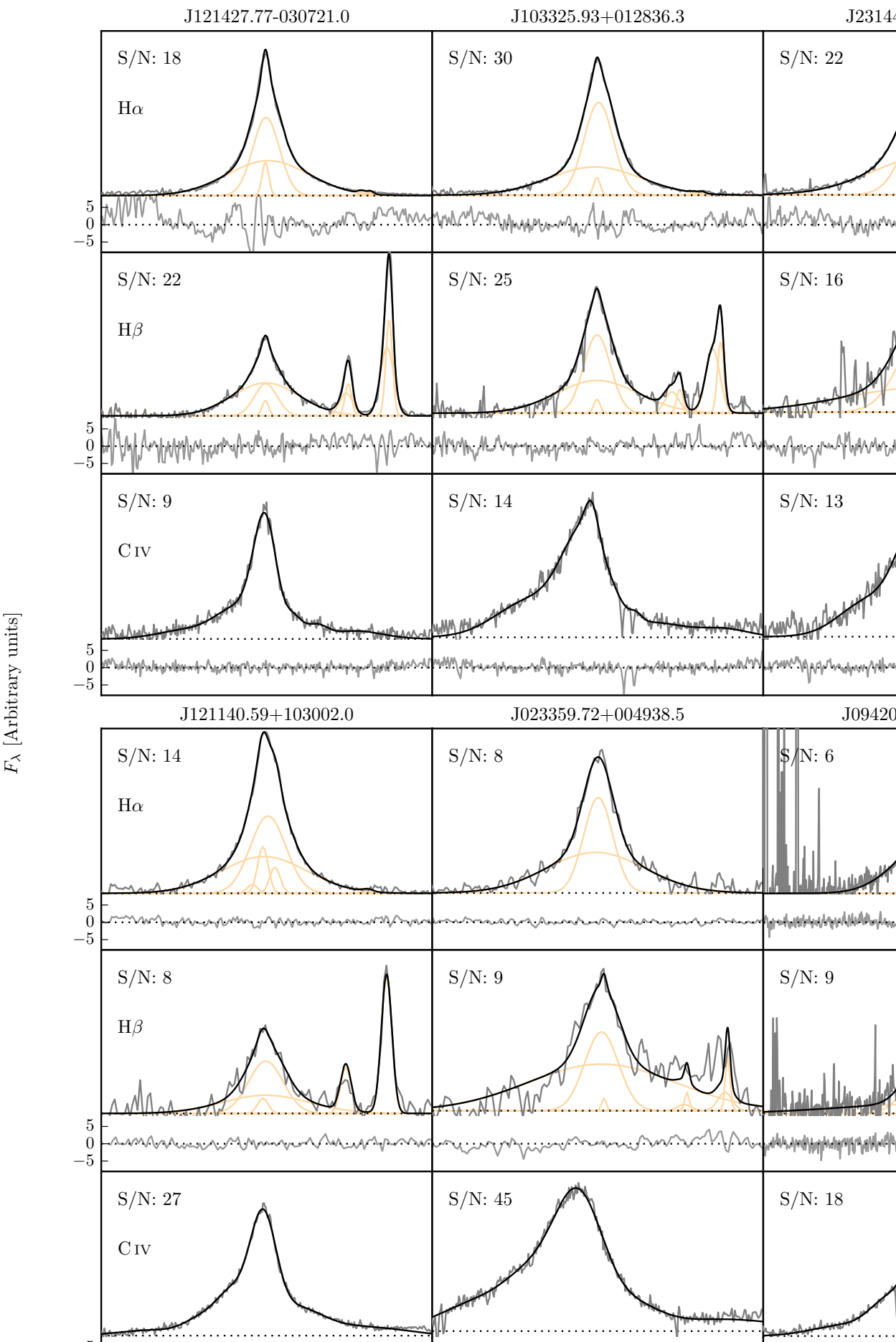
Second, we flagged emission lines where significant regions of the continuum and/or emission line fell outside of the wavelength cov-

Table 6: The format of the table containing the emission line properties from our parametric model fits. The table is available in machine-readable form in the online journal.

	Units	Description
NAME		Catalogue name
FWHM_BROAD_HA	km s^{-1}	FWHM of broad H α line
FWHM_BROAD_HA_ERR	km s^{-1}	
SIGMA_BROAD_HA	km s^{-1}	Dispersion of broad H α line
SIGMA_BROAD_HA_ERR	km s^{-1}	
Z_BROAD_HA		Redshift from broad H α line
FWHM_BROAD_HB	km s^{-1}	FWHM of broad H β line
FWHM_BROAD_HB_ERR	km s^{-1}	
SIGMA_BROAD_HB	km s^{-1}	Dispersion of broad H β line
SIGMA_BROAD_HB_ERR	km s^{-1}	
Z_BROAD_HB		Redshift from broad H β line
FWHM_CIV	km s^{-1}	FWHM of C IV doublet
FWHM_CIV_ERR	km s^{-1}	
SIGMA_CIV	km s^{-1}	Dispersion of C IV doublet
SIGMA_CIV_ERR	km s^{-1}	
BLUESHIFT_CIV_HA	km s^{-1}	Blueshift of C IV relative to centroid of broad H α
BLUESHIFT_CIV_HA_ERR	km s^{-1}	
BLUESHIFT_CIV_HB	km s^{-1}	Blueshift of C IV relative to centroid of broad H β
BLUESHIFT_CIV_HB_ERR	km s^{-1}	
LOGL ₅₁₀₀	erg s^{-1}	Monochromatic continuum luminosity at 5100
LOGL ₁₃₅₀	erg s^{-1}	Monochromatic continuum luminosity at 1350

Table 7: The number of spectra removed from our sample by the cuts described in Section 3.3.5.

	H α sample	H β sample
Total	194	279
H α /H β		
Wavelength	6	27
S/N	8	83
C IV		
Wavelength	6	5
S/N	4	12
Absorption	6	8
Total remaining	164	144



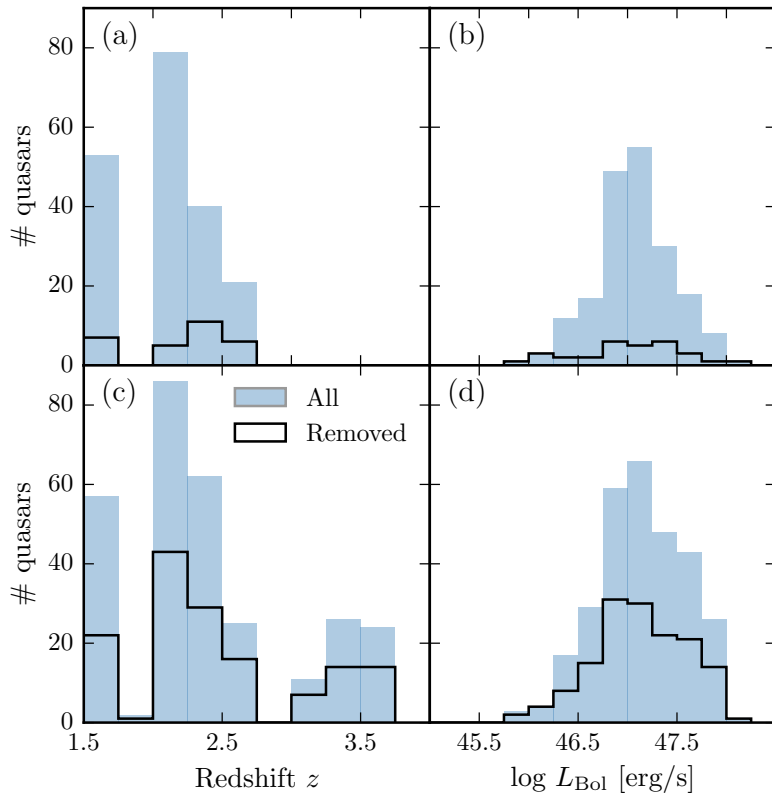


Figure 16: The redshift and luminosity distributions of the spectra removed from our H α /C IV (a, b) and H β /C IV (c, d) samples.

erage of the spectra. Reliable continuum definition and subtraction is not straightforward for emission lines so affected.

Third, we flagged C IV emission lines because of strong, narrow absorption close to the peak of the line where reliable interpolation across the absorption, using our parametric model, was not possible.

The number of spectra that are removed by each cut is given in Table 7 and the distribution in redshift and luminosity is shown in Fig. 16. Unsurprisingly, there is a preferential removal of intrinsically faint quasars, whose spectra can be of poorer S/N, and a loss of quasars at redshifts $z \sim 2.6$ where the H α emission falls at the edge of the K-band. H β is much weaker than H α , and the H β spectra are generally of lower S/N. As a result, the fraction of H β spectra that are flagged – 39 per cent – is particularly high.

3.3.6 Emission-line parameter uncertainties

The 1σ error bars calculated from the covariance matrix in least-squares minimisation will underestimate the true uncertainties on the line parameters, since they do not account for systematic errors such as the

significant uncertainty introduced in the continuum subtraction procedure. To calculate more realistic uncertainties on our fitted variables we employed a Monte Carlo approach. One thousand artificial spectra were synthesised, with the flux at each wavelength drawn from a Normal distribution (mean equal to the measured flux and standard deviation equal to the known error). Our emission-line fitting recipe was then implemented on each of these mock spectra. The uncertainty in each parameter is given by the spread in the best-fitting values from the one thousand realisations of the fitting routine. In some cases the standard deviation of the parameter distribution was biased by extreme values caused by bad fits⁵. We therefore chose to measure the spread in the parameter distribution by fitting a composite model with two Gaussian components – one to model uncertainty in the parameter and the other any possible outlier component. The uncertainty in each line parameter was then taken to be the width of the narrower Gaussian.

3.3.7 *Contemporaneity of spectra*

The epochs of the near-infrared and optical spectra can differ by many years. For example, the NTT SOFI spectra were taken \sim 14 years after the SDSS spectra, and the VLT SINFONI spectra 20 years or more after the Hamburg/ESO observations⁶. If the broad emission line profiles varied significantly on these time-scales the relation between the C IV and Balmer line-width measurements could be blurred.

Cases do exist of dramatic changes in quasar spectra over short time-scales, but this phenomenon is rare (MacLeod et al., 2016). In our spectroscopic catalogue there are 112 SDSS DR7 quasars which are re-observed in BOSS and included in the DR12 quasar catalogue. The mean time elapsed between the two sets of observations is \sim 8 years. The root-mean-square difference in the C IV FWHM measured from the BOSS and SDSS spectra is a modest \simeq 500km s $^{-1}$. Differences in the S/N of the spectra will make a substantial contribution and the scatter due to true variations in the C IV velocity-width will be significantly smaller than 500km s $^{-1}$. We conclude therefore that any intrinsic changes with time do not materially affect the emission line measurements.

3.3.8 *Quasar monochromatic luminosity*

Computing virial BH masses also requires the quasar luminosity in an emission-line free region of the continuum adjacent to the broad line being used. The luminosity is used as a proxy for the size of the

⁵ In the analysis of the real spectra such fits are identified via visual inspection.

⁶ Time differences in the quasar rest-frame are reduced by a factor of $(1+z)$.

BLR. The monochromatic continuum flux is generally measured at 1350 Å for C IV and 5100 Å for H α and H β .

Relative flux-calibration of the infrared spectra as a function of wavelength has been achieved, to $\simeq 10$ per cent, through observations of appropriate flux standards. The absolute flux levels, however, can be in error by large factors due to variable atmospheric conditions combined with the narrow slit widths. For the majority of the quasars we have, therefore, established the absolute flux scale for each near-infrared spectrum using the same quasar SED-model fitting scheme employed in Paper I. The SED model, described in Maddox et al., (2012), gives a very good fit to the SDSS and UKIDSS magnitudes of SDSS DR7 quasars, reproducing the individual magnitudes with a $\sigma < 0.1$ mag. For 207 quasars, (Y)JHK passband magnitudes from the UKIRT Infrared Deep Sky Survey (UKIDSS; Lawrence et al., 2007) Large Area Survey, the Two Micron All Sky Survey (2MASS; Skrutskie et al., 2006) and the Visible and Infrared Survey Telescope for Astronomy (VISTA) Hemisphere Survey (VHS; McMahon et al., 2013) and Kilo-Degree Infrared Galaxy (VIKING; Edge et al., 2013) survey are available. The SED model was fit to the infrared magnitudes; integrating the SED model through the pass-band transmission functions, to give model magnitudes, and performing a variance weighted least-squares fit to the observed magnitudes. The flux at 5100 Å was then taken from the normalised model.

For 19 of the remaining 23 quasars, where near-infrared photometry was not available, the quasar SED model was fit to the SDSS spectra, the flux calibration of which are known to be excellent. The fit was done using a simple variance-weighted chi-squared minimisation procedure in emission line-free intervals of the optical spectra. The model includes a reddening, $E(B - V)$, based on a Small Magellanic Cloud-like extinction curve, and an overall normalisation of the model as free parameters. In practice, the quasars possess only very modest reddenings, with $E(B - V) \simeq 0.0\text{--}0.1$. The flux at 5100 Å was then, again, taken from the normalised SED model. For the four remaining quasars, which possess neither near-infrared photometry nor SDSS DR7 spectra, we fit the SED model to the BOSS DR12 spectra. To avoid the known issues in the flux calibration of the BOSS DR12 quasar spectra at observed-frame blue wavelengths (Lee et al., 2013), our fitting was confined to rest-frame wavelengths long-ward of 1275 Å.

Comparison of the 5100 Å luminosity, computed using the photometry- and spectrum-based methods for 177 quasars, showed a scatter of just ~ 0.1 dex. We therefore assume 0.1 dex to be the measurement uncertainty on the 5100 Å luminosities.

For 34 quasars in the catalogue the optical spectra come from surveys other than SDSS/BOSS and optical magnitudes from recent epochs are not available. In order to obtain an estimate of the luminosity at

1350 Å for the 30 quasars, we take the standard Maddox et al., (2012) quasar SED model, normalised to the near-infrared magnitudes, and read off the flux at 1350 Å.

For all the catalogue quasars, the optical and near-infrared spectra as well as the near-infrared photometry were obtained at different epochs, with rest-frame time differences of up to ∼5 years. Intrinsic quasar photometric variability in the rest-frame ultraviolet and optical will therefore add additional scatter of ∼0.2 mag (e.g. MacLeod et al., 2010) to the derived 1350- and 5100 Å-luminosities.

Given that the luminosity enters into the calculation of BH-mass only as the square-root, the uncertainty on the luminosities does not make a large contribution to the uncertainties in the BH mass estimates.

3.4 AN EMPIRICAL CORRECTION TO C IV-BASED VIRIAL BH-MASS ESTIMATES

3.4.1 H α /H β FWHM comparison

BH-mass calibrations which use the width of the broad H β emission line as a proxy for the virial velocity are widely regarded as the most reliable, since most reverberation mapping employs the H β line and the R – L relation has been established using H β . When H β is not available, H α has been shown to be a reliable substitute (e.g. Greene and Ho, 2005; Shen et al., 2011; Shen and Liu, 2012).

In our sample, we have 99 quasars with reliable measurements of both H α and H β lines. The 99 objects include 21 quasars which were excluded from the main 308-object catalogue because adequate measurements of the C IV FWHM and blueshift could not be acquired. The line widths are compared in Fig. 17 and, as expected, a tight correlation is observed. Greene and Ho, (2005), using a sample of 162 quasars with high S/N SDSS spectra at $z < 0.35$, established the following relation between the H α and H β FWHMs

$$\text{FWHM}(\text{H}_\alpha) = (1.07 \pm 0.07) \times 10^3 \left(\frac{\text{FWHM}(\text{H}_\beta)}{10^3 \text{ km s}^{-1}} \right)^{(1.03 \pm 0.03)} \quad (3)$$

The relation is shown as the dashed line in Fig. 17. The root-mean-square scatter about this relation is 0.07 dex, compared to the ∼0.1 dex found by Greene and Ho, (2005). However, we find a systematic offset, in the sense that the H β line-widths we measure are on average larger by 270 km s $^{-1}$ than predicted by the Greene and Ho, (2005) relation. As our sample covers higher redshifts and luminosities than the sample in Greene and Ho, (2005), we derive a new relation between the H α and H β FWHMs.

We assume a relation of the same form used by Greene and Ho, (2005), i.e. a simple power-law, and infer the model parameters by

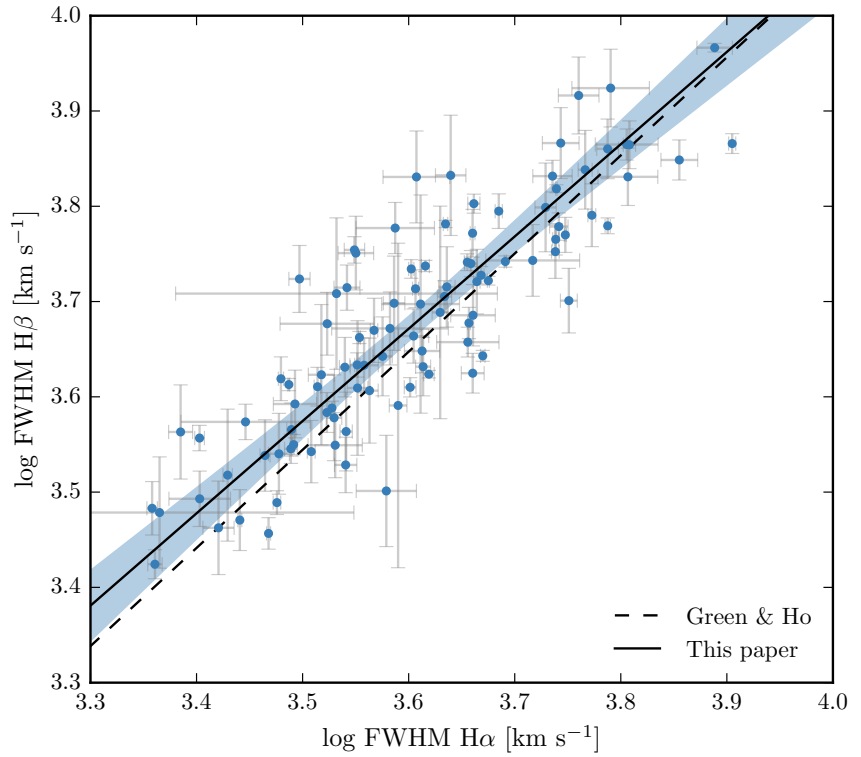


Figure 17: Comparison of H α and H β FWHM measurements for 99 quasars. The solid line is our best-fitting power-law model, and the blue-shaded region shows the 2- σ uncertainties on the model parameters. The dashed line is the relation found by Greene and Ho, (2005) using a sample of $z < 0.35$ SDSS AGN.

fitting a linear model (with slope α and intercept β) in log-log space. The fit is performed within a Bayesian framework described by Hogg, Bovy, and Lang, (2010). Each data point is treated as being drawn from a distribution function that is a convolution of the projection of the point's covariance tensor, of variance Σ_i^2 , with a Gaussian of variance V representing the intrinsic variance in the data. The log-likelihood is then given by

$$\ln \mathcal{L} = - \sum_{i=1}^N \frac{1}{2} \ln [2\pi (\Sigma_i^2 + V)] - \sum_{i=1}^N \frac{\Delta_i^2}{2[\Sigma_i^2 + V]} \quad (4)$$

where Δ_i is the orthogonal displacement of each data point from the linear relationship. An advantage of this approach is that it allows a proper treatment of the measurement errors on both variables, which in this case are comparably large. The model also makes the reasonable assumption that there is an intrinsic scatter in the relationship between the variables that is independent of the measurement errors. Following the suggestion by Hogg, Bovy, and Lang, (2010), the linear model was parametrized in terms of (θ, b_\perp) , where θ is the angle the line makes with the horizontal axis and b_\perp is the perpendicular distance from the line to the origin. Uniform priors were placed on these parameters, and the Jeffreys prior (the inverse variance) was placed on the intrinsic variance. The posterior distribution was sampled using a Markov Chain Monte Carlo (MCMC) method using the Python package emcee (Foreman-Mackey et al., 2013).

The one- and two-dimensional posterior distributions are shown in Fig. 18. The solid line in Fig. 17 is the maximum likelihood solution

$$\text{FWHM}(H_\beta) = (1.23 \pm 0.10) \times 10^3 \left(\frac{\text{FWHM}(H_\alpha)}{10^3 \text{km s}^{-1}} \right)^{0.97 \pm 0.05} \quad (5)$$

and the shaded region shows the 2σ uncertainties on the model parameters.

As discussed above, our relation is displaced to slightly higher $H\beta$ FWHM than the Greene and Ho, (2005) relation – the offset is 210km s^{-1} for a quasar with $H\alpha$ FWHM 4500km s^{-1} . We infer a power-law index that, although slightly shallower, is consistent with the Greene and Ho, (2005) index within the quoted uncertainties. The intrinsic scatter in the data, σ_I , we infer from the fit is 0.04 dex. This is smaller than the total scatter seen in Fig. 17 (0.06 dex), which suggests that measurement errors make a significant contribution to the total scatter in the relation.

For 19 of the 99 quasars with $H\beta$ and $H\alpha$ emission profiles, one of the two Gaussians used to reproduce the $H\beta$ profiles has a FWHM greater than 20000km s^{-1} and a fractional contribution to the total $H\beta$ broad line flux of >0.3 (Marziani et al., 2009; Marziani et al., 2013).

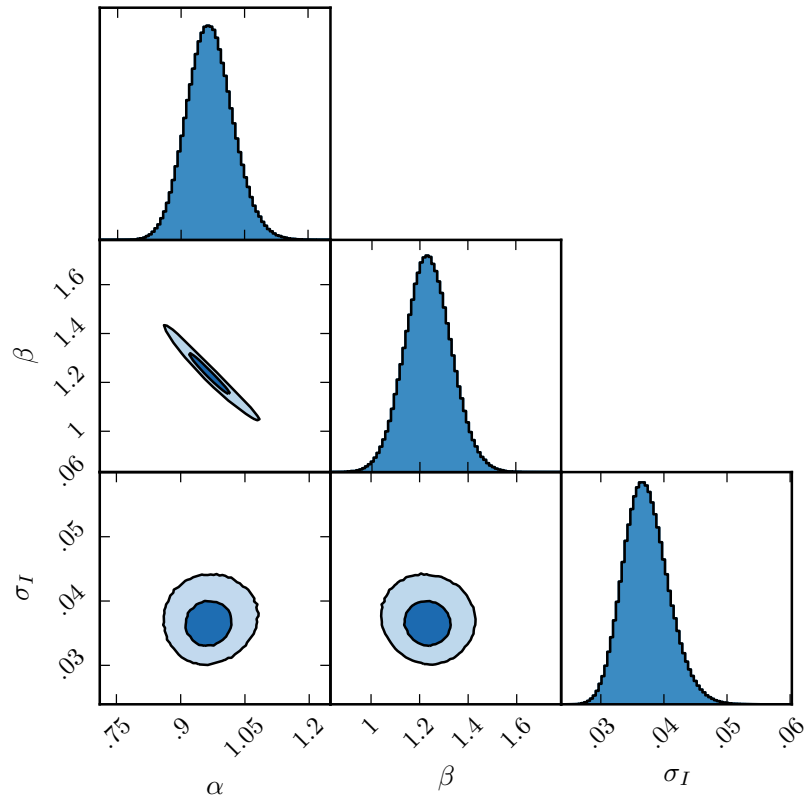


Figure 18: One- and two-dimensional projections of the MCMC sampling of the posterior distribution from the fit in Fig. 17. α is the power-law index, 10^β is the normalisation, and σ_I is the intrinsic scatter. In the two-dimensional projections, 1- and 2- σ contours are shown.

Such a broad component is not seen in the H α profiles and the very broad H β -component may be an artifact of the fitting scheme. A particular issue for H β is the presence of Fe II emission, often at a significant level. Furthermore, additional lines could be contributing to the underlying continuum (e.g. the He I $\lambda\lambda 4922, 5017$ doublet; Véron, Gonçalves, and Véron-Cetty, 2002; Zamfir et al., 2010).

In Sec. 3.4.3 we use the whole of the H β profile to derive an unbiased BH mass. If, instead, the FWHM is calculated from the narrower of the two Gaussian components rather than the composite profile, then the H β FWHM decreases by 630 km s $^{-1}$ on average. The H α FWHM, which are calibrated against the H β FWHM, will also decrease by the same amount on average. This will enhance the C IV FWHM relative to the H α /H β FWHM by \sim 15 per cent and increase the size of the correction which must be applied to the C IV-based BH masses by \sim 30 per cent.

3.4.2 Measuring the quasar systemic redshift

An accurate measure of the quasar's systemic redshift is required in order for the blueshift of the C IV emission line to be determined. Balmer emission centroids, where the centroid, λ_{half} , is the wavelength that bisects the cumulative total flux, are available for all quasars in the catalogue and so we use this to define the systemic redshift.

For 83 and 120 quasars in the H α and H β samples respectively narrow [O III] emission is also detected. In the model fit to the H β region the velocity centroids of the broad H β -line and the core component of the [O III] emission were deliberately determined separately. We find the intrinsic difference in the velocity centroids of the Balmer broad emission and the narrow [O III] emission to have a dispersion of 360 km s $^{-1}$, which is very similar to the value found by Shen et al., (2016). However, the median velocity centroid of the narrow component of the [O III] emission is blueshifted by 270 km s $^{-1}$ relative to the centroid of the broad Balmer line. Applying our parametric model fitting routine to the composite spectrum from Hewett and Wild, (2010), which is constructed using relatively low redshift SDSS quasars with $L_{\text{Bol}} \sim 10^{44}$ erg s $^{-1}$, the centroids of the broad component of H β and the narrow component of [O III] are found to be at essentially identical velocities, suggesting that the blueshifting of narrow [O III] could be luminosity dependent. Regardless, since both the systematic offset and the scatter are small in comparison to the dynamic range in C IV blueshifts, the blueshift-based empirical correction we will derive does not depend on whether the broad Balmer emission or the [O III] centroid is used to define the systemic redshift.

3.4.3 Balmer/C_{IV} line widths as a function of C_{IV}-blueshift

In this section we directly compare the C_{IV} and H α /H β line widths as a function of the C_{IV} blueshift. Because virial BH mass estimates are generally based on the H β FWHM, we first convert our H α FWHM measurements to equivalent H β FWHM using Eq. 5. In Fig. 19a and b we show the C_{IV} FWHM relative to both the (H β -scaled) H α FWHM and the H β FWHM, as a function of the C_{IV} blueshift.

Employing the same Bayesian fitting framework described in Section 3.4.1, we fit independent linear models to the C_{IV} FWHM relative to the H α and H β FWHM as a function of the C_{IV} blueshift. As before, our model has an additional parameter representing any intrinsic scatter in the relationship between the variables which is independent of measurement errors. We also tested a model where some fraction of the data points (which is free to vary) are drawn from an outlier distribution, represented by a broad Gaussian centered on the mean of the data. We found, however, that the inferred outlier fraction was very low (0.004, corresponding to ~ 0.7 data points) and so did not include such a component in our model.

In Fig. 20 we show the one- and two-dimensional projections of the posterior distribution from the linear fit to the FWHM C_{IV}/H α ratio. The projections from the FWHM C_{IV}/H β fit (not shown) have very similar appearances. In Fig. 19a we plot the maximum likelihood model and the 2σ uncertainties on the model parameters. The maximum likelihood line is given by

$$\text{FWHM}(\text{C}_{\text{IV}}, \text{Corr.}) = \frac{\text{FWHM}(\text{C}_{\text{IV}}, \text{Meas.})}{(0.41 \pm 0.02) \left(\frac{\text{C}_{\text{IV}} \text{Blueshift}}{10^3 \text{km s}^{-1}} \right) + (0.62 \pm 0.04)} \quad (6)$$

for the C_{IV}/H α fit and

$$\text{FWHM}(\text{C}_{\text{IV}}, \text{Corr.}) = \frac{\text{FWHM}(\text{C}_{\text{IV}}, \text{Meas.})}{(0.36 \pm 0.03) \left(\frac{\text{C}_{\text{IV}} \text{Blueshift}}{10^3 \text{km s}^{-1}} \right) + (0.61 \pm 0.04)} \quad (7)$$

for the C_{IV}/H β fit. The intercepts of the two relations are consistent, while the difference between the slopes is only marginally inconsistent given the quoted uncertainties.

The intrinsic scatter in the data about the linear relation we infer is 0.23 ± 0.02 and 0.25 ± 0.02 for the H α and H β fits respectively. The intrinsic scatter for the H α fit is represented by the Normal probability density distribution shown in Fig. 21. In the same figure we show the distribution of the orthogonal displacement of each data point from the best-fitting linear relationship. The two distributions are well-matched, which demonstrates that our model is a good representation of the data and the measurement errors on the data points are small relative to the intrinsic scatter.

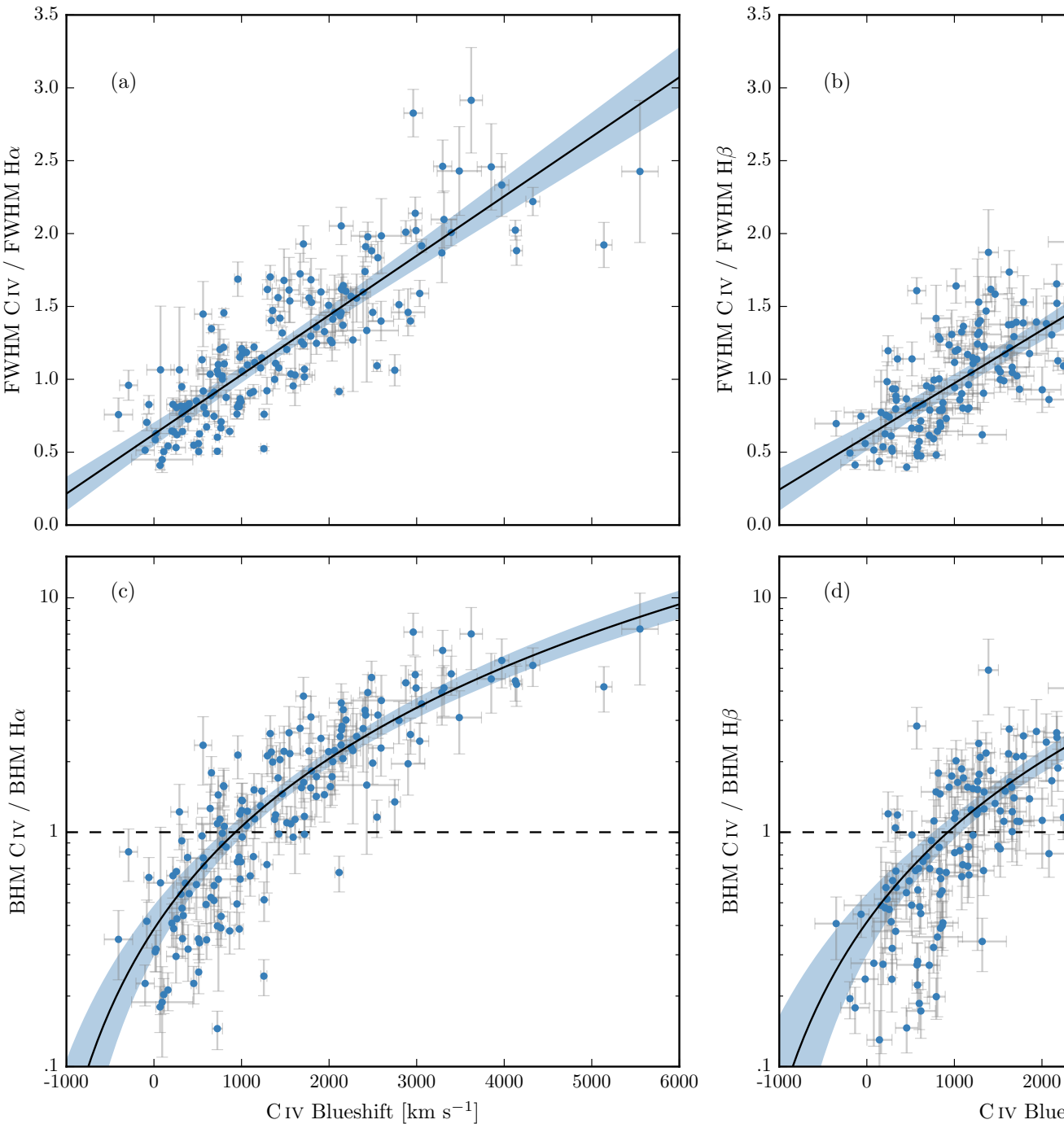


Figure 19: C_{IV} FWHM relative to H_α FWHM (a) and H_β FWHM (b), and C_{IV} based BH mass (BHM) compared to H_α based mass (c) and H_β based mass (d), all as a function of the C_{IV} blueshift. The black line is our best-fit linear model, and the shaded region shows the 2- σ uncertainties on the slope and intercept. The H_α FWHM have been scaled to match the H_β FWHM using Eq. 5.

The overall (intrinsic and measurement) scatter about the best-fitting model is slightly higher when the C IV line-widths are compared to H β (0.12 dex) than when compared to H α (0.10 dex). This is likely due, at least in part, to the generally higher S/N of the H α emission. In addition, contributions from the strong [O III] doublet in the vicinity of H β make de-blending the H β emission more uncertain. As a consequence, for quasars where H α and H β are both measured, the mean uncertainty on the H α FWHM is 130 km s $^{-1}$, compared to 340 km s $^{-1}$ for H β .

In the next section we use both the H α and H β lines to calculate unbiased BH masses. We use the H α measurements to derive an empirical C IV blueshift based correction to the C IV masses (Eq. 8) because of the issues related to the accurate modelling of the H β -profile just described. An extra advantage, which is evident in Fig. 19, is that the H α sample has a better C IV blueshift coverage. However, as can be seen from the similarity of Equations 6 and 7, our results would not change significantly were we instead to use the H β sample.

3.4.4 C IV based virial BH mass estimates

We calculate virial BH mass estimates from C IV, H α and H β using the widely-adopted Vestergaard and Peterson, (2006) scaling relations (their equations 5 and 7 for H α /H β and C IV respectively). In Figs. 19c and d the C IV-based estimates are compared to the H α /H β estimates as a function of the C IV blueshift. There is a strong systematic error in the C IV-based masses as a function of blueshift, which is a direct consequence of the FWHM trend described in the previous section. The C IV emission-based BH-masses are in error by a factor of more than five at 3000 km s $^{-1}$ in C IV emission blueshift and the overestimate of the BH-masses reaches a factor of 10 for quasars exhibiting the most extreme blueshifts, \gtrsim 5000 km s $^{-1}$.

The virial product is the product of the virial velocity squared and the BLR radius (e.g. Shen, 2013), and is proportional to the BH mass. We use the corrected C IV FWHM given by Eq. 6 as an indicator of the virial velocity, and adopt the same R – L relation for the 1350 Å continuum luminosity as Vestergaard and Peterson, (2006) (i.e. $R \propto L^{0.53}$). To find the constant scaling factor necessary to transform the virial product in to a BH mass we compute the inverse-variance weighted mean difference between the virial products and the H α -based masses. The virial BH mass can then be expressed in terms of the corrected C IV FWHM and monochromatic continuum luminosity at 1350 Å

$$MBH(C\text{ IV}, \text{Corr.}) = 10^{6.71} \left(\frac{\text{FWHM}(C\text{ IV}, \text{Corr.})}{10^3 \text{ km s}^{-1}} \right)^2 \left(\frac{-L_{-}(1350\text{\AA})}{10^{44} \text{ erg s}^{-1}} \right)^{0.53}$$

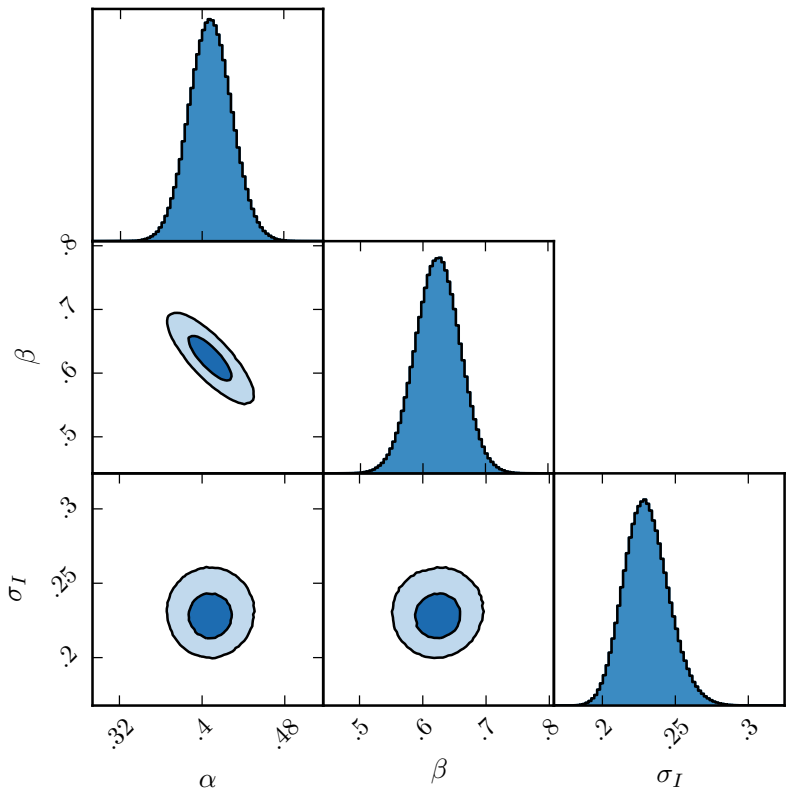


Figure 20: One- and two-dimensional projections of the MCMC sample of the posterior distribution for a linear fit to the FWHM C IV/H α ratio as a function of the C IV blueshift. In the two-dimensional projections we show 1- and 2- σ contours. The posterior distribution for the linear fit to the FWHM C IV/H β ratio, which we do not show, has a very similar appearance.

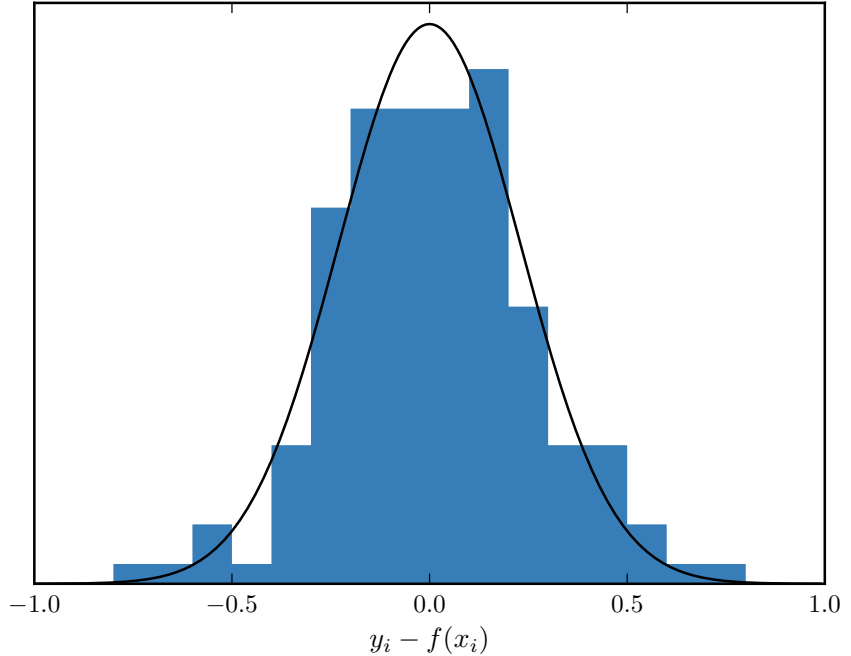


Figure 21: The distribution of the orthogonal displacement of each data point from the best-fitting linear relationship in the fit to FWHM(CIV)/FWHM(H α) as a function of the CIV blueshift (blue histogram). The black curve is a Normal distribution with a width equal to the intrinsic scatter in the population inferred from the fit. The two distributions are well-matched, which demonstrates that our model is a good representation of the data and the measurement errors on the data points are small relative to the intrinsic scatter.

(8)

Given measured C IV emission line FWHM and blueshift, equations 4 and 6 can then be used to provide an unbiased estimate of the quasar BH mass.

3.5 PRACTICAL APPLICATION OF THE C IV-BASED CORRECTION TO VIRIAL BH-MASS ESTIMATES

3.5.1 Recipe for unbiased C IV based BH masses

Equations 4 and 6 together provide an un-biased estimate of the virial BH mass given the FWHM and blueshift of C IV, together with the continuum luminosity at 1350 Å. The FWHM is readily obtained, either directly from the data, or, via the fitting of a parametric model to the C IV-emission line. The blueshift – defined as the bisector of the cumulative line flux – is also straightforward to measure and our preferred procedure is described in Section 3.3.1. The only potential complication arises in establishing the quasar systemic redshift and hence defining the zero-point for the C IV-blueshift measurement, since both the blueshift and the systemic redshift cannot be determined from C IV alone. In practice, when rest-frame optical lines are accessible, as is the case for the quasar sample here, an accurate systemic redshift can be obtained. The [O III] doublet and the Balmer lines all have velocity centroids very close to systemic, and the same is true for the broad Mg II doublet. For quasars at very high redshifts, $z \sim 6$, systemic redshifts can also be derived using the [C II] 158 μm emission in the sub-millimetre band (e.g. Venemans et al., 2016). However, in general, for example in determining the BH-masses of quasars at redshifts $z > 2$, if only the rest-frame ultraviolet region is available determining a reliable systemic redshift is non-trivial.

Shen et al., (2016) and our own work shows that there is an intrinsic variation of $\sigma \approx 220 \text{ km s}^{-1}$ in the velocity centroids of the broad-line region relative to a systemic-frame defined by the quasar narrow-line regions. As we showed in Paper I, the SDSS DR7 pipeline redshifts are not sufficiently reliable to measure the C IV blueshift accurately because, in part, the C IV emission line itself contributes to the determination of the quasar redshifts (see figure 1 in Paper I). The redshift-determination scheme of Hewett and Wild, (2010) provided much improved redshifts for the SDSS DR7 quasar catalogue, not least because the redshift estimates for the majority of quasars were derived using emission-lines other than the C IV-line itself. The redshifts for quasars in the SDSS DR10 and DR12 catalogues (Pâris et al., 2014; Pâris et al., 2017) possess errors of $\approx 500\text{-}750 \text{ km s}^{-1}$ (Pâris et al., 2012; Font-Ribera et al., 2013). The impact of low spectrum S/N for fainter quasars in all the SDSS data releases increases the uncertainty further. Table 8 includes the values for the fractional error in the corrected

Table 8: The fractional error on the corrected BH mass as a function of C IV blueshift for different uncertainties in the quasar systemic redshift.

δv (km s $^{-1}$)	C IV blueshift (km s $^{-1}$)			
	0	1000	2000	4000
250	0.33	0.20	0.14	0.09
500	0.65	0.39	0.28	0.18
1000	1.30	0.79	0.57	0.36

BH-mass that result from a given error in the determination of the systemic rest-frame. For example, the fractional error in the corrected BH mass is 0.39 for a quasar with a 1000 km s $^{-1}$ C IV blueshift when there is a 500 km s $^{-1}$ uncertainty in the quasar systemic redshift.

Of potentially more significance for studies of BH-masses as a function of quasar and host-galaxy properties are redshift errors that depend on the form of the quasar ultraviolet SED. The redshifts from Hewett and Wild, (2010) still suffer from systematic errors that are correlated with the shape, and particularly the blueshift, of the C IV emission line. For the Hewett and Wild, (2010) redshifts, and ultraviolet emission-line based redshifts in general, quasars with large C IV EW and modest blueshifts have relatively small (\simeq 300 km s $^{-1}$) SED-dependent redshift errors. Redshift uncertainties as large as \simeq 1000 km s $^{-1}$ for such quasars are unusual and the large relative error in the corrected C IV BH-mass given in Table 8 is pessimistic.

Conversely, systematic redshift errors are greatest for quasars with large blueshifts, reaching \sim 750 km s $^{-1}$ in the extreme for the Hewett and Wild, (2010) values. The associated error in the corrected C IV BH-masses is, however, mitigated somewhat due to the smaller gradient of the MBH(C IV)/MBH(Balmer) relation at large C IV blueshift (see Fig. 19). A definitive quantification of any systematic SED-dependent errors present in the quasar redshifts contained in the SDSS DR12 catalogue is not yet available but the principal component analysis (PCA) based redshift estimates are expected to be largely free of SED-dependent systematics. Given the importance of generating more accurate redshifts for the SDSS DR7 and DR12 quasar samples we will publish a catalogue of more accurate redshifts in due course (see Section 3.6).

3.5.2 Systematic trends in residuals

The scatter about the best-fitting line in the C IV/H α FWHM versus C IV-blueshift relation is \sim 0.1 dex, an order of magnitude smaller than the size of the C IV-blueshift dependent systematic but, nevertheless, still significant. With a view to reducing the scatter further, we searched for measurable parameters which correlate with the scat-

ter at fixed C_{IV} blueshift, including the luminosity, redshift, [O_{III}] equivalent width (EW), and Fe_{II} EW. The only significant correlation we find is with the H _{α} FWHM (Fig. 22). Quasars with broad H _{α} lines tend to lie below the relation while quasars with narrow H _{α} tend to lie above it. One possibility is that this correlation is simply due to random scatter (either intrinsic or measurement error) in the H _{α} FWHM which, with the other quasar properties fixed, would naturally produce a correlation between FWHM(C_{IV})/FWHM(H _{α}) and FWHM(H _{α}). However, the fact that we see no such correlation between the model residuals and the C_{IV} FWHM suggests that the H _{α} FWHM correlation could be revealing something more fundamental. The H _{α} /H _{β} FWHM is part of ‘eigenvector 1’ (EV1), the first eigenvector in a principal component analysis which originated from the work of Boroson and Green, (1992). While a number of parameters have been considered within the EV1 context (e.g. Brotherton and Francis, 1999), Fig. 22 suggests that part of the scatter between the Balmer and C_{IV} velocity widths might be attributed to differences in the spectral properties which are correlated with EV1 (Marziani et al., 2013).

The residuals and the H _{α} FWHM also correlate with the shape of the line (FWHM/ σ , where σ is the dispersion, derived from the second moment velocity; e.g. Kollatschny and Zetzl, 2011; Kollatschny and Zetzl, 2013). The narrow lines are, on average, ‘peakier’ (with FWHM/ $\sigma \simeq 1$) than the broader lines (with FWHM/ $\sigma \simeq 2$). The origin of the Balmer-line shape correlation is not clear but one possibility is an orientation-dependence of the H _{α} FWHM (e.g. Shen and Ho, 2014). In this scenario quasars with broader emission lines are more likely to be in an edge-on orientation relative to our line of sight.

At radio wavelengths, the morphology of the radio structure, parametrized in terms of ‘core dominance’ is believed, at least in a statistical sense, to be a proxy for the orientation of the accretion disk (e.g. Jackson and Browne, 1991). We matched our sample to the FIRST radio catalogue (White et al., 1997) in an attempt to identify orientation-dependent signatures. Following Shen et al., (2011), we classified quasars with matches within 5 arcseconds as core-dominated, while, if multiple matches were found within 30 arcseconds, quasars were classified as lobe-dominated. Twenty core- quasars and six lobe-dominated quasars resulted but no statistically significant differences in the H _{α} linewidths of the two samples were found. It should be noted that the sub-sample of radio-detected quasars is small and the effectiveness of the test is further compromised by the lack of radio-detected quasars at large blueshifts (see figure 14 of Richards et al., 2011, for example).

There are currently very few reverberation-mapping measurements of quasars with large C_{IV} blueshifts. Looking to the future, the results of the large on-going statistical reverberation mapping projects (e.g. Shen et al., 2015; King et al., 2015) for luminous quasars at high-

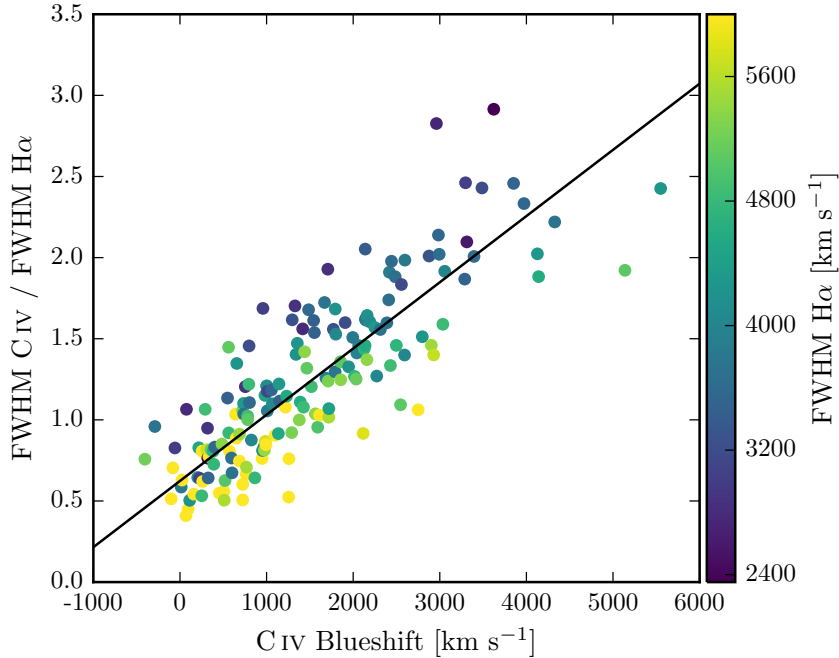


Figure 22: Same as Fig. 19a, with the marker colour representing the $\text{H}\alpha$ FWHM. At fixed CIV blueshift, there is a clear $\text{H}\alpha$ FWHM dependent systematic in the model residuals.

redshift will shed new light on the Balmer line emitting region of the BLR for quasars with a range of CIV blueshifts and lead to a greater understanding of the relation between the Balmer line profile and the BH mass.

3.5.3 Effectiveness of the CIV blueshift based correction to BH masses

Figure 23 demonstrates that our sample has an excellent coverage of the EW-blueshift parameter space in relation to SDSS DR7 quasars at redshifts $1.6 < z < 3.0$. The systematic offset to higher CIV blueshifts for our catalogue relative to the SDSS quasars as a whole is a result of the higher mean luminosity relative to the SDSS sample (Fig. 28). Our sample includes 21 quasars with CIV blueshifts $> 3000 \text{ km s}^{-1}$, and extends to $\sim 5000 \text{ km s}^{-1}$, i.e. at the very extreme of what is observed in this redshift and luminosity range. Our investigation thus demonstrates that the CIV -blueshift based correction derived in this paper is applicable to very high blueshifts. Conversely, there are no quasars in our catalogue with CIV blueshifts $\lesssim 0 \text{ km s}^{-1}$ and we caution against extrapolating the correction formula to negative blueshifts.

Figure 24 compares the CIV - and $\text{H}\alpha$ -based BH masses before and after applying the blueshift-based correction to the CIV FWHM. Before the correction, the correlation between the CIV - and $\text{H}\alpha$ -based BH masses is very weak, and the scatter between the masses is 0.4

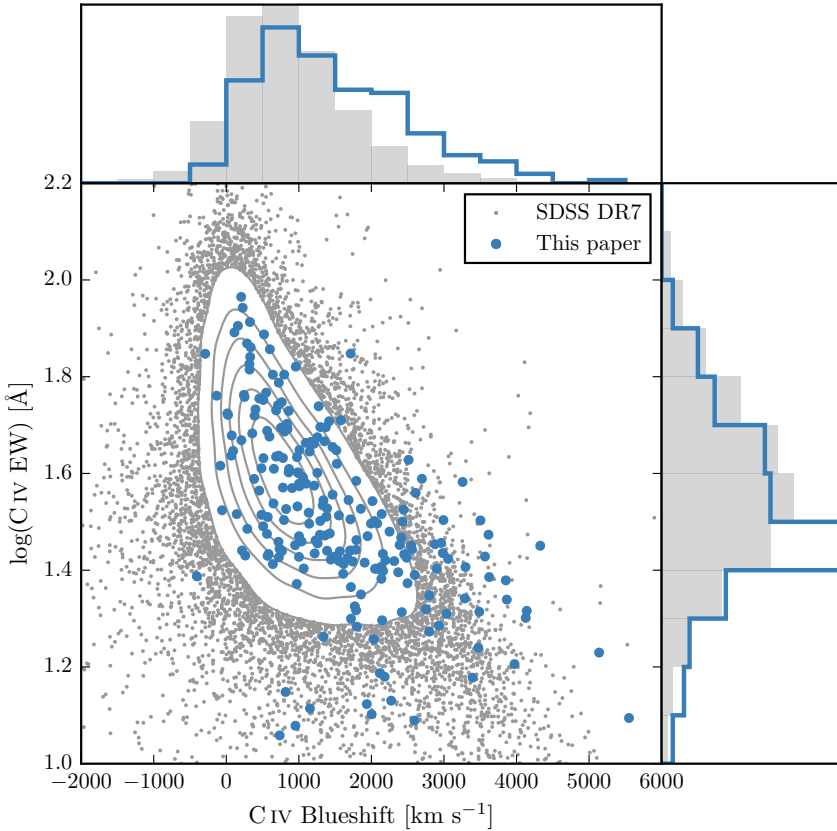


Figure 23: Rest-frame EW versus blueshift of the broad C_{IV}-emission line for 32,157 SDSS DR7 quasars at $1.6 < z < 3.0$ (grey) and our sample (blue). For the SDSS quasars, the systemic redshifts used to calculate the blueshifts are from Hewett and Wild, (2010) and C_{IV} emission properties are described in Paper I. In regions of high point-density, contours show equally-spaced lines of constant probability density generated using a Gaussian kernel-density estimator. Our sample has very good coverage; the shift to high blueshifts is a result of the high luminosity of our sample in relation to the SDSS sample and the correlation between luminosity and blueshift.

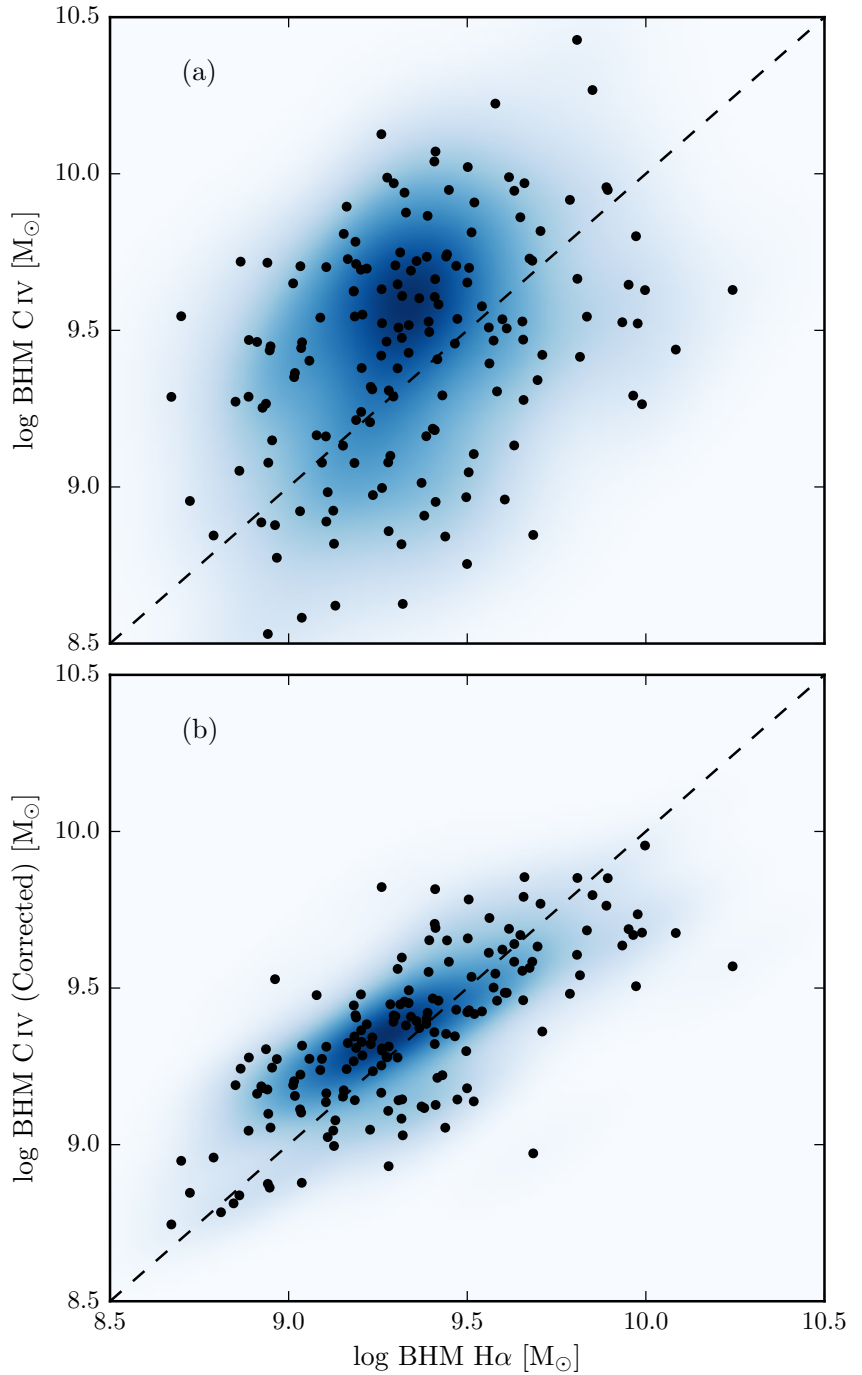


Figure 24: Comparison of the C IV- and H α -based BH masses before (a) and after (b) applying the C IV blueshift-based correction to the C IV FWHM. The density of the plotted points (estimated using a Gaussian kernel density estimator) is represented by the colour. The correction to the C IV BH masses decreases the scatter by from 0.4 to 0.2 dex.

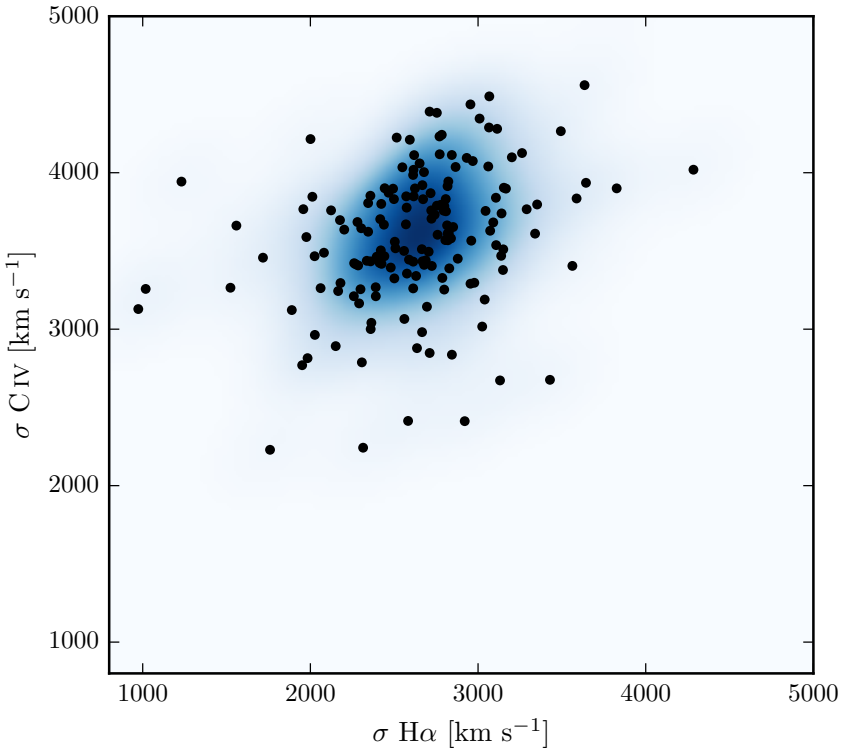


Figure 25: Comparison of the C IV and H α line dispersion, σ . The density of the plotted points (estimated using a Gaussian kernel density estimator) is represented by the colour. Estimating a reliable BH mass from the C IV FWHM and blueshift line is substantially more effective than using the C IV line dispersion with, or without, the line blueshift. The C IV dispersion values are larger than the corresponding H α measurements by a factor of 1.4 on average, which is consistent with reverberation mapping measurements (Vestergaard and Peterson, 2006).

dex. After correcting the C IV FWHM for the non-virial contribution, the correlation improves dramatically. The scatter between the corrected C IV-based masses and the H α -based masses is reduced to 0.2 dex. The scatter is 0.24 dex at low C IV blueshifts ($\sim 0 \text{ km s}^{-1}$) and 0.10 dex at high blueshifts ($\sim 3000 \text{ km s}^{-1}$).

There has been a considerable amount of attention regarding the relative merits of using the FWHM or dispersion to characterise the velocity width (e.g. Denney et al., 2013). As we showed in Paper I, the line dispersion is relatively insensitive to the blueshift and shape of the C IV line. Therefore, without the blueshift information, using the line dispersion would yield a more accurate BH mass than the FWHM (Fig. 25). The correlation between the H α and C IV line dispersion is, however, weak. The Pearson coefficient for the correlation is 0.36 (and just 0.15 when the H β measurements are used in place of H α). Furthermore, there is little dynamic range in the line disper-

sion: the scatter is just 480 and 460 km s⁻¹ for H α and C IV respectively. The observation suggests that the line dispersion does not fully trace the dynamic range in BH mass present in the quasar population. At least part of the reason is that the line dispersion is difficult to measure reliably in current survey-quality data, particularly because of the sensitivity to flux ascribed to the wings of the emission line (e.g. Mejía-Restrepo et al., 2016). Figures 24 and 25 demonstrate that estimating a reliable BH mass from the C IV FWHM and blueshift line is substantially more effective than using the C IV line dispersion with, or without, the line blueshift.

3.5.4 Comparison to previous prescriptions

In Fig. 26 we compare the C IV blueshift-based correction presented in this paper to various prescriptions which have been proposed in the literature to derive BH masses from the C IV line which are consistent with the masses derived from the Balmer lines. In each case we compare the corrected C IV-based masses to the H α -based masses as a function of the C IV blueshift. The correction proposed by Runnoe et al., (2013a) is based on the spectral region at rest-frame wavelengths of \sim 1400 Å (see below). Therefore, our analysis is based on the 123 quasars which satisfy this requirement.

In Fig 26a the C IV BH masses have been corrected using the C IV shape (FWHM/ σ) based correction proposed by Denney, (2012). The correction is not applicable at large C IV blueshifts, since it was calibrated on a sample of low-luminosity AGN which does not include any such objects. Therefore, while the consistency between the H α - and C IV-based masses at low C IV blueshifts is improved, at high C IV blueshifts the C IV-based masses remain seriously overestimated.

Runnoe et al., (2013a) used the continuum-subtracted peak flux ratio of the ultraviolet emission-line blend of Si IV+O IV (at 1400 Å) relative to C IV to correct for non-virial contributions to the C IV velocity-width. Following Runnoe et al., (2013a), we measure the peak flux by fitting a model with four Gaussian components (two for each emission line) to the continuum-subtracted flux. As is evident from Fig. 23, a correlation exists between the blueshift and equivalent width of C IV: C IV emission which is strongly blueshifted is typically weak. The Si IV+O IV emission-line blend, however, shows significantly less systematic variation. Therefore, the Si IV+O IV-based correction is quite effective in practice: the systematic bias in the C IV BH masses at large C IV blueshifts is reduced to a factor of \sim 2 (Fig. 26b). However, the C IV based masses are still systematically overestimated at large C IV blueshifts.

In contrast to the widely-used Vestergaard and Peterson, (2006) C IV-based virial BH mass calibration, the more recent Park et al., (2013) calibration significantly reduces the dependence of the derived

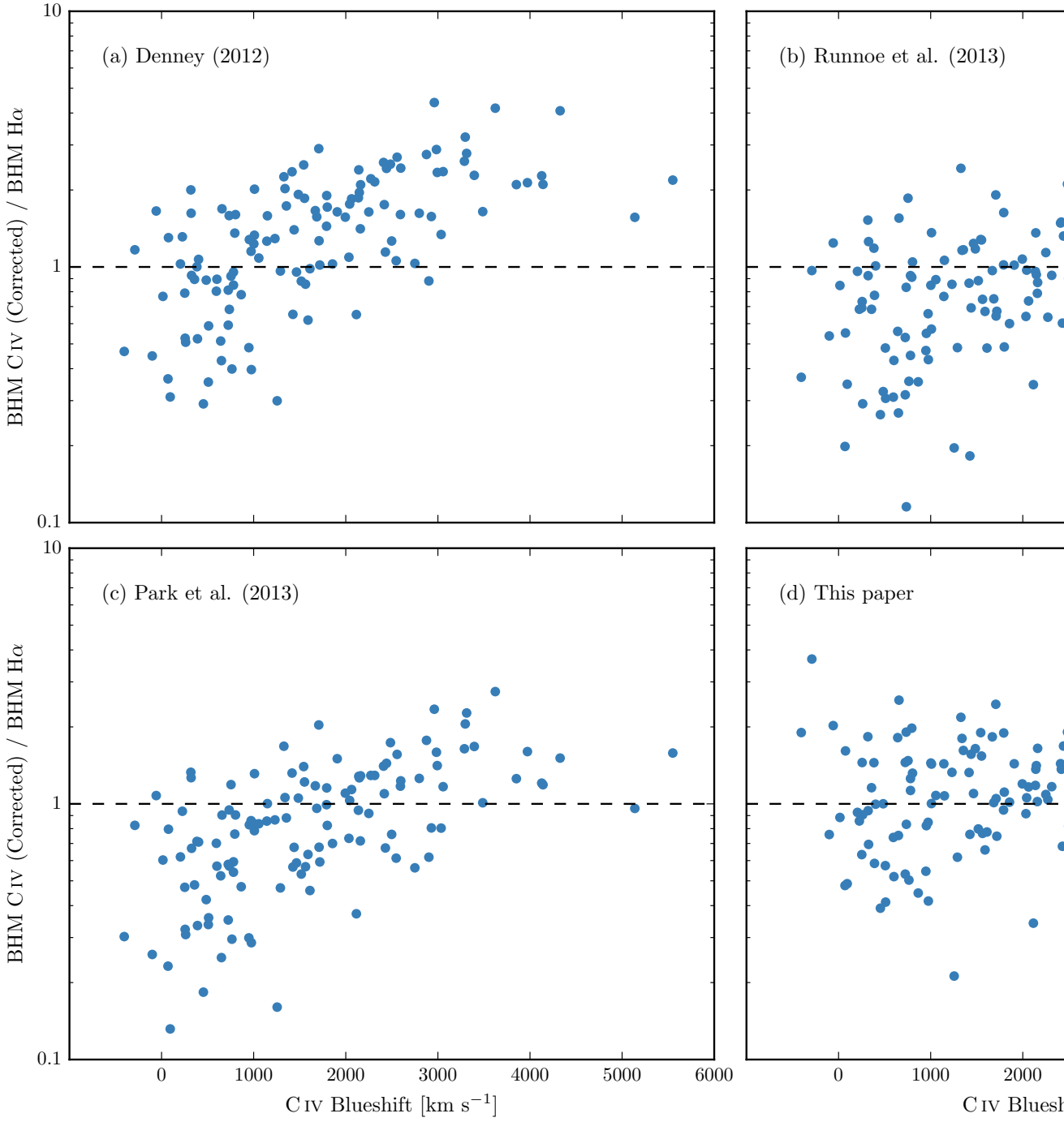


Figure 26: Comparison of BH mass estimates derived from C IV and H α as a function of the C IV blueshift. Corrections to the C IV-based masses have been applied based on the shape (FWHM/ σ) of the C IV emission line (a; Denney, 2012), the peak flux ratio of the Si IV+O IV blend relative to C IV (b; Runnoe et al., 2013a), by significantly reducing the dependence of the derived BH mass on the C IV velocity-width (c; Park et al., 2013), and based on the C IV blueshift (d; this paper).

masses on the emission-line velocity width (from the V^2 dependence predicted assuming a virialized BLR to just $V^{0.56}$). As a consequence, the C IV based masses of the quasars with large C IV blueshifts are much reduced (Fig. 26c). However, the systematic error in the C IV-based BH masses as a function of C IV blueshift remains.

As a comparison, the C IV-based masses shown in Fig 26d have been corrected using to the C IV blueshift-based procedure presented in this paper. No systematic in the BH masses as a function of the C IV blueshift is evident.

3.6 CONCLUSIONS

The main results of this paper are as follows:

- We have analysed the spectra of 230 high-luminosity ($10^{45.5} - 10^{48}$ erg s $^{-1}$), redshift $1.5 < z < 4.0$ quasars for which spectra of the Balmer emission lines and the C IV emission line exist. The large number of quasars in our spectroscopic catalogue and the wide range in C IV blueshifts the quasars possess has allowed us to directly investigate biases in C IV-based BH mass estimates which stem from non-virial contributions to the C IV emission as a function of the C IV blueshift, which, in turn, depends directly on the form of the quasar ultraviolet SEDs (Richards et al., 2011).
- The C IV emission-based BH-masses are systematically in error by a factor of more than five at 3000 km s $^{-1}$ in C IV emission blueshift and the overestimate of the BH-masses reaches a factor of 10 for quasars exhibiting the most extreme blueshifts, $\gtrsim 5000$ km s $^{-1}$.
- We have derived an empirical correction formula for BH-mass estimates based on the C IV emission line FWHM and blueshift. The correction may be applied using equations 4 and 6 in Section 3.4.3. The large SED-dependent systematic error in C IV-based BH-masses is removed using the correction formulae. The remaining scatter between the corrected C IV-based masses and the H α -based masses is 0.24 dex at low C IV blueshifts (~ 0 km s $^{-1}$) and 0.10 dex at high blueshifts (~ 3000 km s $^{-1}$). This is a significant improvement on the 0.40 dex scatter observed between the un-corrected C IV and H α BH masses. The correction depends only on the C IV line properties - i.e. the FWHM and blueshift - and allows single-epoch virial BH mass estimates to be made from optical spectra, such as those provided by the SDSS, out to redshifts exceeding $z \sim 5$.

As discussed in Section 3.5.1, uncertainties in redshift estimation and hence the definition of the systemic rest-frame for quasars impact

on the accuracy of the corrected BH-masses. Using published redshift estimates, notably those from Hewett and Wild, (2010) for the SDSS DR7 quasars and the BOSS PCA-based redshifts from Pâris et al., (2017) for SDSS DR12, the correction formula given in Section 3.4.3 produces significant improvements to C IV-based BH mass estimates. In a forthcoming work, Allen & Hewett (in preparation) will present a new redshift-estimation algorithm that produces redshifts independent of the C IV blueshift and other variations in the ultraviolet SEDs of luminous quasars. Allen & Hewett will publish improved redshifts for all quasars in the SDSS DR7 and DR12 which will reduce SED-dependent systematic errors below the apparent inherent dispersion of $\simeq 220 \text{ km s}^{-1}$ associated with broad emission line redshifts (Shen et al., 2016). At the same time we will publish catalogues of unbiased BH masses for both SDSS DR7 and DR12 based on the Allen & Hewett redshifts. The components from the mean-field independent component analysis (see Allen et al., 2013, for an application to astronomical spectra) used in the Allen & Hewett redshift algorithm will also be published. With these components, if a rest-frame ultraviolet spectrum is available, it will be straightforward to determine the systemic redshift, via a simple optimisation procedure, and hence calculate the C IV blueshift.

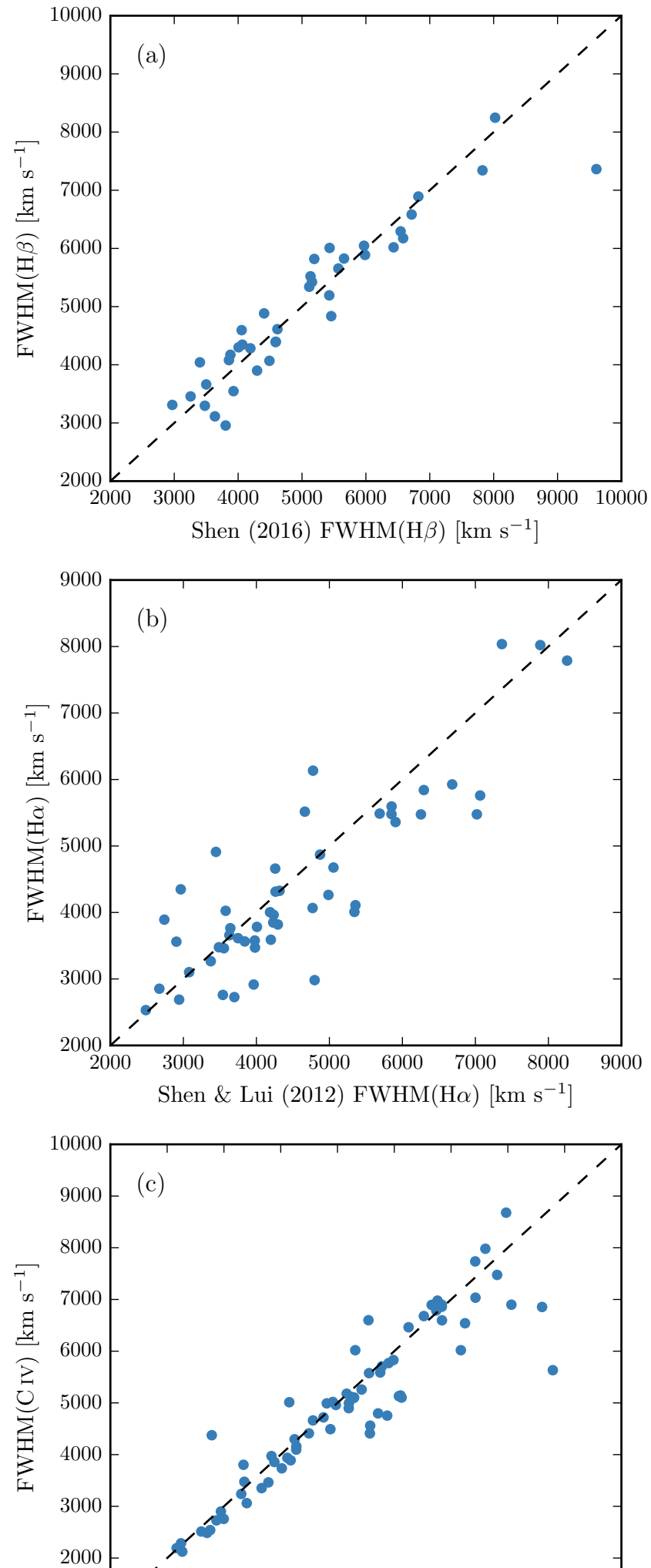
3.7 COMPARISON TO SHEN

In this section we verify the accuracy of our parameter estimation scheme by comparing our FWHM measurements to measurements published in Shen et al., 2011, Shen and Liu, 2012 and Shen, 2016.

The parametric model we fit to the H β /[O III] emission region was very similar to the model employed by Shen, (2016). In Fig. 27a we plot our H β FWHM measurements against the measurements published in Shen, (2016), for 39 quasars in common to both samples. As expected, we observe a very tight correlation, with a scatter of 0.04 dex.

In Fig. 27b we plot our H α FWHM measurements against the measurements published in Shen and Liu, (2012), for 51 quasars in common to both samples. There is a strong correlation and, although the scatter is larger than for the H β comparison (0.07 dex), no significant systematic bias.

Finally, in Fig. 27c we compare our measurements of the C IV FWHM from the 71 SDSS DR7 spectra in our sample with the measurements published in Shen et al., (2011). Shen et al., (2011) fit the C IV line profile with a composite model comprising up to three Gaussian components, whereas we used (up to order six) Gauss-Hermite polynomials. Nevertheless, there is a very strong agreement between our measurements, with a scatter of 0.05 dex.



4

NARROW LINE REGION PROPERTIES

4.1 INTRODUCTION

Correlations between the masses of super-massive black holes and properties of the host galaxy bulges in nearby galaxies (Gebhardt et al., 2000; Ferrarese and Merritt, 2000) and the similarity of the cosmic evolution of star formation and black hole activity (Boyle and Terlevich, 1998; Madau and Dickinson, 2014) suggest that the formation and evolution of supermassive black holes and their host galaxies are linked. Active galactic nuclei (AGN) and quasar feedback, in which star formation in the host galaxy is suppressed by the energy output from the quasar, is a favoured model. This has motivated a considerable amount of observational work searching for feedback signatures (for recent reviews, see Alexander and Hickox, 2012; Fabian, 2012; Heckman and Best, 2014).

The [O III] $\lambda\lambda 4960,5008$ doublet is the strongest narrow line found in optical quasar spectra. It is forbidden line which traces gas on kiloparsec scales. High velocity dispersions or strong asymmetries in forbidden lines are evidence of high velocity extended ionized outflows. Recent studies have provided constraints on the prevalence of ionized outflows traced by [O III] emission in low-redshift type 2 AGN (e.g. Mullaney et al., 2013; Zakamska and Greene, 2014) using spectra from the Sloan Digital Sky Survey (SDSS; York et al., 2000). However, the signatures of feedback are expected to be stronger at higher redshifts ($z \sim 2$) when the black hole accretion and star formation rates both peak.

In this paper we analyse the [O III] properties of a sample of 358 high-luminosity, redshift $1.5 < z < 4$ quasars. In particular, we search for signs of outflowing gas, which include asymmetries and broad velocity widths. Recent near-IR spectroscopy of $z > 1.5$ quasars often report exceptionally large [O III] widths, with $\text{FWHM} > 1000 \text{ km s}^{-1}$ (e.g. Netzer et al., 2004; Nesvadba et al., 2008; Kim et al., 2013; Brusa et al., 2015; Carniani et al., 2015; Perna et al., 2015). **Add reference to WI-SH paper.**

For a subsample where we have spectra covering the rest-frame ultra-violet line C IV, we can test whether the strong outflows, inferred the blueshifting of C IV relative to the systemic redshift, have any effect on the host galaxy on larger scales.

Throughout this paper we adopt a flat Λ CDM cosmology with $h_0 = 0.69$ and $\Omega_M = 0.29$.

The paper is structured as follows.

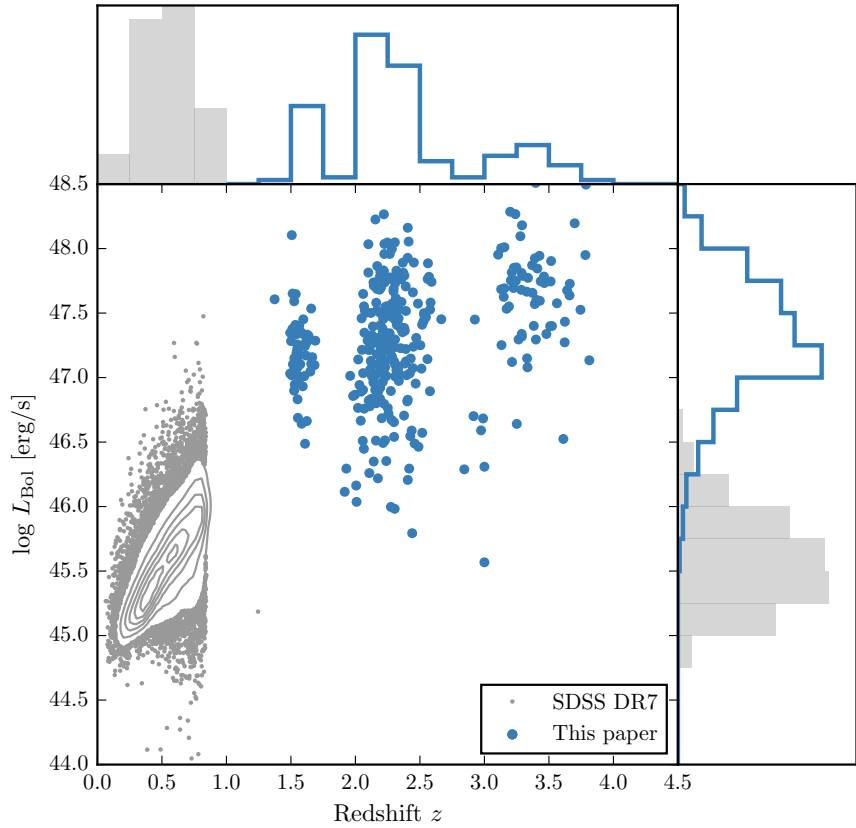


Figure 28: The ranges in redshift and luminosity covered by our sample, relative to the redshift-luminosity distribution of the SDSS DR7 quasar catalogue with measured [O III] line properties (Shen et al., 2011). The gaps in our sample coverage at $z \sim 1.8$ and $z \sim 3$ are due to the near-infrared transmission windows. In regions of high point-density, contours show equally-spaced lines of constant probability density generated using a Gaussian kernel-density estimator.

4.2 QUASAR SAMPLE

We have assembled a catalogue of 358 high-luminosity, redshift $1.5 < z < 4$ quasars, with spectra taken in the near-infrared. At these redshifts the spectra cover the rest-frame optical region, which includes the broad Balmer H β line and the strong, narrow [O III] doublet. There is a significant overlap between the sample presented here and the one used in Coatman et al. (2016b), hereafter paper I. We briefly describe the catalogue below, but refer the reader to Coatman et al. (2016b) for further details, including the reduction procedure.

Two hundred are selected from the SDSS Seventh Data Release (DR7; Schneider et al., 2010). These are observed with LIRIS (Manchado et al., 1998) on the William Herschel Telescope (WHT), Triple-Spec (Wilson et al., 2004) on the Astrophysics Research Consortium

Table 9: The numbers of quasars with [O III] line measurements and the spectrographs and telescopes used to obtain the near-infrared spectra. Further details on the instrumental configurations are given in paper I. **Check numbers.**

Spectrograph	Telescope	Number
FIRE	MAGELLAN	32
GNIRS	GEMINI-N	29
ISAAC	VLT	8
LIRIS	WHT	5
NIRI	GEMINI-N	29
NIRSPEC	Keck II	3
SINFONI	VLT	76
SOFI	NTT	78
TRIPLESPEC	ARC-3.5m	27
TRIPLESPEC	P200	46
XSHOOTER	VLT	25
		144

(ARC) 3.5 m telescope, FIRE (Simcoe et al., 2010) on the Magellan-Baade telescope, the SINFONI integral field spectrograph (Eisenhauer et al., 2003; Bonnet et al., 2004) on the European Southern Observatory (ESO) Very Large Telescope (VLT), SOFI (Moorwood, Cuby, and Lidman, 1998) on the New Technology Telescope (NTT), and TRIPLE-SPEC on the Palomar 200-inch Hale telescope (P200). One hundred and seventeen were observed to measure accurate redshifts of quasar pairs at very close projected separations (Prochaska and Hennawi, 2009; Lau, Prochaska, and Hennawi, 2015; Hennawi et al., 2015). Spectra were taken with GNIRS (Elias et al., 2006) on the Gemini North telescope, ISAAC (Moorwood et al., 1998) on the European Southern Observatory (ESO) Very Large Telescope (VLT), NIRSPEC (McLean et al., 1998) on the Keck-II telescope, NIRI (Hodapp et al., 2003) also on Gemini North, and XSHOOTER (Vernet et al., 2011), again, on the VLT. Seventy-nine are bright Hamburg-ESO quasars observed with SINFONI, ninety are quasars with archival high-resolution optical spectra observed with SOFI, and four are observed with XSHOOTER and presented in the XQ-100 catalogue (Lopez et al., 2016).

This is the largest study of the narrow line region properties of high- z quasars ever undertaken. The redshift and luminosity coverage of the quasars in our sample is shown in Fig. 28, and the quasar sample is summarised in Table 9. Our sample covers much higher redshifts and luminosities than the SDSS sample.

4.3 PARAMETERIC MODEL FITS

In this section we describe how we measure the [O III] velocity-width and parameterize asymmetries in the line. We first fit a parameteric model to the [O III] emission, and the nearby H β peak. This step is taken soley to enhance the signal-to-noise (SNR) of the spectra and to decompose the emission from H β and the [O III] doublet. We then calculate non-parameteric measures of the line profile from the best-fitting model.

Before the model can be fit, the spectra must first be transformed in to the (approximate) quasar rest-frame. This transformation is only for practical purposes and the emission line parameters we will go on to derive are independent of the exact redshift used. The redshift will later be refined using the results from the fit. The redshift used in this transformation is either derived from a multi-component Gaussian fit to the broad H α emission (~ 40 per cent of our sample) or, when this is not possible, from a preliminary fit to the broad H β emission (~ 40 per cent) or narrow [O III] emission (20 per cent). **Should say whether we use peak/median etc.**

The continuum and optical Fe II emission is modelled and subtracted using a recipee that is identical to the one described in paper I. The following model is then fit to the spectra in the wavelength interval 4700–5100 Å. The fit is done as a function of the Doppler velocity shift, and we adopt the wavelength 4862.721 Å (the laboratory H β wavelength) to transform wavelengths into equivalent Doppler velocities.

H β is modelled by two Gaussians with non-negative amplitudes and FWHM greater than 1200 km s $^{-1}$. A handful we fix the centroids of the two Gaussians to be the same, normally because of very low S/N or because the blue wing is below the lower wavelength limit of the spectrograph. Any contribution to the H β emission from the narrow-line region is weak in the vast majority of our sample, and so we do not include an additional Gaussian component to model this emission. Note: we do in fact include narrow components for eight objects in our sample. Although, for some objects, this could bias our estimate of the velocity-width of the broad component, this information is not used in the analysis presented in this paper.

Each component of the [O III] doublet is fit with one or two Gaussians, depending on the fractional reduced χ^2 difference between the one- and two-component models. If the addition of the second Gaussian decreases the reduced χ^2 by more than 5 per cent then the double-Gaussian model is accepted. One hundred and twenty-five are fit with a single Gaussian, 147 with two Gaussians, and [O III] is undetected in a further 78 quasars. When a single Gaussian is used to model each line, the peak flux ratio of the [O III] 4960 Å and 5008 Å components are fixed at the expected 1:3 ratio and the width and

Table 10: Approximate physical origin of the ICA components.

Component	Origin
w_1	Fe II
w_2	H β
w_3	H β
w_4	[O III] core
w_5	[O III] core
w_6	[O III] wing

velocity offsets are set to be equal. In the double Gaussian fit, the peak flux ratio of the second components is again fixed at 1:3, and the width and velocity offsets are again set to be equal.

In six quasars a significantly better fit was obtained by allowing the flux ratio between the two components to vary. In these quasars the best-fitting peak ratio varies from 0.50 to 0.84, with mean 0.70. **Check ICA component fits to see if this looks real.**

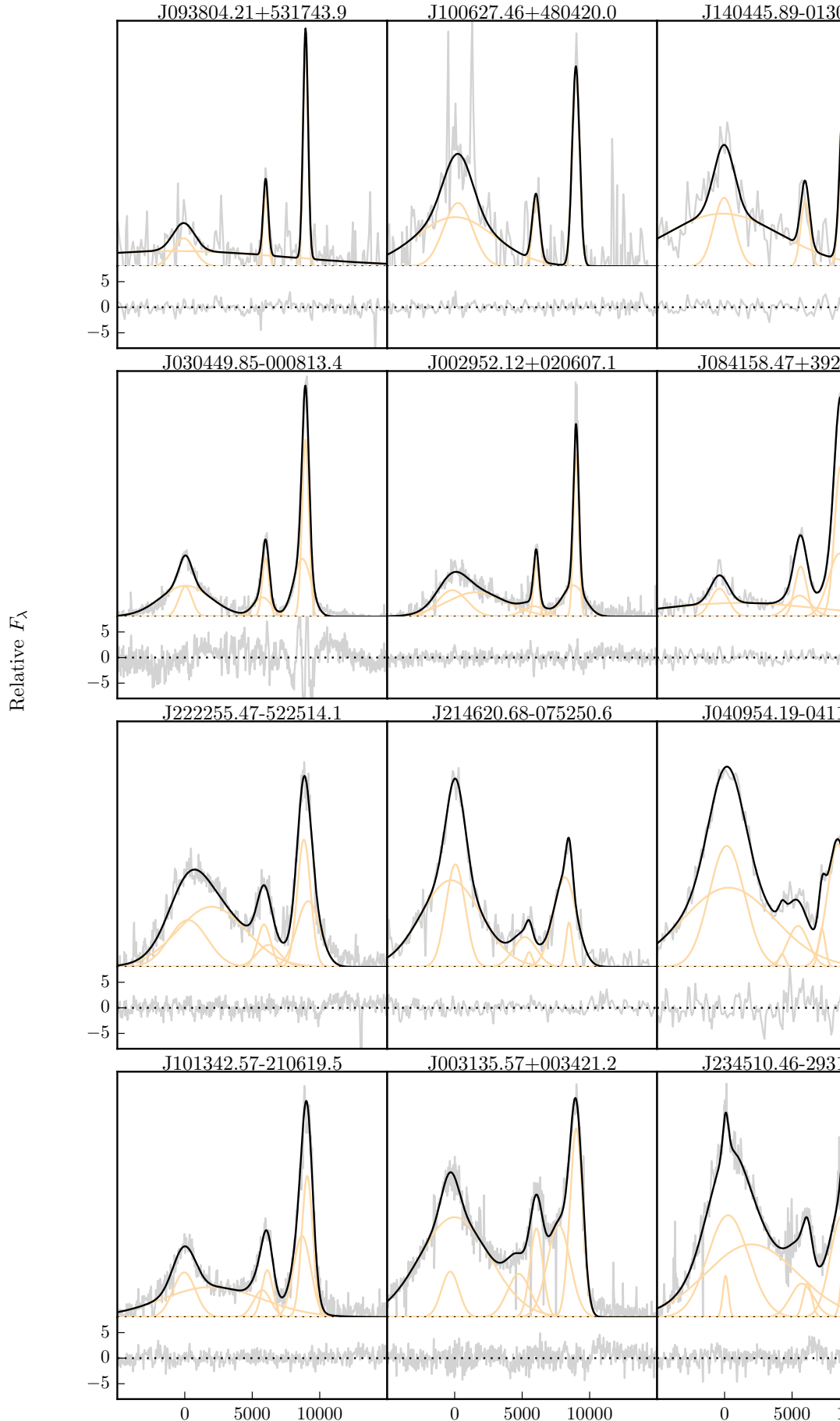
Model parameters were derived using a standard variance-weighted least-squares minimisation procedure employing the Levenberg-Marquardt algorithm. Prior to the fit, the spectra were inspected visually and regions significantly affected by telluric absorption or of low S/N were masked out.

However, the fits aren't always good. How to be quantitative about this? Chi-squared values indicating bad fits? Also the fact that we sometimes model Fe as OIII. Discuss the limitations of using the Boroson & Greene template? Even if don't use results, should discuss Gaussian fits and their limitations, because that's what most people will be using.

4.3.1 Derived Parameters

All [O III] line properties are derived from the [O III]5008 emission, but, as described below, the kinematics of the peak at 4960Å are constrained by our fitting routine to be identical.

We do not attach any physical meaning to the individual Gaussian components used in the model. While it is true that in some quasars the [O III] emission can be clearly separated into a narrow component at the systemic redshift and a lower-amplitude, blueshifted broad component (e.g. Shen, 2016), often this decomposition is highly uncertain. Furthermore, often the S/N is not sufficient to statistically justify the addition of a second Gaussian component. Instead, we characterize the [O III] line profile using a number of non-parameteric measures, which are commonly used in the literature (e.g. Zakamska and Greene, 2014; Zakamska et al., 2016). A normalised cumulative velocity distribution is constructed from the best-fitting model,



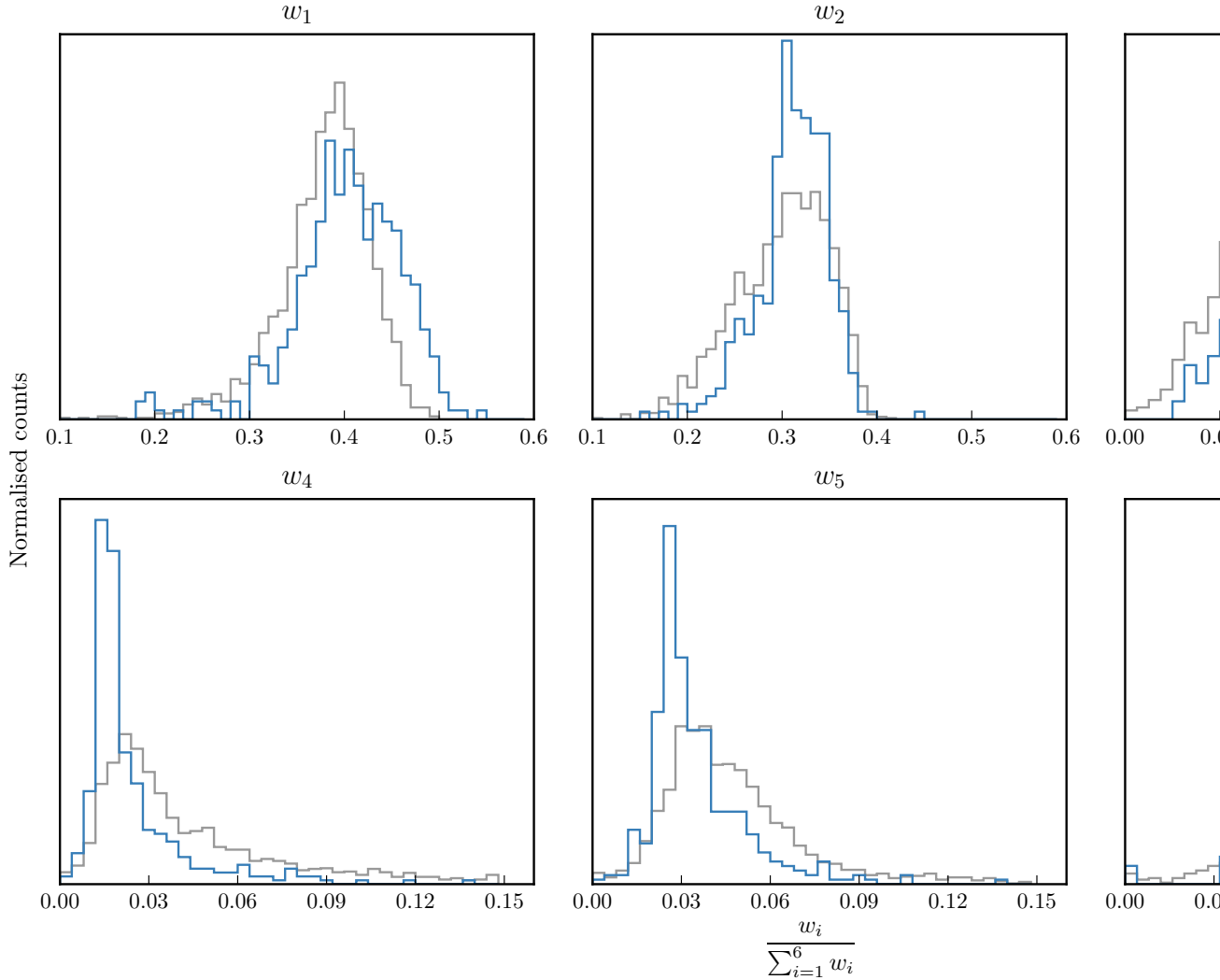


Figure 30: The relative weight in each of the six positive ICA components for the high-luminosity (blue) and low luminosity samples (grey). In the high-luminosity sample Fe II emission is stronger (component w_1). The core [O III] emission is weaker (components w_4 , w_5) but the strength of the blueshifted wing is the same (w_6).

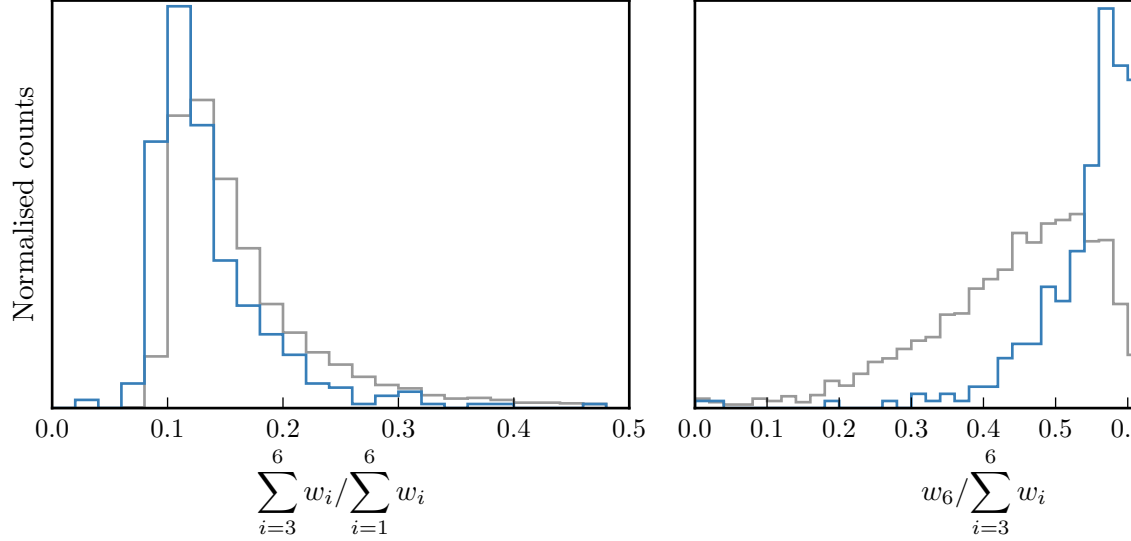


Figure 31: The relative weight in the three ICA components corresponding to [O III] emission (*left*) and the relative weight of the component most closely related to blueshifted [O III] emission relative to all three [O III] components (*right*). [O III] emission is weaker in the high-luminosity sample, but the relative contribution but the fractional contribution from the blueshifted component to the total [O III] emission is higher. Hence [O III] is weaker, broader, and more asymmetric in the high-luminosity sample. See Zakamska discussion.

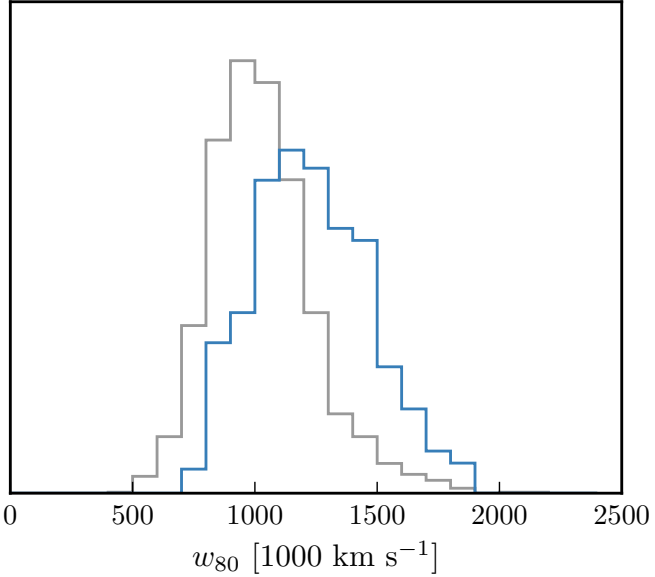


Figure 32: Comparison of [O III] velocity-widths in the high and low luminosity samples using the ICA component fits. If keep this need to explain in text how w_{80} is calculated from ICA component fits.

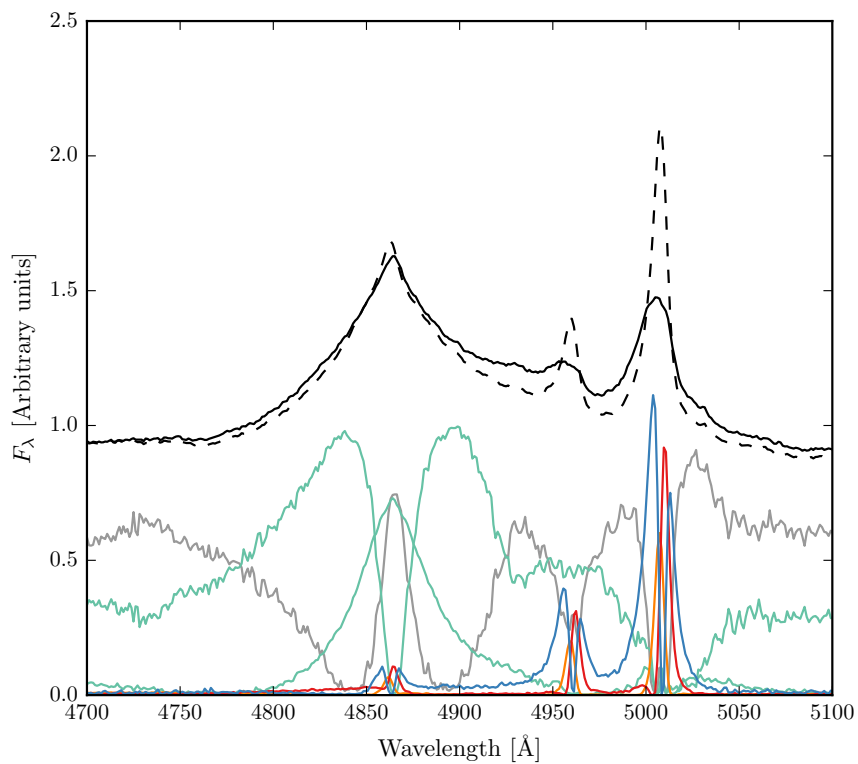


Figure 33: Black solid line is the median from the ICA fits to the high-luminosity sample. Black dashed line shows the median from the low-luminosity sample. The six positive ICA components are also shown.

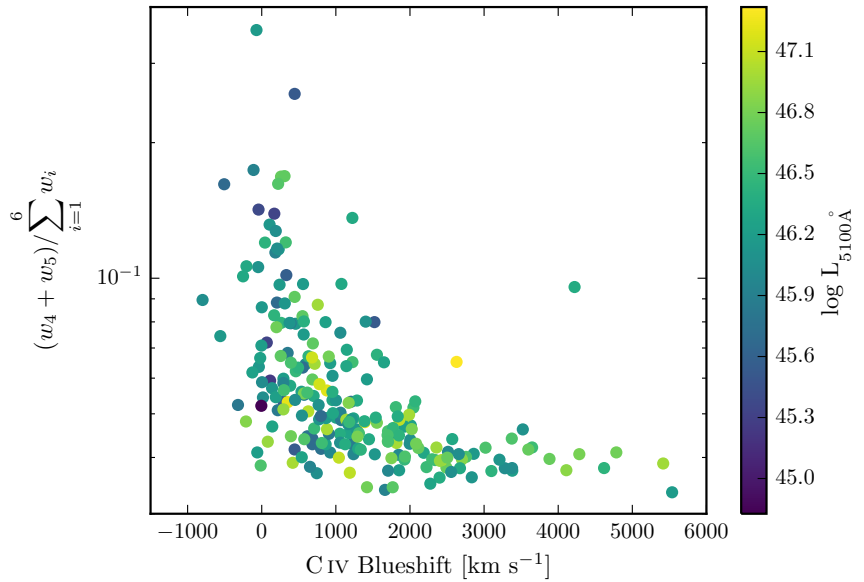


Figure 34: [OIII] strength decreases as the CIV blueshift increases, I run into problems comparing the CIV blueshift to the [OIII] blueshift / velocity-width. See similar thing if I use [OIII] EQW instead. Need to fix y ticks. Only showing the core components here. The CIV blueshift is now measured relative to the NIR ICA redshift. I think this trend is mostly being driven by the Eigenvector 1 correlations: as the blueshift increases the FeII strength increases and the [OIII] strength decreases. Doesn't appear to be driven by the luminosity. Is this tighter than EV1 trend shown with Fe/OIII strength by other authors?

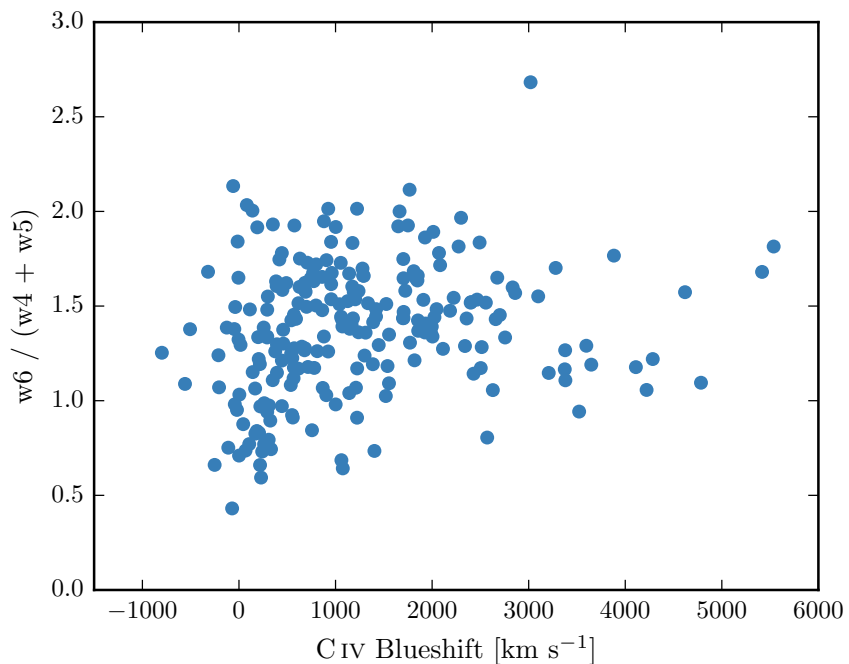


Figure 35: I think there is a trend here but at high blueshifts the OIII is undetected / very low S/N. Need to determine when we can believe OIII parameters. Why at low CIV blueshift is there a much bigger dynamic range than in [O III] blueshifts in Fig. 13. Is it just because we have more objects?

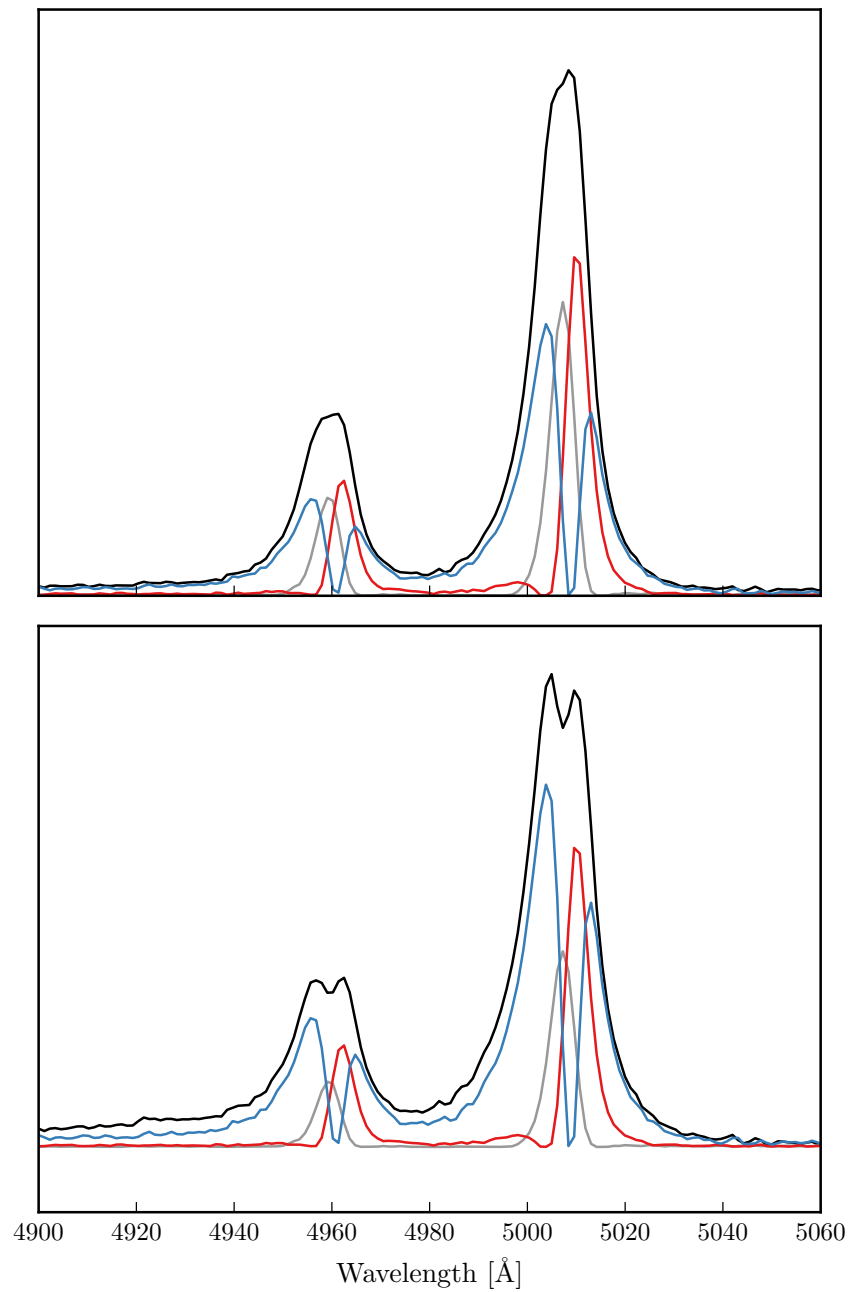


Figure 36: Comparison of median [O III] profiles from ICA fits it low- and high-luminosity samples.

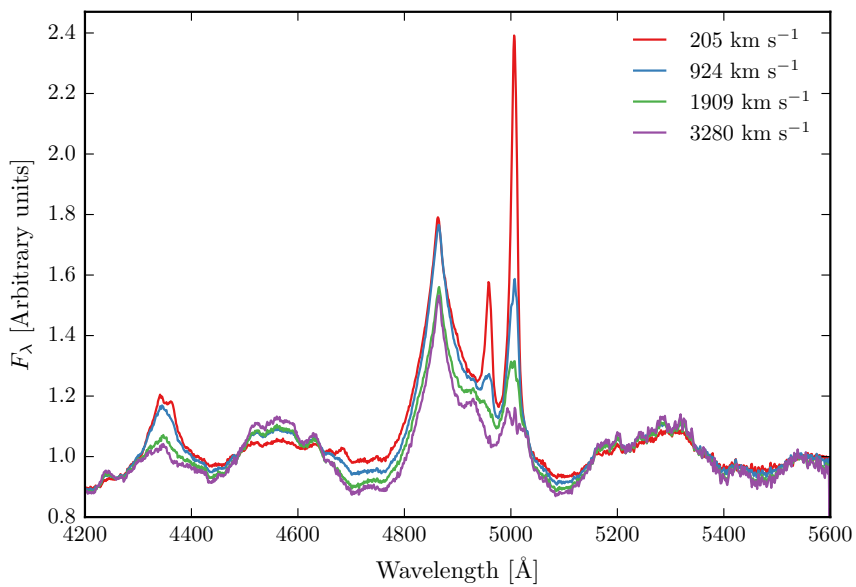


Figure 37: ICA median weights as a function of the CIV blueshift.

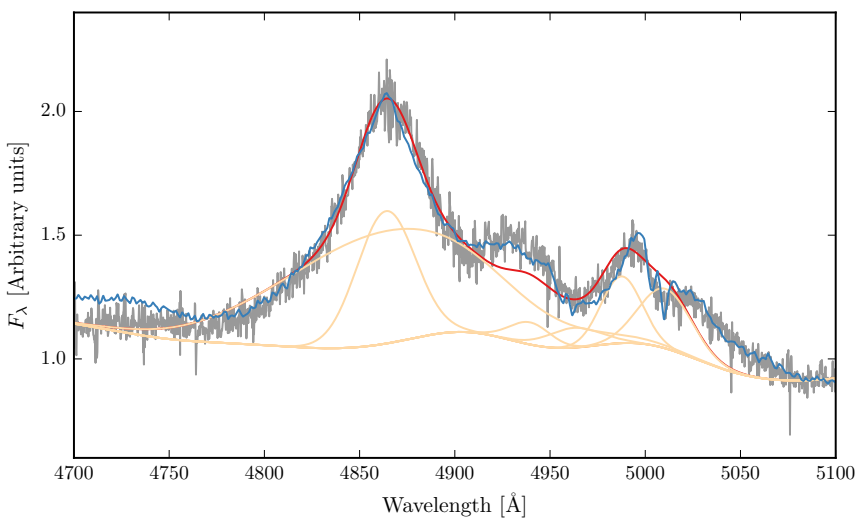


Figure 38: Example where poorly subtracting the iron can be confused with [O III].

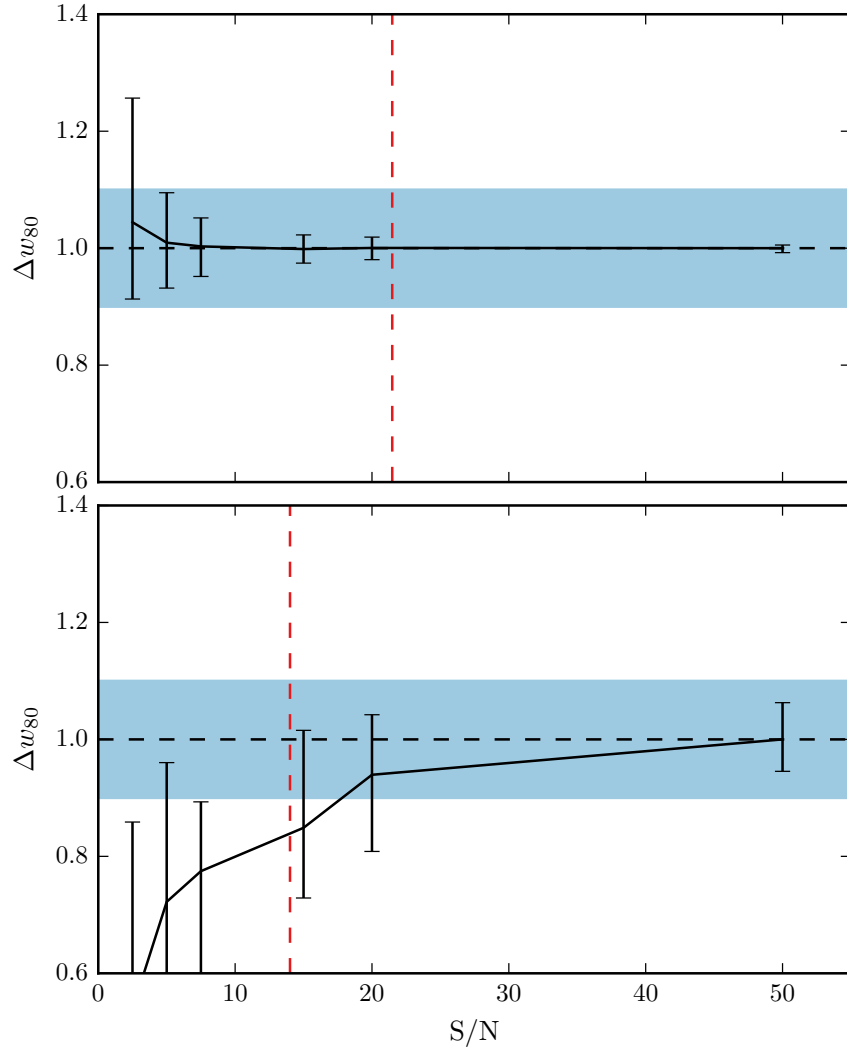


Figure 39

from which the velocities below which 5, 10, 25, 50, 75, 90, and 95 per cent of the total flux accumulates can be read off. The width of the emission line can then be defined, for example, using $w_{80} = v_{90} - v_{10}$. The absolute assymetry in the line profile A is defined as $((v_{95} - v_{50}) - (v_{50} - v_5)) / (v_{95} - v_5)$ (Zakamska and Greene, 2014).

We also define the blueshift of the [O III] emission, which is a measure of the velocity shift of the profile from the expected position. This requires a measure of the observed line position, and an accurate measurement of the quasar systemic redshift. We use v_{10} to measure the location of the [O III] emission. Note that v_{50} is not suitable because when [O III] is low S/N we fit with single Gaussian.

The line width measures are not at present corrected for instrumental broadening, but this can easily be done.

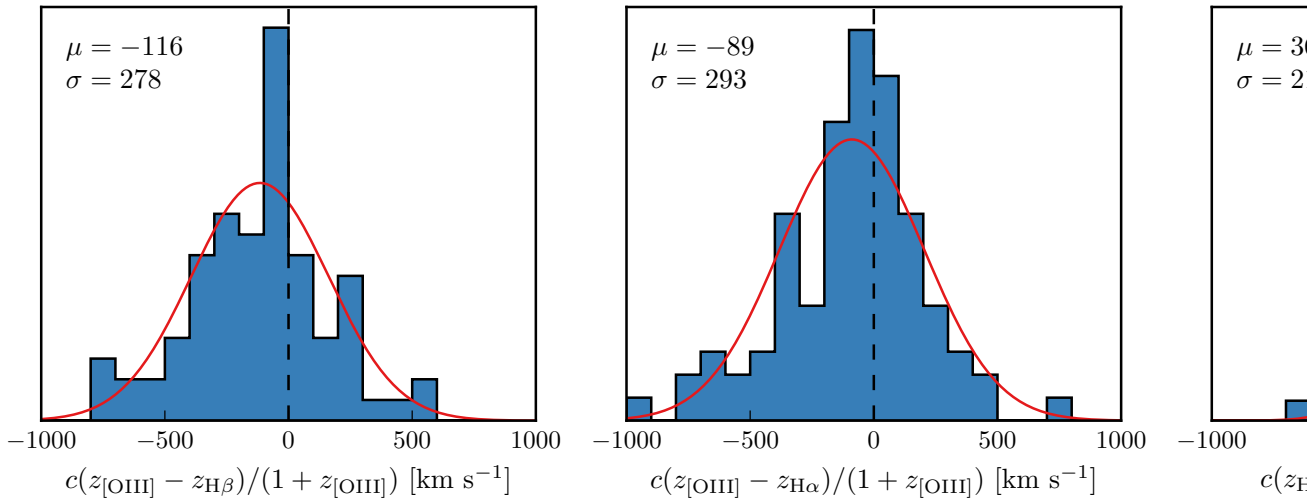


Figure 40: Redshift comparisons. Lots have been excluded from Ha/Hb so need to look at flags greater than one. What is the big peak?

4.3.2 Other flags

4.3.2.1 Flag 2

Low S/N. Includes some of the strong iron emitters.

4.3.2.2 Flag 3

74 objects where [O III] is undetected, although I don't have a rigorous definition of what this means. Merge with 2?

4.4 ICA COMPONENT FITS

What is the segue here? Sometimes Gaussians give poor fit? Not clear what is Hb, what is OIII, what is Fe? Show some examples of when the multi-Gaussian fits fail. Need to describe sample used in ICA component decomposition and briefly describe method (or refer to Allen & Hewett).

4.5 MEASURING THE QUASAR SYSTEMIC REDSHIFT

Explain flags Need to send paul redshifts

4.5.1 H α

There are 224 quasars in our sample with spectra covering the H α emission line. We discard seven of these from our sample because of very low S/N (<2.5 measured in the H α line), leaving 217 To measure the

position of the line we fit a parameteric model, which is very similar to the model described in Paper I. The continuum emission is first modeled and subtracted using the procedure described in Paper I. We then test five different models with increasing degrees of freedom to model the H α emission. The model we select is the simplest model for which the fractional change in the reduced chi-squared from the model with the lowest reduced chi-squared is less than ten per cent.

The models we test are: (1) a single broad Gaussian; (2) two broad Gaussians with identical velocity centroids; (3) two broad Gaussians with different velocity centroids; (4) two broad Gaussians with identical velocity centroids, and additional narrower Gaussians to model the narrow H α emission, and the narrow components of [N II] $\lambda\lambda 6548,6584$ and [S II] $\lambda\lambda 6717,6731$; (5) two broad Gaussians with different velocity centroids, and additional narrower Gaussians. If used, the width and velocity of all narrow components are set to be equal in the fit, and the relative flux ratio of the two [N II] components is fixed at the expected value of 2.96. The number of quasars fit by each model is: model 1 - 10; model 2 - 71; model 3 - 32; model 4 - 51; model 5 - 53. The redshift is then measured at the peak flux of the H α model, including both the broad and narrow components of H α if appropriate.

4.5.2 ICA

The only sensible way to measure the systemic redshift is using the NIR ICA fit. H α and H β seem to give no systematic offset but large scatter, and they are often asymmetric, so should only use peak. And H α isn't always available, and have other narrow components need to decompose. O III peak is mostly fine to use, but then there are some objects where the whole line is blueshifted. And critically, at large CIV blueshifts the [O III] emission is often undetected. Can show comparison of NIR ICA redshifts to... Optical ICA? Hewett & Wild?

Should emphasise that most people use [O III] to get the most reliable systemic redshift. While this is fine at low luminosities, at high luminosities this can result in large errors (profile can be dominated by blueshifted component, Fe emission can be improperly subtracted, or [O III] might not be detected at all. Publish ICA components with this paper?)

Can also describe what I found trying to get redshifts from broad H α , H β ? (Narrow components generally very weak at these luminosities so can't be used.) Generally find no systematic errors but large ($\sim 1000 \text{ km s}^{-1}$ scatter). Comparing NIR ICA to [O III] for the [O III] with high S/N I find small (few hundred km s^{-1}) scatter.

Should publish [O III] redshifts with this paper for people to use.

4.5.3 Parameter uncertainties and upper limits

Describe how uncertainties on best-fitting parameters were calculated.

In 78 quasars, or approximately 25 per cent of our sample, the [O III] is undetected, or detected with very low S/N. In this section we describe how upper limits on the [O III] equivalent width were calculated. Firstly, the best-fitting model comprising the continuum, Fe II, and H β emission is subtracted from the spectra, leaving behind only emission due to [O III]. From this spectra we generate 100 mock spectra, where the flux at each wavelength is randomly drawn from a Normal distribution with a mean equal to the flux convolved with a Gaussian of width 200 km s $^{-1}$ and a width equal to the known error. We then perform an error-weighted linear least-squares regression with an [O III] template derived from a fit to a very high S/N low redshift SDSS composite spectra. The equivalent width of the best-fitting model is recorded for each of the 100 realisations of the spectra. The error in the equivalent width is defined as the root-mean-square of these values.

Calculated uncertainties using Monte Carlo. Uncertainties on v10 are very large, which I think makes sense since the wing Gaussian will be appearing and disappearing, giving a large dispersion in v10. Or regardless v10 is just very sensitive to the noise. Maybe I should be using v25 instead?

4.5.4 Absolute flux calibration of spectra and continuum luminosities

Relative flux-calibration of the infrared spectra as a function of wavelength has been achieved, to \approx 10 per cent, through observations of appropriate flux standards. The absolute flux levels, however, can be in error by large factors due to variable atmospheric conditions combined with the narrow slit widths. For the majority of the quasars we have, therefore, established the absolute flux scale for each near-infrared spectrum using the same quasar SED-model fitting scheme employed in Paper I. Briefly, the SED-model was fit, with the normalisation and E(B-V) as free variables, to optical/infrared magnitudes, or SDSS/BOSS spectra (check order I do this.) This allows us to extrapolate from the optical when we do not have photometric data in the near-infrared. The spectra were then normalised to the SED model using a linear error-weighted least-squares regression in the the regions of the spectra covered by the H/K bands. The monochromatic continuum luminosity at 5100Å was calculated directly from the normalised SED-model. **If this sounds strange can also calculate from fit to normalised spectra. Check if any missing normalisation / monochromatic luminosities.**

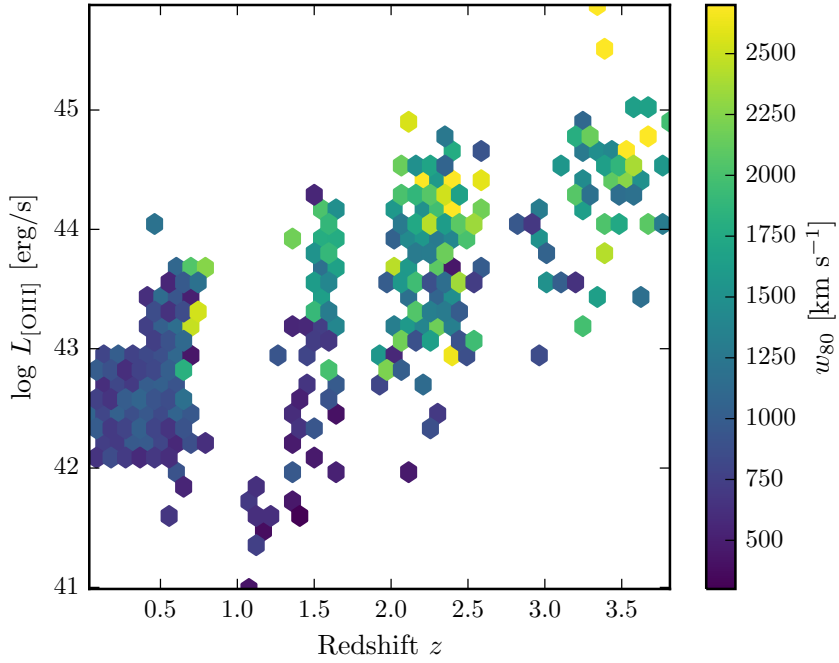


Figure 41: The [O III] velocity-width, characterised by w_{80} , as a function the [O III] luminosity and the quasar redshift. The color of each hexagon denotes the mean w_{80} for the objects in that luminosity-redshift bin. We have supplemented our sample with low-z objects from Zakamska and Greene, (2014) and medium ($z \sim 1.5$) redshift objects from Harrison et al., (2016). If I keep this plot make sure its clear which points belong to which sample.

4.6 RESULTS FROM ICA FITS

Need to convince the reader that the ICA components approximately correspond to real components. Explain how non-parametric measures derived from ICA reconstructions.

We find there is a decreasing symmetric component at high luminosities. Relates directly to Shen and Ho, (2014). A stable narrow line region is removed by the outflowing material. Shen and Ho, (2014) showed that the strength of the core [O III] component decreases with quasar luminosity and optical Fe II strength faster than the wing component, leading to overall broader and more blueshifted profiles as luminosity and Fe II strength (or C IV blueshift) increases.

4.7 LUMINOSITY/REDSHIFT-EVOLUTION OF [O III] PROPERTIES

In this section we look for any luminosity/redshift dependent changes in the [O III] line properties. To do this we extend the dynamic range of our samples in terms of both luminosity and redshift by sup-

plementing our sample with quasars presented by Zakamska and Greene, (2014) and Harrison et al., (2016).

The Zakamska and Greene, (2014) objects are a sample of 568 obscured luminous quasars selected from SDSS (Reyes et al., 2008; Yuan, Strauss, and Zakamska, 2016). They are selected to have [O III] luminosities above $10^{8.5} L_\odot$ and have a median redshift $z = 0.397$.

We also include 40 quasars at redshifts $1.1 \leq z \leq 1.7$ from the KMOS AGN Survey at High redshift (KASHz) with [O III] line measurements.

We also have the same information for $\sim 20\,000$ SDSS spectra from Mullaney et al., (2013).

In Figure 41 we show the [O III] velocity width as a function of the [O III] luminosity and the quasar redshift. The lack of any redshift-evolution between $z = 0$ and $z = 1.5$ was reported by Harrison et al., (2016). Our additional data suggests that this continues to $z \sim 2.5$. On the other hand, at fixed redshift, we see a significant correlation between the [O III] velocity width and the luminosity.

The fact that we don't see many broad lines in the Zakamska and Greene, (2014) objects even at luminosities > 43 erg/s could be due to the fact that these are all type II quasars, whereas the sample presented in this paper are all type I. Mullaney et al., (2013) showed that the [O III] lines of type I quasars are typically broader than in type II quasars.

Looking at the [O III] velocity width as a function of luminosity tells us about the physical drivers of the outflows observed in [O III]. The correlation with luminosity suggests that the highest velocity outflows are associated with the most luminous AGN. This has been reported for low-redshift AGN, for both ionized and molecular outflows (e.g. Westmoquette et al. 2012; Veilleux et al. 2013; Arribas et al. 2014; Cicone et al. 2014; Hill & Zakamska 2014).

This suggests that the outflows are driven by radiative forces. On the other hand, Mullaney et al., (2013) find that once the correlation between the [O III] luminosity and the radio luminosity has been taken in to account, the [O III] velocity width is more strongly related to the radio luminosity of the AGN.

4.8 EQUIVALENT WIDTH

In Fig. 42 we show the [O III] $_{5008}$ EW as a function of the quasar bolometric luminosity. Bolometric luminosity is estimated from the monochromatic continuum luminosity at 5100Å using the correction factor given by Richards et al., (2006a). For comparison, we also show the low- z sample from Shen et al., (2011).

The equivalent width of [O III] has been found to strongly decrease as a function of redshift and/or luminosity (e.g. Brotherton, 1996; Netzer et al., 2004; Sulentic et al., 2004; Baskin and Laor, 2005b).

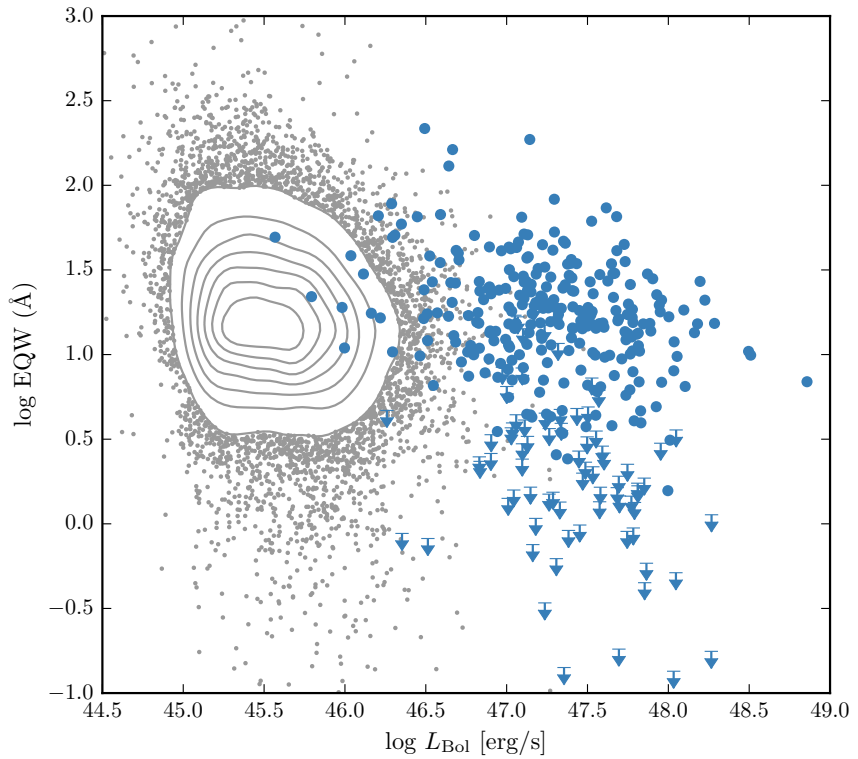


Figure 42: The [O III] EW as a function of the quasar bolometric luminosity for the sample presented in this paper (blue circles) and the low- z SDSS sample (grey points and contours). Upper limits are denoted by the downward arrows.

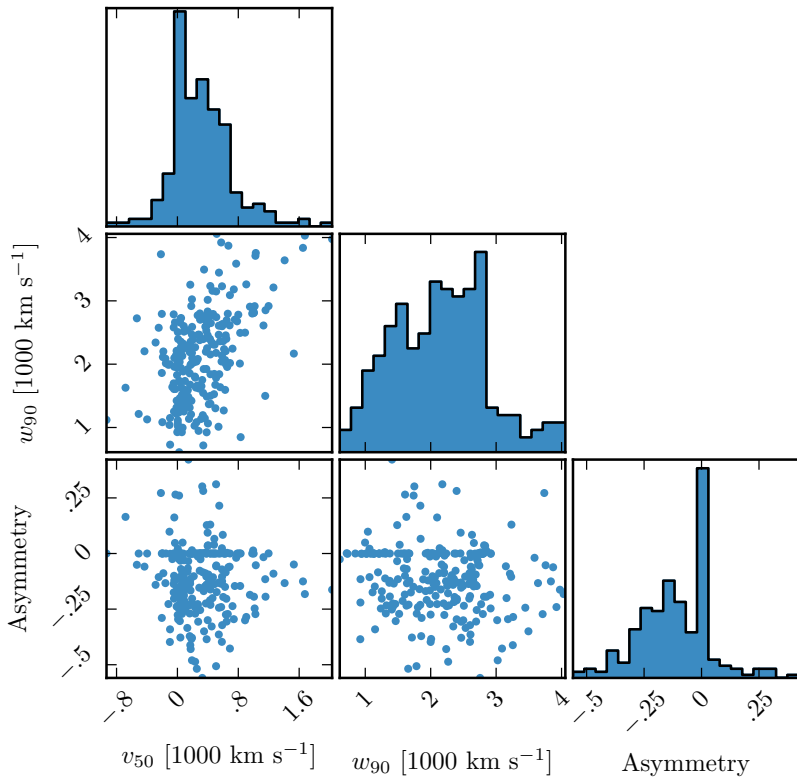


Figure 43: The distributions of and correlations between a subset of the non-parametric measures we made of the best-fitting [O III] models.

The size of the narrow line region is roughly expected to scale as $L^{0.5}$ (e.g. Netzer et al., 2004). However, for high luminosity quasars with strong [O III] this gives NLR sizes which are unreasonably large (~ 100 kpc; Netzer et al., 2004).

Netzer et al., (2004) found 1/3 of their high luminosity sample had very weak [O III], whereas quasars with weak [O III] are very rare for nearby AGN. We find a very similar fraction. Netzer et al., (2004) claim that for the population of strong [O III] emitters there is no reduction of EW with increasing source luminosity. On the other hand, there are many weak or no [O III] emitters at high luminosity that could give the impression that the line EQW decreases with increasing source luminosity.

4.8.1 OIII outflows

Our best-fitting profiles show a strongly blue-asymmetric profile (Fig. 43), with a significant fraction of the total emission in a blue wing. The luminous blueshifted broad wing and the extremely broad profile reveals high-velocity outflowing ionized gas. This can be explained if

the far-side of any outflowing gas, that is moving away from the line of sight, is obscured by dust in the host galaxies (e.g. Heckman et al. 1981; Vrtilek 1985). Observations at both low and high redshifts commonly observe this blueshifted component. Our results, and those of other authors, suggest that kpc-scale outflows in ionized gas are common among the most luminous high-redshift actively accreting SMBHs.

The situation is very different in nearby AGN, where the [O III] velocity width is dominated by the galactic potential and correlates well with the stellar velocity dispersion. HI, CO and absorption line measures of the host galaxy rest frame suggest that [O III] usually gives consistent results within 200 km/s (de Robertis 1985; Whittle 1985; Wilson & Heckman 1985; Condon et al. 1985; Stripe 1990; Alloin et al. 1992; Evans et al. 2001).

We see a correlation between the [O III] velocity width and blueshift. As the blueshift of the line increases it gets broader. This is consistent with Shen and Ho, (2014), where the strength of the narrow core is decreasing, leading to a broader and more blueshifted profile.

4.8.2 [O III] and C IV outflows are linked

As described in Paper I, we have searched for optical counterparts to our near-infrared spectra. Optical spectra are available for XXX quasars in our catalogue, and cover the broad C IV doublet. As we described in Paper I and Coatman et al., (2016), C IV is often blueshifted, which almost certainly signal the presence of strong outflows, most likely originating in a disc wind. In Paper I we demonstrated that the quasars in our sample cover the full range of C IV blueshifts seen in the SDSS quasar population, which makes our sample unique in that it allows us to study properties of the quasar across the full parameter range.

The C IV velocity centroid measurements are taken directly from paper I. We define the ‘location’ of the [O III] emission using v_{10} , although the results are the same if v_{20} , v_{50} etc. are used instead.

In Figure 44 we show the C IV blueshifts against the [O III] blueshifts. This comparison is done for a sub-sample of 146 objects where we have good measurements of the C IV, [O III], and H β (to measure the systemic redshift) profiles. Objects with $S/N > 3$ are shown as blue filled circles and objects with $S/N < 3$ as open grey circles. We calculated the median S/N per pixel in the best-fitting model for the [O III]5008 emission.

There is a clear and strong correlation. Similar correlations have been tentatively found in lower redshift quasars and AGN (Zamanov et al., 2002).

The blueshifting of C IV is known to correlate with luminosity (Richards et al., 2011). In [O III], the blueshifted wing becomes relatively more

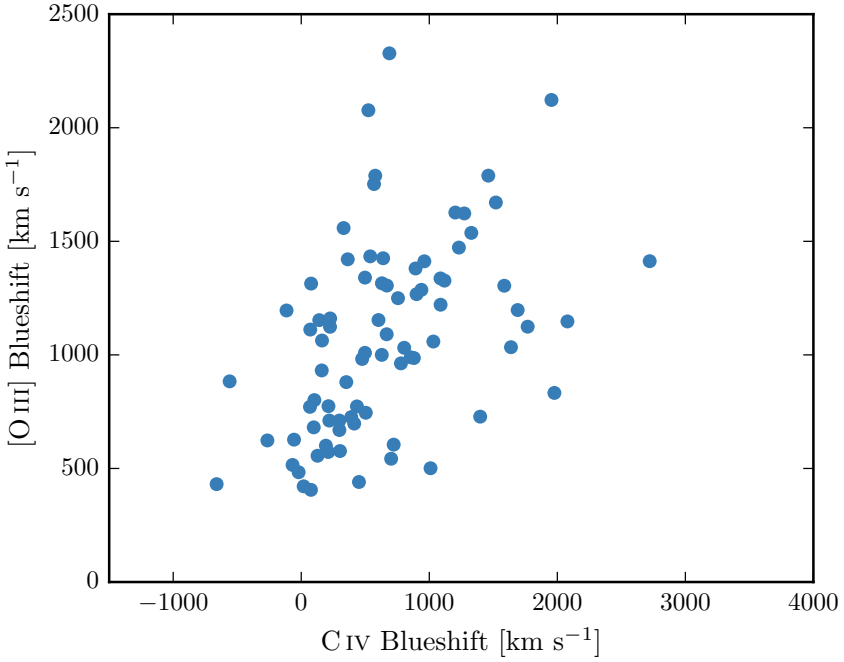


Figure 44: The relation between the blueshifts of C IV and [O III]. Equivalent to Fig 8. We use the H β peak in this figure, which I think is responsible for some of the trend. However, we do see a correlation (albeit noisier) using the NIR ICA redshifts. Not a sensible to use the [O III] redshifts, since these become much more unreliable at the high C IV blueshift end (when [O III] is weaker: figure 7. Note that we are using v_{10} for the [O III] position and v_{50} for the C IV position. We can't use v_{50} for [O III] because sometimes we are using a single Gaussian, especially if the [O III] is weaker and we miss the broad component. Need to remake this plot / don't use at all because I don't believe some of the Gaussian fits to [O III], especially at high C IV blueshifts when [O III] is weak and Fe II is strong.) Only objects where fit with two components.

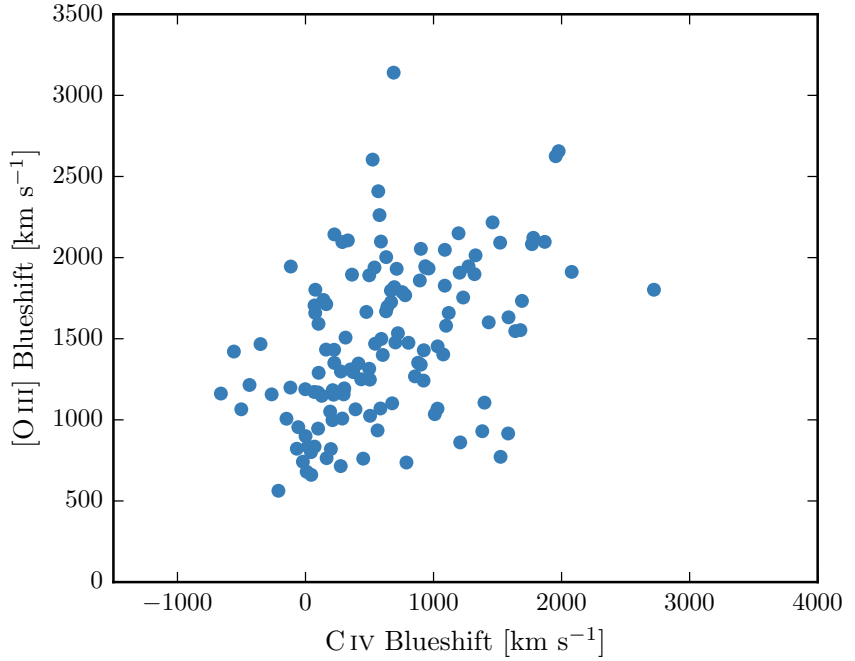


Figure 45

prominent as the luminosity of the quasar increases (Shen and Ho, 2014). Therefore, it is plausible that the correlation between the C IV and [O III] blueshifts is a secondary effect that is driven by the correlation of each with the luminosity. In Figure ?? we color the data points by the luminosity, and no luminosity-dependent trends are apparent. We find that both the [O III] and C IV blueshifts are correlated with the luminosity, but that these correlations are much weaker than the correlation between the [O III] and C IV blueshifts.

4.9 EIGENVECTOR ONE CORRELATIONS

In Figure 46 we show the [O III] EQW as a function of the H β FWHM and the optical Fe II strength. The optical Fe II strength is defined as the ratio of the Fe II and H β EQW, where the Fe II EQW is measured between 4434 and 4684Å. These parameters form part of ‘eigenvector 1’ (EV1), the first eigenvector in a principal component analysis which originated from the work of Boroson and Green, (1992). In our sample, these parameters follow very similar correlations to what is observed at low-z (e.g. Shen and Ho, 2014). In particular, the anti-correlation between the [O III] and Fe II EQWs.

Same as Shen, (2016), we confirm that the EV1 correlations hold at high luminosities/redshifts. See also Sulentic et al. 2004, 2006; Runnoe et al. 2013. Make sure it’s clear that Shen, (2016) quasars make up a significant chunk of our sample.

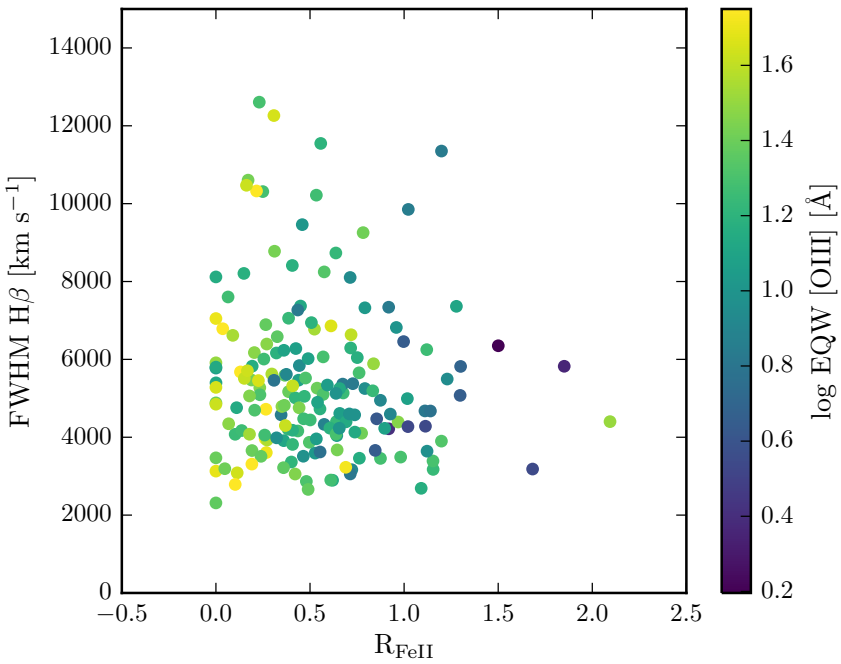


Figure 46: The [O III] EQW as a function of the H β FWHM and the optical Fe II strength (EQW Fe II / EQW H β).

4.10 SIGNAL TO NOISE TESTS

4.11 BROAD ABSORPTION LINE QUASARS

19 quasars in our catalogue are classified as broad absorption line (BAL) quasars, using the either the SDSS classification flags or the Allen et al., (2011) catalogue. We find that the BAL quasars have typically broader [O III] than the rest of the sample. Note that in the Zakamska et al., (2016) sample of very red quasars, the incidence of BALs is very high, and these objects have extremely broad [O III] profiles. A two-sided Kolmogorov-Smirnov statistic on the w_{80} distributions returned a p-value of 0.10. What does this mean? Try with different parameters? Histograms look rubbish so maybe just give the numbers.

4.12 DISCUSSION

4.12.1 Type II quasars

Implications of our findings on searches for high-redshift type 2 quasars. It could be that type II quasars exist. If you look at CIV/MgII the narrow line components are very weak. So the contribution from the narrow line region is very weak in luminous quasars, and you just

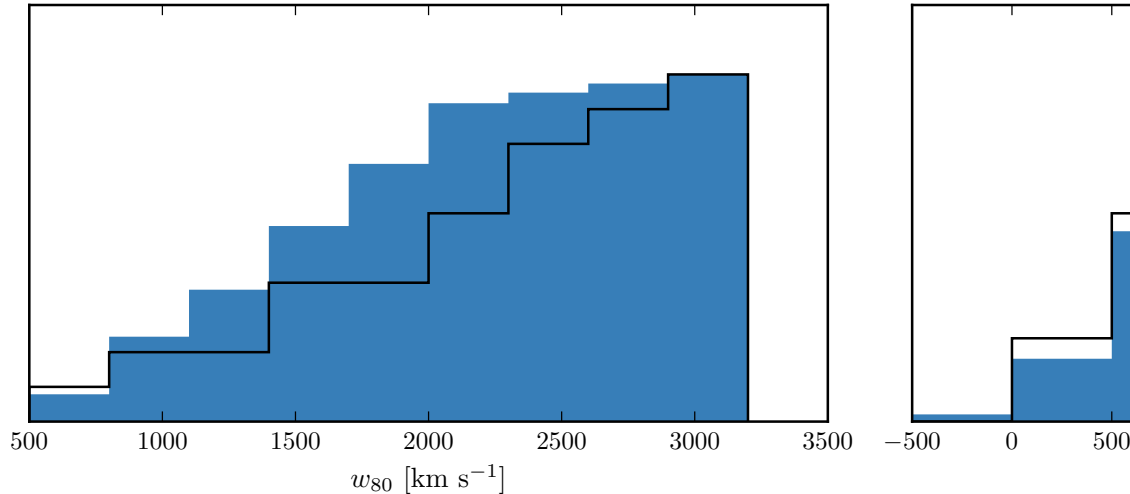


Figure 47: The distribution of w_{80} and v_{10} for the 19 BALs are compared to the distribution for the non-BALs. These look rubbish. Cumulative distributions instead?

won't see it even if the broad line region is obscured. Findings in this paper seem to suggest that the startic narrow line region is very weak in luminous quasars.

SECOND YEAR REPORT

5.1 INTRODUCTION

In the $1\text{-}3\mu\text{m}$ region, the SED is believed to be dominated by thermal emission from hot ($\sim 1200\text{K}$) dust very close to the central engine and possibly at the inner edge of a dusty torus. By fitting my SED model to the UKIDSS-WISE photometric data I can measure the temperature and abundance of this hot dust component and therefore place constraints on the location and covering factor. We have uncovered a number of interesting results, for example an anti-correlation between the AGN luminosity and the temperature of the hot dust (see Figure 83).

High-ionization, broad emission lines, such as CIV, are shifted by up to ~ 3000 km/s blue-ward of the systemic redshift, and the blue-shifted component is thought to arise in an out-flowing wind of highly-ionised material from the accretion disc. A new and much improved scheme from Paul Hewett for determining systemic redshifts allows the blue-shift of the CIV line to be measured very accurately. This has allowed us to show that the blue-shift of the CIV line is correlated with the amount of hot dust emission we measure from the SED. This suggests that either a significant amount of the dust is in the outflow itself or there is some other property of the quasar, such as the orientation with respect to our line-of-sight, which the hot dust and outflows are both dependent on.

At the end of March we spent four nights using the near-infrared spectrograph on the WHT. We were able to obtain spectra covering H α , H β and [OIII] for a sample of ~ 20 quasars with a wide range of outflow and hot dust properties. We have used the broad Balmer lines to measure single-epoch (SE) virial BH mass estimates and have

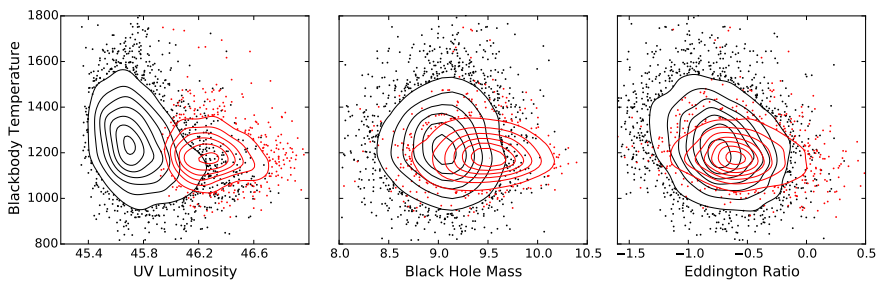


Figure 48: Black-body temperature plotted (from left to right) as a function of the ultra-violet luminosity, the black-hole mass and the Eddington ratio.

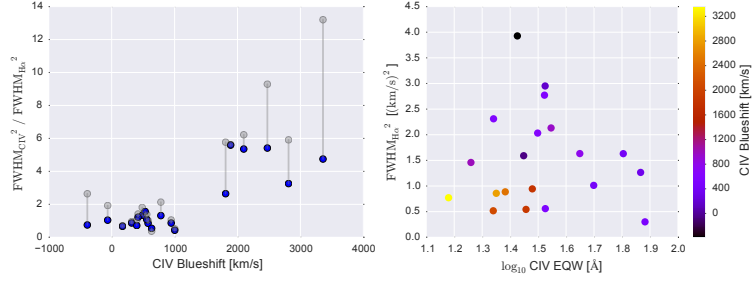


Figure 49: *Left:* Ratio of $\text{FWHM}_{\text{CIV}}^2$ and $\text{FWHM}_{\text{H}\alpha}^2$ plotted as a function of the CIV blue-shift. *Right:* $\text{FWHM}_{\text{H}\alpha}^2$ plotted as function of CIV equivalent width. Note how at high blue-shifts CIV-based BH masses will be overestimated, and how, at low CIV equivalent width, the H α -based BH masses are systematically lower for the quasars with blue-shifted CIV.

used these estimates to show that BH mass estimates based on the CIV emission line may be overestimated by a factor of ~ 4 when the CIV line has a significant blue-shifted component (see Figure 49). We can also use the narrow [OIII] emission line to study outflows on kilo-parsec scales.

5.2 FUTURE WORK

This work will be built on by, for example, investigating dust-extinction (combining our sample with moderately-reddened quasars from Mad-dox et al. 2012 and heavily-reddened quasars from Banerji et al. 2012–2015), broad-absorption line quasars, and/or radio properties. We will also investigate the sub-population of quasars for which we don’t observe any emission from hot dust.

6

HOT DUST

While many authors have focused on studies of specific sub-sets of active galactic nuclei with extreme observational properties, what is missing is an understanding of how these extreme subsets relate to the population as a whole. I have made some progress in addressing this problem using multi-wavelength spectral energy distributions of large ($\sim 100,000$) samples of quasars. I have constructed an SED model which is able to reproduce the average optical to near-infrared (NIR) colours of 10,000s of AGNs spanning a broad range in redshift/luminosity. The goal of this work is to relate the intrinsic spread in SED properties to physical properties of the AGN.

First we will present model, show it can reproduce the average optical to near-infrared (NIR) colours of 10,000s of AGNs spanning a broad range in redshift/luminosity. Then focus on the diversity in near-infrared emission, and relation to physical properties of quasars.

6.1 DATA

In the next two sections I will describe how I have modelled the SED in the quasar rest-frame UV to near-IR spectral region. We begin by fitting the same model to a large sample of quasars to emphasise common features, and then look for differences from the typical model in various sub-populations. The systematic study of the dependence of the SED shape on physical parameters has, until very recently, been limited by the difficulty in obtaining a large sample of quasars with good multi-wavelength coverage and large dynamic range in luminosity and redshift. In this work, we take advantage of a number of recent, sensitive, wide-field surveys, covering the UV to mid-IR spectral region. We will now describe these surveys, and how we combined them to create a large sample of quasars with multi-wavelength photometry.

6.2 SURVEYS

6.2.1 *The Sloan Digital Sky Survey*

We use the spectroscopic quasar catalogues of the Sloan Digital Sky Survey (SDSS; York et al., 2000) Seventh Data Release (DR7Q; Schneider et al., 2010) and Tenth Data Release (DR10Q; Pâris et al., 2014). The SDSS obtained images in five broad optical passbands: u ($\lambda_{\text{eff}} = 3543\text{\AA}$), g ($\lambda_{\text{eff}} = 4770\text{\AA}$), r ($\lambda_{\text{eff}} = 6231\text{\AA}$), i ($\lambda_{\text{eff}} = 7625\text{\AA}$), and z

($\lambda_{\text{eff}} = 9134\text{\AA}$). The SDSS spectra cover $\sim 3000 - 9000\text{\AA}$ at a spectral resolution of ~ 2000 .

We use BEST point-spread function (PSF) magnitudes from the DR7Q catalogue, which are uncorrected for Galactic extinction. The Galactic extinction, which is calculated using the maps of Schlegel, Finkbeiner, and Davis, (1998), is given in the u band only. The Galactic extinction in the griz passbands is calculated using a Milky Way (MW) extinction curve (Pei, 1992) and assuming an extinction to reddening ratio $A(V)/E(B-V) = 3.1$. We use the PSF magnitudes from the DR10Q catalogue, correcting for Galactic extinction using the maps of Schlafly and Finkbeiner, (2011).

SDSS uses ‘asinh’ magnitudes, rather than conventional Pogson magnitudes. Although the photometry is intended to be on the AB system Oke and Gunn, (1983), the photometric zero-points are known to be slightly off the AB standard. To account for this we add 0.03 mag to the u, g, r and i magnitudes, and 0.05 mag to the z magnitude.

DR7Q and DR10Q include 105,783 objects across 9380 deg^2 , and 166,583 objects across $6,370 \text{ deg}^2$, respectively, with 16,420 objects in common to both catalogues. In Figure 50 we compare the distributions of redshift, apparent i magnitude and absolute i magnitude of objects in the two catalogues.

6.2.1.1 Redshift Distribution (Figure 50; Top panel)

The median redshift of the DR7Q sample is 1.49 and 77% are at redshifts < 2 . DR10Q quasars were selected to have redshifts > 2 with the goal of studying the Ly- α forest; the smaller peaks in the distribution at $z \sim 0.8$ and $z \sim 1.6$ are due to degeneracies in the color selection space. At $z < 2$ the incompleteness of the DR10Q catalogue is high, and so the DR7Q catalogue is more suitable for studying systematic changes in quasar properties with redshift.

6.2.1.2 Observed i Magnitude Distribution (Figure 50; Middle panel)

DR7Q quasar targets were primarily selected to have $i \leq 19.1$ if the colours were consistent with being at redshift $z < 3$, and $i \leq 20.2$ if consistent with $z > 3$ (Richards et al., 2002). The large number of objects at $z < 3$ with $i > 19.1$ were selected by algorithms other than the main quasar selection. For example, quasar targets were also selected if they matched within $2''$ of an object in the Faint Images of the Radio Sky at Twenty-cm (FIRST) catalogue of radio sources (Becker, White, and Helfand, 1995). DR10Q targets were primarily selected to have $g \leq 22.0$ or $r \leq 21.85$, which means the DR10Q catalogue goes to much fainter magnitudes than the DR7Q catalogue and is, for example, more sensitive to populations of reddened quasars.

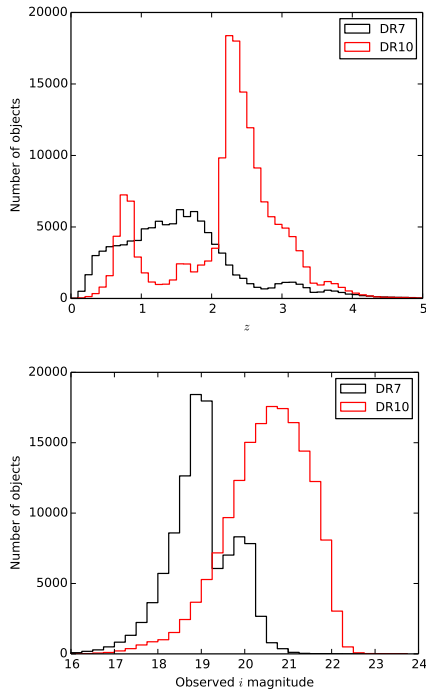


Figure 50: Histograms comparing the DR7Q and DR10Q catalogues: *Top*: Redshift distribution; *Middle*: Distribution of apparent i-band magnitudes; *Bottom*: Distribution of absolute i-band magnitudes **missing this**.

6.2.1.3 Absolute i Magnitude Distribution (Figure 50; Middle panel)

Both samples are composed primarily of luminous quasars; the absolute magnitude distributions are roughly symmetric around $M_i \simeq -26.0$ and $M_i \simeq -25.6$ for DR7Q and DR10Q respectively, with DR10Q extending to lower luminosities.

6.2.2 UKIDSS Large Area Survey

We use the UKIRT Infrared Deep Sky Survey (UKIDSS; Lawrence et al., 2007) Large Area Survey (ULAS) which has observed $\sim 3,200 \text{ deg}^2$ in four near-IR passbands: Y ($\lambda_{\text{eff}} = 1.0305 \mu\text{m}$), J ($\lambda_{\text{eff}} = 1.2483 \mu\text{m}$), H ($\lambda_{\text{eff}} = 1.6313 \mu\text{m}$), and K ($\lambda_{\text{eff}} = 2.2010 \mu\text{m}$). We used the ninth data release (DR9) of the ULAS. Cross-matching (with a $2''$ radius and picking only the nearest neighbour) the SDSS DR7Q catalogue with the ULAS catalogue, which covers only $\sim 38\%$ of the SDSS footprint, resulted in 37,893 matches. The ULAS magnitudes are aperture corrected magnitudes in a $2''$ diameter aperture and are not corrected for Galactic extinction.

UKIDSS fluxes and their associated errors are included in the DR10Q catalogue. These were converted to Vega magnitudes using flux zero points 2026, 1530, 1019, and $631 \times 10^{-26} \text{ W m}^{-2} \text{ Hz}^{-1}$ for the Y, J,

Band-pass	$m_{\text{Vega}} \rightarrow m_{\text{AB}}$
Y	+0.634
J	+0.938
H	+1.379
K	+1.900
W1	+2.699
W2	+3.339
W3	+5.174
W4	+6.620

Table 11: Vega to AB magnitude conversion factors for UKIDSS (Hewett et al., 2006) and WISE (Cutri et al., 2013) photometry.

H, and K passbands respectively. Vega magnitudes were then converted to the AB system using the conversions given in Table 11. The UKIDSS fluxes in the DR10Q catalogue were obtained via forced photometry of UKIDSS observations at the SDSS DR8 centroids (Aihara et al., 2011). This method underestimates the intrinsic magnitude, as flux which falls outside of the aperture used is unaccounted for. We estimated the correction required to recover the intrinsic magnitudes by finding the median magnitude offset between the sub-sample of objects which have both UKIDSS DR10Q magnitudes and magnitudes from our SDSS DR7Q match to the ULAS DR9 catalogue, which is aperture corrected. We found the median offsets in the Y-, J-, H- and K- bands to be -0.083 , -0.081 , -0.085 and -0.085 respectively, and so corrected all DR10Q UKIDSS magnitudes by these amounts.

6.2.3 WISE All-WISE Survey

The Wide-field Infrared Explorer (WISE; Wright et al., 2010) mapped almost the sky in four mid-IR band-passes: W1 ($\lambda_{\text{eff}} = 3.4\mu\text{m}$), W2 ($\lambda_{\text{eff}} = 4.6\mu\text{m}$), W3 ($\lambda_{\text{eff}} = 12\mu\text{m}$), and W4 ($\lambda_{\text{eff}} = 22\mu\text{m}$). The WISE AllWISE Data Release ('AllWISE') combines data from the nine month cryogenic phase of the mission that led to the 'AllSky' data release with data from the NEOWISE program (Mainzer et al., 2011).

Cross-referencing the SDSS DR7Q catalogue with the AllWISE catalogue resulted in 102,734 matches. Two objects (SDSS J083746.57+085839.6 and SDSS J092021.93+331125.7) were matched to multiple AllWISE objects, and were discarded from the sample. Cross-referencing the SDSS DR10Q catalogue with the AllWISE catalogue produced 116,666 matches. Four objects (SDSS J165812.28+3109000.6, SDSS J013053.17+034934.5, SDSS J151446.14+304241.8, and SDSS J015615.57+034604.4) were matched to multiple AllWISE objects, and were discarded from the sample.

6.3 COMPLETENESS OF PHOTOMETRY

We can set the brightness of our sample of quasars by excluding all objects with observed i or g magnitudes fainter than i_{\min} or g_{\min} . Objects which are very bright in the i or g band-passes will also be detected at longer wavelengths. However, objects which are fainter in the i or g band-passes are more likely to have magnitudes which fall below the limiting magnitudes of the UKIDSS and WISE band-passes, and so will not be detected at these longer wavelengths. For a given i or g magnitude, a quasar with a blue spectrum (i.e. a spectrum which is fainter than usual at longer wavelengths) is more likely to be undetected at longer wavelengths than a quasar with a red spectrum (i.e. a spectrum which is brighter than usual at longer wavelengths). Therefore, as we allow fainter quasars in to our sample we will be biased towards objects with redder spectra. We can avoid this bias by carefully selecting the minimum i or g magnitude of the sample such that a large fraction (e.g. $\sim 95\%$) of objects are detected in all band-passes and the fraction is not changing rapidly with the brightness of the sample (which would indicate we are close to the limiting magnitude of the survey). Figure 51 shows the fraction of objects which were matched to the SDSS DR7Q/DR10Q catalogue and have WISE and UKIDSS photometry with $S/R > 5$ as a function of the minimum observed i/g magnitude for the DR7Q/DR10Q sample. S/N ratios were calculated using

$$S/R = (0.4 \times \log(10) \times \sigma_m)^{-1} \quad (9)$$

where σ_m is the uncertainty in the magnitude. We see that the DR7Q-matched sample is 95% complete in all band-passes (excluding W3) if the minimum i magnitude of the sample is above ~ 20 . The DR10Q-matched sample is $\sim 95\%$ complete in all band-passes (again, excluding W3) if the minimum g magnitude of the sample is above ~ 20.5 .

In this chapter, we have described how we have constructed two large multi-wavelength quasar samples, one matched to the SDSS DR7Q catalogue and the other matched to the SDSS DR10Q catalogue. In addition to 13-band photometry we have moderate resolution spectra from SDSS in the $\sim 3000 - 9000\text{\AA}$ region. We will use the spectra to complement our SED fitting by measuring, for example, SMBH masses, metallicities, and properties of absorbers and outflows.

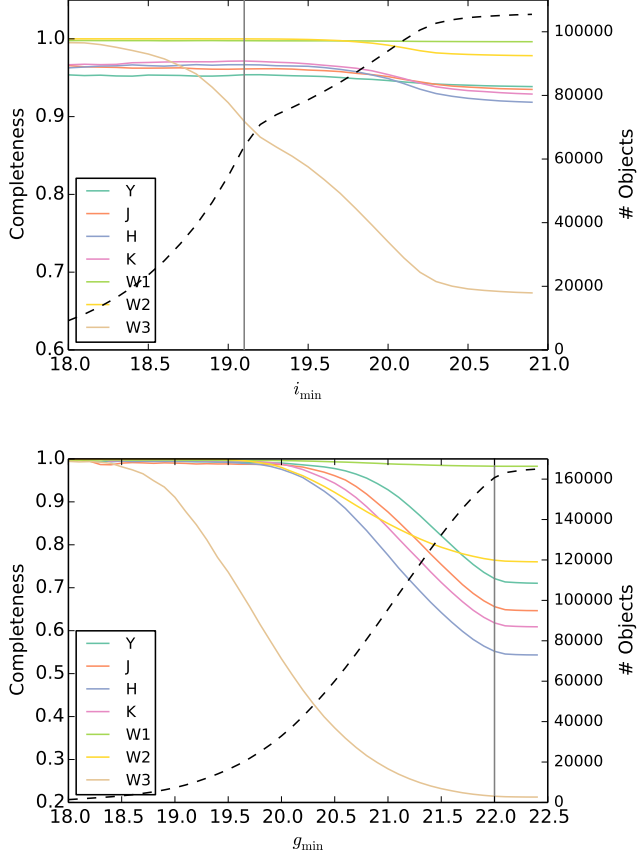


Figure 51: *Top:* Fraction of objects which were matched to DR7Q catalogue with WISE and UKIDSS photometry ($\text{SNR} > 5$) as a function of minimum i -band magnitude of the sample (*coloured lines*). Total number of objects in DR7Q catalogue as function of minimum i -band magnitude (*black dashed line*). Primary quasar colour selection minimum i magnitude (*grey line*). *Bottom:* Fraction of objects which were matched to DR10Q catalogue with WISE and UKIDSS photometry ($\text{SNR} > 5$) as a function of minimum g -band magnitude of sample (*coloured lines*). Total number of objects in DR10Q catalogue as function of minimum g -band magnitude (*black dashed line*). Primary quasar colour selection minimum g magnitude (*grey line*).

6.4 SED MODEL

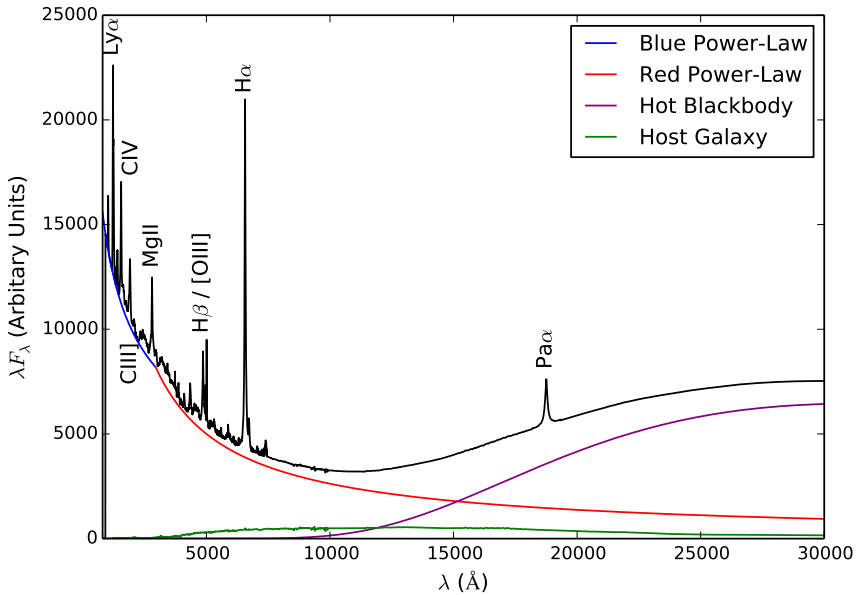


Figure 52: Model spectrum at $z = 1$, showing the contributions to the total flux from the blue power-law slope, red power-law slope, blackbody and host galaxy. The locations of the most prominent emission lines in the spectrum are also indicated.

I have constructed a new SED model which attempts to reproduce the SEDs of AGNs from the rest-frame UV ($\sim 0.1\mu\text{m}$) to the rest-frame near-IR ($\sim 3\mu\text{m}$). In this chapter, I will describe how I have modelled the emission from the various components contributing to the emission in this spectral region. The model spectrum is shown in Figure 64, with each of the main components indicated.

6.5 MODEL COMPONENTS

6.5.1 Accretion Disk

As we described in Section 1.6, more than half the bolometric luminosity of an unobscured AGN is emitted in the Big Blue Bump, which extends from the near-IR at $1\mu\text{m}$ to past $0.1\mu\text{m}$ in the UV, and possibly all the way to the soft X-ray region (see Figure 2), and is thought to arise from an accretion disc. In the $0.1 - 1\mu\text{m}$ region the spectrum is generally characterised by a power-law of the form $F_\nu = Cv^{-\alpha}$ where α is the power-law index, C is a constant, and F_ν is the flux per unit frequency, usually measured in units of $\text{erg s}^{-1}\text{cm}^{-2}\text{Hz}^{-1}$. Equivalently this can be expressed as $F_\lambda = C'\lambda^{\alpha-2}$ where F_λ is the flux per unit wavelength, usually measured in units of $\text{s}^{-1}\text{cm}^{-2}\text{\AA}^{-1}$.

The value of the power-law index is uncertain. From a theoretical perspective, models of geometrically thin accretion discs (Shakura and Sunyaev, 1973) assume, in particular, that the disc is stationary, axisymmetric, and extends down to the innermost stable circular orbit, and that angular momentum is transported by local ‘viscous’ stresses that convert gravitational energy entirely into heat. This gives the dependence of the effective temperature on radius as $t_{\text{eff}} \propto r^{-3/4}$. A spectrum is then calculated by dividing the disc into concentric annuli, calculating the spectrum emitted by each annulus and then summing them all together. Assuming that each annulus radiates like a blackbody, the $r^{-3/4}$ effective temperature distribution gives $F_v \propto v^{1/3}$ (Peterson, 1997), although it is unclear whether this is consistent with observations.

In our model we characterised the Big Blue Bump from $\sim 0.1 - 1 \mu\text{m}$ as a broken power-law with three free parameters: a break-wavelength λ_{break} , a blue power-law index α_{blue} for wavelengths shorter than the break wavelength, and a red power-law index α_{red} for wavelengths longer than the break wavelength.

6.5.2 Hot Dust

At wavelengths longer than $1 \mu\text{m}$, emission from hot dust begins to dominate over emission from the accretion disc. The SED in this region is generally characterised either by a power-law ($\propto \lambda^{\beta_{\text{NIR}}}$), with $\beta \simeq 0.5$ (e.g. Richards et al., 2006a; Zhang et al., 2014), or by a blackbody at $\sim 1300 \text{ K}$, thus peaking in the near-IR (e.g. Leipski et al., 2014). We modelled the hot dust emission using a simple blackbody:

$$F_\lambda = \frac{2hc^2}{\lambda^5} \frac{1}{e^{\frac{hc}{\lambda k_B T}} - 1} \quad (10)$$

The blackbody component has two free parameters: the temperature of the blackbody T_{BB} and the overall normalisation.

6.5.3 Emission Lines

Hundreds of emission lines are present in a typical AGN spectra. Some of the most prominent lines are shown in Figure 64. The emission line spectrum is taken from Maddox and Hewett, (2006), who extend the composite of Francis et al., (1991) to include the H α (6560Å) and Pa α (18750Å) emission lines. A single parameter, EL_{scale} , scales the equivalent widths of all emission lines equally:

$$F_\lambda = EL_{\text{scale}} \times \frac{F_{\lambda, \text{el}}}{F_{\lambda, \text{cont}}} \times F_\lambda \quad (11)$$

where $F_{\lambda, \text{el}}$ is the line flux in the template, $F_{\lambda, \text{cont}}$ is the continuum flux in the template, and F_λ is the continuum flux in the model.

6.5.4 Host Galaxy

Emission from the host galaxy is important, particularly in the region around the $1\mu\text{m}$ inflection point in the quasar SED. While the host galaxies of bright quasars tend to be massive, bright ellipticals, the hosts of lower luminosity AGN can have disc components (e.g. Dunlop et al., 2003). Our model incorporates $z = 0$ Sa, Sb, Sc and elliptical-type templates from Mannucci et al., (2001), which for simplicity do not evolve with redshift. We characterise the relationship between the luminosity of the AGN L_{AGN} and the luminosity of the host galaxy L_{Gal} as a power-law

$$L_{\text{Gal}} = L_{\text{AGN}}^\beta \quad (12)$$

with power-law index $\beta = 0.42$ (Maddox and Hewett, 2006). Dividing both sides of Equations 12 by the luminosity of the AGN gives the luminosity of the host galaxy relative to the luminosity of the AGN

$$\frac{L_{\text{Gal}}}{L_{\text{AGN}}} = L_{\text{AGN}}^{\beta-1} \quad (13)$$

which for $\beta < 1$ decreases with increasing AGN luminosity. In a flux limited sample, the AGN luminosity will tend to increase with redshift and so the luminosity of the host galaxy relative to the luminosity of the quasar will decrease with increasing redshift. Hence, the contribution from the host galaxy to the total flux is important at low redshift, but becomes gradually less significant towards higher redshifts.

Since the contribution from the host galaxy to the flux changes as a function of AGN luminosity, and hence redshift, we choose a reference redshift z_{nrm} where we set the fractional contribution of the host galaxy to the total flux, η . In an arbitrary region of the spectrum (we use $4000 - 5000 \text{ \AA}$) we calculate both the AGN continuum flux $F_{\text{AGN}}(z_{\text{nrm}})$ and the flux from our host galaxy template spectrum $F_{\text{Gal}}(z_{\text{nrm}})$. The fractional contribution from the host galaxy to the total flux is then:

$$\eta = \frac{C F_{\text{Gal}}(z_{\text{nrm}})}{F_{\text{AGN}}(z_{\text{nrm}}) + C F_{\text{Gal}}(z_{\text{nrm}})} \quad (14)$$

where the constant C is the factor by which we must multiply the unnormalised galaxy spectrum in order for Equation 14 to hold true. Rearranging for the constant C we find

$$C = \frac{\eta}{1-\eta} \frac{F_{AGN}(z_{nrm})}{F_{Gal}(z_{nrm})} \quad (15)$$

Hence at redshift z_{nrm} the host galaxy flux we add to our rest frame quasar continuum is

$$F_\lambda = \frac{\eta}{1-\eta} \frac{F_{AGN}(z_{nrm})}{F_{Gal}(z_{nrm})} F_{\lambda, Gal} \quad (16)$$

where $F_{\lambda, Gal}$ is our host galaxy template spectrum in the quasar rest frame. The contribution from the host galaxy at a different redshift z is given by

$$F_\lambda = \frac{\eta}{1-\eta} \frac{F_{AGN}(z)}{F_{Gal}(z)} \frac{F_{AGN}(z_{nrm})}{F_{Gal}(z_{nrm})} \left(\frac{F_{AGN}(z)}{F_{Gal}(z)} \right)^{-1} F_{\lambda, Gal} \quad (17)$$

$$= \frac{\eta}{1-\eta} \frac{F_{AGN}(z)}{F_{Gal}(z)} \frac{F_{AGN}(z_{nrm})}{F_{Gal}(z_{nrm})} \frac{F_{Gal}(z)}{F_{AGN}(z)} F_{\lambda, Gal} \quad (18)$$

$$= \frac{\eta}{1-\eta} \frac{F_{AGN}(z)}{F_{Gal}(z)} \frac{L_{AGN}(z_{nrm})}{L_{Gal}(z_{nrm})} \frac{L_{Gal}(z)}{L_{AGN}(z)} F_{\lambda, Gal} \quad (19)$$

$$= \frac{\eta}{1-\eta} \frac{F_{AGN}(z)}{F_{Gal}(z)} \frac{L_{AGN}(z_{nrm})}{L_{AGN}(z_{nrm})^\beta} \frac{L_{AGN}(z)^\beta}{L_{AGN}(z)} F_{\lambda, Gal} \quad (20)$$

$$= \frac{\eta}{1-\eta} \frac{F_{AGN}(z)}{F_{Gal}(z)} \left(\frac{L_{AGN}(z)}{L_{AGN}(z_{nrm})} \right)^{\beta-1} F_{\lambda, Gal} \quad (21)$$

We need to know how the luminosity of the AGN depends on redshift. This is given by:

$$\frac{L_{AGN}(z)}{L_{AGN}(z_{nrm})} = 10^{-0.4(M_{AGN}(z) - M_{AGN}(z_{nrm}))} \quad (22)$$

where $M_{AGN}(z)$, the absolute magnitude of an AGN at redshift z , is given by

$$M(z) = m - 5(\log_{10}D_L(z) - 1) \quad (23)$$

and $D_L(z)$ is the luminosity distance to a source at redshift z in parsecs. Hence:

$$\frac{L_{AGN}(z)}{L_{AGN}(z_{nrm})} = 10^{-0.4(M_{AGN}(z) - M_{AGN}(z_{nrm}))} \quad (24)$$

$$= 10^{(\log_{10}\left(\frac{D_L(z)}{D_L(z_{nrm})}\right)^2)} \quad (25)$$

6.5.5 Lyman- α Forest Absorption

The optical spectra of high redshift quasars show hundreds of sharp absorption lines, which mostly correspond to the redshifted neutral hydrogen Ly α 1216Å transition. These absorption features are collectively referred to as the *Lyman- α forest*. To simulate the effect of Lyman- α forest absorption on our model SED we use the parametrisation of Becker et al., (2013), who derived an analytic function for the effective optical depth τ_{eff} over the redshift range $2 < z < 5$ made using 6065 quasar spectra from SDSS DR7. In their model the effective optical depth τ_{eff} is given by

$$\tau_{\text{eff}} = \tau_0 \times \left(\left(\frac{1+z}{1+z_0} \right)^b + C \right) \quad (26)$$

where,

$$\begin{aligned} t_0 &= 0.751 \\ b &= 2.9 \\ C &= -0.132 \\ z_0 &= 3.5 \end{aligned}$$

The transmitted flux $F_{\lambda, \text{trans}}$ at redshift z is then given by

$$f_{\lambda, \text{trans}} = F_{\lambda} \times e^{-\tau_{\text{eff}}} \quad (27)$$

An absorption line at λ_{abs} in the rest-frame of an AGN at redshift z_{AGN} has wavelength

$$(1 + z_{\text{AGN}})\lambda_{\text{abs}} \quad (28)$$

in the rest frame of an observer on Earth. In the rest-frame of a cloud of neutral hydrogen at redshift z_{cloud} the absorption line has wavelength

$$\frac{(1 + z_{\text{AGN}})\lambda_{\text{abs}}}{(1 + z_{\text{cloud}})} \quad (29)$$

and so to absorb Lyman- α at 1216 Å the gas cloud must be at a redshift

$$z_{\text{cloud}} = \frac{(1 + z_{\text{AGN}})\lambda_{\text{abs}}}{1216\text{\AA}} - 1 \quad (30)$$

For every wavelength $\lambda_{\text{abs}} < 1216\text{\AA}$ in the rest-frame of an AGN at redshift $z > 2$ we calculate z_{cloud} using Equation 30 and then calculate the transmitted flux at λ_{abs} by substituting z_{cloud} in to Equations 26 and 27.

6.5.6 Lyman-Limit Systems

Lyman-limit systems are clouds of HI which are optically thick at the Lyman limit (912Å), which generally implies a neutral hydrogen column density $N(\text{HI}) > 10^{17} \text{ cm}^{-2}$. Photons at wavelengths shorter than the Lyman-limit will be absorbed, which creates a sharp break in the observed continuum. We model the effect of a Lyman-limit system at the redshift of the quasar by setting the flux at wavelengths less than 912Å in the quasar rest frame to zero.

6.5.7 Dust Extinction

The selection criteria of the SDSS DR7Q catalogue, and particularly the DR10Q catalogue, are sensitive to quasars with moderate amounts of dust reddening (possibly as high as $E(B-V) \sim 0.5$; Richards et al., 2003) at the redshift of the quasar, and so we included the effect of dust extinction in our model. We considered four types of extinction curve: the Large Magellanic Cloud (LMC), Small Magellanic Cloud (SMC), Milky-Way (MW) extinction curves from Pei, (1992) and an extinction curve appropriate for the quasar population which has been derived by Paul Hewett. To derive the quasar extinction curve, UKIDSS photometry was used to provide an $E(B-V)$ estimate, via the magnitude displacement of each quasar from the locus of unreddened objects. At redshifts $2 < z < 3$ the reddening measure is made at rest-frame wavelengths 3500-7000Å, where Galaxy, LMC and SMC extinction curves are very similar. The SDSS spectra of the same objects are then employed to generate an empirical extinction curve in the ultraviolet, down to 1200Å. The resulting curve has no 2200Å feature and rises rapidly with decreasing wavelength but is not as steep as the SMC curve. The extinction curves give the colour excess $E(B-\lambda)$ relative to the colour excess $E(B-V)$ as a function of wavelength λ . The colour excess $E(B-V)$ is related to the extinction in the V band, $A(V)$, via a parameter R ,

$$A(V) = R \times E(B-V) \quad (31)$$

where $R = 3.1$ in the MW and $R \simeq 3$ in the Magellanic Clouds. Hence the extinction at a wavelength λ is

$$A(\lambda) = E(B-V) \times \left[\frac{E(\lambda-V)}{E(B-V)} + R \right] \quad (32)$$

where the colour excess $E(B-V)$ is a free parameter in our model. The attenuation of the flux at a given wavelength is then:

$$F_\lambda = F_{\lambda 0} 10^{-A(\lambda)/2.5} \quad (33)$$

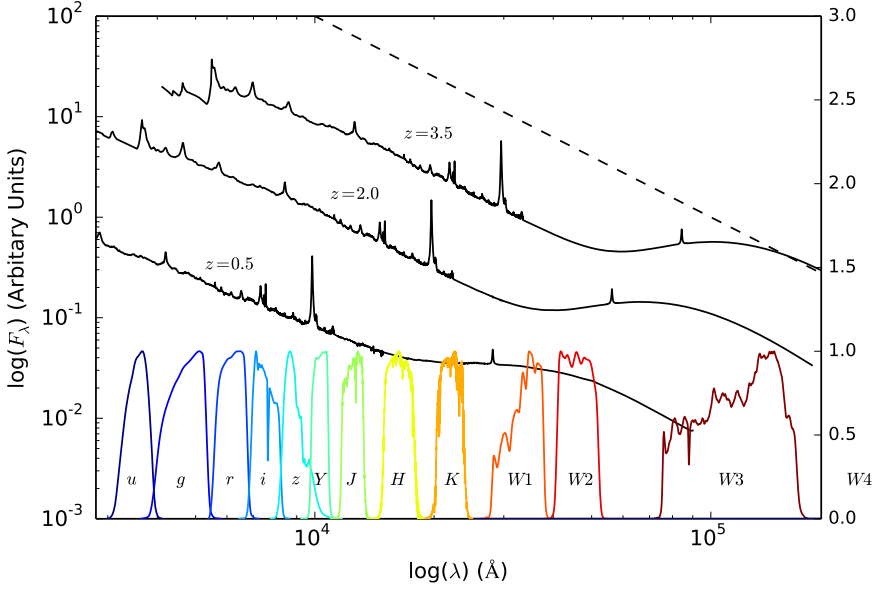


Figure 53: Model spectrum at three different redshifts (each arbitrarily scaled), and throughput functions for SDSS, UKIDSS and WISE band-passes (scaled so that the peak transmission is equal to one.) The dashed line indicates the slope of the AB magnitude system zero point.

in the rest frame of the quasar.

6.6 CONVERTING SPECTRUM INTO OBSERVED SED

The model spectrum was redshifted to the observed frame so that the apparent magnitude through each band-pass could be calculated. The throughput functions of the SDSS ugriz, UKIDSS YJHK and WISE W1W2W3 band-passes are shown in Figure 53, along with our model AGN spectra at three different redshifts. The mean flux density in a band-pass P is given by

$$f_\lambda(P) = \frac{\int P(\lambda) f_\lambda(\lambda) \lambda d\lambda}{\int P(\lambda) \lambda d\lambda} \quad (34)$$

where $P(\lambda)$ is the dimensionless throughput function of the band-pass. The corresponding magnitude, $m_\lambda(P)$, is then

$$m_\lambda(P) = -2.5 \log(f_\lambda(P)) - m_0(P) \quad (35)$$

where $m_0(P)$ is the zero-point magnitude of band P. In the AB magnitude system, the zero-point flux per unit wavelength is

$$\frac{f_\lambda(\lambda)}{\text{erg cm}^{-2} \text{s}^{-1} \text{\AA}^{-1}} = 0.1087 \left(\frac{\lambda}{\text{\AA}} \right)^{-2}. \quad (36)$$

This is substituted into Equation 34 to give a zero-point mean flux density which is then converted into a corresponding magnitude.

6.7 RESULTS FROM FIT

6.8 FITTING PROCEDURE

In this chapter, we will describe the results of fitting our model to the SEDs of different samples of quasars. We will begin by deriving a ‘standard’ SED model by constraining a single set of parameters with a large sample of $0.2 < z < 4$ quasars encompassing a range of luminosities, accretion rates etc. We will then go on to study the diversity of SED shapes in our quasar sample. In particular, we will search for the most heavily reddened quasars in the sample and also explore the redshift dependence of the hot dust properties of individual quasars.

6.8.1 *The ‘Standard’ SED Model*

We use our SDSS DR7Q-matched sample which, as we saw in Figure 50, is more complete over a wider redshift range than the DR10Q-matched sample. We impose an observed i magnitude lower limit of 19.1 mag, which is the magnitude limit of the main SDSS colour-selection algorithm. We also exclude the objects flagged as BALQSOs by Shen et al., (2011), since our model is unable to reproduce the broad absorption troughs that appear in the spectra of these objects. The final sample contains 61,411 objects in the redshift range $0.2 < z < 3.8$.

The free parameters in our model are the blue power-law slope, the red power-law slope, the power-law break wavelength, the blackbody temperature, the blackbody normalisation, the emission line equivalent width scaling, and the fractional contribution from the host galaxy to the total flux. The reddening $E(B-V)$ is fixed to zero, since a large fraction of SDSS quasars have very small amounts of dust reddening (Richards et al., 2003). For the host galaxy we use a Sb-type template derived by Mannucci et al., (2001). With some choice of initial parameters, we generate a set of model observed spectra at redshifts from $z = 0.25$ to $z = 3.75$ in intervals of $\Delta z = 0.1$. We then transform our set of model spectra into a set of model ugrizYJHKW1W2 SEDs using the procedure described in Section 6.6, which we normalise such that the i magnitude of each model SED is 18.0 mag. This gives us an array of model magnitudes as a function of redshift and band-pass. We generate an equivalent data array by dividing our quasar sample into redshift bins from $z = 0.2$ to $z = 3.8$ with bin width $\Delta z = 0.1$. We normalise the individual quasar SEDs such that the observed i magnitude is equal to 18.0 mag, and then calculate a median SED in each redshift bin.

To fit the model to the data we minimise the sum of the squares of the differences between the elements in the model magnitude array and the elements in the data magnitude array. The minimisation

Parameter	Symbol	Before Correction	After Correction
Blue power-law index	α_{blue}	0.58	0.58
Red power-law index	α_{red}	-0.04	-0.05
Power-law break	λ_{break}	2945	2957
Blackbody temperature	T_{BB}	1216 K	1186 K
Blackbody normalisation	C_{BB}	0.22	0.21
Emission line scaling	C_{EL}	0.63	0.73
Galaxy fraction	η	0.29	0.28
$E(B-V)$	$E(B-V)$	0.00	0.00

Table 12: Best-fitting parameters from fit to DR7Q-matched sample.

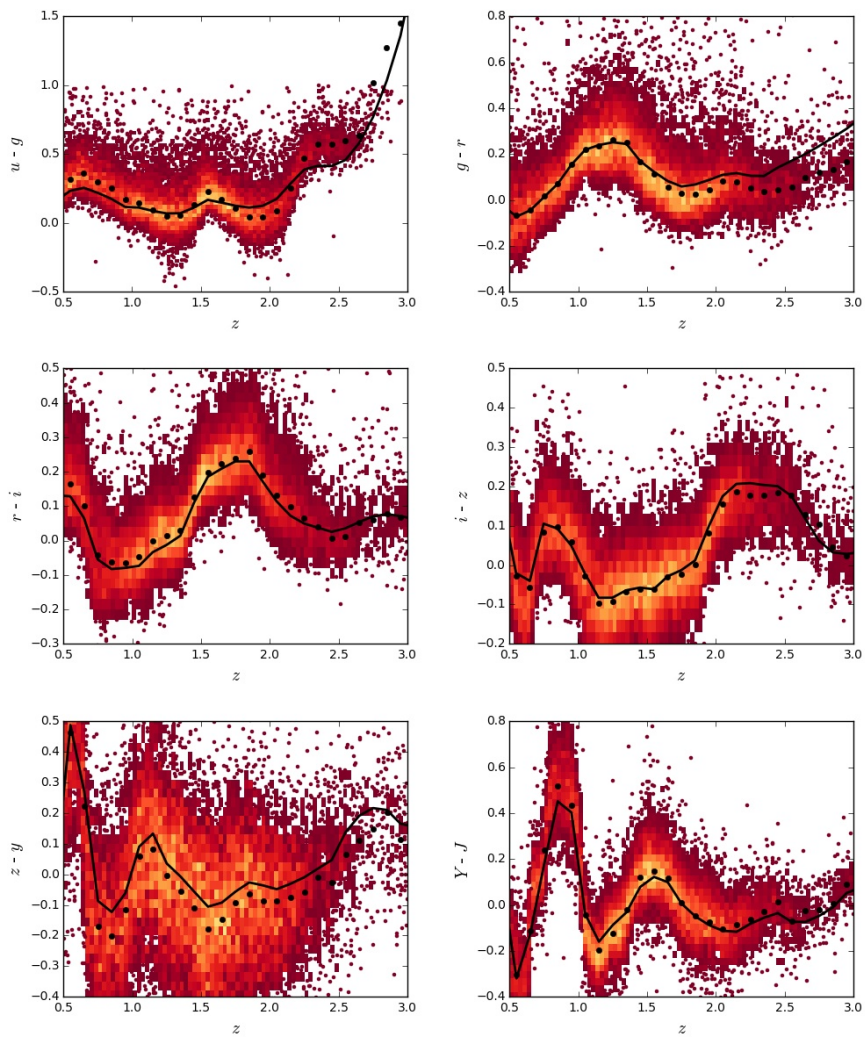
is done using the ‘nelder-mead’ method (also known as the downhill simplex method or amoeba method), as implemented in the `minimize` function from the Python module `scipy`. Our SED model is valid only up to $\lambda \sim 3\mu\text{m}$ in the quasar rest frame (the approximate wavelength of the peak in hot dust emission); beyond this additional contributions to the total flux from cooler dust will become significant. This prevents us from using the two highest wavelength WISE bands in the fit. We also exclude the SDSS u and g band-passes from the fit at $z > 2.7$ and $z > 3.7$ respectively, where absorption in the Lyman α forest becomes large.

The best-fitting parameters from the fit are shown in Table 12. The colours ($u - g$, $g - r$, etc.) of the median SED, the individual quasars, and the best-fitting model are plotted as a function of redshift in Figure 54. Most of the large variations that can be seen in the median colours of the quasars as a function of redshift are due to strong emission lines being redshifted in to and out of the bandpasses of the band-passes being used.

6.8.2 Discussion of Fit

In Figure 55 we show the difference between the magnitudes from the best-fitting model and the median magnitudes from the sample. We have transformed the effective wavelengths of the band-passes to the rest frame of the quasars in each redshift bin, to give to the residuals as a function of rest-frame wavelength. In Figure 55 we represent the residuals measured in each band-pass using a different coloured line. Differences between residuals from different band-passes at the same rest-frame wavelength could indicate redshift evolution of the typical quasar SED.

The residuals indicate that over a large redshift range the model does a fairly good at reproducing the median observed colours of the DR7Q-matched sample. Most discrepancies are at the < 0.1 mag



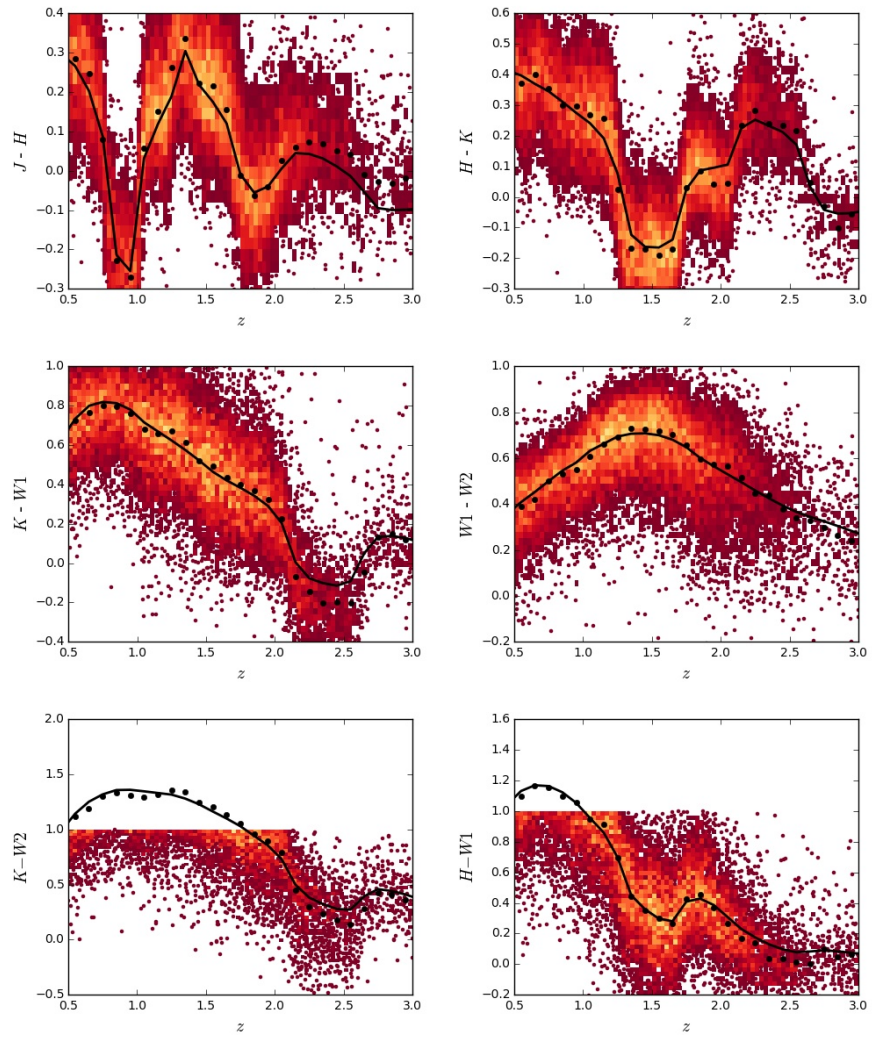


Figure 54: Colours of median SED (black circles), individual objects (grey points), best-fitting uncorrected model (black line) and best-fitting corrected model (red line) as a function of redshift.

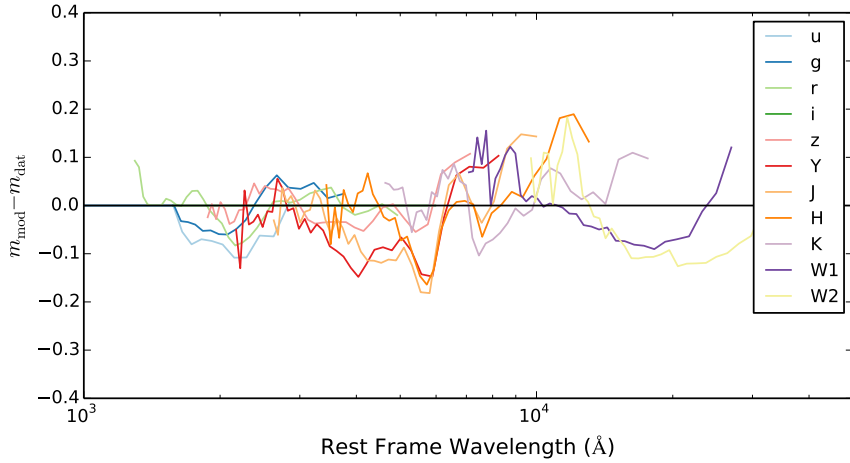


Figure 55: Residuals from fit to DR7Q-matched catalogue as a function of rest-frame wavelength.

level. The most noticeable feature in Figure 55 is a bump around $1\mu\text{m}$, where the model underestimates the flux of the population by ~ 0.1 mag. Later on in Section 6.10.2 we will derive an empirical correction to the model which increases the flux slightly in the 8000 to 17000 Å region of the rest frame spectrum. The red lines in Figure 54 show the colours of this corrected model as a function of redshift. Although the correction improves the fit slightly, significant discrepancies do remain. The model’s underestimation of the flux at in the $3\mu\text{m}$ region is probably due to the increasingly significant contribution to the flux from cooler dust at longer wavelengths, which is not included in our model. We will discuss this in more detail in Section 6.10.1.

Our fitting scheme scales the equivalent width of every emission line by the same amount. Observationally, the emission line ratios are not the same for every quasar, and the model to data discrepancies in certain regions are likely to be the result of this. In Figure 55 we mark the position of the $\text{H}\alpha$ emission line, which is typically very strong and broad and can contribute significantly to the flux even in a broad band-pass. The relatively large residuals around the wavelength of the $\text{H}\alpha$ line may suggest that our simple scaling scheme is insufficient, and we may need to allow the equivalent widths of certain prominent emission lines to vary freely.

6.9 REDDENED QUASARS

Having derived a ‘standard’ SED model, we will now focus on a sub-sample of quasars with SEDs that are best fit by a standard model in addition to moderate amounts of dust reddening ($0.1 < E(\text{B}-\text{V}) < 0.2$). Numerous studies have identified quasars with extreme amounts of dust reddening; in this study it is our aim to first identify and then to

study the properties of quasars with moderate amounts of dust reddening in order to understand the relationship between the extremely dust reddened and ‘normal’ blue populations. Although heavily biased towards selecting blue, unobscured quasars, the SDSS is sensitive to quasars with dust reddening up to $E(B-V) \lesssim 0.5$ (Richards et al., 2003).

6.9.1 Colour Selection

As we saw in Figure 54, quasar colours are a strong function of redshift, which is partly due to strong emission lines being shifted in to and out of the band-passes. Therefore, defining an object as ‘red’ based on a colour cut is subject to redshift-dependent systematic errors. Instead, we calculate the $i - K$ colours of the quasars in the DR10Q-matched catalogue, which is deeper, and therefore more sensitive to reddened quasars, than the DR7Q-matched catalogue, relative to the $i - K$ colours of our standard SED model with $E(B-V) = 0.0, 0.1$, and 0.2 . This is shown in Figure 56. Most of the DR10Q catalogue quasars lie in the $2 < z < 4$ redshift range in which both the SDSS i band-pass and the UKIDSS K band-pass are observing the UV/optical power-law spectrum, the shape of which is the most sensitive to dust reddening. We therefore restrict ourselves to the $2 < z < 4$ redshift range. Most of the scatter in the $i - K$ colours of the individual quasars can be attributed to variations in the power-law slope and emission line strength of individual objects from the standard model. However, there is also a population in the red tail of the distribution with colours that can only be explained by dust reddening at the redshift of the source (Hall et al., 2004).

We estimated an $E(B-V)$ value for each object by interpolating between the reddened models in Figure 56. We selected a sample of 303 objects which have $i - K$ colours which are redder than the standard model with dust reddening $E(B-V) = 0.2$ (i.e. the grey points which lie above the top curve in Figure 56). We visually inspected the SDSS optical spectra of these objects and found a diverse range of properties. Approximately a third of the sample could be characterised visually as having reddened continuum emission. Many had very strong emission lines; some of these had normal blue continua and were probably included in the sample due strong $H\alpha$ emission in the K band-pass. Up to $\sim 20\%$ were BALQSOs, and up to $\sim 10\%$ were Type II quasars. In Figure 57, we show an example of an SDSS spectrum of an object we classified as being a reddened quasar (SDSS J150019.64+082643.6) and an example of an SDSS spectrum of an object which has very strong emission lines, but an otherwise normal blue continuum (SDSS J0240000.6+010317.0).

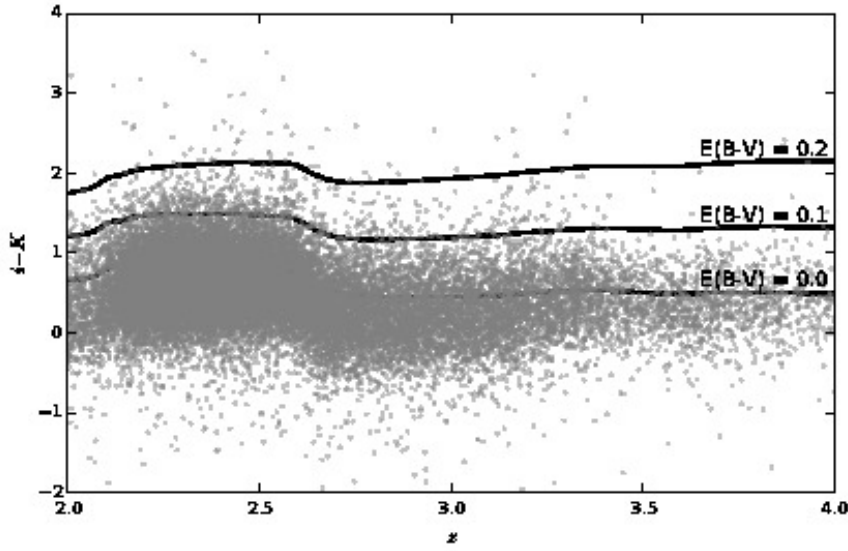


Figure 56: $i - K$ colours of DR10Q-matched catalogue quasars as a function of redshift z (grey points). $i - K$ colours of ‘standard’ SED model as a function of redshift z with dust reddening $E(B-V)=0.0$, 0.1 , and 0.2 (black lines).

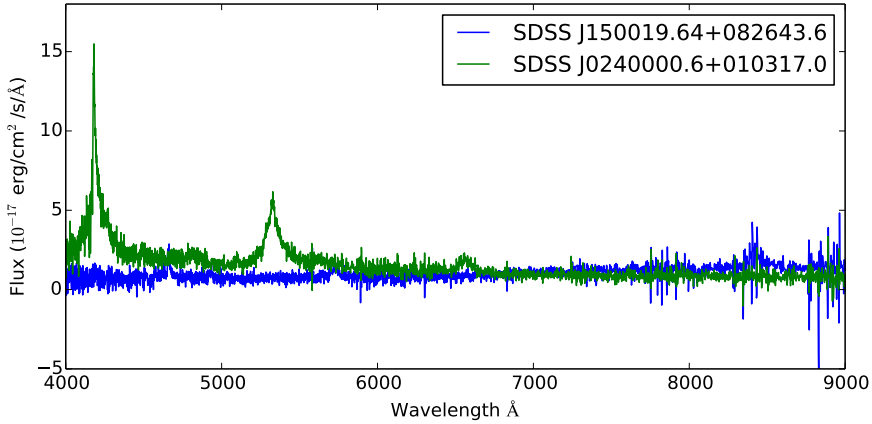


Figure 57: SDSS spectra of two quasars with red $i - K$ colours relative to our unreddened SED model. Whereas the optical spectrum of SDSS J150019.64+082643.6 suggests it may be a genuinely dust-reddened quasar, the red colour of SDSS J0240000.6+010317.0 is probably due to strong H α emission in the K band-pass.

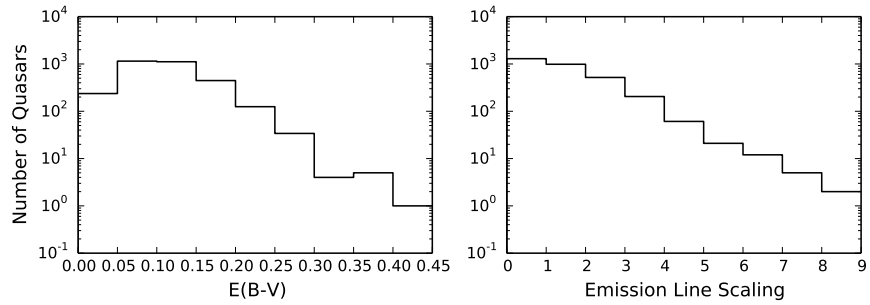


Figure 58: Dust reddening $E(B-V)$ and emission line equivalent width distributions from SED fitting.

6.9.2 Model Fitting

In order to select a sample of genuinely reddened quasars while excluding the strong emission line quasars that are contaminating our sample, we fit our model to the SEDs of the individual quasars. We are unable to constrain every parameter in our model with just 11 photometric data points, and so we fix all the parameters except the emission line strength and the dust reddening to the standard values we derived from the fit to the whole sample. To account for the dispersion of the colours of the individual quasars about the median line (see Figure 54) we set a minimum error of 0.1 mag on the magnitudes. Our model was fit to the data using a standard χ^2 minimisation which, as before, was implemented using the ‘nelder-mead’ algorithm as implemented in the `minimize` module from the `scipy` Python package with standard options. We used a larger sample of 3,117 quasars, which were selected to have $i - K$ colours above the $E(B-V) = 0.1$ dust reddened model in Figure 56.

In Figure 58 we show the $E(B-V)$ and emission line equivalent width scaling values we derived from the fit. The median dust reddening $E(B-V)$ is 0.1, and the maximum is 0.61. 543 quasar SEDs were best fit by models with extremely weak emission lines (emission line equivalent width scaling parameter < 0.01). Of these quasars approximately 30% were classified as BALQSOs. These objects have strong absorption troughs in their spectra which, when integrated over the wavelength range of a band-pass, could cancel out the emission line flux. However, visual inspection of the SDSS optical spectra of a sub-sample of the non-BALQSOs revealed the presence of significant emission lines when the best-fitting model suggested there should be none. In Figure 59 we show how the fraction of objects in the sample which are best fit by models with emission line equivalent width scaling parameter < 0.01 is a strong function of redshift, with significant peaks at $z \sim 2$ and $z \sim 2.7$. We interpret these peaks as being regions of redshift space for which strong emission lines do not affect the SED because they have been redshifted to wavelengths that

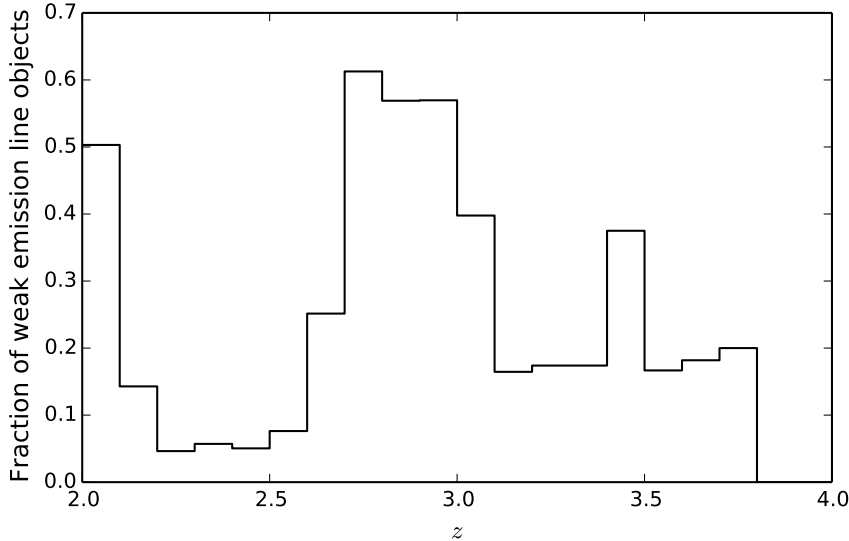


Figure 59: Fraction of quasars in 3,117 object sample which are best fit by models with emission line equivalent width scaling parameter < 0.01 as a function of redshift.

are not probed by our set of band-passes. If we increase the emission line equivalent width scaling parameter to a value typical of the whole population (i.e. ~ 0.8), we find that the majority of χ^2 values from the fit increase by less than one. This demonstrates that the parameter is not well constrained by the data; the emission lines can be of any strength without significantly changing the SED.

6.9.3 MCMC Fitting

We decided to address this limitation by imposing a prior on the emission line equivalent width scaling parameter. To do this we implemented a monte-carlo markov-chain (MCMC) fitting method using the Python module *pymc*. We determined a sensible prior on the emission line equivalent width scaling parameter by looking at the distribution of CIV equivalent widths in the DR10Q catalogue (excluding BALQSOs). We found that the equivalent width values were well fit by a lognormal distribution with location parameter $\mu = 3.737$ and scale parameter $\sigma = 0.58$. This motivated us to impose a lognormal prior on the emission line equivalent width scaling parameter with location parameter $\mu = 0$ and scale parameter $\sigma = 0.58$. We imposed uniform priors on the other two free parameters, the reddening $E(B-V)$ and the overall normalisation of the spectrum. We our MCMC fits with 10,000 iterations and a burn-in length of 500. An example of a posterior plot for quasar SDSS J121956.49-011907.8 is shown in Figure 60. Some degeneracy between the parameters is evident, most

obviously between the overall normalisation of the SED and the emission line equivalent width scaling.

We found the mean E(B-V) values from the MCMC fit to be very similar to the best-fitting values from the χ^2 fit (see Figure 58). The prior on the emission line equivalent width scaling parameter has ensured that we no longer have a significant population of objects which are incorrectly best-fit by models with very weak emission lines.

6.9.4 Acquiring Near-IR Spectroscopy

In the previous section we described how we have collected a sample of quasars with moderate amounts of dust reddening ($E(B-V) \lesssim 0.5$) at the redshift of the quasar. The next stage in our investigation is to study the physical properties of these dust reddened objects, and to compare these to the properties of the population of unreddened quasars and the population of heavily reddened quasars (e.g. Banerji et al., 2012). We are particularly interested in discovering how these populations are related. For example, are the moderately dust reddened quasars in our sample being observed as the quasar makes the transition from being heavily dust reddened to unobscured as it clears out its surrounding dust, or can their dust properties be explained in the context of orientation-based unification schemes.

To help address this question, we plan to obtain near-IR spectra for a sub-sample of our moderately dust reddened quasars using the LIRIS instrument on the William Herschel Telescope at the Isaac Newton Group of telescopes. For quasars in the redshift range $2 \lesssim z \lesssim 2.5$, the H α emission line should be observable using the K band-pass on this instrument. The shape and width of this spectral line will provide us with information on the nature of the obscuring dust. For example, the presence of a broad component to the line would suggest that the dust extinction is occurring in the host galaxy rather than in a circum-nuclear torus, in which case the broad component should be obscured. The H α line properties can be used to infer black hole masses, bolometric luminosities, and Eddington ratios (Banerji et al., 2012), and these physical properties can then be compared to other populations.

Due to the obvious constraints on obtaining telescope time, we needed to define a short-list of candidates for follow-up. To be a candidate we required the objects to pass the following criteria:

- Be viewable during the August - January observing window.
- Have a high S/N in the K band-pass; the higher the S/N, the shorter the exposure time we will require.
- Be at a redshift $2 \lesssim z \lesssim 2.5$

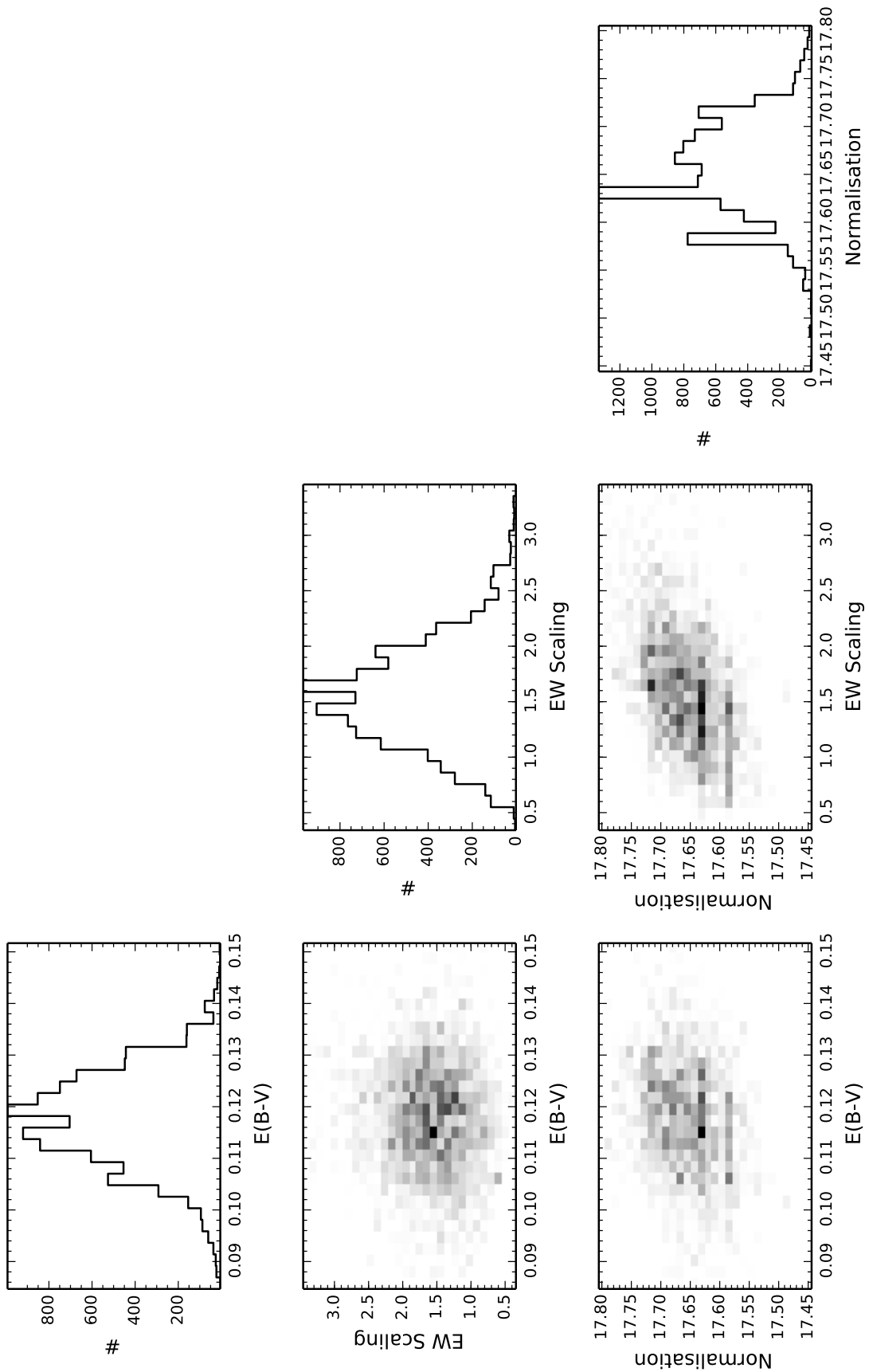


Figure 60: Posterior plots from MCMC fit to SDSS J121956.49-011907.8.

- Be well fit by the reddened standard SED model, with otherwise ‘normal’ features, e.g. not a Type II quasar, BALQSO etc.

Of the 3,117 quasars in our sample, 858 were observable during the 1st August to 31st January observing semester¹. Of these quasars, 567 were at redshifts for which the H α emission line will be observable in the K band-pass ($2 \lesssim z \lesssim 2.5$). Of these, 252 were fit reasonably well by the standard model when the amount of dust reddening and the emission line equivalent width scaling strength were free to vary ($\chi^2 \leq 10$). Of these, 19 quasars are brighter than 18 mag in the K band-pass (for an object of this brightness we will require a ~ 3000 s exposure to obtain a spectra with a $S/R \sim 10^2$). The maximum amount of dust reddening E(B-V) (from our MCMC fit) in this sample of 19 quasars is 0.2, with 0.12 the median. Given the small number of objects in the sample with even modest amounts of reddening, we decided to delay the proposal until the next observing semester, which runs from 1st February to 31st July. During this period 2.6 times as many objects will be observable, which should significantly increase the number of moderately reddened objects in the sample.

6.10 HOT DUST

In Figure 66 we plot the $W1 - W2$ colors of the DR7Q-matched sample as a function of redshift from $z = 0.2$ to $z = 1.8$. In this redshift range the $W1$ and $W2$ band-passes are probing the 12,000 - 28,000 Å and 16,000 - 38,000 Å region of the rest frame SED respectively, and the $W1 - W2$ color is therefore predominantly tracing emission from hot dust at temperatures ~ 1200 K. At any given redshift or equivalently, region of the rest-frame SED, we see a ~ 0.5 mag dispersion in the $W1 - W2$ colors. On the same axes in Figure 66 we have plotted the $W1 - W2$ colors derived from our SED model with blackbody temperatures ranging from 1000 - 1600 K and blackbody normalisation factors (i.e. the flux from the blackbody component relative to the power-law continuum at a reference wavelength) from 0 - 0.5, with the other parameters as reported in Table 12. A blackbody with a single temperature and normalisation is clearly not a very good representation of the hot dust properties of the whole sample. For example, dust which is further from the accretion disc will be at a lower temperature, and if the covering factor of the dust around the accretion disc is smaller then the ratio of near-IR luminosity to UV/optical luminosity (which the blackbody normalisation is proportional to) will decrease. We aim to study the diversity hot dust properties of the quasars in our sample to learn about the nature of

¹ We made use of the on-line tool Staralt. Available at: <http://catserver.ing.iac.es/staralt/index.php>.

² We made use of the LIRIS exposure time calculator. Available at: http://www.iac.es/proyecto/LIRIS/simulator/form_LIRIS_spect.html.

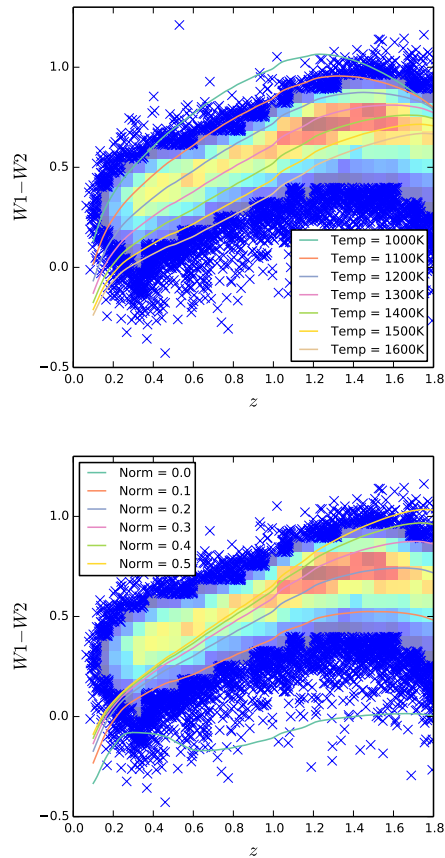


Figure 61: $W1 - W2$ colours of DR7 sample as a function of redshift, up to $z = 1.8$. Above a certain density threshold points are represented by a density plot. On top we plot our standard model, with a blackbody temperature varying from 1000 - 1600 K (*top figure*) and a blackbody normalisation between 0 and 0.5 (*bottom figure*).

the hot dust, and to link the hot dust properties to other physical quantities such as the luminosity and redshift of the quasar.

6.10.1 Defining Sample

We decided to explore the diversity of hot dust properties by fitting our standard model, with the blackbody temperature and normalisation as free parameters, to the individual quasar SEDs. The first step was to define a sample of quasars from the DR7Q-matched catalogue which were well fit by our standard un-reddened SED model. To achieve this we discarded from our sample quasars with $i - K$ colors redder than our standard model with dust reddening $E(B-V) = 0.1$ (see Figure 56). As we discussed in Section 6.9, this region of the $i - K$ colour space includes both quasars with significant amounts of dust reddening and quasars with extreme emission line equivalent widths. We exclude quasars with observed magnitudes fainter than 19.1 in the i band-pass, as well as quasars with upper-limit or $S/R < 5$ magnitudes in the K , $W1$ and $W2$ band-passes (without these we will be unable to properly constrain the blackbody slope). We exclude quasars flagged as BALQSOs from the sample, since these objects may be in a special evolutionary stage and have different hot dust properties (we will consider this in future work). Finally, from all of the objects which passed the above criteria, we discarded the 10% of quasars which were least well fit by our standard model.

It is important to consider the redshift range over which we can reasonably expect to be able to constrain the shape of the blackbody component. The amount by which the observed spectrum is redshifted determines the position of the hot dust feature in the spectrum relative to the wavelength coverage of our set of band-passes. For a redshift $z \sim 1.5$ quasar, only the $W2$ band-pass, at $\sim 2\mu\text{m}$ in the rest frame of the quasar, is probing the wavelength region dominated by the blackbody emission (the peak in a $T \sim 1200\text{K}$ blackbody is at $\sim 2.4\mu\text{m}$). At $z \gtrsim 1.5$, we found that we could no longer constrain the shape of the blackbody component in our SED model using the $ugrizYJHKW1W2$ band-passes. Although we could include magnitude constraints from the longer-wavelength WISE $W3$ band-pass ($\lambda_{\text{eff}} \simeq 12\mu\text{m}$), at $z \sim 1.5$ this is observing $\sim 5\mu\text{m}$ in the quasar's rest frame. In this region there will be extra contributions to the flux, possibly from cooler dust, which are not accounted for in our model. This was clearly demonstrated by the increase in the $m_{\text{model}} - m_{\text{data}}$ residuals beyond $\sim 3\mu\text{m}$ in the rest frame. At lower redshifts, the $W3$ band-pass is probing even longer-wavelengths, where the component we are missing from our model will be greater. To compensate our SED model will move the blackbody component to lower temperatures, which shifts the peak to longer wavelengths. The result will be a downward trend in the blackbody temperature with decreasing redshift. Given that one

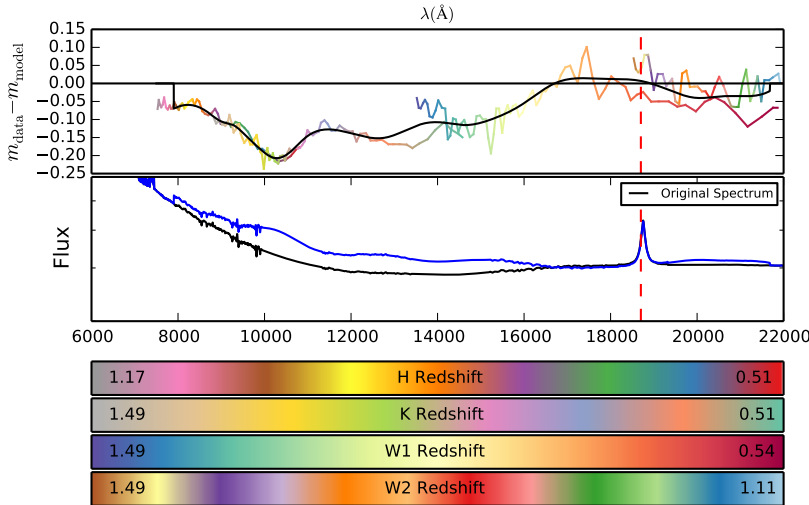


Figure 62: *Top:* Residuals from fitting the overall normalisation of the SED as a function of wavelength in the quasar rest frame. The different lines correspond to 101-point running medians for the H, K, W1 and W2 band-passes, and have been colour-coded to indicate the redshift for which the given quasar rest frame wavelength corresponds to the un-redshifted effective wavelength of the band-pass. The black line is a cubic interpolation of a 801-point running-median through all residuals, irrespective of the band-pass used. The red dashed line marks the wavelength of the $\text{Pa}\alpha$ emission line. *Bottom:* The spectral model before and after the flux correction (see main text).

question we are interested in addressing is variations in the hot dust properties with redshift, we have to be very wary of systematic effects such as these. With these considerations in mind, we restricted ourselves to determining the hot dust properties of our quasar sample in the redshift range $0.5 < z < 1.5$.

6.10.2 Flux Correction

In Figure 55 we saw how the model appeared to be underestimating the observed flux in the region around $1\mu\text{m}$ in the quasar rest frame spectrum. Since we are aiming to carefully constrain the shape of the blackbody component just long-ward of this wavelength region, we need to be very careful in how we deal with this discrepancy. A blackbody component with a higher temperature would contribute more flux in this region, which could potentially lead to redshift-dependent systematic errors very similar to those we have just described above. To avoid this we derived a correction to our model which accounted for the $1\mu\text{m}$ flux discrepancy.

We fit the overall normalisation of the model SED only; this is a constant vertical displacement we add to the model magnitudes. This fit is done in the 2000 - 9000 Å region of the rest frame spectrum using our sample of ‘standard’ quasars. We calculate the $m_{\text{data}} - m_{\text{model}}$ residuals for each quasar, and calculate the effective wavelength of each band-pass in the rest frame of the quasar. In Figure 62 we show a 101-point running median through the residuals of each band-pass in the 6000 - 22000 Å region of the quasar rest frame. The lines have been colour-coded to show the redshifts of the quasars which are contributing to the residuals in the corresponding region of the quasar rest frame. The black line in the Figure 62 is a cubic interpolation of a 801-point running-median through all residuals as a function of the quasar rest frame wavelength, irrespective of the band-pass used. It shows quite clearly that the model is underestimating the observed flux over the $\sim 8,000 - 17,000 \text{ \AA}$ rest frame wavelength region. We calculated the multiplicative factor which when applied to the model spectrum accounted for the model to data magnitude discrepancy, i.e. the amount of flux ‘missing’ from the model. In the bottom panel of Figure 62 we show our model spectrum both with and without this correction term. In Figure 54 we show how the fit is improved in the $\sim 1 \mu\text{m}$ region of the rest frame spectrum.

6.11 RESULTS FROM BLACKBODY FIT

We fixed the overall normalisation of the quasar SEDs to values from the 2000 - 9000 Å fit, and fit for the temperature and normalisation of the blackbody component in the 10,000 - 23,000 Å region of the rest frame spectrum (i.e. the spectral region most sensitive to hot dust emission). In Figure 63 we show the best-fitting blackbody temperature for the quasars in our sample as a function of redshift. The solid lines are running-medians through the points, calculated both before and after we applied the correction to the model described in the preceding section. The difference is stark; after we apply the flux correction the median best-fitting blackbody temperature drops by $\sim 200\text{K}$ to $\sim 1200\text{K}$. This is encouraging, since 1200K is the best-fitting blackbody temperature from the fit to the whole DR7Q-matched sample. Although we see no significant evolution of the hot dust properties in this redshift range, we plan to test this at higher redshift. We will also compare the hot dust properties of interesting subpopulations (e.g. Type II quasars, BALQSOs) and look for correlations with physical parameters of the quasar (e.g. luminosity, Eddington ratio).

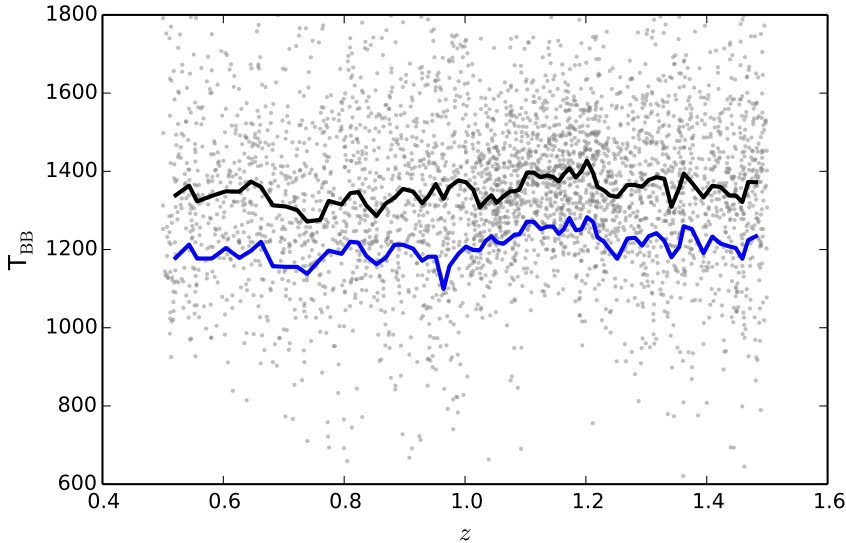


Figure 63: Blackbody temperature from fit against redshift before correction (grey circles). Black line is running median through blackbody temperatures before correction, blue line is running median after correction.

6.12 CONCLUSIONS AND FUTURE WORK

While many authors have focused on studies of specific sub-sets of AGN with extreme observational properties, what is missing is an understanding of how these extreme subsets relate to the population as a whole. In particular, we will focus on merger-based scenarios for quasar/galaxy co-evolution, which predict an obscured growth phase before the enshrouding dust is blown out, and schemes which explain the variety of observational properties as being only apparent differences due to non-spherical source geometries. We will study this issue by combining large-area photometric surveys from SDSS, UKIDSS and WISE. Multi-wavelength surveys allow us to gain a more holistic view of quasar properties by sampling their entire SED. We have developed a model to fit the quasar SED in the $1 - 3 \mu\text{m}$ spectral region which, at present, can constrain the following features:

- **Power-law slope**, which relates to properties of the accretion disk.
- **Blackbody temperature and normalisation**, which relates to properties of circum-nuclear hot dust.
- **Dust Reddening**, at redshift of quasar, which relates to dust properties of the quasar and its host galaxy.
- **Emission line strength**, which relates to properties of emission line regions and absorbing dust.

The SDSS DR10Q catalogue, which was made available in late 2013, contains $\sim 120,000$ quasars at $z \gtrsim 2$ (~ 5 times the number previously known). This will allow us to study quasar properties at the epoch when quasar activity peaked. Crucially, moderate-resolution optical spectra are available for all sources in the SDSS catalogue, which will allow us to relate SED properties to, for example, the black-hole mass and properties of outflowing gas. There is also the possibility, at least for a sub-set of objects, of extending our multi-wavelength SED coverage using data from, for example, FIRST in the radio and Spitzer in the far-IR.

6.12.0.1 *Specific Investigations*

6.12.0.2 *Hot Dust Properties*

The near-IR excess in the SED is believed by many to be emission from dust at its sublimation temperature at the inner edge of a torus structure. We are able to test this by linking properties of the hot dust (e.g. the luminosity) to other properties of the quasar (e.g. bolometric luminosity, redshift). For example, is there any evidence for the inner edge of the torus being further from the nucleus in more luminous quasars (i.e. a decrease in near-IR to optical/UV luminosity ratio with increasing optical/UV luminosity)? Are there quasars in our sample which are deficient in hot dust and, if so, are these objects being observed before a dusty torus has formed or are the torus and accretion disk misaligned?

6.12.0.3 *E(B-V) Distribution*

Deriving the dust-reddening E(B-V) distribution of our optically selected sample will allow us to relate the small samples of extremely reddened objects which have been found to the population of mildly reddened quasars. Are these extreme objects in the tail of a population of mildly reddened quasars or are there equal distributions of mildly reddened and extremely reddened quasars? A similar analysis was done by Richards et al., (2003), but with the DR10Q catalogue we are able to pick up far more objects during the peak epoch when both quasar activity and star-formation rates peaked ($2 \lesssim z \lesssim 4$). Obtaining near-IR spectra for a sample of moderately reddened quasars will give us crucial information about the level and scale of the dust extinction. We will also use our sample to derive a new extinction curve appropriate for the quasar population.

6.12.0.4 *BALQSOs*

Broad, blue-shifted absorption lines are associated with AGN-driven out-flowing gas, and outflows are a key component in galaxy evolution models with AGN feedback. With an adapted model, we will de-

rive information from the SED (e.g. the dust-reddening) which, when combined with outflow properties measured in the SDSS spectra, will allow us to study the population of BALQSOs in relation to the population as a whole. Are BALQSOs observed during a special ‘blow-out’ phase in a quasars lifetime, or is outflowing gas only detected along certain sight-lines?

6.12.0.5 *Type II Quasars*

How are the population of obscured Type II quasars related to the Type I population? Does the Seyfert Type I/II dusty-torus unification scheme extend to higher luminosities or are Type II quasars observed in a special phase of quasar growth? Again, properties derived from the multi-wavelength SEDs and optical spectra will help to relate these objects to the population as a whole.

6.13 DRAFT PAPER

6.14 INTRODUCTION

Understanding the link between supermassive black-hole growth and the properties of Active Galactic Nuclei (AGN) host galaxies is one of the most important areas of galaxy-formation research. It is now well established that non-spherical geometries including some form of obscuring material on parsec scales (possibly in the form of a torus), can explain much of the observed diversity seen in the spectral energy distributions (SEDs) of AGN. At the same time, AGN-driven outflows are present in a large fraction of the luminous quasar population. The mass and energy associated with these outflows is believed to be significant in the context of feedback and its effect on the host galaxy. Punctuated fuelling episodes, e.g. driven by galaxy mergers, satellite accretion and even secular processes, almost certainly lead to AGN experiencing activity-, outflow- and obscuration-dominated cycles with some overlap between phases. Quantitatively, however, it remains unclear how these phases relate to the fundamental properties of the accreting black-hole (e.g. mass (M_{BH})), bolometric luminosity (L_{bol}) and Eddington ratio (L/L_{Edd}) and the elements of the non-spherical geometry).

With large-scale surveys from SDSS, UKIDSS, and *WISE* providing information on the SEDs covering rest-frame 0.1-3.0 μm wavelengths for thousands of AGN at redshifts $2 \lesssim z \lesssim 3$ it is finally possible to study the link between outflow diagnostics from ultra-violet spectra, e.g. as measured from the C IV emission line, and emission from hot ($T \simeq 1200\text{K}$) dust peaking in the NIR, which provides information about the amount and geometry of gas and dust on parsec scales. In one model, quasars are surrounded by an inner ‘wall’ of gas and dust, in a cylinder-like geometry. As a radiatively-driven outflow develops,

material at the extremes of the cylinder is driven-off, exposing more of the inner edge of the obscuring material at the equator (a ‘torus’), which contains the hot dust. Quasars are also observed with a wide distribution of reddening from dust on galactic scales. It is believed that luminous highly dust-reddened quasars may be in the process of expelling their dust and transitioning to ultra-violet bright objects which make up to the majority of the SDSS sample.

6.15 DATA

The systematic study of the dependence of the SED shape on physical parameters has, until very recently, been limited by the difficulty in obtaining a large sample of quasars with good multi-wavelength coverage and large dynamic range in luminosity and redshift. In this work, we take advantage of a number of recent, sensitive, wide-field surveys, covering the UV to mid-IR spectral region.

We use the spectroscopic quasar catalogues of the Sloan Digital Sky Survey (SDSS; York et al., 2000) Seventh Data Release (DR7Q; Schneider et al., 2010) and Tenth Data Release (DR10Q; Pâris et al., 2014). DR7Q and DR10Q include 105,783 objects across 9380 deg^2 , and 166,583 objects across $6,370 \text{ deg}^2$, respectively, with 16,420 objects in common to both catalogues. The SDSS obtained images in five broad optical passbands: u ($\lambda_{\text{eff}} = 3543\text{\AA}$), g ($\lambda_{\text{eff}} = 4770\text{\AA}$), r ($\lambda_{\text{eff}} = 6231\text{\AA}$), i ($\lambda_{\text{eff}} = 7625\text{\AA}$), and z ($\lambda_{\text{eff}} = 9134\text{\AA}$). The SDSS spectra cover $\sim 3000 - 9000\text{\AA}$ at a spectral resolution of ~ 2000 . We use BEST point-spread function (PSF) magnitudes from the DR7Q catalogue, correcting for Galactic extinction using the maps of Schlegel, Finkbeiner, and Davis, (1998), assuming a Milky Way (MW) extinction curve (Pei, 1992) and an extinction to reddening ratio $A(V)/E(B-V) = 3.1$. We use the PSF magnitudes from the DR10Q catalogue, correcting for Galactic extinction using the maps of Schlafly and Finkbeiner, (2011). Although the SDSS asinh magnitude system is intended to be on the AB system (Oke and Gunn, 1983), the photometric zero-points are known to be slightly off the AB standard. To account for this we add 0.03 mag to the u , g , r and i magnitudes, and 0.05 mag to the z magnitude.

We use the UKIRT Infrared Deep Sky Survey (UKIDSS; Lawrence et al., 2007) Large Area Survey (ULAS) which has observed $\sim 3,200 \text{ deg}^2$ in four near-IR passbands: Y ($\lambda_{\text{eff}} = 1.0305\mu\text{m}$), J ($\lambda_{\text{eff}} = 1.2483\mu\text{m}$), H ($\lambda_{\text{eff}} = 1.6313\mu\text{m}$), and K ($\lambda_{\text{eff}} = 2.2010\mu\text{m}$)). We used the ninth data release (DR9) of the ULAS. Cross-matching (with a $2''$ radius and picking only the nearest neighbour) the SDSS DR7Q catalogue with the ULAS catalogue, which covers only $\sim 38\%$ of the SDSS foot-print, resulted in 37,893 matches. The ULAS magnitudes are aperture corrected magnitudes in a $2''$ diameter aperture and are not corrected for Galactic extinction. UKIDSS fluxes and their associated errors are

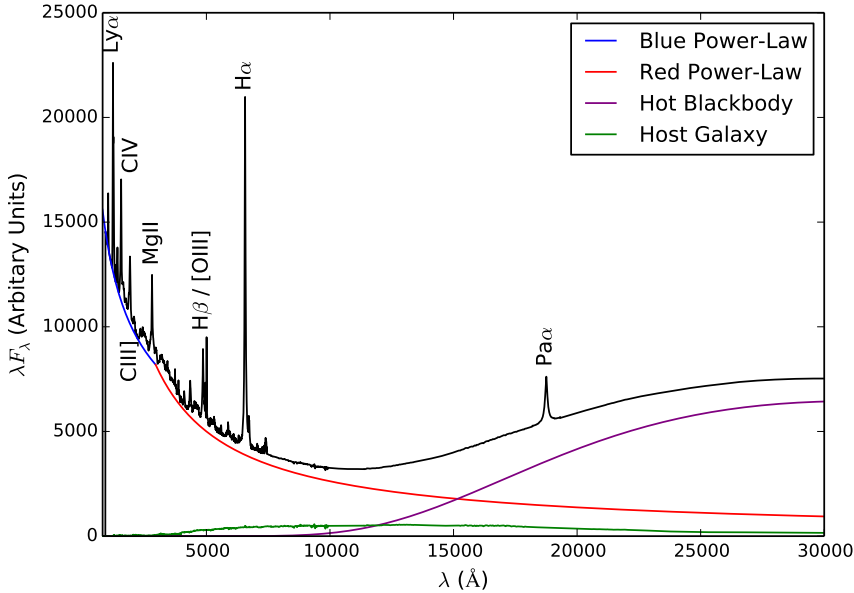


Figure 64: Model spectrum at $z = 1$, showing the contributions to the total flux from the blue power-law slope, red power-law slope, blackbody and host galaxy. The locations of the most prominent emission lines in the spectrum are also indicated.

included in the DR10Q catalogue. These were converted to Vega magnitudes using flux zero points 2026, 1530, 1019, and 631×10^{-26} W m $^{-2}$ Hz $^{-1}$ for the Y, J, H, and K passbands respectively. Vega magnitudes were then converted to the AB system using the conversions given by Hewett et al., (2006). Mention correction?

The Wide-field Infrared Explorer (WISE; Wright et al., 2010) mapped almost the sky in four mid-IR band-passes: W1 ($\lambda_{\text{eff}} = 3.4\mu\text{m}$), W2 ($\lambda_{\text{eff}} = 4.6\mu\text{m}$), W3 ($\lambda_{\text{eff}} = 12\mu\text{m}$), and W4 ($\lambda_{\text{eff}} = 22\mu\text{m}$). The WISE AllWISE Data Release ('AllWISE') combines data from the nine month cryogenic phase of the mission that led to the 'AllSky' data release with data from the NEOWISE program (Mainzer et al., 2011). Cross-referencing the SDSS DR7Q catalogue with the AllWISE catalogue resulted in 102,734 matches. Cross-referencing the SDSS DR10Q catalogue with the AllWISE catalogue produced 116,666 matches.

6.16 UV SPECTRA PARAMETERS

6.17 MODEL DESCRIPTION

Our model aims to reproduce the SEDs of AGNs from the rest-frame UV ($\sim 0.1\mu\text{m}$) to the rest-frame near-IR ($\sim 3\mu\text{m}$). The model spectrum is shown in Figure 64, with each of the main components indicated. We characterise the Big Blue Bump from $\sim 0.1 - 1\mu\text{m}$ as a broken power-law with three free parameters: a break-wavelength $\lambda_{\text{break}} =$

2822Å, a blue power-law index $\alpha_{\text{blue}} = 0.46$ for wavelengths shorter than the break wavelength, and a red power-law index $\alpha_{\text{red}} = 0.03$ for wavelengths longer than the break wavelength. At wavelengths longer than 1μm, emission from hot ($T \simeq 1200\text{K}$) dust begins to dominate over emission from the accretion disc. We modelled the hot dust emission using a simple blackbody:

$$F_\lambda = \frac{2hc^2}{\lambda^5} \frac{1}{e^{\frac{hc}{\lambda k_B T}} - 1} \quad (37)$$

Hundreds of emission lines are present in a typical AGN spectra. Some of the most prominent lines are shown in Figure 64. The emission line spectrum is taken from Maddox and Hewett, (2006), who extend the composite of Francis et al., (1991) to include the Hα (6560Å) and Paα (18750Å) emission lines. A single parameter, EL_{scale}, scales the equivalent widths of all emission lines equally:

$$F_\lambda = \text{EL}_{\text{scale}} \times \frac{F_{\lambda, \text{el}}}{F_{\lambda, \text{cont}}} \times F_\lambda \quad (38)$$

where $F_{\lambda, \text{el}}$ is the line flux in the template, $F_{\lambda, \text{cont}}$ is the continuum flux in the template, and F_λ is the continuum flux in the model.

Emission from the host galaxy is important, particularly in the region around the 1μm inflection point in the quasar SED. While the host galaxies of bright quasars tend to be massive, bright ellipticals, the hosts of lower luminosity AGN can have disc components (e.g. Dunlop et al., 2003). Our model incorporates $z = 0$ Sa, Sb, Sc and elliptical-type templates from Mannucci et al., (2001), which for simplicity do not evolve with redshift. We characterise the relationship between the luminosity of the AGN L_{AGN} and the luminosity of the host galaxy L_{Gal} as a power-law $L_{\text{Gal}} = L_{\text{AGN}}^\beta$ with power-law index $\beta = 0.42$ (Maddox and Hewett, 2006).

To simulate the effect of dust extinction at the redshift of the quasar we used an extinction curve appropriate for the quasar population. To derive the quasar extinction curve, UKIDSS photometry was used to provide an E(B-V) estimate, via the magnitude displacement of each quasar from the locus of unreddened objects. At redshifts $2 < z < 3$ the reddening measure is made at rest-frame wavelengths 3500–7000Å, where Galaxy, LMC and SMC extinction curves are very similar. The SDSS spectra of the same objects are then employed to generate an empirical extinction curve in the ultraviolet, down to 1200Å. The resulting curve has no 2200Å feature and rises rapidly with decreasing wavelength but is not as steep as the SMC curve.

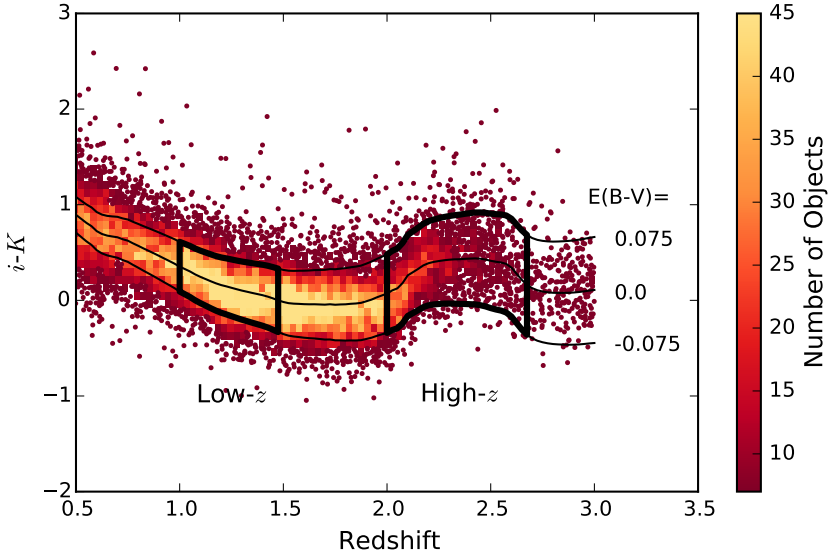


Figure 65: $i - K$ vs z . Demonstrates how sample was defined. The grey points show, as a function of redshift, the $i - K$ colours of all DR7Q quasars which are not classified as broad-absorption line quasars by Shen et al. and i magnitude > 19.1 . The black line shows the $i - K$ colour of our standard, unreddened SED model as a function of redshift. The red and blue lines show the $i - K$ colours of our SED model with dust reddening $E(B-V) = 0.075$ and $E(B-V) = -0.075$ respectively. A significant amount of this reddening can be attributed to intrinsic variations in the UV power-law slopes of the individual quasars, which is why we allow a negative reddening. However, there is a clear ‘red tail’ to the colour distribution which can be explained by dust reddening at the redshift of the quasar. We defined two samples, at low ($0.5 < z < 1.5$) and high ($2 < z < 2.7$) redshift, which are shown in the figure.

6.17.1 Sample

We selected quasars from the SDSS DR7 catalogue. We included only quasars targeted by the main quasar selection algorithm (i.e. $i < 19.1$), and quasars classified by ?? as lacking broad (width $<$ something) absorption troughs. Furthermore, we excluded quasars with $S/N < 5.0$ in the K , $W1$, and $W2$ passbands. After fits, excluded 10% of outliers.

6.18 RESULTS

6.19 HOT DUST

In Figure 66 we plot the $W1 - W2$ colors of the DR7Q-matched sample as a function of redshift from $z = 0.2$ to $z = 1.8$. In this redshift range the $W1$ and $W2$ band-passes are probing the $12,000 - 28,000 \text{ \AA}$ and $16,000 - 38,000 \text{ \AA}$ region of the rest frame SED respectively,

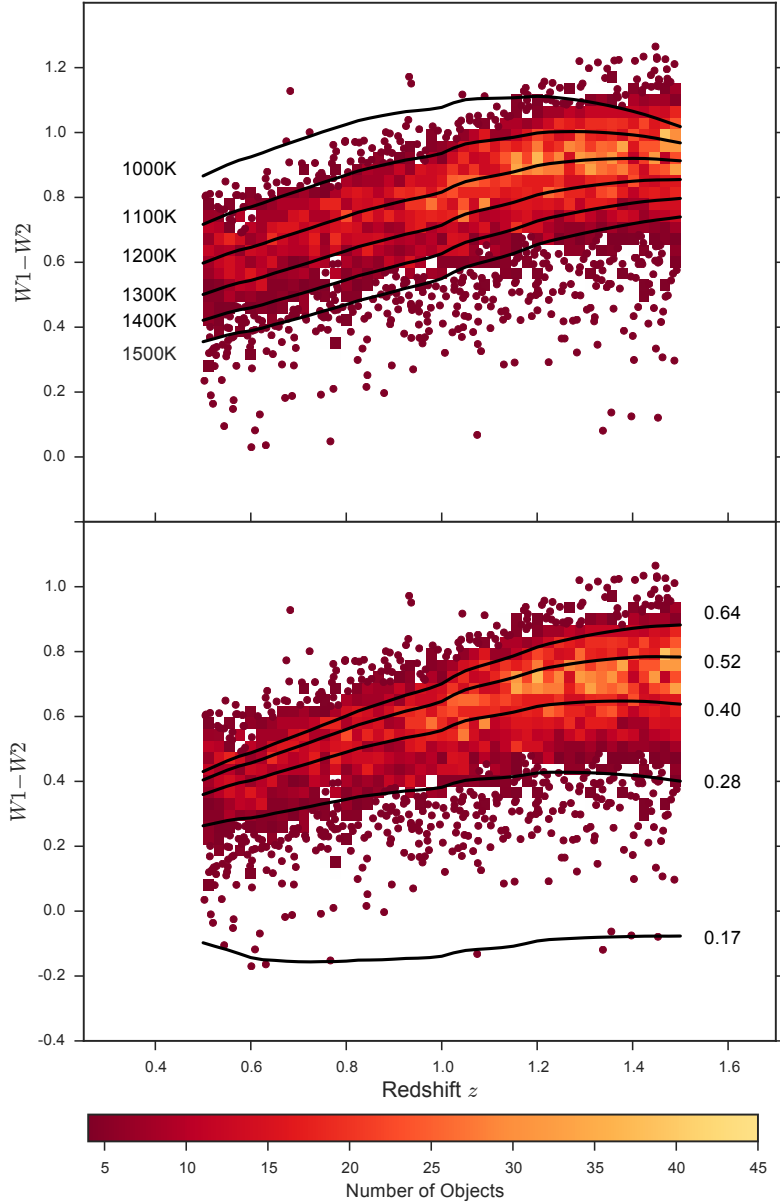


Figure 66: $W1 - W2$ colours of DR7 sample as a function of redshift, up to $z = 1.8$. Above a certain density threshold points are represented by a density plot. On top we plot our standard model, with a blackbody temperature varying from 1000 - 1600 K (*top figure*) and a blackbody normalisation between 0 and 0.5 (*bottom figure*). Around $z = 1.5$ the model no longer appears to be a very good fit to the data, which I suppose is just the fact that the blackbody is turning over, whereas in the data the flux keeps increasing (additional contributions from cooler components.) Add ticks to top of top panel. Think about how useful these plots really are. In top plot I'm changing the temperature, which is changing the normalisation (Lum IR). This is effectively same as bottom plot, except here I'm keeping the shape the same, just moving it up and down. Even if this is fine these plots are probably a bit misleading as they are (need to be clear normalisation will also be changing in the top plot.)

and the $W1 - W2$ color is therefore predominantly tracing emission from hot dust at temperatures ~ 1200 K. At any given redshift or, equivalently, region of the rest-frame SED, we see a ~ 0.5 mag dispersion in the $W1 - W2$ colors. On the same axes in Figure 66 we have plotted the $W1 - W2$ colors derived from our SED model with blackbody temperatures ranging from 1000 - 1600 K and blackbody normalisation factors (i.e. the flux from the blackbody component relative to the power-law continuum at a reference wavelength) from 0 - 0.5, with the other parameters as reported in Table 12. A blackbody with a single temperature and normalisation is clearly not a very good representation of the hot dust properties of the whole sample. We aim to study the diversity hot dust properties of the quasars in our sample to learn about the nature of the hot dust, and to link the hot dust properties to other physical quantities such as the luminosity and redshift of the quasar.

We decided to explore the diversity of hot dust properties by fitting our standard model, with the blackbody temperature and normalisation as free parameters, to the individual quasar SEDs.

The first step was to define a sample of quasars from the DR7Q-matched catalogue which were well fit by our standard un-reddened SED model. To achieve this we discarded from our sample quasars with $i - K$ colors redder than our standard model with dust reddening $E(B-V) = 0.1$. This region of the $i - K$ colour space includes both quasars with significant amounts of dust reddening and quasars with extreme emission line equivalent widths. We exclude quasars with observed magnitudes fainter than 19.1 in the i band-pass, as well as quasars with upper-limit or $S/N < 5$ magnitudes in the K , $W1$ and $W2$ band-passes (without these we will be unable to properly constrain the blackbody slope). We exclude quasars flagged as broad-absorption line quasars (BALQSOs; Weymann et al., 1991) from the sample, since these objects may be in a special evolutionary stage and have different hot dust properties. Finally, from all of the objects which passed the above criteria, we discarded the 10% of quasars which were least well fit by our standard model.

It is important to consider the redshift range over which we can reasonably expect to be able to constrain the shape of the blackbody component. The amount by which the observed spectrum is redshifted determines the position of the hot dust feature in the spectrum relative to the wavelength coverage of our set of band-passes. For a redshift $z \sim 1.5$ quasar, only the $W2$ band-pass, at $\sim 2\mu\text{m}$ in the rest frame of the quasar, is probing the wavelength region dominated by the blackbody emission (the peak in a $T \sim 1200$ K blackbody is at $\sim 2.4\mu\text{m}$). At $z \gtrsim 1.5$, we found that we could no longer constrain the shape of the blackbody component in our SED model using the $ugrizYJHKW1W2$ band-passes. Although we could include magnitude constraints from the longer-wavelength WISE $W3$ band-pass ($\lambda_{\text{eff}} \simeq 12\mu\text{m}$), at $z \sim 1.5$

this is observing $\sim 5\mu\text{m}$ in the quasar's rest frame. In this region there will be extra contributions to the flux, possibly from cooler dust, which are not accounted for in our model. This was clearly demonstrated by the increase in the $m_{\text{model}} - m_{\text{data}}$ residuals beyond $\sim 3\mu\text{m}$ in the rest frame. At lower redshifts, the W3 band-pass is probing even longer-wavelengths, where the component we are missing from our model will be greater. To compensate our SED model will move the blackbody component to lower temperatures, which shifts the peak to longer wavelengths. The result will be a downward trend in the blackbody temperature with decreasing redshift. Given that one question we are interested in addressing is variations in the hot dust properties with redshift, we have to be very wary of systematic effects such as these. With these considerations in mind, we restricted ourselves to determining the hot dust properties of our quasar sample in the redshift range $0.5 < z < 1.5$.

In Figure 55 we saw how the model appeared to be underestimating the observed flux in the region around $1\mu\text{m}$ in the quasar rest frame spectrum. Since we are aiming to carefully constrain the shape of the blackbody component just long-ward of this wavelength region, we need to be very careful in how we deal with this discrepancy. A blackbody component with a higher temperature would contribute more flux in this region, which could potentially lead to redshift-dependent systematic errors very similar to those we have just described above. To avoid this we derived a correction to our model which accounted for the $1\mu\text{m}$ flux discrepancy.

6.19.1 Low- z Results

6.20 RESULTS FROM BLACKBODY FIT

We fixed the overall normalisation of the quasar SEDs to values from the 2000 - 9000 Å fit, and fit for the temperature and normalisation of the blackbody component in the 10,000 - 24,000 Å region of the rest frame spectrum (i.e. the spectral region most sensitive to hot dust emission).

6.20.1 Results 1: β_{NIR} , T_{BB} , $R_{\text{UV/NIR}}$

Even with $T = 1600\text{K}$, contribution from blackbody to UV luminosity only $\simeq 1\%$.

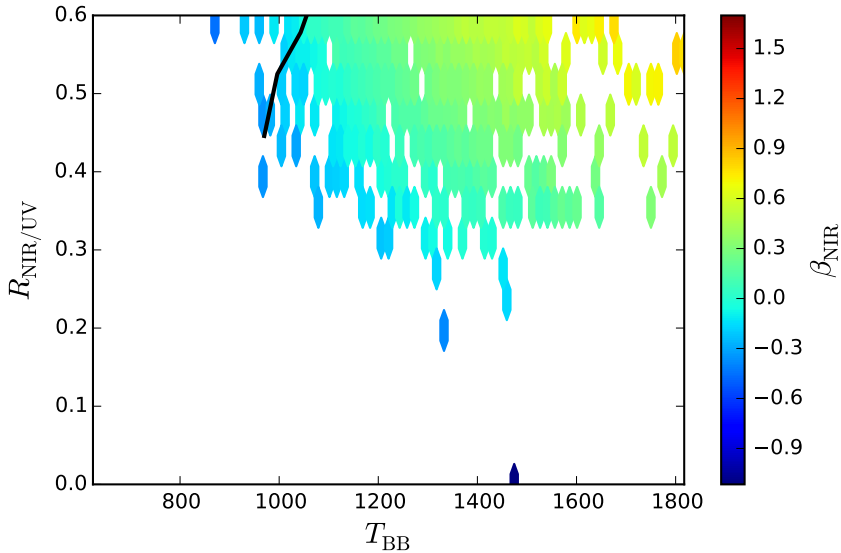


Figure 67

Figure 68: Need to somehow show the uncertainty in the parameters and demonstrate how the spread is real and not just due to the uncertainties in the photometry.

6.20.2 Results 2: Redshift

6.20.3 Results 3: Luminosity

No correlation between β (or $R_{\text{UV/NIR}}$) and L_{UV} (or any other measure of bolometric luminosity) but negative correlation with blackbody temperature.

6.20.4 Results 4: Eddington Ratio/ Black Hole Mass

6.20.5 C IV Emission Line Properties

6.20.6 Reddening

6.20.7 BALs

At low- z , don't have sufficient numbers for reliable BAL/non-BAL comparison. At high- z BALs appear to redder ($\beta = 0.54$) than non-BALs ($\beta = 0.43$).

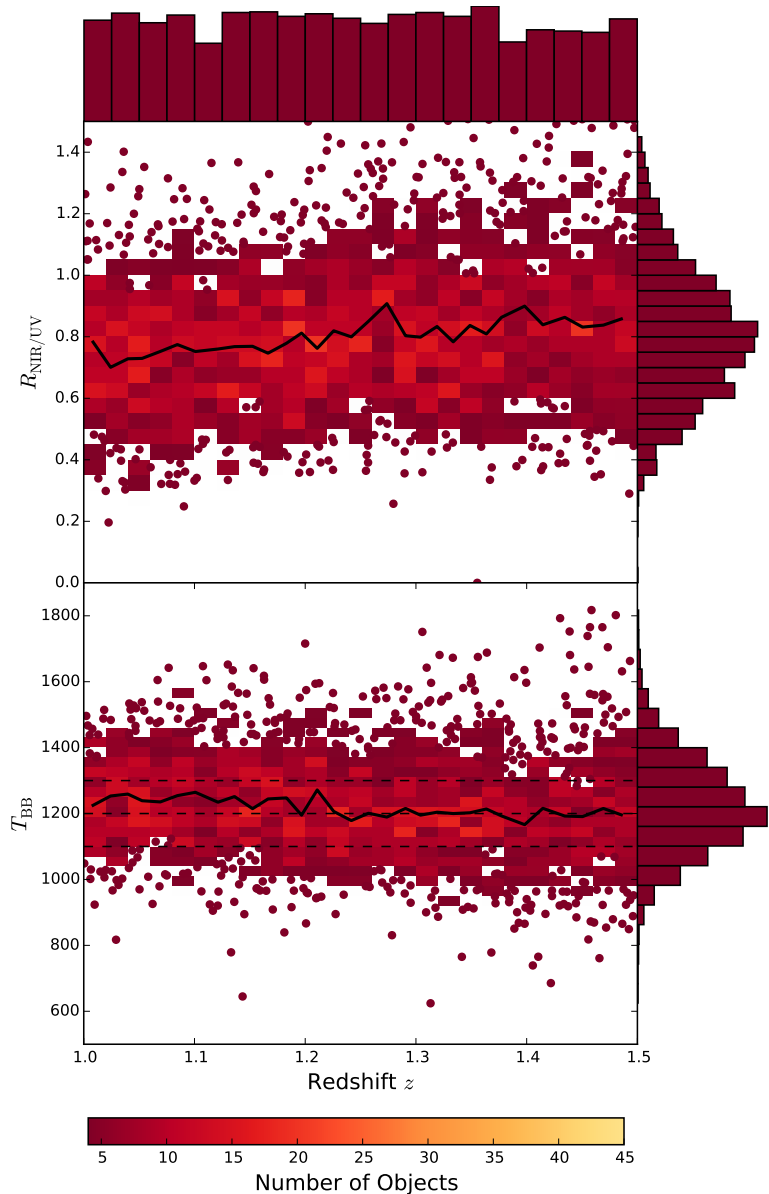


Figure 69

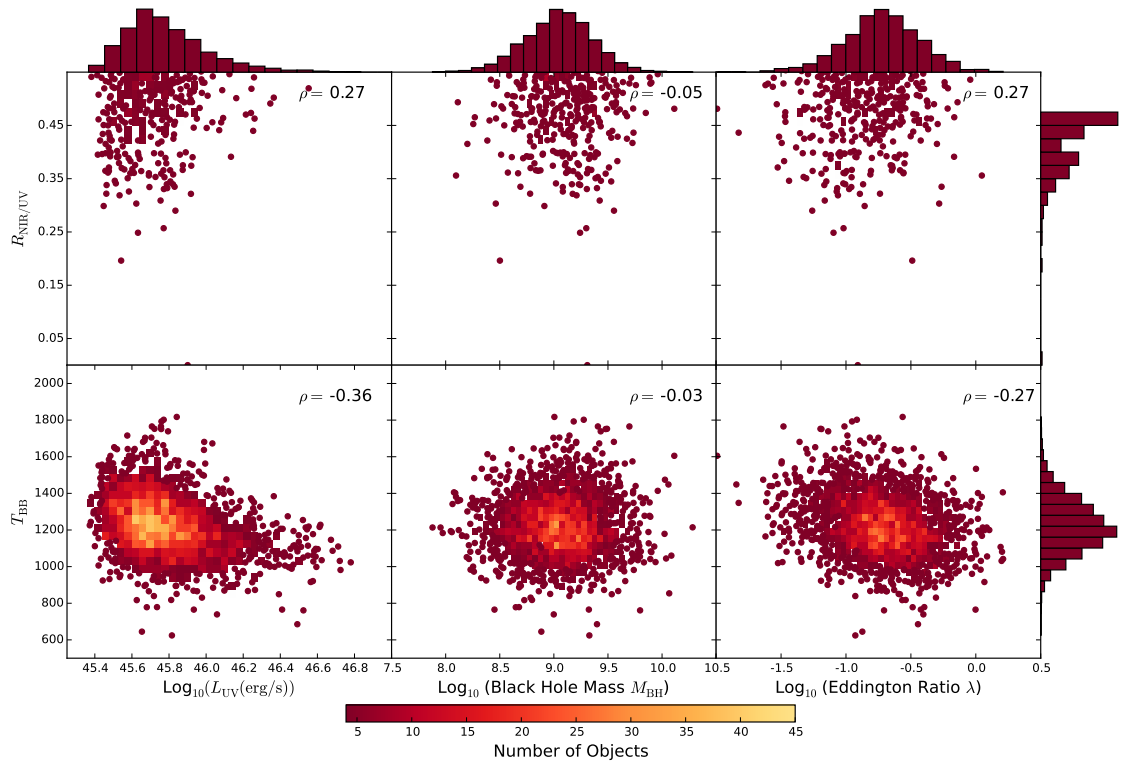


Figure 70: Colour-bar might not be accurate for each subfigure. CIV blueshift also positively correlated w/ Eddington Ratio.

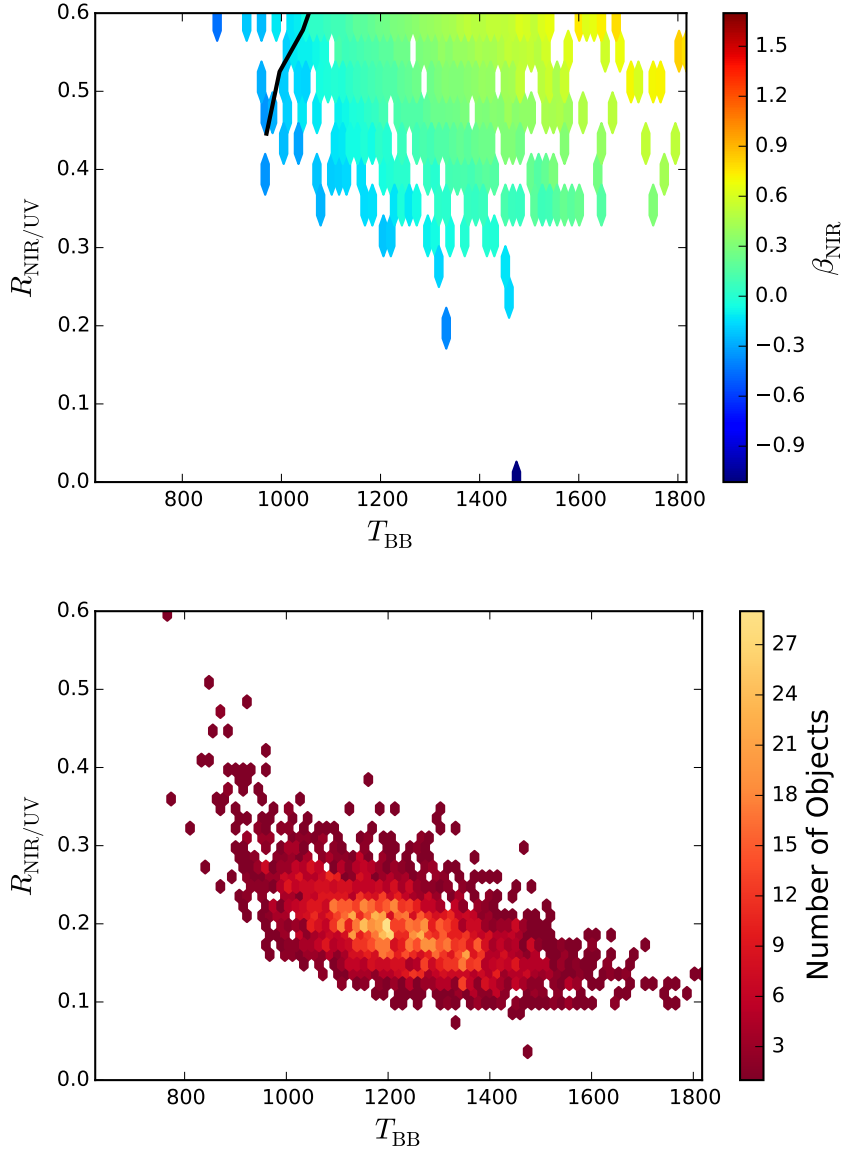


Figure 71: Plot of the near-IR/ultra violet luminosity ratio ($R_{\text{NIR/UV}}$) against the NIR power-law slope for the low- z sample. The NIR luminosity is measured by integrating the best-fit model spectrum (with a black body component) in the rest-frame of the quasar between 0.2 and 1 μm . The NIR power-law slope is fit between 1 and 2.4 μm (although the exact wavelength region being fit depends on the redshift of the quasar; see somewhere else). This allows us to extend our investigation to high- z , where we are unable to constrain both the temperature and normalisation of the black-body component, but can constrain the slope of a single power-law. Included the second plot because I want to emphasise that the density of points is not constant - i.e. if you measure a certain value for beta, say 0.6, it's much more likely to be around (1200,0.2) than it is, say, (1100,0.3). Must be some way of quantifying this.

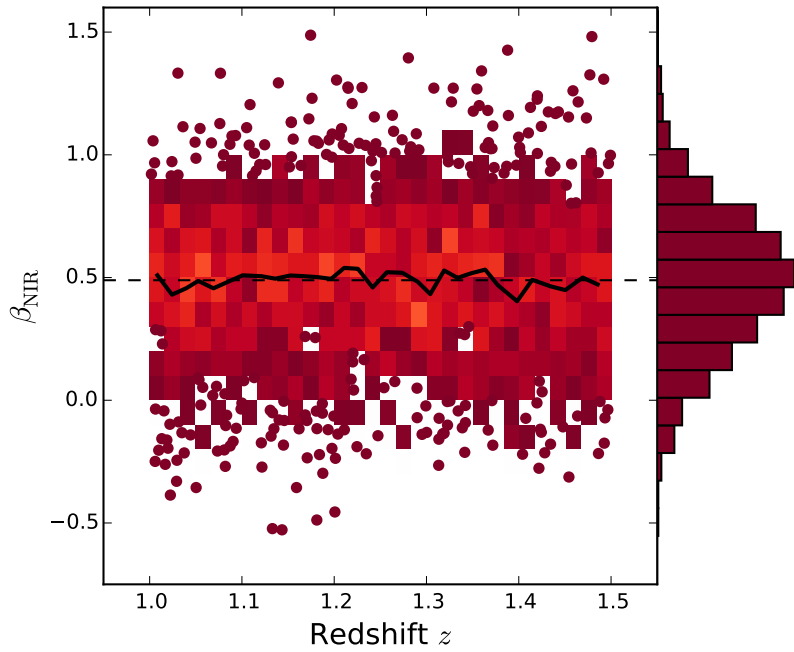


Figure 72: fgh

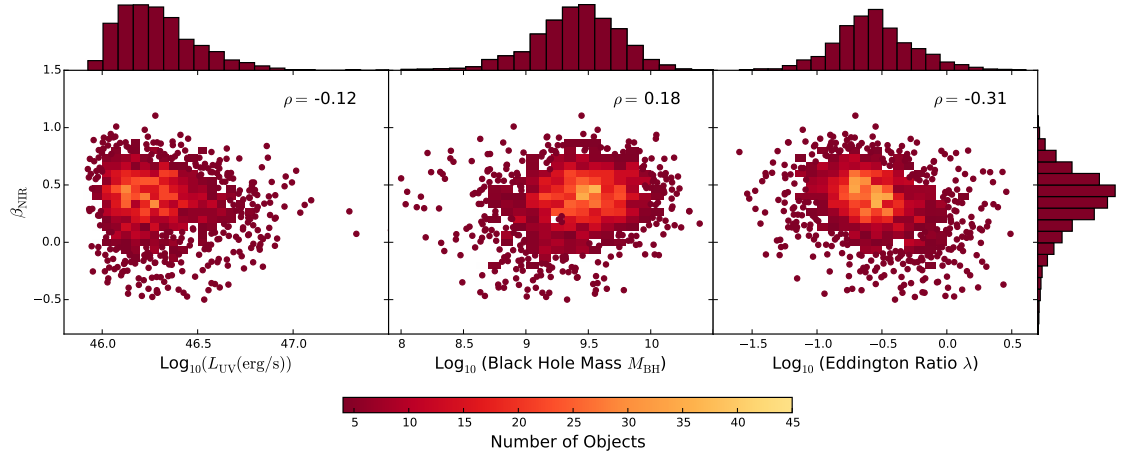


Figure 73: IR/UV luminosity ratio versus black hole mass (Shen et al.) for high-z sample. Fairly strong negative correlation. We believe that this is just a manifestation of the fact that at high redshift the blackhole masses are derived from CIV. We already know that the FWHM of CIV has a positive correlation with the hot dust abundance, and large CIV FWHM leads to larger black hole mass estimates. This explains the apparent correlation between the IR/UV ratio and the black hole mass. Eddington ratio measures the luminosity relative to the Eddington luminosity. Higher blackhole mass estimates will lead to lower Eddington ratios, which is why the Eddington ratio appears to decrease with increasing IR/UV ratio.

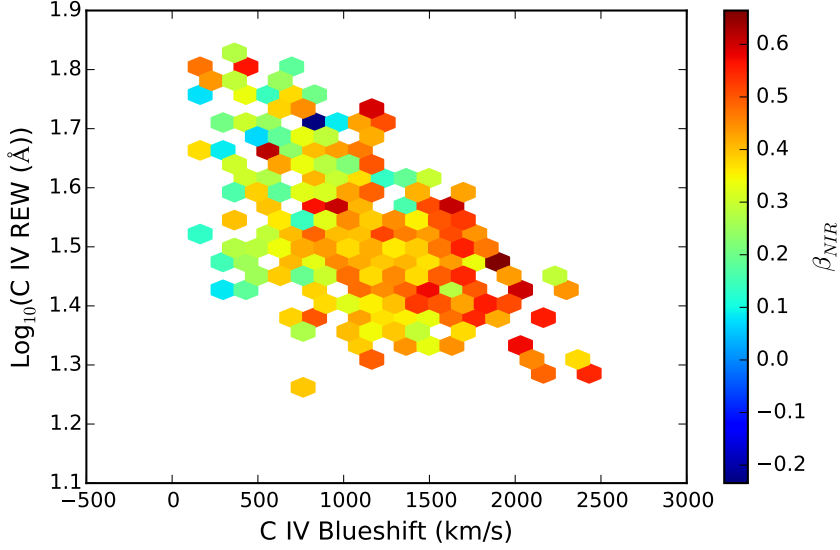


Figure 74: Now using same high-redshift sample as Figure 8 (with cut on beta uncertainty). I'm only plotting where I have a minimum of two objects per bin, which is probably not acceptable. Clear non-virial component to CIV line - caveat about CIV based black hole masses.

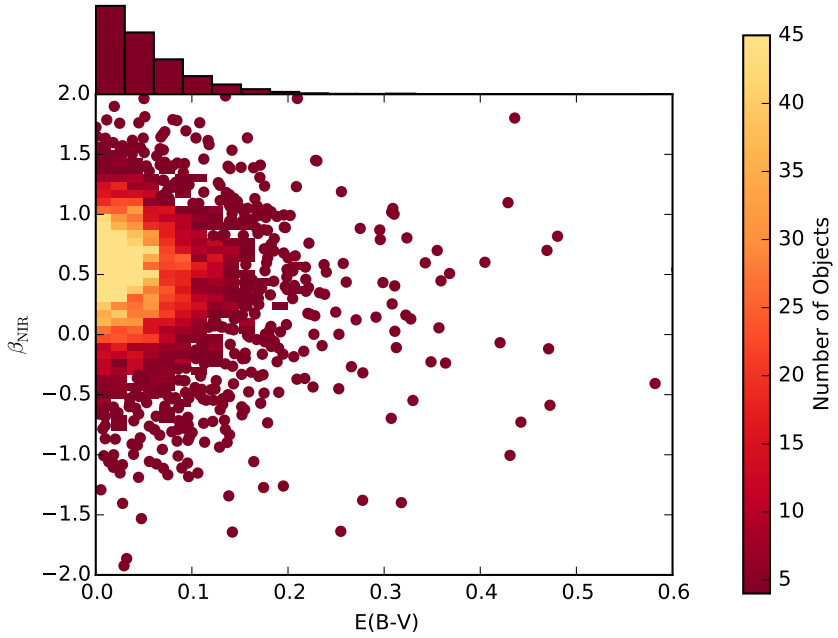


Figure 75: Plot E(B-V) versus β . Just fit $E(B-V) < 1$ micron and $z > 1$ to avoid galaxy contribution. No cuts made to sample. No correlation/weak negative.

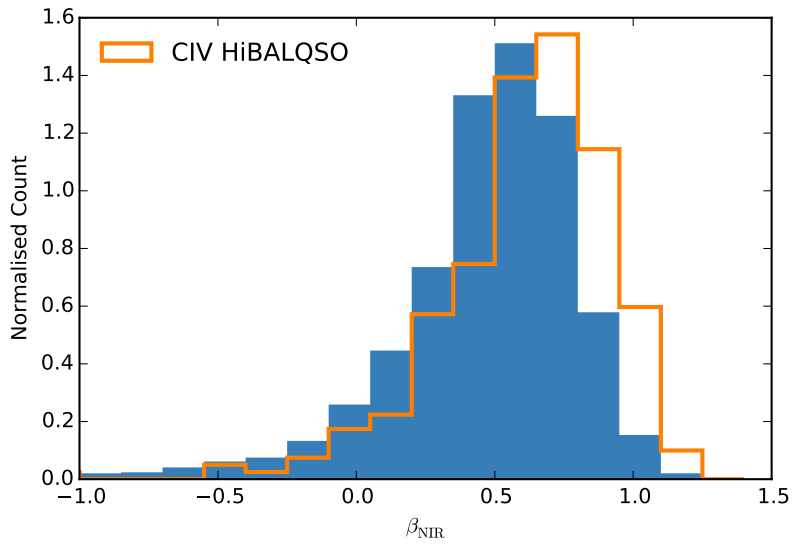


Figure 76: High-z only since very few BALs in low-z sample. β on x-axis. BALs clearly have bigger NIR slopes, so I would expect to also see β increase with E(B-V), which I don't.

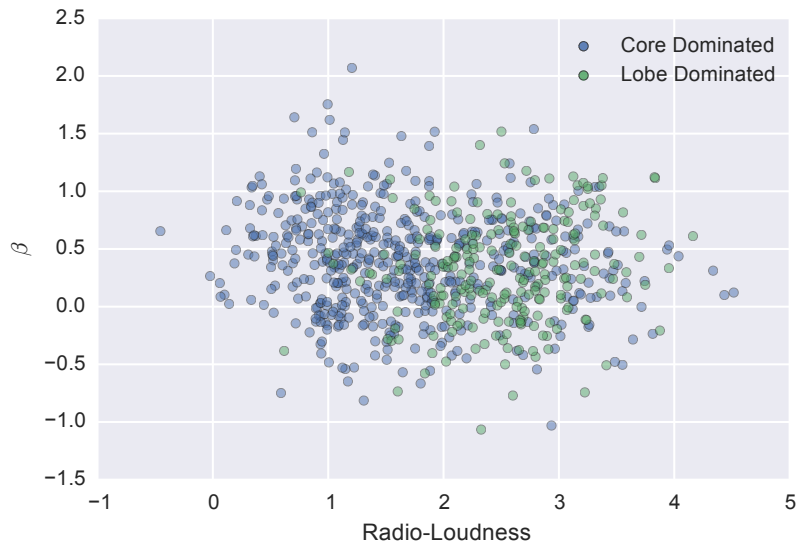


Figure 77: Weak negative correlation for core-dominated sources and weak positive correlation for lobe-dominated sources.

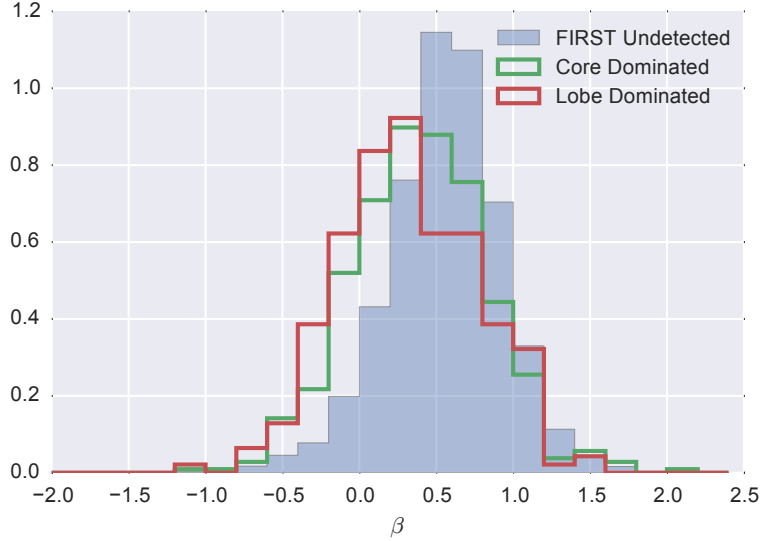


Figure 78: Radio-loud objects appear to have less hot dust on average. Statistically at least, the "radio-loud" objects are thought to have high black-hole masses and there is some form of radio-mode feedback (jet related) which is very different from the much more common (almost certainly wider opening-angle) outflow objects with large CIV-blueshifts.

6.20.8 RL/RQ

6.21 WHT TELESCOPE PROPOSAL

We propose to obtain near infrared spectroscopy for a well-defined sample of luminous quasars at $z \sim 2 - 3$ from the Sloan Digital Sky Survey. We have shown that blue asymmetries in the CIV $\lambda 1550$ emission line, indicative of parsec-scale outflows, correlate with the amount of hot-dust emission in luminous quasars. By measuring the [OIII] line profiles associated with more extended gas in this sample, we will determine if the outflows are accelerated out to kiloparsec scales. Measurements of H α and H β will also provide improved black-hole mass, Eddington ratio and reddening estimates. Comparing the H α line profiles to existing observations of our sample of extremely red quasars, we will determine if outflow signatures seen in the line profiles of such extreme objects, are ubiquitous in luminous AGN at these redshifts.

Background: Understanding the link between supermassive black-hole growth and the properties of Active Galactic Nuclei (AGN) host galaxies, is one of the most important areas of galaxy formation research. It is now well established that non-spherical geometries including some form of obscuring material/torus on parsec scales, can explain much of the observed diversity seen in the spectral energy dis-

tributions (SEDs) of AGN. At the same time, AGN-driven outflows are present in a large fraction of the luminous quasar population. The mass and energy associated with these outflows is believed to be significant in the context of feedback and its effect on the host galaxy. Punctuated fuelling episodes, e.g. driven by galaxy mergers, satellite accretion and even secular processes, almost certainly lead to AGN experiencing activity-, outflow- and obscuration-dominated cycles with some overlap between phases. However, quantitatively, it remains unclear how these phases relate to the fundamental properties of the accreting black-hole (e.g. mass (M_{BH})), bolometric luminosity (L_{bol}) and Eddington ratio (L/L_{Edd}) and the elements of the non-spherical geometry).

To date, the focus has been extreme, rare, AGN sub-populations, e.g. highly reddened and obscured AGN (Banerji et al. 2012, 2013, 2014, Eisenhardt et al. 2012, Ross et al. 2014). These populations provide insight into relatively short-lived phases in the AGN activity cycle. A more complete understanding of AGN-evolution and the physical link with the host galaxies requires the rare, extreme, sub-populations to be placed in the context of the AGN population as a whole. Photometry from the *WISE* satellite now provides information about the properties of the hot, dusty obscuring medium in the most luminous AGN. With information on the rest-frame SEDs covering rest-frame 0.1-3.0 μm wavelengths for thousands of AGN at redshifts $z=2-3$ it is finally possible to study the link between outflow diagnostics from ultraviolet spectra, e.g. as measured from the CIV emission line, and emission from hot dust, which provides information about the amount and geometry of gas and dust on parsec scales. In one model, quasars are surrounded by an inner ‘wall’ of gas and dust, in a cylinder-like geometry. As a radiatively-driven outflow develops, material at the extremes of the cylinder is driven-off, exposing more of the inner edge of the obscuring material at the equator (a ‘torus’), which contains the hot dust.

Proposed Observations: We have obtained measurements of the ultraviolet outflow properties (Figure 1) and the hot-dust content (Figure 2) for the SDSS-quasar sample at $z=2-3$. Figure 1 shows that quasars with strong CIV outflows are also hot-dust rich. We propose to obtain near infrared spectroscopy of the H α , H β and [OIII] regions for a sample of quasars chosen to systematically explore the full-range of outflow and dust properties. The observations will provide multiple diagnostics of the geometry and kinematics of different elements of the central regions of the AGN allowing us to provide new constraints on outflow properties and the evolution of AGN. Specific information/questions addressed by the WHT LIRIS observations include:

- The [OIII] $\lambda\lambda 4969,5007$ line is associated with low-density gas on kiloparsec scales in AGN (the so-called ‘narrow-line region’ - NLR) and typically exhibits blue asymmetries indicative of outflows. Few spectra of the [OIII] emission exist for ‘typical’ luminous quasars at redshifts $z > 2$. The near infrared spectra would allow us to determine the relationship between the high-ionisation outflows on small scales and the AGN environment on kiloparsec scales. A prediction of some models is that the AGN NLR will essentially be absent in objects where outflows have reached kiloparsec scales, sweeping up the low-density material responsible for the [OIII]-emission.

- Black-hole masses for quasars at redshifts $z=2-3$ are derived using the velocity-width of the CIV $\lambda 1550$ emission line. However, the CIV line-profile possesses a non-virial component, due to the outflow, that varies systematically with location in Figure 1. Near-infrared spectra would provide M_{BH} from the H β line, giving independent and robust estimates of both M_{BH} and L/L_{Edd} .

- The H α to H β line ratio will provide a reddening estimate towards the quasar line-of-sight, enabling us to constrain the geometry of the central regions and, specifically, the location of the hot dust.

- Near-infrared spectra of highly reddened quasars (Banerji et al. 2012, 2013, 2014) are already available, with many of the H α line profiles showing strong asymmetries, indicative of outflows. Similar line profiles are also seen for a population of optically luminous, submillimetre-bright quasars (Orellana et al. 2011). H α line profiles for our optically-selected sample, will show if the H α outflow signatures are ubiquitous in the luminous AGN population or if they are only associated with rare/short-lived phases in the AGN cycle represented by the reddened/submillimetre-bright quasars.

Target Selection: We have assembled a large flux-limited sample of $\simeq 600$ quasars, redshifts $z \sim 2 - 3$ and $K < 16.5$ (Vega), with SDSS spectra and SDSS, UKIDSS and *WISE* photometry, that are visible in Semester 2015A. The goal of the WHT LIRIS proposal is to obtain observations of the rest-frame optical properties of sub-samples of 6-8 quasars that possess CIV-outflow and near-infrared properties that span the full dynamic range present in our SDSS+UKIDSS+WISE sample (regions A, B and C in Figure 1). A representative sample of targets are included in Section 15 but the actual target list will be determined following the exact scheduling of the observations.

Observational Strategy: The broad ($\simeq 2000-5000 \text{ km s}^{-1}$ FWHM) H α and H β emission line profiles can be determined using the low-resolution ($R \simeq 700$) LIRIS grating. Target redshifts have been chosen to place H β and H α in the H- and K-bands respectively.

Kinematic information from the [OIII]-emission ($\sim 1000 \text{ km s}^{-1}$ FWHM) requires higher resolution observations. The presence of [OIII] $\lambda\lambda 4959,5007$ emission shows large variations among the quasar population and we expect that the line-strength may well depend systematically on the

CIV-outflow and near-infrared properties of the targets. To maximise the efficiency of the observations we will thus first observe a minimum of 18 targets at low-resolution during the first 2 nights. Objects which show [OIII]-emission will then be observed using the LIRIS high-resolution ($R \approx 2500$) configuration on subsequent nights. We expect that approximately 50% will possess [OIII]-emission that merit high-resolution exposures. However, if fewer targets have [OIII] emission, we will obtain low-resolution observations for a larger sample (aiming at 25 targets).

With such information available for each quasar target we can:

- measure the broad emission-line velocity widths and obtain black-hole mass estimates based on the H β emission line.
- measure the line-of-sight extinction to the broadline region via H α and H β line strengths.
- investigate whether the H α profiles provide any evidence for high-velocity outflows, as has been found in samples of more highly reddened quasars (Banerji et al. 2012, 2013).
- determine the strength of the [OIII] $\lambda\lambda 4959,5007$ emission and hence investigate the relationship between high-velocity outflow strength (revealed by the existing CIV $\lambda 1550$ observations) and the extent of the narrow line region associated with each quasar.
- for quasars with narrow-line regions, use [OIII] $\lambda\lambda 4959,5007$ emission profiles to determine the kinematics of the narrow-line region gas (on scales of kiloparsecs) and any relation with the CIV-outflow properties and the hot-dust contribution to the quasar SED.

We use the LIRIS Exposure Time Calculator to estimate that for the $R=700$ H+K low-resolution observations, a $K=16.0$ source would require an exposure time of 240s to reach a S/N of >10 per pixel in the K-band. Brighter targets will require shorter integrations while fainter targets will require slightly longer exposures. We propose to split these observations into 10 cycles of 240s exposures on average. High-resolution H-band observations will be conducted for $\sim 50\%$ of the sample. As a conservative estimate, assuming these targets are all at $K=16.5$ at the faint limit of our survey, we estimate that 360s exposures will be required to measure the [OIII] line profiles at a S/N of 10 per pixel. Observing overheads include 10 minutes for pointing and acquisition, ~ 30 s per nodding offset giving 5 minutes for 10 nods in low-resolution mode and 7.5 minutes for 15 nods in high resolution mode. The readout time should be absorbed in the nodding overhead. Therefore we estimate total overheads of 15-18 mins per object leading to total exposure times of 55 mins in low-resolution and 78 mins in high-resolution. To observe a sample of 18-25 objects at low resolution and ~ 10 at high resolution, we therefore require 4 nights.

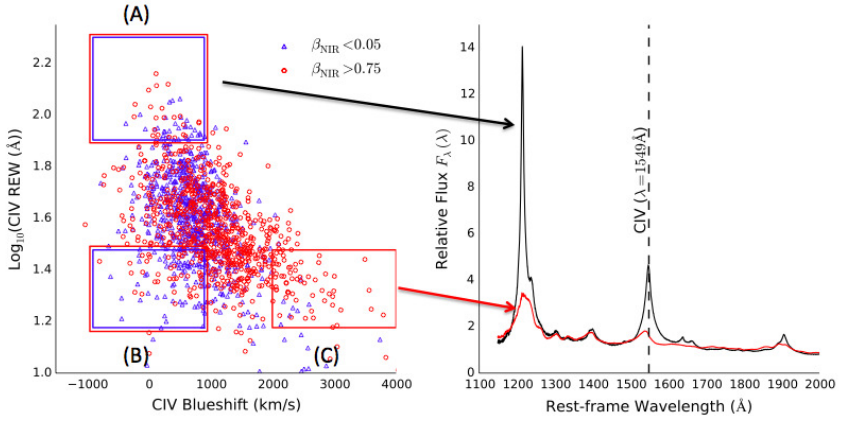


Figure 79: Figure 1: The rest-frame equivalent width of the CIV line plotted against a measure of its blueshift, for 1,464 SDSS DR7 quasars. The red circles represent hot-dust ($T \simeq 1200$ K) rich quasars which have the steepest near-infrared slopes (measured by fitting single power-law beyond $1\text{ }\mu\text{m}$ in the quasar rest-frame). The blue triangles represent quasars that are hot dust poor (i.e. have the shallowest near-infrared slopes). Quasars with the most extreme outflow signatures (in box C) are hot-dust rich. The measure of the CIV-emission blueshift is obtained from the wavelength of the centroid of the emission line relative to the predicted location for emission at the systemic velocity of each quasar. Systemic redshifts are obtained from Hewett and Wild (2010).

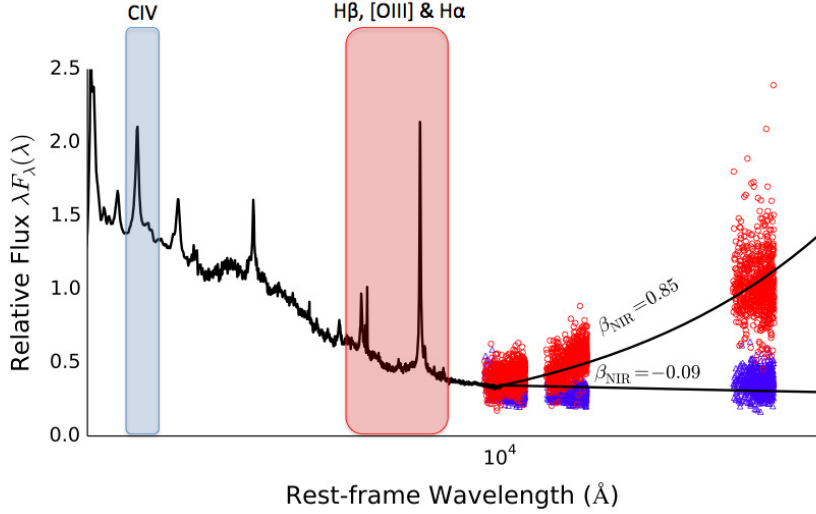


Figure 80: Rest-frame model quasar spectra for the hot-dust rich and hot-dust poor subsamples, corresponding to $\beta_{\text{NIR}} = 0.85$ and $\beta_{\text{NIR}} = -0.09$ respectively. Circles are observed fluxes for individual objects in the WISE W₁, W₂, and W₃ bands, transformed to the rest frame of the quasar.

6.22 NTT PROPOSAL

We propose to obtain near-infrared (NIR) spectroscopy for a well-defined sample of luminous quasars at $2 \lesssim z \lesssim 3$. Our sample includes objects with low ($E(B-V) \simeq 0$) and high ($0.5 \lesssim E(B-V) \lesssim 1.0$) amounts of dust reddening. For our unreddened quasars, we have shown that blue asymmetries in the C₄ emission line, indicative of parsec-scale outflows, correlate with the amount of hot-dust emission. By measuring the [O₃] line profiles, we will determine if the outflows are accelerated to kiloparsec scales. Measurements of H β will also provide improved black-hole mass and Eddington ratio estimates. Many of our highly reddened quasars show evidence for strong outflows in the broad H α line profile, which we will link to the hot-dust emission and kiloparsec-scale gas properties.

Understanding the link between supermassive black-hole growth and the properties of Active Galactic Nuclei (AGN) host galaxies is one of the most important areas of galaxy-formation research. It is now well established that non-spherical geometries including some form of obscuring material on parsec scales (possibly in the form of a torus), can explain much of the observed diversity seen in the spectral energy distributions (SEDs) of AGN. At the same time, AGN-driven outflows are present in a large fraction of the luminous quasar population. The mass and energy associated with these outflows is believed to be significant in the context of feedback and its effect on the host galaxy. Punctuated fuelling episodes, e.g. driven by galaxy mergers, satellite accretion and even secular processes, almost certainly lead to AGN experiencing activity-, outflow- and obscuration-dominated cycles with some overlap between phases. Quantitatively, however, it remains unclear how these phases relate to the fundamental properties of the accreting black-hole (e.g. mass (M_{BH})), bolometric luminosity (L_{bol}) and Eddington ratio (L/L_{Edd}) and the elements of the non-spherical geometry).

With large-scale surveys from SDSS, UKIDSS, and *WISE* providing information on the SEDs covering rest-frame 0.1-3.0 μm wavelengths for thousands of AGN at redshifts $2 \lesssim z \lesssim 3$ it is finally possible to study the link between outflow diagnostics from ultra-violet spectra, e.g. as measured from the C₄ emission line, and emission from hot ($T \simeq 1200\text{K}$) dust peaking in the NIR, which provides information about the amount and geometry of gas and dust on parsec scales. In one model, quasars are surrounded by an inner ‘wall’ of gas and dust, in a cylinder-like geometry. As a radiatively-driven outflow develops, material at the extremes of the cylinder is driven-off, exposing more of the inner edge of the obscuring material at the equator (a ‘torus’), which contains the hot dust. Quasars are also observed with a wide distribution of reddening from dust on galactic scales. It is believed that luminous highly dust-reddened quasars may be in the process

of expelling their dust and transitioning to ultra-violet bright objects which make up to the majority of the SDSS sample. Outflow signatures are very common in the rest-frame optical H α line profiles of the heavily reddened quasars (Banerji et al. 2012, 2013), but it isn't clear how significant these outflows are on larger, kiloparsec scales.

We have assembled a large flux-limited sample of $\simeq 600$ quasars, redshifts $2 \lesssim z \lesssim 3$ and $H < 17.3$ (Vega), with SDSS spectra and SDSS, UKIDSS and *WISE* photometry, that are visible with the NTT in Period 95. We have obtained measurements of the ultra-violet outflow properties (Figure 1) and the hot-dust content (Figure 2) for the SDSS-quasar sample at $2 \lesssim z \lesssim 3$. Figure 1 shows that quasars with strong C₄ outflows are also hot-dust rich. We already have NIR-spectra of the rest-frame region around the H α emission line for a sample of 38 luminous, highly reddened quasars (Banerji et al. 2012, 2013, 2014). Many of the H α line profiles show strong asymmetries, indicative of outflows.

We propose to obtain NIR spectroscopy of the H β and [O₃] regions for a sample of unreddened quasars chosen to systematically explore the full-range of C₄-outflow and NIR dust properties (regions A, B, and C in Figure 1). We will complement this with NIR spectroscopy of a sample of highly dust reddened quasars, for which we have previously obtained VLT SINFONI observations of the H α emission. The observations will provide multiple diagnostics of the geometry and kinematics of different elements of the central regions of the AGN, allowing us to provide new constraints on outflow properties and the evolution of AGN. The presence of [O₃] emission shows large variations among the quasar population and we expect that the line-strength may well depend systematically on the C₄-outflow, near-infrared properties and dust-reddening of the targets. Specific information/questions addressed by the NTT SOFI observations include:

- The [O₃] line is associated with low-density gas on kiloparsec scales in AGN (the so-called 'narrow-line region' - NLR) and typically exhibits blue asymmetries indicative of outflows. The NIR spectra would allow us to determine the relationship between the high-ionisation outflows and hot dust on small scales and the AGN environment on kiloparsec scales. In particular, we will determine the strength of the [O₃] emission and hence investigate the relationship between high-velocity outflow strength (revealed by the existing C₄ observations) and the extent of the narrow line region associated with each quasar. A prediction of some models is that the AGN NLR will essentially be absent in objects where outflows have reached kiloparsec scales, sweeping up the low-density material responsible for the [O₃]-emission. We will also measure the [O₃] emission profiles to determine the kinematics of the NLR gas and any relation with the C₄-outflow properties and the hot-dust contribution to the quasar SED.

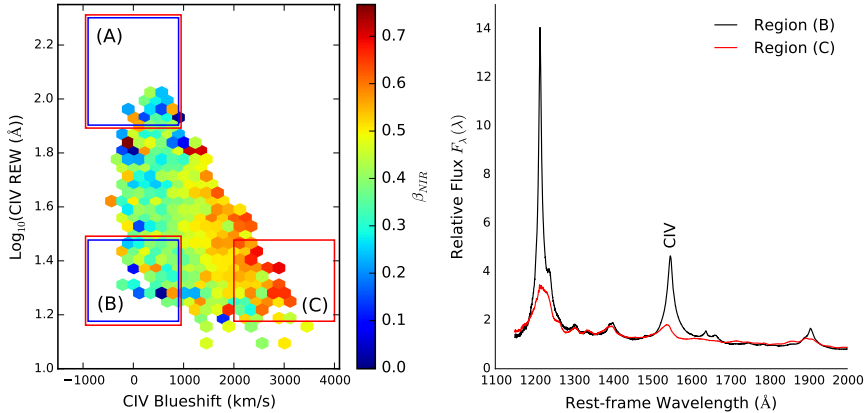


Figure 81: Rest-frame equivalent width and blueshift of the C₄ line for 7,115 SDSS DR7 quasars. The colours of the hexagons denote the median hot dust ($T \approx 1200$ K) abundance for all quasars at a given equivalent width and blueshift. The hot dust abundance is parameterised by fitting a single power-law with slope β_{NIR} beyond 1 μm in the quasar rest-frame. Quasars with the most extreme outflow signatures (in region C) are predominantly hot-dust rich. The C₄ emission line blueshift is obtained from the wavelength of the centroid of the emission line relative to the predicted location for emission at the systemic velocity of each quasar. Systemic redshifts are obtained from Hewett and Wild (2010).

- For the highly-dust reddened quasars with VLT SINFONI H α emission line profiles, we will relate the H α outflows to [O₃] outflows. If the highly dust-reddened quasars are being observed in a blowout/feedback phase in galaxy formation the NLR may have been swept away, depending on the duration of the fast outflow phase.
- Black-hole masses for quasars at redshifts $2 \lesssim z \lesssim 3$ are derived using the velocity-width of the C₄ emission line. However, the C₄ line profile possesses a non-virial component, due to the outflow, that varies systematically with location in Figure 1. NIR spectra would provide M_{BH} from the H β line, giving independent and robust estimates of both M_{BH} and L/L_{Edd}.
- For the highly reddened objects where we have VLT SINFONI observations of the H α emission, the H α to H β line ratio will provide a reddening estimate along the line of sight to the central region of the quasars, enabling us to constrain the geometry of the central regions and, specifically, the location of the hot dust.

6.23 FUTURE WORK

This work will be built on by, for example, investigating dust-extinction (combining our sample with moderately-reddened quasars from Maddox et al. 2012 and heavily-reddened quasars from Banerji et al. 2012–2015), broad-absorption line quasars, and/or radio properties. We

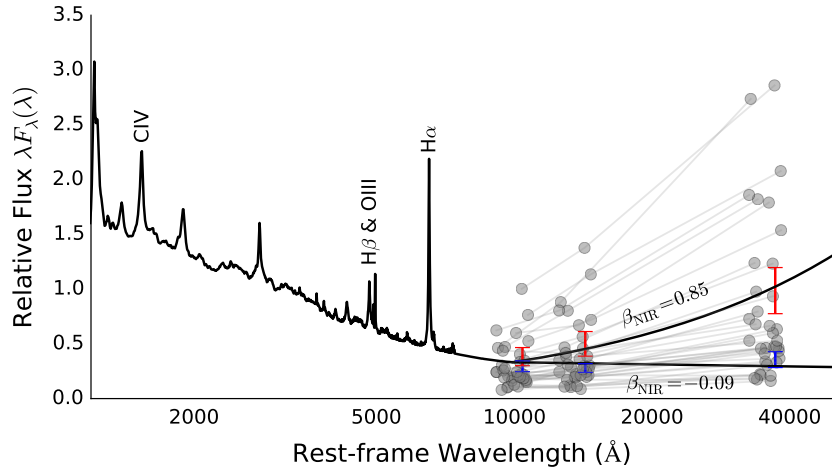


Figure 82: Representative rest-frame model spectra for the most hot-dust rich and hot-dust poor quasars in our SDSS sample, with error bars indicating the range of *WISE* W₁, W₂, and W₃ magnitudes for the objects in these subsamples, transformed to the rest frame of the quasar. Grey lines show the W₁, W₂, and W₃ fluxes for our sample of highly reddened quasars.

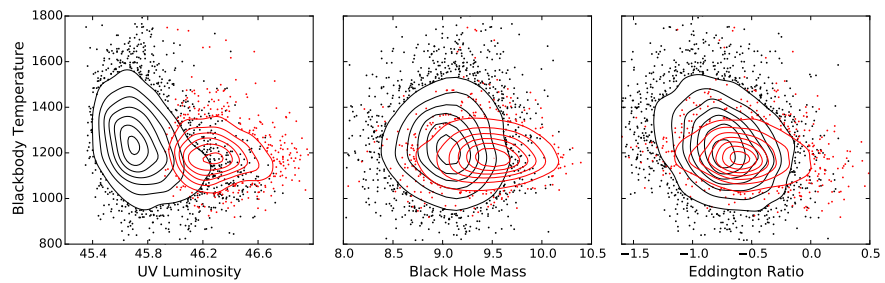


Figure 83: Black-body temperature plotted (from *left* to *right*) as a function of the ultra-violet luminosity, the black-hole mass and the Eddington ratio.

will also investigate the sub-population of quasars for which we don't observe any emission from hot dust.

7

CONCLUSIONS / FUTURE WORK

Put some stuff from research proposals here

Name	Date	<i>z</i>	Instrument	Telescope
J000039.00001803.9	2015-09-02		SofI	NTT
J000322.78-260319.0	2012-10-19		XSHOOTER	VLT
J000344.92232354.8	2011-09-18		SofI	NTT
J000345.00232353.4	2009-07-07	2.2657	SINFONI	VLT
J000450.66-084449.6	2013-07-12	3.0038	XSHOOTER	VLT
J000450.90-084451.9	2013-08-08	2.9991	XSHOOTER	VLT
J000500.42003348.2	2015-09-01		SofI	NTT
J000500.53010220.8	2015-09-02		SofI	NTT
J000651.61-620803.7	2012-10-09		XSHOOTER	VLT
J001016.49001227.6	2015-09-04		SofI	NTT
J001247.12+001239.4	2013-06-06		ISAAC	VLT
J001708.48813508.1	2012-08-04		TRIPLESPEC	Palomar 200-inch
J001919.31010152.2	2015-09-04	2.3120	SofI	NTT
J001954.66-091316.4	2004-11-26		GNIRS	Gemini-N
J002018.41233653.8	2009-07-07	2.2975	SINFONI	VLT
J002023.38414638.9	2009-07-08	1.5733	SINFONI	VLT
J002110.90242247.2	2009-07-16	2.2622	SINFONI	VLT
J002329.60003219.8	2015-09-04	2.3970	SofI	NTT
J002948.04095639.4	100102/101128	1.6159	TRIPLESPEC	ARC 3.5m
J002952.12020607.1	2009-07-14	2.3338	SINFONI	VLT
J003034.40-512946.0	2012-10-11		XSHOOTER	VLT
J003135.57+003421.2	2011-10-03	2.2354	XSHOOTER	VLT
J003454.82+163919.5	2012-10-19		XSHOOTER	VLT
J004131.44493611.8	2011-09-19		SofI	NTT
J004149.64094705.0	100102/101128		TRIPLESPEC	ARC 3.5m
J004219.74-102009.5	2012-10-10		XSHOOTER	VLT
J004300.55280543.5	2009-07-07	2.3293	SINFONI	VLT
J004417.12311436.0	2009-07-07	2.3499	SINFONI	VLT
J004418.05305720.6	2009-07-07		SINFONI	VLT
J004613.48002358.0	2015-09-03		SofI	NTT
J004834.60-244206.0	2012-11-10		XSHOOTER	VLT
J005202.40010129.2	2015-09-02		SofI	NTT
J005202.51010130.5	2009-08-18		SINFONI	VLT
J005412.55275533.8	2009-07-15		SINFONI	VLT
J005441.08533217.6	2009-07-15	2.2749	SINFONI	VLT
J005454.84004244.0	2015-09-03	2.2184	SofI	NTT
J005534.31344434.3	2009-08-16	2.3130	SINFONI	VLT
J005546.77635853.7	2009-07-16		SINFONI	VLT
J005613.47323432.6	2009-08-22	2.2153	SINFONI	VLT
J005625.07-280832.9	2012-10-17		XSHOOTER	VLT
J005717.36-000113.3	2013-06-07		ISAAC	VLT
J005717.37000113.2	2011-09-09		TRIPLESPEC	Palomar 200-inch
J005758.00264314.9	2011-09-20	3.6591	SofI	NTT
J005758.01-264314.9	2012-11-19		XSHOOTER	VLT

Jo05814.31011530.2	2015-09-03		SofI	NTT
Jo05925.10411043.4	2011-09-22		SofI	NTT
Jo10012.31-270853.3	2012-11-08		XSHOOTER	VLT
Jo10058.40023132.0	2011-09-10		TRIPLESPEC	Palomar 200-inch
Jo10156.75364353.0	2009-07-15		SINFONI	VLT
Jo10737.26385324.5	2009-08-22	2.3337	SINFONI	VLT
Jo10806.41163550.0	2011-09-10		TRIPLESPEC	Palomar 200-inch
Jo11143.62350300.4	2011-09-19	2.4049	SofI	NTT
Jo11150.06+140141.3	2007-10-02		NIRI	Gemini-N
Jo11344.40-280318.0	2012-11-10		XSHOOTER	VLT
Jo11731.20+155216.0	2012-10-19		XSHOOTER	VLT
Jo11827.98-005239.9	2004-11-29	2.1929	GNIRS	Gemini-N
Jo12126.20+034705.0	2012-10-16		XSHOOTER	VLT
Jo12139.70335358.5	2009-08-26		SINFONI	VLT
Jo12257.07334844.4	2009-08-22		SINFONI	VLT
Jo12305.13545303.6	2009-07-16	2.3070	SINFONI	VLT
Jo12329.12353502.5	2009-08-19		SINFONI	VLT
Jo12337.01323828.5	2009-08-22		SINFONI	VLT
Jo12403.77+004432.6	2012-11-18		XSHOOTER	VLT
Jo12417.38374422.9	2011-09-21		SofI	NTT
Jo12656.07320810.7	2009-08-23		SINFONI	VLT
Jo12745.30503706.9	2009-08-23	1.4963	SINFONI	VLT
Jo13014.30000639.2	2015-08-31		SofI	NTT
Jo13209.90+134139.0	2012-10-18		XSHOOTER	VLT
Jo13340.40+040059.0	2012-10-19		XSHOOTER	VLT
Jo13417.02394106.6	2009-08-22		SINFONI	VLT
Jo13433.99295813.6	2009-08-23	2.2298	SINFONI	VLT
Jo13529.83372610.0	2009-08-23		SINFONI	VLT
Jo13724.41-422416.8	2012-10-17		XSHOOTER	VLT
Jo13929.51+001330.8	2004-12-01	2.1017	GNIRS	Gemini-N
Jo14018.33013804.8	2009-08-19	2.2342	SINFONI	VLT
Jo14419.92083811.0	2011-09-08	2.3877	TRIPLESPEC	Palomar 200-inch
Jo14705.42133210.0	090909/091107	1.5945	TRIPLESPEC	ARC 3.5m
Jo14809.64-001017.7	2004-11-29		GNIRS	Gemini-N
Jo14944.43150106.6	090909/101128	2.0730	TRIPLESPEC	ARC 3.5m
Jo15057.99264448.7	2009-07-16		SINFONI	VLT
Jo15339.61-001104.9	2012-10-16		XSHOOTER	VLT
Jo15733.87004824.4	091107/101128		TRIPLESPEC	ARC 3.5m
Jo20044.50122319.1	100102/101128		TRIPLESPEC	ARC 3.5m
Jo20143.48+003222.7	2013-12-03	2.2972	XSHOOTER	VLT
Jo20301.94281317.7	2009-08-23	2.3247	SINFONI	VLT
Jo20327.29003938.1	2015-09-04		SofI	NTT
Jo20505.80011415.8	2015-09-01		SofI	NTT
Jo20806.18391637.6	2009-08-23		SINFONI	VLT
Jo20902.86-082531.8	2004-10-01		GNIRS	Gemini-N
Jo21120.10+110716.0	2012-11-07		XSHOOTER	VLT

Jo21429.30-051745.0	2012-10-16	XSHOOTER	VLT	
Jo22517.67+004821.9	2009-01-07	NIRSPEC	Keck-II	
Jo22839.19101109.4	2009-08-26	SINFONI	VLT	
Jo23011.28005913.7	2011-09-09	TRIPLESPEC	Palomar 200-inch	
Jo23145.89132254.7	2011-09-10	2.0665	TRIPLESPEC	Palomar 200-inch
Jo23359.72004938.5	2015-09-03	SofI	NTT	
Jo23455.14-180608.5	2012-12-12	XSHOOTER	VLT	
Jo23946.42-010640.5	2012-08-26	2.2984	XSHOOTER	VLT
Jo23946.44-010644.1	2012-08-26	XSHOOTER	VLT	
Jo24008.18230915.8	2011-09-18	SofI	NTT	
Jo24008.24230915.2	2009-09-19	SINFONI	VLT	
Jo24401.84-013403.7	2012-11-10	XSHOOTER	VLT	
Jo24650.93004457.3	2015-09-01	SofI	NTT	
Jo24756.50-055558.0	2012-10-17	XSHOOTER	VLT	
Jo24854.25+180249.5	2012-11-07	XSHOOTER	VLT	
Jo25021.76075749.9	131228	3.3376	FIRE	Magellan-Baade
Jo25055.44361634.9	2009-09-17	SINFONI	VLT	
Jo25140.39220026.5	2011-09-20	3.2046	SofI	NTT
Jo25518.57+004847.4	2012-10-18	XSHOOTER	VLT	
Jo25634.03401300.3	2011-09-19	SofI	NTT	
Jo25634.11401259.3	2009-09-17	SINFONI	VLT	
Jo25644.82001247.1	2009-09-24	SINFONI	VLT	
Jo25905.63001121.9	131230	3.3723	FIRE	Magellan-Baade
Jo30211.44314029.7	2009-09-17	SINFONI	VLT	
Jo30341.05002321.9	2011-09-08	TRIPLESPEC	Palomar 200-inch	
Jo30449.85000813.4	131229	3.2856	FIRE	Magellan-Baade
Jo30449.86000813.6	2011-09-08	TRIPLESPEC	Palomar 200-inch	
Jo30722.80-494548.0	2012-10-10	XSHOOTER	VLT	
Jo31115.20-172247.7	2012-11-08	XSHOOTER	VLT	
Jo31404.44003947.3	2015-09-02	SofI	NTT	
Jo32158.40-001102.6	2004-11-26	GNIRS	Gemini-N	
Jo32943.87233834.7	2009-09-23	SINFONI	VLT	
Jo33106.41382404.6	2011-09-22	2.4352	SofI	NTT
Jo33244.10445557.4	2012-03-05	SofI	NTT	
Jo34145.86264936.9	2009-09-23	2.3123	SINFONI	VLT
Jo34943.68381031.1	2011-09-21	SofI	NTT	
Jo35053.30003114.7	2011-09-10	TRIPLESPEC	Palomar 200-inch	
Jo35220.69051702.6	131230	FIRE	Magellan-Baade	
Jo35856.73054023.4	100102/101128	TRIPLESPEC	ARC 3.5m	
Jo40356.60-170323.0	2012-10-16	XSHOOTER	VLT	
Jo40757.12330143.0	2009-08-23	SINFONI	VLT	
Jo40954.19-041137.0	2004-10-31	2.1860	GNIRS	Gemini-N
Jo41255.16061210.3	100102/101128	TRIPLESPEC	ARC 3.5m	
Jo41515.20-435752.0	2012-10-09	XSHOOTER	VLT	
Jo42214.79384452.9	2013-03-19	SofI	NTT	
Jo42353.96261801.1	2012-03-07	SofI	NTT	

Jo42408.57020424.9	2012-03-09	2.0570	SofI	NTT
Jo42610.35-220218.0	2012-10-18		XSHOOTER	VLT
Jo42644.53520819.8	2012-03-06		SofI	NTT
Jo42644.70520819.2	2009-09-17	2.2635	SINFONI	VLT
Jo42707.30130253.6	2011-09-18	2.1681	SofI	NTT
Jo42741.17305322.5	2009-08-23	2.2333	SINFONI	VLT
Jo43038.80133546.0	2012-03-08		SofI	NTT
Jo44534.66354704.0	2013-03-21		SofI	NTT
Jo45523.05421617.4	2013-03-20		SofI	NTT
Jo45754.37181914.7	2009-09-20	1.5263	SINFONI	VLT
Jo52506.17-334305.3	2012-11-07		XSHOOTER	VLT
Jo52915.90-352604.0	2012-11-19		XSHOOTER	VLT
Jo52920.80-355234.0	2012-12-12		XSHOOTER	VLT
Jo53320.77542648.2	2009-09-17		SINFONI	VLT
Jo55246.19363727.6	2011-09-19		SofI	NTT
Jo55246.19363727.6	2012-03-08		SofI	NTT
Jo60008.10504036.8	2013-03-23		SofI	NTT
Jo64632.03445116.6	2011-09-10	3.4070	TRIPLESPEC	Palomar 200-inch
Jo71431.37-645510.6	2012-11-19		XSHOOTER	VLT
Jo73813.19271038.1	2015-04-03	2.4376	LIRIS	WHT
Jo74029.82281458.5	091108	1.5447	TRIPLESPEC	ARC 3.5m
Jo74352.61245743.6	2015-03-31		LIRIS	WHT
Jo74711.14+273903.3	2012-12-19		XSHOOTER	VLT
Jo74831.86392913.2	2012-04-04	2.5789	TRIPLESPEC	Palomar 200-inch
Jo75112.31291938.3	2012-04-02		TRIPLESPEC	Palomar 200-inch
Jo75552.41+134551.1	2012-12-20		XSHOOTER	VLT
Jo80048.74+354231.3	2006-02-17	2.0657	NIRI	Gemini-N
Jo80049.90+354249.6	2006-02-17	1.9821	NIRI	Gemini-N
Jo80050.27+192058.9	2013-11-29		XSHOOTER	VLT
Jo80150.95113455.6	2011-04-16	2.3865	TRIPLESPEC	Palomar 200-inch
Jo80651.54245526.3	2015-04-04		LIRIS	WHT
Jo81011.97093648.2	131229		FIRE	Magellan-Baade
Jo81227.19075732.9	101202		TRIPLESPEC	ARC 3.5m
Jo81331.28254503.0	101122	1.5065	TRIPLESPEC	ARC 3.5m
Jo81344.15152221.5	091108		TRIPLESPEC	ARC 3.5m
Jo81419.59+325018.7	2006-03-06	2.1740	NIRI	Gemini-N
Jo81701.91385936.3	2012-04-03	2.2408	TRIPLESPEC	Palomar 200-inch
Jo81855.77+095848.0	2012-12-20		XSHOOTER	VLT
Jo82146.22571226.0	091108/100104	1.5445	TRIPLESPEC	ARC 3.5m
Jo82644.70163548.0	2013-03-23	2.1895	SofI	NTT
Jo82906.63242322.9	2015-03-31		LIRIS	WHT
Jo83322.50+095941.2	2012-12-22		XSHOOTER	VLT
Jo83510.92+065052.8	2012-12-21		XSHOOTER	VLT
Jo83757.91+383727.1	2011-03-14		GNIRS	Gemini-N
Jo83850.15261105.4	091108		TRIPLESPEC	ARC 3.5m
Jo83941.45+031817.1	2013-03-04		XSHOOTER	VLT

Jo84158.47+392120.9	2007-04-24	2.0410	NIRI	Gemini-N
Jo84159.25+392139.9	2007-04-24	2.2137	NIRI	Gemini-N
Jo84312.64075029.3	131229	3.2645	FIRE	Magellan-Baade
Jo84401.95050357.9	131228		FIRE	Magellan-Baade
Jo84451.91282607.5	101202		TRIPLESPEC	ARC 3.5m
Jo85358.36-001108.0	2010-01-29	2.4014	NIRSPEC	Keck-II
Jo85437.59031734.8	2015-04-01		LIRIS	WHT
Jo85543.26002908.5	110426	1.5267	FIRE	Magellan-Baade
Jo85856.00015219.4	2015-04-01		LIRIS	WHT
Jo90223.32283930.2	2011-04-16		TRIPLESPEC	Palomar 200-inch
Jo91046.40+041458.4	2008-04-19	2.0456	NIRI	Gemini-N
Jo91046.69+041448.3	2008-04-19	2.3800	NIRI	Gemini-N
Jo91054.79023704.5	131230		FIRE	Magellan-Baade
Jo91208.75+005857.3	2004-11-27	2.1847	GNIRS	Gemini-N
Jo91210.35054742.1	2013-03-21		SofI	NTT
Jo91338.30-010708.6	2013-03-31		XSHOOTER	VLT
Jo91338.97-010704.6	2013-04-11	2.9145	XSHOOTER	VLT
Jo91432.01+010912.4	2012-01-23	2.1410	XSHOOTER	VLT
Jo91510.01475658.8	2013-01-29		TRIPLESPEC	Palomar 200-inch
Jo91754.44043652.1	110427	1.5838	FIRE	Magellan-Baade
Jo92041.76+072544.0	2013-12-27		XSHOOTER	VLT
Jo92129.36261843.3	2012-03-07		SofI	NTT
Jo92743.02+290734.7	2006-05-15	2.2529	NIRI	Gemini-N
Jo92747.27+290720.6	2006-05-15		NIRI	Gemini-N
Jo92914.49282529.2	2012-04-04	3.4110	TRIPLESPEC	Palomar 200-inch
Jo92952.17355449.8	2011-04-18		TRIPLESPEC	Palomar 200-inch
Jo93226.34+092526.1	2011-04-04	2.4172	XSHOOTER	VLT
Jo93318.49141340.1	100126	1.5597	TRIPLESPEC	ARC 3.5m
Jo93337.28284532.4	2012-04-04	3.4358	TRIPLESPEC	Palomar 200-inch
Jo93556.91+002255.6	2013-03-30		XSHOOTER	VLT
Jo93643.51292713.7	2012-04-04	2.9231	TRIPLESPEC	Palomar 200-inch
Jo93714.48+082858.5	2013-12-27		XSHOOTER	VLT
Jo93804.21+531743.9	2011-03-14	2.0665	GNIRS	Gemini-N
Jo93849.67090509.7	2013-03-19		SofI	NTT
Jo94126.49044328.7	110427	1.5679	FIRE	Magellan-Baade
Jo94202.04042244.5	131228	3.2793	FIRE	Magellan-Baade
Jo94202.05042244.5	2012-03-08		SofI	NTT
Jo94206.96352307.3	2011-04-18	2.0227	TRIPLESPEC	Palomar 200-inch
Jo94253.49110425.9	2013-03-20		SofI	NTT
Jo94913.05175155.9	100126		TRIPLESPEC	ARC 3.5m
Jo95333.70033623.7	131230		FIRE	Magellan-Baade
Jo95434.93091519.6	131230		FIRE	Magellan-Baade
Jo95500.10-013007.0	2014-01-03		XSHOOTER	VLT
Jo95543.66-012351.5	2014-01-04	2.8388	XSHOOTER	VLT
Jo95544.29-012357.5	2014-03-01		XSHOOTER	VLT
Jo95852.19120245.0	2012-03-09		SofI	NTT

J095937.11+131215.4	2013-12-27		XSHOOTER	VLT
J100246.85+002104.0	2005-01-16		GNIRS	Gemini-N
J100401.27423123.1	100104		TRIPLESPEC	ARC 3.5m
J100627.46+480420.0	2011-03-15	2.3026	GNIRS	Gemini-N
J100745.65+033746.2	2013-06-04		ISAAC	VLT
J100930.51023052.4	110426	1.5538	FIRE	Magellan-Baade
J101001.50403755.5	2012-04-03	2.1844	TRIPLESPEC	Palomar 200-inch
J101155.60294141.6	2012-04-04		TRIPLESPEC	Palomar 200-inch
J101342.57210619.5	2009-05-13	1.5353	SINFONI	VLT
J101347.29+065015.7	2012-12-21		XSHOOTER	VLT
J101447.54521320.2	110124	1.5498	TRIPLESPEC	ARC 3.5m
J101504.75123022.2	110124		TRIPLESPEC	ARC 3.5m
J101723.98204658.6	2012-03-08	2.5565	SofI	NTT
J101818.45+054822.8	2013-04-03	3.5131	XSHOOTER	VLT
J101859.96-005420.2	2005-01-15	2.1823	GNIRS	Gemini-N
J101908.26025431.9	131229	3.3850	FIRE	Magellan-Baade
J102040.62+092254.2	2012-05-21		XSHOOTER	VLT
J102357.31+044405.5	2013-06-06		ISAAC	VLT
J102456.61+181908.7	2013-06-10		XSHOOTER	VLT
J102457.57001740.4	2009-04-19	1.4997	SINFONI	VLT
J102509.64045246.8	2013-03-21	3.2393	SofI	NTT
J102618.80+461445.2	2009-01-07	3.3366	NIRSPEC	Keck-II
J102734.16183428.0	2012-04-04		TRIPLESPEC	Palomar 200-inch
J102838.98093540.9	2009-04-19		SINFONI	VLT
J102906.66+020500.0	2005-01-15	2.1390	GNIRS	Gemini-N
J103221.11+092749.0	2013-06-10		XSHOOTER	VLT
J103325.93+012836.3	2005-01-16	2.1833	GNIRS	Gemini-N
J103359.91251427.4	2012-03-05	2.5521	SofI	NTT
J103446.54+110214.4	2014-01-03		XSHOOTER	VLT
J103456.31035859.4	131229		FIRE	Magellan-Baade
J103456.31035859.4	2013-03-20		SofI	NTT
J103623.70-034320.0	2013-12-29		XSHOOTER	VLT
J103730.33+213531.3	2014-02-23		XSHOOTER	VLT
J103732.38+070426.2	2014-02-09		XSHOOTER	VLT
J103857.37+502707.9	2006-05-09	3.1322	NIRI	Gemini-N
J103909.52231326.2	2013-03-22		SofI	NTT
J104121.89+563001.3	2007-05-17		NIRI	Gemini-N
J104121.89563001.3	2011-04-18		TRIPLESPEC	Palomar 200-inch
J104234.00+195718.6	2014-02-22		XSHOOTER	VLT
J104603.22112828.1	110426	1.6044	FIRE	Magellan-Baade
J104910.31143227.1	100126		TRIPLESPEC	ARC 3.5m
J104915.44-011038.1	2005-01-15		GNIRS	Gemini-N
J104915.44011038.1	2013-03-22		SofI	NTT
J105158.74401736.7	2013-01-29		TRIPLESPEC	Palomar 200-inch
J105340.75+010335.7	2013-04-12		XSHOOTER	VLT
J105434.17+021551.9	2012-06-09		XSHOOTER	VLT

J105651.44114122.2	2009-05-13	SINFONI	VLT	
J105705.37+191042.8	2012-06-08	XSHOOTER	VLT	
J105858.38+124555.0	2014-02-03	XSHOOTER	VLT	
J105951.05090905.7	110124	TRIPLESPEC	ARC 3.5m	
J110240.16394730.1	110222	1.6654	TRIPLESPEC	ARC 3.5m
J110325.31264515.9	2012-03-06	SofI	NTT	
J110352.74+100403.1	2014-02-23	XSHOOTER	VLT	
J110454.73095714.8	2015-04-03	LIRIS	WHT	
J110610.74640009.6	2011-04-15	TRIPLESPEC	Palomar 200-inch	
J110633.39182123.8	2012-03-09	2.3184	SofI	NTT
J110708.41043617.9	2013-03-19	SofI	NTT	
J110855.46+120953.3	2014-02-10	XSHOOTER	VLT	
J110915.92115449.2	2009-07-06	SINFONI	VLT	
J111008.61+024458.0	2012-05-21	XSHOOTER	VLT	
J111113.60-080402.0	2013-03-06	XSHOOTER	VLT	
J111119.11133603.9	2013-03-22	SofI	NTT	
J111119.11133603.9	2013-03-22	SofI	NTT	
J111242.68+661152.8	2006-06-02	NIRI	Gemini-N	
J111245.70+661215.4	2006-06-02	NIRI	Gemini-N	
J111350.61153333.9	2013-03-21	3.3662	SofI	NTT
J111350.93401721.4	2013-01-29	TRIPLESPEC	Palomar 200-inch	
J111701.89+131115.4	2014-02-23	XSHOOTER	VLT	
J111949.30233249.1	110124	1.6228	TRIPLESPEC	ARC 3.5m
J112442.87170517.5	2012-03-05	SofI	NTT	
J112542.29000101.3	110427	1.6890	FIRE	Magellan-Baade
J112617.40-012632.6	2014-02-22	XSHOOTER	VLT	
J112617.40012632.6	2011-04-18	3.6175	TRIPLESPEC	Palomar 200-inch
J112634.28-012436.9	2013-05-11	XSHOOTER	VLT	
J113334.23130553.2	2013-01-05	SINFONI	VLT	
J113536.40+084219.0	2014-02-22	XSHOOTER	VLT	
J113621.05005021.2	2013-03-23	SofI	NTT	
J113829.33040101.0	110426	1.5706	FIRE	Magellan-Baade
J114023.40301651.5	100126	1.5961	TRIPLESPEC	ARC 3.5m
J114145.42+072423.2	2014-03-29	XSHOOTER	VLT	
J114146.18+072410.9	2014-03-27	XSHOOTER	VLT	
J114155.42+531307.9	2007-04-04	NIRI	Gemini-N	
J114156.88+531358.1	2007-04-04	2.2127	NIRI	Gemini-N
J114254.26265457.5	2013-03-23	SofI	NTT	
J114254.26265457.5	2012-04-02	TRIPLESPEC	Palomar 200-inch	
J114435.54+095921.6	2009-01-07	2.9726	NIRSPEC	Keck-II
J114706.51353150.4	2011-04-16	TRIPLESPEC	Palomar 200-inch	
J115151.69224210.8	2013-01-06	SINFONI	VLT	
J115235.77175702.6	2009-05-13	2.2113	SINFONI	VLT
J115301.60215117.5	2013-03-11	SINFONI	VLT	
J115510.56223246.5	2009-05-13	SINFONI	VLT	
J115538.60053050.7	2013-03-23	3.4642	SofI	NTT

J120044.94185944.5	2012-03-06	2.4482	SofI	NTT
J120144.36011611.6	2011-04-15		TRIPLESPEC	Palomar 200-inch
J120147.90+120630.2	2013-03-04		XSHOOTER	VLT
J120147.91120630.3	2012-03-09		SofI	NTT
J120210.08-005425.5	2013-01-14		XSHOOTER	VLT
J120417.47+022104.7	2006-03-27	2.4358	GNIRS	Gemini-N
J120818.84045905.7	2009-05-10	2.3225	SINFONI	VLT
J121117.59042222.3	2011-04-15		TRIPLESPEC	Palomar 200-inch
J121140.59103002.0	2013-03-20	2.1909	SofI	NTT
J121303.02171423.3	2011-04-15		TRIPLESPEC	Palomar 200-inch
J121427.78-030721.1	2005-01-16	2.1242	GNIRS	Gemini-N
J121558.82+571555.5	2007-05-23	1.9591	NIRI	Gemini-N
J121558.99+571616.6	2007-05-23	1.9296	NIRI	Gemini-N
J121911.23004345.6	2013-01-19 / 2013-01-23		SINFONI	VLT
J121911.34004348.7	2009-05-10	2.2968	SINFONI	VLT
J122039.45000427.6	110427	2.0473	FIRE	Magellan-Baade
J122310.62181642.4	2012-03-07	2.1670	SofI	NTT
J122516.79+042537.8	2013-06-07	2.3938	ISAAC	VLT
J122637.54082929.6	2012-03-05		SofI	NTT
J123141.73+002913.9	2013-04-27		XSHOOTER	VLT
J123143.09+002846.2	2013-04-27	3.2018	XSHOOTER	VLT
J123355.21031327.6	110427		FIRE	Magellan-Baade
J123442.16052126.7	110513	1.5455	TRIPLESPEC	ARC 3.5m
J123511.10-010829.5	2013-06-05		ISAAC	VLT
J123514.36+030416.7	2005-01-20	2.1995	GNIRS	Gemini-N
J123611.21112921.6	2015-04-01		LIRIS	WHT
J123749.00012607.1	2011-04-18		TRIPLESPEC	Palomar 200-inch
J124006.70474003.3	110222		TRIPLESPEC	ARC 3.5m
J124524.60000938.0	2013-03-23		SofI	NTT
J124602.05042658.4	2015-04-01		LIRIS	WHT
J124837.31+130440.9	2012-05-23		XSHOOTER	VLT
J124913.98055918.4	2009-04-17		SINFONI	VLT
J124924.87023339.8	2013-03-20		SofI	NTT
J124948.18+060714.0	2006-02-18	2.0056	GNIRS	Gemini-N
J124957.23-015928.8	2014-01-28		XSHOOTER	VLT
J124957.24015928.8	2012-03-07		SofI	NTT
J125123.78+271524.6	2014-07-03		XSHOOTER	VLT
J125140.82080718.4	110426		FIRE	Magellan-Baade
J125353.71681714.3	2012-04-04	3.4750	TRIPLESPEC	Palomar 200-inch
J130124.73475909.6	2012-04-03		TRIPLESPEC	Palomar 200-inch
J130331.28162146.6	2013-01-23		SINFONI	VLT
J130343.47103113.3	2013-01-29		TRIPLESPEC	Palomar 200-inch
J130452.57+023924.9	2013-03-05		XSHOOTER	VLT
J130524.90+031135.1	2013-06-05		ISAAC	VLT
J130524.90031135.2	2012-04-03		TRIPLESPEC	Palomar 200-inch
J130605.19+615823.7	2011-02-18		GNIRS	Gemini-N

J130618.60151017.9	2015-04-01	LIRIS	WHT	
J130710.25123021.7	2013-02-23	SINFONI	VLT	
J131011.61460124.5	2011-04-16	2.1376	TRIPLESPEC	Palomar 200-inch
J131242.86+084105.0	2012-04-17	3.7351	XSHOOTER	VLT
J131749.78080616.2	2015-04-05	LIRIS	WHT	
J131914.20520200.1	2012-04-03	TRIPLESPEC	Palomar 200-inch	
J132029.98-052335.5	2012-06-16	XSHOOTER	VLT	
J132029.98052335.5	2012-03-07	SofI	NTT	
J132109.49113930.6	2009-04-17	2.3061	SINFONI	VLT
J132346.05+140517.6	2012-06-25	XSHOOTER	VLT	
J132427.71095017.3	2009-04-17	2.3268	SINFONI	VLT
J132948.73324124.4	2015-04-04	LIRIS	WHT	
J133052.10-252219.0	2012-04-17	XSHOOTER	VLT	
J133150.69+101529.4	2013-04-03	XSHOOTER	VLT	
J133254.50+005250.6	2012-06-12	3.5052	XSHOOTER	VLT
J133254.50005250.6	2012-03-08	SofI	NTT	
J133321.90005824.3	110426	1.5071	FIRE	Magellan-Baade
J133322.01005825.8	2009-05-10	SINFONI	VLT	
J133335.78164903.9	2012-03-05	SofI	NTT	
J133646.87144334.2	2015-04-04	LIRIS	WHT	
J133653.44+024338.1	2013-03-06	XSHOOTER	VLT	
J133757.87021821.0	2013-03-22	SofI	NTT	
J133916.88151507.6	2015-04-01	2.3149	LIRIS	WHT
J134103.60073947.3	2009-07-07	SINFONI	VLT	
J134115.56+010812.7	2006-02-26	2.2092	GNIRS	Gemini-N
J134204.55181801.4	2009-07-07	SINFONI	VLT	
J134258.86135559.8	2013-03-19	SofI	NTT	
J134427.07103541.9	2012-03-06	2.1434	SofI	NTT
J134838.05+053114.8	2013-06-06	2.1152	ISAAC	VLT
J134844.12035322.8	2009-07-07	SINFONI	VLT	
J135023.68265243.1	110222	1.6242	TRIPLESPEC	ARC 3.5m
J135029.92-014331.6	2013-06-06	ISAAC	VLT	
J135038.88251216.8	2012-03-05	SofI	NTT	
J135247.97+130311.5	2014-02-02	XSHOOTER	VLT	
J135417.91334859.8	2011-04-15	2.2436	TRIPLESPEC	Palomar 200-inch
J135425.34001357.1	2009-05-13	SINFONI	VLT	
J135439.70301649.2	110422	TRIPLESPEC	ARC 3.5m	
J135719.08+011705.4	2013-06-07	ISAAC	VLT	
J140039.00112022.9	2012-03-06	SofI	NTT	
J140047.45120504.6	2015-04-04	LIRIS	WHT	
J140146.53+024434.7	2012-04-17	XSHOOTER	VLT	
J140208.10+470111.1	2007-05-02	1.9142	NIRI	Gemini-N
J140209.52+470117.8	2007-05-02	NIRI	Gemini-N	
J140445.89013021.8	2012-03-09	2.5165	SofI	NTT
J140747.23645419.9	2012-04-04	TRIPLESPEC	Palomar 200-inch	
J141608.38+181144.0	2012-05-20	XSHOOTER	VLT	

J141949.39060654.0	110426		FIRE	Magellan-Baade
J142003.67+022726.6	2011-06-22	3.6167	GNIRS	Gemini-N
J142054.41+160333.3	2012-07-03		XSHOOTER	VLT
J142054.42+160333.3	2007-07-27		NIRI	Gemini-N
J142054.92+160342.9	2007-07-27		NIRI	Gemini-N
J142107.76-064356.3	2013-04-03		XSHOOTER	VLT
J142108.71224117.4	100520/110513	2.1890	TRIPLESPEC	ARC 3.5m
J142438.10225600.5	2012-03-08	3.6269	SofI	NTT
J142656.19602550.9	2011-04-16	3.2040	TRIPLESPEC	Palomar 200-inch
J142758.89-012130.4	None		GNIRS	Gemini-N
J142815.67+023243.5	2013-04-30		XSHOOTER	VLT
J142816.51+023229.2	2013-04-30		XSHOOTER	VLT
J142841.97592552.0	110414/110418	1.6539	TRIPLESPEC	ARC 3.5m
J142903.03014519.4	2012-03-06		SofI	NTT
J143128.42-004450.0	2013-06-06		ISAAC	VLT
J143148.09053558.0	100520	2.1004	TRIPLESPEC	ARC 3.5m
J143229.25010616.0	2012-03-08		SofI	NTT
J143230.57012435.1	110427		FIRE	Magellan-Baade
J143345.50+064109.9	2012-03-19	2.2931	XSHOOTER	VLT
J143645.80633637.9	100520/110513	2.0675	TRIPLESPEC	ARC 3.5m
J143912.04111740.5	2012-03-09	2.5811	SofI	NTT
J144245.66-024250.1	2013-06-05		ISAAC	VLT
J144250.11+092001.5	2012-05-21		XSHOOTER	VLT
J144424.38104542.4	2009-04-23	2.3583	SINFONI	VLT
J144516.46+095836.0	2012-06-11		XSHOOTER	VLT
J144516.47095836.1	2011-04-16		TRIPLESPEC	Palomar 200-inch
J145102.51232931.1	2012-03-05	2.2218	SofI	NTT
J145408.96511443.7	2012-04-02	3.6360	TRIPLESPEC	Palomar 200-inch
J145649.89193852.1	2013-03-21	3.1636	SofI	NTT
J150328.88+041949.0	2014-02-11		XSHOOTER	VLT
J150959.16074450.1	2015-09-03		SofI	NTT
J151756.18+051103.5	2012-05-23		XSHOOTER	VLT
J151912.81+374918.4	2007-04-02	2.1608	NIRI	Gemini-N
J151920.75+374902.2	2007-04-02	2.1114	NIRI	Gemini-N
J152111.86470539.1	110422	1.5153	TRIPLESPEC	ARC 3.5m
J152156.48520238.6	2012-04-02		TRIPLESPEC	Palomar 200-inch
J152436.08+212309.1	2012-05-19		XSHOOTER	VLT
J152529.17292813.2	2015-04-05		LIRIS	WHT
J153027.37062330.8	2015-04-04		LIRIS	WHT
J153848.64023341.1	2015-04-02		LIRIS	WHT
J153859.45053705.3	110426	1.6854	FIRE	Magellan-Baade
J154058.70473827.5	2012-04-03	2.5591	TRIPLESPEC	Palomar 200-inch
J154212.90111226.7	110427	1.5391	FIRE	Magellan-Baade
J154237.71+095558.8	2012-04-23		XSHOOTER	VLT
J154432.33020442.0	2015-09-02		SofI	NTT
J154503.20015614.0	2013-03-23		SofI	NTT

J155013.60200154.0	2013-03-19	2.1884	SofI	NTT
J155233.88491008.3	2012-04-03	2.0523	TRIPLESPEC	Palomar 200-inch
J155240.40194816.7	110414/110418	1.6165	TRIPLESPEC	ARC 3.5m
J155255.04+100538.3	2012-04-23		XSHOOTER	VLT
J155325.60+192140.9	2011-07-17	2.0102	XSHOOTER	VLT
J155814.51405337.0	2011-09-10		TRIPLESPEC	Palomar 200-inch
J155949.72080517.6	2013-03-19		SofI	NTT
J160222.73084538.4	2013-03-22	2.2781	SofI	NTT
J160355.93573054.4	2012-08-03		TRIPLESPEC	Palomar 200-inch
J160456.14001907.1	110426	1.6362	FIRE	Magellan-Baade
J161009.43472444.5	2011-09-08		TRIPLESPEC	Palomar 200-inch
J161024.88+044218.4	2013-06-05		ISAAC	VLT
J161458.30144836.0	2012-07-21		SofI	NTT
J161805.85092004.1	2013-03-21		SINFONI	VLT
J161842.44234131.7	2015-04-01		LIRIS	WHT
J162014.19103621.1	2013-02-24	2.0944	SINFONI	VLT
J162103.98002905.8	110714		FIRE	Magellan-Baade
J162116.92-004250.8	2012-05-19		XSHOOTER	VLT
J162116.92004250.9	2011-09-20	3.7051	SofI	NTT
J162141.02+350712.8	2006-04-24		NIRI	Gemini-N
J162145.41+350807.2	2006-04-24		NIRI	Gemini-N
J162323.67331232.6	2011-04-15		TRIPLESPEC	Palomar 200-inch
J162548.08+264432.5	2006-04-17	2.4664	NIRI	Gemini-N
J162548.79264658.7	2012-04-02		TRIPLESPEC	Palomar 200-inch
J162548.80+264658.7	2006-04-14	2.5341	NIRI	Gemini-N
J162701.94313549.2	2015-04-02		LIRIS	WHT
J162736.39+221538.0	2011-05-02		XSHOOTER	VLT
J162736.40+221538.0	2008-04-19		NIRI	Gemini-N
J162738.63+460538.3	2007-05-29	3.8140	NIRI	Gemini-N
J163319.63+141142.0	2012-06-12		XSHOOTER	VLT
J163412.78320335.5	2011-04-16	2.3552	TRIPLESPEC	Palomar 200-inch
J163456.15+301437.7	2006-05-13		NIRI	Gemini-N
J163456.15301437.8	2015-04-04		LIRIS	WHT
J164547.28+224534.4	2013-06-07		ISAAC	VLT
J165844.06-073917.6	2012-06-12		XSHOOTER	VLT
J165914.54380900.7	2011-09-09	2.3475	TRIPLESPEC	Palomar 200-inch
J170100.62641209.1	2011-09-09		TRIPLESPEC	Palomar 200-inch
J171030.20602347.5	110414/110418	1.5436	TRIPLESPEC	ARC 3.5m
J172252.98245834.7	2012-04-04		TRIPLESPEC	Palomar 200-inch
J172323.10+224356.9	2012-05-20		XSHOOTER	VLT
J173352.24540030.5	2011-04-16	3.4276	TRIPLESPEC	Palomar 200-inch
J193957.25100241.5	2011-09-22	3.7919	SofI	NTT
J194025.51690756.9	2011-09-18		SofI	NTT
J200324.12325145.0	2011-09-19	3.7829	SofI	NTT
J204009.62065402.5	110426		FIRE	Magellan-Baade
J204536.56010147.9	110426	1.6570	FIRE	Magellan-Baade

J204538.96005115.5	110427	1.5867	FIRE	Magellan-Baade
J205344.60354655.0	2011-09-20		SofI	NTT
J205554.08004311.4	110427	1.6222	FIRE	Magellan-Baade
J205954.51-001917.4	2004-09-30		GNIRS	Gemini-N
J211155.81434531.6	2009-05-14	2.2728	SINFONI	VLT
J211832.88+004219.0	2004-10-31	2.1717	GNIRS	Gemini-N
J211927.60353740.6	2011-09-21	2.3397	SofI	NTT
J212159.04005224.1	2015-09-04		SofI	NTT
J212329.47005052.9	2011-09-08		TRIPLESPEC	Palomar 200-inch
J212329.47005052.9	2011-09-22		SofI	NTT
J212512.66421844.6	2009-05-14		SINFONI	VLT
J212747.43004929.5	2015-09-01		SofI	NTT
J212912.18153841.0	2011-09-22		SofI	NTT
J212912.18153841.0	2011-09-09	3.2882	TRIPLESPEC	Palomar 200-inch
J213125.52001910.4	2015-09-03		SofI	NTT
J213235.95001350.6	2015-09-03		SofI	NTT
J213438.96+000953.7	2013-06-07	2.4056	ISAAC	VLT
J213623.52003410.9	2015-08-30		SofI	NTT
J213748.44001220.0	110713		FIRE	Magellan-Baade
J214225.81442018.2	2011-09-19		SofI	NTT
J214501.70-303122.0	2013-05-15	2.2218	XSHOOTER	VLT
J214507.10-303046.0	2013-05-15		XSHOOTER	VLT
J214620.68-075250.6	2006-04-09	2.1159	GNIRS	Gemini-N
J214950.14444404.7	2009-04-17		SINFONI	VLT
J215052.44315824.0	2009-04-23		SINFONI	VLT
J215615.18003057.8	2015-09-01		SofI	NTT
J215727.26+001558.4	2013-06-09		XSHOOTER	VLT
J215728.35+001545.6	2013-08-10		XSHOOTER	VLT
J215743.63233037.3	2012-08-03	3.1455	TRIPLESPEC	Palomar 200-inch
J215859.35010147.5	2015-08-31		SofI	NTT
J215954.69400550.4	2012-07-21		SofI	NTT
J220013.54001912.1	2015-09-02		SofI	NTT
J220248.30+123656.2	2007-07-23	2.5182	NIRI	Gemini-N
J220248.61+123645.5	2007-07-23		NIRI	Gemini-N
J220529.91254221.6	2009-05-14		SINFONI	VLT
J220734.41403656.0	2011-09-19		SofI	NTT
J221527.30-161133.0	2013-11-21		XSHOOTER	VLT
J221531.67174408.3	2011-09-20		SofI	NTT
J221531.79174407.0	2009-05-14	2.2286	SINFONI	VLT
J221651.98-671443.5	2012-10-09		XSHOOTER	VLT
J221851.00615043.0	2011-09-21		SofI	NTT
J222006.76280323.3	2011-09-18	2.4164	SofI	NTT
J222255.47522514.1	2009-06-25	1.5459	SINFONI	VLT
J223135.46393853.2	2009-06-16	2.2103	SINFONI	VLT
J223245.59363202.9	2009-06-05		SINFONI	VLT
J223246.80134702.0	091107	1.5529	TRIPLESPEC	ARC 3.5m

J223358.87010000.4	2011-09-08		TRIPLESPEC	Palomar 200-inch
J223358.88-010000.5	2013-06-07		ISAAC	VLT
J223819.76092106.0	120529		FIRE	Magellan-Baade
J223850.10-295612.0	2013-06-22	2.4696	XSHOOTER	VLT
J223850.90-295301.0	2013-05-27	2.3904	XSHOOTER	VLT
J223953.62-055220.0	2012-06-15		XSHOOTER	VLT
J224026.21003940.1	2015-08-31		SofI	NTT
J224559.09513342.8	2009-06-25		SINFONI	VLT
J225118.10-122703.0	2012-08-10		XSHOOTER	VLT
J225535.43403626.4	2009-07-05	1.5186	SINFONI	VLT
J225800.02084143.7	091107		TRIPLESPEC	ARC 3.5m
J225921.59+140256.1	2004-10-01		GNIRS	Gemini-N
J225931.72004751.7	2015-09-01		SofI	NTT
J230006.31023558.5	2009-06-26		SINFONI	VLT
J230015.69+003119.3	2013-06-06	2.1772	ISAAC	VLT
J230959.53+005537.3	2013-08-09		XSHOOTER	VLT
J230959.79+005600.9	2013-07-22		XSHOOTER	VLT
J231043.29003151.0	2015-09-04		SofI	NTT
J231441.64-082406.8	2004-09-30	2.2049	GNIRS	Gemini-N
J232043.65052443.5	2009-06-26	1.3725	SINFONI	VLT
J232154.99155834.2	2012-08-04		TRIPLESPEC	Palomar 200-inch
J232539.44065258.6	2009-06-26		SINFONI	VLT
J233722.45292514.4	2009-07-07	1.5626	SINFONI	VLT
J233845.18-000327.1	2012-09-13	2.4387	XSHOOTER	VLT
J233845.44-000331.8	2012-09-13	2.9896	XSHOOTER	VLT
J233939.31410318.4	2009-07-02		SINFONI	VLT
J234403.20+034226.0	2012-06-16		XSHOOTER	VLT
J234510.46293153.7	2009-06-29	2.3820	SINFONI	VLT
J234625.67001600.4	2012-08-03		TRIPLESPEC	Palomar 200-inch
J234628.20124900.0	2011-09-22		SofI	NTT
J234704.25+150146.3	2012-10-01	2.1565	XSHOOTER	VLT
J234856.49104131.2	2011-09-21		SofI	NTT
J234913.76-371258.9	2012-10-15		XSHOOTER	VLT
J235443.75293850.6	2009-07-02	2.3782	SINFONI	VLT
J235808.55012507.3	2011-09-10		TRIPLESPEC	Palomar 200-inch
J235843.28021220.1	2011-09-08		TRIPLESPEC	Palomar 200-inch

BIBLIOGRAPHY

- Aihara, H. et al. (2011). "The Eighth Data Release of the Sloan Digital Sky Survey: First Data from SDSS-III." In: *ApJS* 193, 29, p. 29. DOI: [10.1088/0067-0049/193/2/29](https://doi.org/10.1088/0067-0049/193/2/29). arXiv: [1101.1559 \[astro-ph.IM\]](https://arxiv.org/abs/1101.1559).
- Alexander, D. M. and R. C. Hickox (2012). "What drives the growth of black holes?" In: *New Astron. Rev.* 56, pp. 93–121. DOI: [10.1016/j.newar.2011.11.003](https://doi.org/10.1016/j.newar.2011.11.003). arXiv: [1112.1949](https://arxiv.org/abs/1112.1949).
- Allen, J. T., P. C. Hewett, N. Maddox, G. T. Richards, and V. Belokurov (2011). "A strong redshift dependence of the broad absorption line quasar fraction." In: *MNRAS* 410, pp. 860–884.
- Allen, J. T., P. C. Hewett, C. T. Richardson, G. J. Ferland, and J. A. Baldwin (2013). "Classification and analysis of emission-line galaxies using mean field independent component analysis." In: *MNRAS* 430, pp. 3510–3536. DOI: [10.1093/mnras/stt151](https://doi.org/10.1093/mnras/stt151). arXiv: [1301.5930](https://arxiv.org/abs/1301.5930).
- Antonucci, R. (1993). "Unified models for active galactic nuclei and quasars." In: *ARA&A* 31, pp. 473–521. DOI: [10.1146/annurev.aa.31.090193.002353](https://doi.org/10.1146/annurev.aa.31.090193.002353).
- Assef, R. J. et al. (2011). "Black Hole Mass Estimates Based on C IV are Consistent with Those Based on the Balmer Lines." In: *ApJ* 742, p. 93.
- Banerji, M., R. G. McMahon, P. C. Hewett, S. Alaghband-Zadeh, E. Gonzalez-Solares, B. P. Venemans, and M. J. Hawthorn (2012). "Heavily reddened quasars at $z \sim 2$ in the UKIDSS Large Area Survey: a transitional phase in AGN evolution." In: *MNRAS* 427, pp. 2275–2291. DOI: [10.1111/j.1365-2966.2012.22099.x](https://doi.org/10.1111/j.1365-2966.2012.22099.x). arXiv: [1203.5530 \[astro-ph.CO\]](https://arxiv.org/abs/1203.5530).
- Banerji, M., R. G. McMahon, P. C. Hewett, E. Gonzalez-Solares, and S. E. Koposov (2013). "Hyperluminous reddened broad-line quasars at $z \sim 2$ from the VISTA Hemisphere Survey and WISE all-sky survey." In: *MNRAS* 429, pp. L55–L59. DOI: [10.1093/mnrasl/sls023](https://doi.org/10.1093/mnrasl/sls023). arXiv: [1210.6668 \[astro-ph.CO\]](https://arxiv.org/abs/1210.6668).
- Barvainis, R. (1992). "Dust reverberation - A model for the infrared variations of Fairall 9." In: *ApJ* 400, pp. 502–509. DOI: [10.1086/172012](https://doi.org/10.1086/172012).
- Baskin, A. and A. Laor (2005a). "What controls the CIV line profile in active galactic nuclei?" In: *MNRAS* 356, pp. 1029–1044.
- (2005b). "What controls the [OIII] $\lambda 5007$ line strength in active galactic nuclei?" In: *MNRAS* 358, pp. 1043–1054. DOI: [10.1111/j.1365-2966.2005.08841.x](https://doi.org/10.1111/j.1365-2966.2005.08841.x). eprint: [astro-ph/0501436](https://arxiv.org/abs/astro-ph/0501436).
- Becker, G. D., P. C. Hewett, G. Worseck, and J. X. Prochaska (2013). "A refined measurement of the mean transmitted flux in the Ly α

- forest over $2 < z < 5$ using composite quasar spectra." In: *MNRAS* 430, pp. 2067–2081. doi: [10.1093/mnras/stt031](https://doi.org/10.1093/mnras/stt031). arXiv: [1208.2584 \[astro-ph.CO\]](https://arxiv.org/abs/1208.2584).
- Becker, R. H., R. L. White, and D. J. Helfand (1995). "The FIRST Survey: Faint Images of the Radio Sky at Twenty Centimeters." In: *ApJ* 450, p. 559. doi: [10.1086/176166](https://doi.org/10.1086/176166).
- Bentz, M. C. et al. (2009). "The Lick AGN Monitoring Project: Broad-line Region Radii and Black Hole Masses from Reverberation Mapping of H β ." In: *ApJ* 705, pp. 199–217. doi: [10.1088/0004-637X/705/1/199](https://doi.org/10.1088/0004-637X/705/1/199). arXiv: [0908.0003](https://arxiv.org/abs/0908.0003).
- Blecha, L., T. J. Cox, A. Loeb, and L. Hernquist (2011). "Recoiling black holes in merging galaxies: relationship to active galactic nucleus lifetimes, starbursts and the $M_{BH}-\sigma_*$ relation." In: *MNRAS* 412, pp. 2154–2182. doi: [10.1111/j.1365-2966.2010.18042.x](https://doi.org/10.1111/j.1365-2966.2010.18042.x). arXiv: [1009.4940 \[astro-ph.CO\]](https://arxiv.org/abs/1009.4940).
- Bonnet, H. et al. (2004). "First light of SINFONI at the VLT." In: *The Messenger* 117, pp. 17–24.
- Boroson, T. A. and R. F. Green (1992). "The emission-line properties of low-redshift quasi-stellar objects." In: *ApJS* 80, pp. 109–135.
- Boyle, B. J. and R. J. Terlevich (1998). "The cosmological evolution of the QSO luminosity density and of the star formation rate." In: *MNRAS* 293, pp. L49–L51.
- Brandt, W. N. and G. Hasinger (2005). "Deep Extragalactic X-Ray Surveys." In: *ARA&A* 43, pp. 827–859.
- Brotherton, M. S. (1996). "The Profiles of H beta and [O iii] lambda 5007 in Radio-loud Quasars." In: *ApJS* 102, p. 1. doi: [10.1086/192249](https://doi.org/10.1086/192249). eprint: [astro-ph/9507067](https://arxiv.org/abs/astro-ph/9507067).
- Brotherton, M. S. and P. J. Francis (1999). "The Intermediate Line Region and the Baldwin Effect." In: *Quasars and Cosmology*. Ed. by G. Ferland and J. Baldwin. Vol. 162. Astronomical Society of the Pacific Conference Series, p. 395. eprint: [astro-ph/9811088](https://arxiv.org/abs/astro-ph/9811088).
- Brotherton, M. S., V. Singh, and J. Runnoe (2015). "Orientation and quasar black hole mass estimation." In: *MNRAS* 454, pp. 3864–3871.
- Brotherton, M. S., J. C. Runnoe, Z. Shang, and M. A. DiPompeo (2015). "Bias in C IV-based quasar black hole mass scaling relationships from reverberation mapped samples." In: *MNRAS* 451, pp. 1290–1298.
- Brusa, M. et al. (2010). "The XMM-Newton Wide-field Survey in the Cosmos Field (XMM-COSMOS): Demography and Multiwavelength Properties of Obscured and Unobscured Luminous Active Galactic Nuclei." In: *ApJ* 716, pp. 348–369. doi: [10.1088/0004-637X/716/1/348](https://doi.org/10.1088/0004-637X/716/1/348). arXiv: [1004.2790 \[astro-ph.CO\]](https://arxiv.org/abs/1004.2790).
- Brusa, M. et al. (2015). "X-shooter reveals powerful outflows in $z \sim 1.5$ X-ray selected obscured quasi-stellar objects." In: *MNRAS* 446, pp. 2394–2417. doi: [10.1093/mnras/stu2117](https://doi.org/10.1093/mnras/stu2117). arXiv: [1409.1615](https://arxiv.org/abs/1409.1615).

- Cappellari, M., E. K. Verolme, R. P. van der Marel, G. A. Verdoes Kleijn, G. D. Illingworth, M. Franx, C. M. Carollo, and P. T. de Zeeuw (2002). "The Counterrotating Core and the Black Hole Mass of IC 1459." In: *ApJ* 578, pp. 787–805.
- Carniani, S. et al. (2015). "Ionised outflows in $z \sim 2.4$ quasar host galaxies." In: *A&A* 580, A102, A102. DOI: [10.1051/0004-6361/201526557](https://doi.org/10.1051/0004-6361/201526557). arXiv: [1506.03096](https://arxiv.org/abs/1506.03096).
- Coatman, L., P. C. Hewett, M. Banerji, and G. T. Richards (2016). "CIV emission-line properties and systematic trends in quasar black hole mass estimates." In: *MNRAS* 461, pp. 647–665. DOI: [10.1093/mnras/stw1360](https://doi.org/10.1093/mnras/stw1360). arXiv: [1606.02726](https://arxiv.org/abs/1606.02726).
- Collin, S., T. Kawaguchi, B. M. Peterson, and M. Vestergaard (2006). "Systematic effects in measurement of black hole masses by emission-line reverberation of active galactic nuclei: Eddington ratio and inclination." In: *A&A* 456, pp. 75–90. DOI: [10.1051/0004-6361:20064878](https://doi.org/10.1051/0004-6361:20064878). eprint: [astro-ph/0603460](https://arxiv.org/abs/astro-ph/0603460).
- Cutri, R. M. et al. (2013). *Explanatory Supplement to the AllWISE Data Release Products*. Tech. rep., p. 1.
- Dall'Aglio, A., L. Wisotzki, and G. Worseck (2008). "An unbiased measurement of the UV background and its evolution via the proximity effect in quasar spectra." In: *A&A* 491, pp. 465–481. DOI: [10.1051/0004-6361:200810724](https://doi.org/10.1051/0004-6361:200810724). arXiv: [0807.5089](https://arxiv.org/abs/0807.5089).
- Dawson, K. S. et al. (2013). "The Baryon Oscillation Spectroscopic Survey of SDSS-III." In: *AJ* 145, p. 10.
- Dekker, H., S. D'Odorico, A. Kaufer, B. Delabre, and H. Kotzlowski (2000). "Design, construction, and performance of UVES, the echelle spectrograph for the UT2 Kueyen Telescope at the ESO Paranal Observatory." In: *Optical and IR Telescope Instrumentation and Detectors*. Ed. by M. Iye and A. F. Moorwood. Vol. 4008. Proc. SPIE, pp. 534–545.
- Denney, K. D. (2012). "Are Outflows Biassing Single-epoch C IV Black Hole Mass Estimates?" In: *ApJ* 759, p. 44.
- Denney, K. D. et al. (2010). "Reverberation Mapping Measurements of Black Hole Masses in Six Local Seyfert Galaxies." In: *ApJ* 721, pp. 715–737.
- Denney, K. D., R. W. Pogge, R. J. Assef, C. S. Kochanek, B. M. Peterson, and M. Vestergaard (2013). "C IV Line-width Anomalies: The Perils of Low Signal-to-noise Spectra." In: *ApJ* 775, p. 60.
- Dunlop, J. S., R. J. McLure, M. J. Kukula, S. A. Baum, C. P. O'Dea, and D. H. Hughes (2003). "Quasars, their host galaxies and their central black holes." In: *MNRAS* 340, pp. 1095–1135. DOI: [10.1046/j.1365-8711.2003.06333.x](https://doi.org/10.1046/j.1365-8711.2003.06333.x). eprint: [astro-ph/0108397](https://arxiv.org/abs/astro-ph/0108397).
- Edge, A., W. Sutherland, K. Kuijken, S. Driver, R. McMahon, S. Eales, and J. P. Emerson (2013). "The VISTA Kilo-degree Infrared Galaxy (VIKING) Survey: Bridging the Gap between Low and High Redshift." In: *The Messenger* 154, pp. 32–34.

- Eisenhauer, F. et al. (2003). "SINFONI - Integral field spectroscopy at 50 milli-arcsecond resolution with the ESO VLT." In: *Instrument Design and Performance for Optical/Infrared Ground-based Telescopes*. Ed. by M. Iye and A. F. M. Moorwood. Vol. 4841. Proc. SPIE, pp. 1548–1561. doi: [10.1117/12.459468](https://doi.org/10.1117/12.459468). eprint: [astro-ph/0306191](https://arxiv.org/abs/astro-ph/0306191).
- Elias, J. H., R. R. Joyce, M. Liang, G. P. Muller, E. A. Hileman, and J. R. George (2006). "Design of the Gemini near-infrared spectrograph." In: *Society of Photo-Optical Instrumentation Engineers (SPIE) Conference Series*. Vol. 6269. Proc. SPIE, p. 62694C. doi: [10.1117/12.671817](https://doi.org/10.1117/12.671817).
- Elvis, M., B. J. Wilkes, J. C. McDowell, R. F. Green, J. Bechtold, S. P. Willner, M. S. Oey, E. Polomski, and R. Cutri (1994). "Atlas of quasar energy distributions." In: *ApJS* 95, pp. 1–68. doi: [10.1086/192093](https://doi.org/10.1086/192093).
- Elvis, M. et al. (2012). "Spectral Energy Distributions of Type 1 Active Galactic Nuclei in the COSMOS Survey. I. The XMM-COSMOS Sample." In: *ApJ* 759, 6, p. 6. doi: [10.1088/0004-637X/759/1/6](https://doi.org/10.1088/0004-637X/759/1/6). arXiv: [1209.1478 \[astro-ph.CO\]](https://arxiv.org/abs/1209.1478).
- Everett, J. E. (2005). "Radiative Transfer and Acceleration in Magnetocentrifugal Winds." In: *ApJ* 631, pp. 689–706.
- Fabian, A. C. (2012). "Observational Evidence of Active Galactic Nuclei Feedback." In: *ARA&A* 50, pp. 455–489. doi: [10.1146/annurev-astro-081811-125521](https://doi.org/10.1146/annurev-astro-081811-125521). arXiv: [1204.4114](https://arxiv.org/abs/1204.4114).
- Ferrarese, L. and D. Merritt (2000). "A Fundamental Relation between Supermassive Black Holes and Their Host Galaxies." In: *ApJ* 539, pp. L9–L12.
- Font-Ribera, A. et al. (2013). "The large-scale quasar-Lyman α forest cross-correlation from BOSS." In: *J. Cosmology Astropart. Phys.* 5, 018, p. 018. doi: [10.1088/1475-7516/2013/05/018](https://doi.org/10.1088/1475-7516/2013/05/018). arXiv: [1303.1937](https://arxiv.org/abs/1303.1937).
- Foreman-Mackey, D., D. W. Hogg, D. Lang, and J. Goodman (2013). "emcee: The MCMC Hammer." In: *PASP* 125, pp. 306–312. doi: [10.1088/670067](https://doi.org/10.1088/670067). arXiv: [1202.3665 \[astro-ph.IM\]](https://arxiv.org/abs/1202.3665).
- Francis, P. J., P. C. Hewett, C. B. Foltz, F. H. Chaffee, R. J. Weymann, and S. L. Morris (1991). "A high signal-to-noise ratio composite quasar spectrum." In: *ApJ* 373, pp. 465–470. doi: [10.1086/170066](https://doi.org/10.1086/170066).
- Gallagher, S. C., J. E. Everett, M. M. Abado, and S. K. Keating (2015). "Investigating the structure of the windy torus in quasars." In: *MNRAS* 451, pp. 2991–3000.
- Gaskell, C. M. (1982). "A redshift difference between high and low ionization emission-line regions in QSOs - Evidence for radial motions." In: *ApJ* 263, pp. 79–86.
- Gavignaud, I. et al. (2008). "Eddington ratios of faint AGN at intermediate redshift: evidence for a population of half-starved black holes." In: *A&A* 492, pp. 637–650.

- Gebhardt, K. et al. (2000). "A Relationship between Nuclear Black Hole Mass and Galaxy Velocity Dispersion." In: *ApJ* 539, pp. L13–L16.
- Glikman, E. et al. (2012). "FIRST-2MASS Red Quasars: Transitional Objects Emerging from the Dust." In: *ApJ* 757, 51, p. 51. doi: [10.1088/0004-637X/757/1/51](https://doi.org/10.1088/0004-637X/757/1/51). arXiv: [1207.2175 \[astro-ph.CO\]](https://arxiv.org/abs/1207.2175).
- Greene, J. E. and L. C. Ho (2005). "Estimating Black Hole Masses in Active Galaxies Using the H α Emission Line." In: *ApJ* 630, pp. 122–129. doi: [10.1086/431897](https://doi.org/10.1086/431897). eprint: [astro-ph/0508335](https://arxiv.org/abs/astro-ph/0508335).
- Hall, P., P. Hopkins, M. Strauss, G. Richards, and J. Brinkmann (2004). "SDSS Quasars and Dust Reddening." In: *AGN Physics with the Sloan Digital Sky Survey*. Ed. by G. T. Richards and P. B. Hall. Vol. 311. Astronomical Society of the Pacific Conference Series, p. 65. eprint: [astro-ph/0312281](https://arxiv.org/abs/astro-ph/0312281).
- Hao, H. et al. (2010). "Hot-dust-poor Type 1 Active Galactic Nuclei in the COSMOS Survey." In: *ApJ* 724, pp. L59–L63. doi: [10.1088/2041-8205/724/1/L59](https://doi.org/10.1088/2041-8205/724/1/L59). arXiv: [1009.3276 \[astro-ph.CO\]](https://arxiv.org/abs/1009.3276).
- Hao, H., M. Elvis, F. Civano, and A. Lawrence (2011). "Hot-dust-poor Quasars in Mid-infrared and Optically Selected Samples." In: *ApJ* 733, 108, p. 108. doi: [10.1088/0004-637X/733/2/108](https://doi.org/10.1088/0004-637X/733/2/108). arXiv: [1011.0429 \[astro-ph.CO\]](https://arxiv.org/abs/1011.0429).
- Hao, H. et al. (2013). "A quasar-galaxy mixing diagram: quasar spectral energy distribution shapes in the optical to near-infrared." In: *MNRAS* 434, pp. 3104–3121. doi: [10.1093/mnras/stt1228](https://doi.org/10.1093/mnras/stt1228). arXiv: [1210.3044 \[astro-ph.GA\]](https://arxiv.org/abs/1210.3044).
- Harrison, C. M., D. M. Alexander, J. R. Mullaney, J. P. Stott, A. M. Swinbank, V. Arumugam, F. E. Bauer, R. G. Bower, A. J. Bunker, and R. M. Sharples (2016). "The KMOS AGN Survey at High redshift (KASHz): the prevalence and drivers of ionized outflows in the host galaxies of X-ray AGN." In: *MNRAS* 456, pp. 1195–1220. doi: [10.1093/mnras/stv2727](https://doi.org/10.1093/mnras/stv2727).
- Heckman, T. M. and P. N. Best (2014). "The Coevolution of Galaxies and Supermassive Black Holes: Insights from Surveys of the Contemporary Universe." In: *ARA&A* 52, pp. 589–660. doi: [10.1146/annurev-astro-081913-035722](https://doi.org/10.1146/annurev-astro-081913-035722). arXiv: [1403.4620](https://arxiv.org/abs/1403.4620).
- Hennawi, J. F. et al. (2006a). "Binary Quasars in the Sloan Digital Sky Survey: Evidence for Excess Clustering on Small Scales." In: *AJ* 131, pp. 1–23. doi: [10.1086/498235](https://doi.org/10.1086/498235). eprint: [astro-ph/0504535](https://arxiv.org/abs/astro-ph/0504535).
- Hennawi, J. F. et al. (2006b). "Quasars Probing Quasars. I. Optically Thick Absorbers near Luminous Quasars." In: *ApJ* 651, pp. 61–83. doi: [10.1086/507069](https://doi.org/10.1086/507069). eprint: [astro-ph/0603742](https://arxiv.org/abs/astro-ph/0603742).
- Hennawi, J. F. et al. (2010). "Binary Quasars at High Redshift. I. 24 New Quasar Pairs at $z \sim 3\text{--}4$." In: *ApJ* 719, pp. 1672–1692. doi: [10.1088/0004-637X/719/2/1672](https://doi.org/10.1088/0004-637X/719/2/1672). arXiv: [0908.3907](https://arxiv.org/abs/0908.3907).
- Hennawi, J. F., J. X. Prochaska, S. Cantalupo, and F. Arrigoni-Battaia (2015). "Quasar quartet embedded in giant nebula reveals rare

- massive structure in distant universe." In: *Science* 348, pp. 779–783. doi: [10.1126/science.aaa5397](https://doi.org/10.1126/science.aaa5397). arXiv: [1505.03786](https://arxiv.org/abs/1505.03786).
- Hewett, P. C. and V. Wild (2010). "Improved redshifts for SDSS quasar spectra." In: *MNRAS* 405, pp. 2302–2316.
- Hewett, P. C., S. J. Warren, S. K. Leggett, and S. T. Hodgkin (2006). "The UKIRT Infrared Deep Sky Survey ZY JHK photometric system: passbands and synthetic colours." In: *MNRAS* 367, pp. 454–468. doi: [10.1111/j.1365-2966.2005.09969.x](https://doi.org/10.1111/j.1365-2966.2005.09969.x). eprint: [astro-ph/0601592](https://arxiv.org/abs/astro-ph/0601592).
- Higginbottom, N. and D. Proga (2015). "Coronae and Winds from Irradiated Disks in X-Ray Binaries." In: *ApJ* 807, p. 107.
- Hodapp, K. W. et al. (2003). "The Gemini Near-Infrared Imager (NIRI)." In: *PASP* 115, pp. 1388–1406. doi: [10.1086/379669](https://doi.org/10.1086/379669).
- Hogg, D. W., J. Bovy, and D. Lang (2010). "Data analysis recipes: Fitting a model to data." In: *ArXiv e-prints*. arXiv: [1008.4686](https://arxiv.org/abs/1008.4686) [[astro-ph.IM](#)].
- Hopkins, P. F. and L. Hernquist (2006). "Fueling Low-Level AGN Activity through Stochastic Accretion of Cold Gas." In: *ApJS* 166, pp. 1–36. doi: [10.1086/505753](https://doi.org/10.1086/505753). eprint: [astro-ph/0603180](https://arxiv.org/abs/astro-ph/0603180).
- Hopkins, P. F., L. Hernquist, T. J. Cox, T. Di Matteo, B. Robertson, and V. Springel (2006). "A Unified, Merger-driven Model of the Origin of Starbursts, Quasars, the Cosmic X-Ray Background, Supermassive Black Holes, and Galaxy Spheroids." In: *ApJS* 163, pp. 1–49. doi: [10.1086/499298](https://doi.org/10.1086/499298). eprint: [astro-ph/0506398](https://arxiv.org/abs/astro-ph/0506398).
- Jackson, N. and I. W. A. Browne (1991). "Optical Properties of Quasars - Part Two - Emission Line Geometry and Radio Properties." In: *MNRAS* 250, p. 422. doi: [10.1093/mnras/250.2.422](https://doi.org/10.1093/mnras/250.2.422).
- Jarvis, M. J. and R. J. McLure (2006). "Orientation dependency of broad-line widths in quasars and consequences for black hole mass estimation." In: *MNRAS* 369, pp. 182–188.
- Jiang, L. et al. (2010). "Dust-free quasars in the early Universe." In: *Nature* 464, pp. 380–383. doi: [10.1038/nature08877](https://doi.org/10.1038/nature08877). arXiv: [1003.3432](https://arxiv.org/abs/1003.3432) [[astro-ph.CO](#)].
- Kaspi, S., P. S. Smith, H. Netzer, D. Maoz, B. T. Jannuzi, and U. Giveon (2000). "Reverberation Measurements for 17 Quasars and the Size-Mass-Luminosity Relations in Active Galactic Nuclei." In: *ApJ* 533, pp. 631–649.
- Kaspi, S., W. N. Brandt, D. Maoz, H. Netzer, D. P. Schneider, and O. Shemmer (2007). "Reverberation Mapping of High-Luminosity Quasars: First Results." In: *ApJ* 659, pp. 997–1007.
- Kauffmann, G. and M. Haehnelt (2000). "A unified model for the evolution of galaxies and quasars." In: *MNRAS* 311, pp. 576–588. doi: [10.1046/j.1365-8711.2000.03077.x](https://doi.org/10.1046/j.1365-8711.2000.03077.x). eprint: [astro-ph/9906493](https://arxiv.org/abs/astro-ph/9906493).

- Kelly, B. C. and Y. Shen (2013). "The Demographics of Broad-line Quasars in the Mass-Luminosity Plane. II. Black Hole Mass and Eddington Ratio Functions." In: *ApJ* 764, p. 45.
- Kelly, B. C., M. Vestergaard, X. Fan, P. Hopkins, L. Hernquist, and A. Siemiginowska (2010). "Constraints on Black Hole Growth, Quasar Lifetimes, and Eddington Ratio Distributions from the SDSS Broad-line Quasar Black Hole Mass Function." In: *ApJ* 719, pp. 1315–1334.
- Kim, M., L. C. Ho, C. J. Lonsdale, M. Lacy, A. W. Blain, and A. E. Kimball (2013). "Evidence for Active Galactic Nucleus Driven Outflows in Young Radio Quasars." In: *ApJ* 768, L9, p. L9. doi: [10.1088/2041-8205/768/1/L9](https://doi.org/10.1088/2041-8205/768/1/L9). arXiv: [1303.7194](https://arxiv.org/abs/1303.7194).
- King, A. L. et al. (2015). "Simulations of the OzDES AGN reverberation mapping project." In: *MNRAS* 453, pp. 1701–1726.
- King, A. and K. Pounds (2015). "Powerful Outflows and Feedback from Active Galactic Nuclei." In: *ARA&A* 53, pp. 115–154.
- Kollatschny, W. and M. Zetzl (2011). "Broad-line active galactic nuclei rotate faster than narrow-line ones." In: *Nature* 470, pp. 366–368. doi: [10.1038/nature09761](https://doi.org/10.1038/nature09761).
- (2013). "The shape of broad-line profiles in active galactic nuclei." In: *A&A* 549, A100, A100. doi: [10.1051/0004-6361/201219411](https://doi.org/10.1051/0004-6361/201219411). arXiv: [1211.3065](https://arxiv.org/abs/1211.3065).
- Kollmeier, J. A. et al. (2006). "Black Hole Masses and Eddington Ratios at $0.3 < z < 4$." In: *ApJ* 648, pp. 128–139. doi: [10.1086/505646](https://doi.org/10.1086/505646). eprint: [astro-ph/0508657](https://arxiv.org/abs/astro-ph/0508657).
- Konigl, A. and J. F. Kartje (1994). "Disk-driven hydromagnetic winds as a key ingredient of active galactic nuclei unification schemes." In: *ApJ* 434, pp. 446–467.
- Kormendy, J. and L. C. Ho (2013). "Coevolution (Or Not) of Supermassive Black Holes and Host Galaxies." In: *ARA&A* 51, pp. 511–653.
- Kratzer, R. M. and G. T. Richards (2015). "Mean and Extreme Radio Properties of Quasars and the Origin of Radio Emission." In: *AJ* 149, p. 61.
- Krawczyk, C. M., G. T. Richards, S. S. Mehta, M. S. Vogeley, S. C. Gallagher, K. M. Leighly, N. P. Ross, and D. P. Schneider (2013). "Mean Spectral Energy Distributions and Bolometric Corrections for Luminous Quasars." In: *ApJS* 206, p. 4.
- Krolik, J. H. and M. C. Begelman (1988). "Molecular tori in Seyfert galaxies - Feeding the monster and hiding it." In: *ApJ* 329, pp. 702–711. doi: [10.1086/166414](https://doi.org/10.1086/166414).
- Kuraszkiewicz, J. K. et al. (2003). "The Far-Infrared Spectral Energy Distributions of X-Ray-selected Active Galaxies." In: *ApJ* 590, pp. 128–148. doi: [10.1086/374919](https://doi.org/10.1086/374919). eprint: [astro-ph/0302572](https://arxiv.org/abs/astro-ph/0302572).
- Lau, M. W., J. X. Prochaska, and J. F. Hennawi (2015). "Quasars Probing Quasars VIII. The Physical Properties of the Cool Circum-

- galactic medium Surrounding $z \sim 2\text{--}3$ Massive Galaxies." In: *ArXiv e-prints*. arXiv: [1510.06018](#).
- Lawrence, A. (1991). "The relative frequency of broad-lined and narrow-lined active galactic nuclei - Implications for unified schemes." In: *MNRAS* 252, pp. 586–592.
- Lawrence, A. and M. Elvis (2010). "Misaligned Disks as Obscurers in Active Galaxies." In: *ApJ* 714, pp. 561–570. DOI: [10.1088/0004-637X/714/1/561](#).
- Lawrence, A. et al. (2007). "The UKIRT Infrared Deep Sky Survey (UKIDSS)." In: *MNRAS* 379, pp. 1599–1617.
- Lee, K.-G. et al. (2013). "The BOSS Ly α Forest Sample from SDSS Data Release 9." In: *AJ* 145, 69, p. 69. DOI: [10.1088/0004-6256/145/3/69](#). arXiv: [1211.5146](#).
- Leighly, K. M. (2004). "Hubble Space Telescope STIS Ultraviolet Spectral Evidence of Outflow in Extreme Narrow-Line Seyfert 1 Galaxies. II. Modeling and Interpretation." In: *ApJ* 611, pp. 125–152.
- Leipski, C., K. Meisenheimer, F. Walter, U. Klaas, H. Dannerbauer, G. De Rosa, X. Fan, M. Haas, O. Krause, and H.-W. Rix (2014). "Spectral Energy Distributions of QSOs at $z > 5$: Common Active Galactic Nucleus-heated Dust and Occasionally Strong Star-formation." In: *ApJ* 785, 154, p. 154. DOI: [10.1088/0004-637X/785/2/154](#). arXiv: [1402.5976 \[astro-ph.GA\]](#).
- Lopez, S. et al. (2016). "XQ-100: A legacy survey of one hundred $3.5 < z < 4.5$ quasars observed with VLT/XSHOOTER." In: *ArXiv e-prints*. arXiv: [1607.08776](#).
- Luo, B. et al. (2015). "X-ray Insights into the Nature of PHL 1811 Analogs and Weak Emission-line Quasars: Unification with a Geometrically Thick Accretion Disk?" In: *ApJ* 805, p. 122.
- Lusso, E. et al. (2010). "The X-ray to optical-UV luminosity ratio of X-ray selected type 1 AGN in XMM-COSMOS." In: *A&A* 512, A34, A34. DOI: [10.1051/0004-6361/200913298](#). arXiv: [0912.4166 \[astro-ph.CO\]](#).
- Lynden-Bell, D. (1969). "Galactic Nuclei as Collapsed Old Quasars." In: *Nature* 223, pp. 690–694. DOI: [10.1038/223690a0](#).
- MacLeod, C. L. et al. (2010). "Modeling the Time Variability of SDSS Stripe 82 Quasars as a Damped Random Walk." In: *ApJ* 721, pp. 1014–1033. DOI: [10.1088/0004-637X/721/2/1014](#). arXiv: [1004.0276 \[astro-ph.CO\]](#).
- MacLeod, C. L. et al. (2016). "A systematic search for changing-look quasars in SDSS." In: *MNRAS* 457, pp. 389–404. DOI: [10.1093/mnras/stv2997](#). arXiv: [1509.08393](#).
- Madau, P. and M. Dickinson (2014). "Cosmic Star-Formation History." In: *ARA&A* 52, pp. 415–486. DOI: [10.1146/annurev-astro-081811-125615](#). arXiv: [1403.0007](#).

- Maddox, N. and P. C. Hewett (2006). "Simulating wide-field quasar surveys from the optical to near-infrared." In: *MNRAS* 367, pp. 717–731.
- Maddox, N., P. C. Hewett, C. Péroux, D. B. Nestor, and L. Wisotzki (2012). "The large area KX quasar catalogue - I. Analysis of the photometric redshift selection and the complete quasar catalogue." In: *MNRAS* 424, pp. 2876–2895. DOI: [10.1111/j.1365-2966.2012.21427.x](https://doi.org/10.1111/j.1365-2966.2012.21427.x). arXiv: [1206.1434](https://arxiv.org/abs/1206.1434).
- Mainzer, A. et al. (2011). "Preliminary Results from NEOWISE: An Enhancement to the Wide-field Infrared Survey Explorer for Solar System Science." In: *ApJ* 731, 53, p. 53. DOI: [10.1088/0004-637X/731/1/53](https://doi.org/10.1088/0004-637X/731/1/53). arXiv: [1102.1996 \[astro-ph.EP\]](https://arxiv.org/abs/1102.1996).
- Manchado, A. et al. (1998). "LIRIS: a long-slit intermediate-resolution infrared spectrograph for the WHT." In: *Infrared Astronomical Instrumentation*. Ed. by A. M. Fowler. Vol. 3354. Proc. SPIE, pp. 448–455.
- Mannucci, F., F. Basile, B. M. Poggianti, A. Cimatti, E. Daddi, L. Pozzetti, and L. Vanzi (2001). "Near-infrared template spectra of normal galaxies: k-corrections, galaxy models and stellar populations." In: *MNRAS* 326, pp. 745–758. DOI: [10.1046/j.1365-8711.2001.04628.x](https://doi.org/10.1046/j.1365-8711.2001.04628.x). eprint: [astro-ph/0104427](https://arxiv.org/abs/astro-ph/0104427).
- Marchese, E., R. Della Ceca, A. Caccianiga, P. Severgnini, A. Corral, and R. Fanali (2012). "The optical-UV spectral energy distribution of the unabsorbed AGN population in the XMM-Newton Bright Serendipitous Survey." In: *A&A* 539, A48, A48. DOI: [10.1051/0004-6361/201117562](https://doi.org/10.1051/0004-6361/201117562). arXiv: [1111.4409 \[astro-ph.CO\]](https://arxiv.org/abs/1111.4409).
- Marziani, P., R. K. Zamanov, J. W. Sulentic, and M. Calvani (2003). "Searching for the physical drivers of eigenvector 1: influence of black hole mass and Eddington ratio." In: *MNRAS* 345, pp. 1133–1144.
- Marziani, P., J. W. Sulentic, G. M. Stirpe, S. Zamfir, and M. Calvani (2009). "VLT/ISAAC spectra of the H β region in intermediate-redshift quasars. III. H β broad-line profile analysis and inferences about BLR structure." In: *A&A* 495, pp. 83–112. DOI: [10.1051/0004-6361:200810764](https://doi.org/10.1051/0004-6361:200810764). arXiv: [0812.0251](https://arxiv.org/abs/0812.0251).
- Marziani, P., J. W. Sulentic, I. Plauchu-Frayn, and A. del Olmo (2013). "Is MgII λ 2800 a reliable virial broadening estimator for quasars?" In: *A&A* 555, A89, A89. DOI: [10.1051/0004-6361/201321374](https://doi.org/10.1051/0004-6361/201321374). arXiv: [1305.1096](https://arxiv.org/abs/1305.1096).
- Marziani, P., M. A. Martínez Carballo, J. W. Sulentic, A. Del Olmo, G. M. Stirpe, and D. Dultzin (2016). "The most powerful quasar outflows as revealed by the Civ λ 1549 resonance line." In: *Ap&SS* 361, 29, p. 29. DOI: [10.1007/s10509-015-2611-1](https://doi.org/10.1007/s10509-015-2611-1). arXiv: [1512.00381](https://arxiv.org/abs/1512.00381).

- McGill, K. L., J.-H. Woo, T. Treu, and M. A. Malkan (2008). "Comparing and Calibrating Black Hole Mass Estimators for Distant Active Galactic Nuclei." In: *ApJ* 673, pp. 703–714.
- McLean, I. S. et al. (1998). "Design and development of NIRSPEC: a near-infrared echelle spectrograph for the Keck II telescope." In: *Infrared Astronomical Instrumentation*. Ed. by A. M. Fowler. Vol. 3354. Proc. SPIE, pp. 566–578.
- McLure, R. J. and M. J. Jarvis (2002). "Measuring the black hole masses of high-redshift quasars." In: *MNRAS* 337, pp. 109–116. doi: [10.1046/j.1365-8711.2002.05871.x](https://doi.org/10.1046/j.1365-8711.2002.05871.x). eprint: [astro-ph/0204473](https://arxiv.org/abs/astro-ph/0204473).
- McMahon, R. G., M. Banerji, E. Gonzalez, S. E. Koposov, V. J. Bejar, N. Lodieu, R. Rebolo, and VHS Collaboration (2013). "First Scientific Results from the VISTA Hemisphere Survey (VHS)." In: *The Messenger* 154, pp. 35–37.
- Mejía-Restrepo, J. E., B. Trakhtenbrot, P. Lira, H. Netzer, and D. M. Capellupo (2016). "Active galactic nuclei at $z \sim 1.5$ - II. Black hole mass estimation by means of broad emission lines." In: *MNRAS* 460, pp. 187–211.
- Moorwood, A., J.-G. Cuby, and C. Lidman (1998). "SOFI sees first light at the NTT." In: *The Messenger* 91, pp. 9–13.
- Moorwood, A. et al. (1998). "ISAAC sees first light at the VLT." In: *The Messenger* 94, pp. 7–9.
- Mortlock, D. J. et al. (2011). "A luminous quasar at a redshift of $z = 7.085$." In: *Nature* 474, pp. 616–619. doi: [10.1038/nature10159](https://doi.org/10.1038/nature10159). arXiv: [1106.6088 \[astro-ph.CO\]](https://arxiv.org/abs/1106.6088).
- Mullaney, J. R., D. M. Alexander, S. Fine, A. D. Goulding, C. M. Harrison, and R. C. Hickox (2013). "Narrow-line region gas kinematics of 24–264 optically selected AGN: the radio connection." In: *MNRAS* 433, pp. 622–638. doi: [10.1093/mnras/stt751](https://doi.org/10.1093/mnras/stt751). arXiv: [1305.0263](https://arxiv.org/abs/1305.0263).
- Murray, N., J. Chiang, S. A. Grossman, and G. M. Voit (1995). "Accretion Disk Winds from Active Galactic Nuclei." In: *ApJ* 451, p. 498.
- Narayanan, D. et al. (2010). "A physical model for $z \sim 2$ dust-obscured galaxies." In: *MNRAS* 407, pp. 1701–1720. doi: [10.1111/j.1365-2966.2010.16997.x](https://doi.org/10.1111/j.1365-2966.2010.16997.x). arXiv: [0910.2234 \[astro-ph.CO\]](https://arxiv.org/abs/0910.2234).
- Nesvadba, N. P. H., M. D. Lehnert, C. De Breuck, A. M. Gilbert, and W. van Breugel (2008). "Evidence for powerful AGN winds at high redshift: dynamics of galactic outflows in radio galaxies during the ‘Quasar Era’." In: *A&A* 491, pp. 407–424. doi: [10.1051/0004-6361:200810346](https://doi.org/10.1051/0004-6361:200810346). arXiv: [0809.5171](https://arxiv.org/abs/0809.5171).
- Netzer, H. (2015). "Revisiting the Unified Model of Active Galactic Nuclei." In: *ARA&A* 53, pp. 365–408. doi: [10.1146/annurev-astro-082214-122302](https://doi.org/10.1146/annurev-astro-082214-122302). arXiv: [1505.00811](https://arxiv.org/abs/1505.00811).
- Netzer, H., O. Shemmer, R. Maiolino, E. Oliva, S. Croom, E. Corbett, and L. di Fabrizio (2004). "Near-Infrared Spectroscopy of High-Redshift Active Galactic Nuclei. II. Disappearing Narrow-Line

- Regions and the Role of Accretion." In: *ApJ* 614, pp. 558–567. DOI: [10.1086/423608](https://doi.org/10.1086/423608). eprint: [astro-ph/0406560](https://arxiv.org/abs/astro-ph/0406560).
- Oke, J. B. and J. E. Gunn (1983). "Secondary standard stars for absolute spectrophotometry." In: *ApJ* 266, pp. 713–717. DOI: [10.1086/160817](https://doi.org/10.1086/160817).
- Onken, C. A. and J. A. Kollmeier (2008). "An Improved Method for Using Mg II to Estimate Black Hole Masses in Active Galactic Nuclei." In: *ApJ* 689, p. L13.
- Onken, C. A. and B. M. Peterson (2002). "The Mass of the Central Black Hole in the Seyfert Galaxy NGC 3783." In: *ApJ* 572, pp. 746–752. DOI: [10.1086/340351](https://doi.org/10.1086/340351). eprint: [astro-ph/0202382](https://arxiv.org/abs/astro-ph/0202382).
- Pâris, I. et al. (2012). "The Sloan Digital Sky Survey quasar catalog: ninth data release." In: *A&A* 548, A66, A66. DOI: [10.1051/0004-6361/201220142](https://doi.org/10.1051/0004-6361/201220142). arXiv: [1210.5166](https://arxiv.org/abs/1210.5166).
- Pâris, I. et al. (2014). "The Sloan Digital Sky Survey quasar catalog: tenth data release." In: *A&A* 563, A54.
- Pâris, I. et al. (2017). "The Sloan Digital Sky Survey Quasar Catalog: Twelfth data release." In: *A&A* 597, A79.
- Park, D., J.-H. Woo, K. D. Denney, and J. Shin (2013). "Calibrating C-IV-based Black Hole Mass Estimators." In: *ApJ* 770, p. 87.
- Pei, Y. C. (1992). "Interstellar dust from the Milky Way to the Magellanic Clouds." In: *ApJ* 395, pp. 130–139. DOI: [10.1086/171637](https://doi.org/10.1086/171637).
- Perna, M. et al. (2015). "Galaxy-wide outflows in $z \sim 1.5$ luminous obscured quasars revealed through near-IR slit-resolved spectroscopy." In: *A&A* 574, A82, A82. DOI: [10.1051/0004-6361/201425035](https://doi.org/10.1051/0004-6361/201425035). arXiv: [1410.5468](https://arxiv.org/abs/1410.5468).
- Peterson, B. M. (1993). "Reverberation mapping of active galactic nuclei." In: *PASP* 105, pp. 247–268.
- (1997). *An Introduction to Active Galactic Nuclei*.
- (2010). "Toward Precision Measurement of Central Black Hole Masses." In: *Co-Evolution of Central Black Holes and Galaxies*. Ed. by B. M. Peterson, R. S. Somerville, and T. Storchi-Bergmann. Vol. 267. IAU Symposium, pp. 151–160.
- (2014). "Measuring the Masses of Supermassive Black Holes." In: *Space Sci. Rev.* 183, pp. 253–275.
- Peterson, B. M. et al. (2004). "Central Masses and Broad-Line Region Sizes of Active Galactic Nuclei. II. A Homogeneous Analysis of a Large Reverberation-Mapping Database." In: *ApJ* 613, pp. 682–699.
- Plotkin, R. M. et al. (2015). "Detection of Rest-frame Optical Lines from X-shooter Spectroscopy of Weak Emission Line Quasars." In: *ApJ* 805, p. 123.
- Polletta, M., T. J.-L. Courvoisier, E. J. Hooper, and B. J. Wilkes (2000). "The far-infrared emission of radio loud and radio quiet quasars." In: *A&A* 362, pp. 75–96. eprint: [astro-ph/0006315](https://arxiv.org/abs/astro-ph/0006315).

- Polletta, M. et al. (2007). "Spectral Energy Distributions of Hard X-Ray Selected Active Galactic Nuclei in the XMM-Newton Medium Deep Survey." In: *ApJ* 663, pp. 81–102. doi: [10 . 1086 / 518113](https://doi.org/10.1086/518113). eprint: [astro-ph/0703255](https://arxiv.org/abs/astro-ph/0703255).
- Prochaska, J. X. and J. F. Hennawi (2009). "Quasars Probing Quasars. III. New Clues to Feedback, Quenching, and the Physics of Massive Galaxy Formation." In: *ApJ* 690, pp. 1558–1584. doi: [10 . 1088 / 0004-637X/690/2/1558](https://doi.org/10.1088/0004-637X/690/2/1558). arXiv: [0806 . 0862](https://arxiv.org/abs/0806.0862).
- Proga, D., J. M. Stone, and T. R. Kallman (2000). "Dynamics of Line-driven Disk Winds in Active Galactic Nuclei." In: *ApJ* 543, pp. 686–696.
- Rafiee, A. and P. B. Hall (2011). "Supermassive Black Hole Mass Estimates Using Sloan Digital Sky Survey Quasar Spectra at $0.7 < z < 2$." In: *ApJS* 194, 42, p. 42. doi: [10 . 1088 / 0067 - 0049 / 194 / 2 / 42](https://doi.org/10.1088/0067-0049/194/2/42). arXiv: [1104 . 1828](https://arxiv.org/abs/1104.1828).
- Reyes, R., N. L. Zakamska, M. A. Strauss, J. Green, J. H. Krolik, Y. Shen, G. T. Richards, S. F. Anderson, and D. P. Schneider (2008). "Space Density of Optically Selected Type 2 Quasars." In: *AJ* 136, pp. 2373–2390. doi: [10 . 1088 / 0004 - 6256 / 136 / 6 / 2373](https://doi.org/10.1088/0004-6256/136/6/2373). arXiv: [0801 . 1115](https://arxiv.org/abs/0801.1115).
- Richards, G. T. (2006). "AGN Outflows in Emission and Absorption: The SDSS Perspective." In: *AGN Winds in the Caribbean*. arXiv: [astro-ph/0603827](https://arxiv.org/abs/astro-ph/0603827).
- Richards, G. T., D. E. Vanden Berk, T. A. Reichard, P. B. Hall, D. P. Schneider, M. SubbaRao, A. R. Thakar, and D. G. York (2002). "Broad Emission-Line Shifts in Quasars: An Orientation Measure for Radio-Quiet Quasars?" In: *AJ* 124, pp. 1–17.
- Richards, G. T. et al. (2003). "Red and Reddened Quasars in the Sloan Digital Sky Survey." In: *AJ* 126, pp. 1131–1147. doi: [10 . 1086 / 377014](https://doi.org/10.1086/377014). eprint: [astro-ph/0305305](https://arxiv.org/abs/astro-ph/0305305).
- Richards, G. T. et al. (2006a). "Spectral Energy Distributions and Multiwavelength Selection of Type 1 Quasars." In: *ApJS* 166, pp. 470–497.
- Richards, G. T. et al. (2006b). "The Sloan Digital Sky Survey Quasar Survey: Quasar Luminosity Function from Data Release 3." In: *AJ* 131, pp. 2766–2787.
- Richards, G. T., N. E. Kruczek, S. C. Gallagher, P. B. Hall, P. C. Hewett, K. M. Leighly, R. P. Deo, R. M. Kratzer, and Y. Shen (2011). "Unification of Luminous Type 1 Quasars through CIV Emission." In: *AJ* 141, p. 167.
- Risaliti, G. and M. Elvis (2004). "A Panchromatic View of AGN." In: *Supermassive Black Holes in the Distant Universe*. Ed. by A. J. Barger. Vol. 308. Astrophysics and Space Science Library, p. 187. eprint: [astro-ph/0403618](https://arxiv.org/abs/astro-ph/0403618).

- Ross, N. P. et al. (2013). "The SDSS-III Baryon Oscillation Spectroscopic Survey: The Quasar Luminosity Function from Data Release Nine." In: *ApJ* 773, p. 14.
- Ross, N. P. et al. (2014). "Extremely Red Quasars from SDSS, BOSS and WISE: Classification of Optical Spectra." In: *ArXiv e-prints*. arXiv: [1405.1047](#).
- Runnoe, J. C., M. S. Brotherton, Z. Shang, and M. A. DiPompeo (2013a). "Rehabilitating C IV-based black hole mass estimates in quasars." In: *MNRAS* 434, pp. 848–861.
- Runnoe, J. C., M. S. Brotherton, Z. Shang, B. J. Wills, and M. A. DiPompeo (2013b). "The orientation dependence of quasar single-epoch black hole mass scaling relationships." In: *MNRAS* 429, pp. 135–149.
- Runnoe, J. C., M. S. Brotherton, M. A. DiPompeo, and Z. Shang (2014). "The behaviour of quasar C IV emission-line properties with orientation." In: *MNRAS* 438, pp. 3263–3274.
- Sanders, D. B., B. T. Soifer, J. H. Elias, B. F. Madore, K. Matthews, G. Neugebauer, and N. Z. Scoville (1988). "Ultraluminous infrared galaxies and the origin of quasars." In: *ApJ* 325, pp. 74–91. doi: [10.1086/165983](#).
- Sanders, D. B., E. S. Phinney, G. Neugebauer, B. T. Soifer, and K. Matthews (1989). "Continuum energy distribution of quasars - Shapes and origins." In: *ApJ* 347, pp. 29–51. doi: [10.1086/168094](#).
- Schlafly, E. F. and D. P. Finkbeiner (2011). "Measuring Reddening with Sloan Digital Sky Survey Stellar Spectra and Recalibrating SFD." In: *ApJ* 737, 103, p. 103. doi: [10.1088/0004-637X/737/2/103](#). arXiv: [1012.4804 \[astro-ph.GA\]](#).
- Schlegel, D. J., D. P. Finkbeiner, and M. Davis (1998). "Maps of Dust Infrared Emission for Use in Estimation of Reddening and Cosmic Microwave Background Radiation Foregrounds." In: *ApJ* 500, pp. 525–553. doi: [10.1086/305772](#). eprint: [astro-ph/9710327](#).
- Schneider, D. P. et al. (2010). "The Sloan Digital Sky Survey Quasar Catalog. V. Seventh Data Release." In: *AJ* 139, p. 2360.
- Shakura, N. I. and R. A. Sunyaev (1973). "Black holes in binary systems. Observational appearance." In: *A&A* 24, pp. 337–355.
- Shang, Z. et al. (2011). "The Next Generation Atlas of Quasar Spectral Energy Distributions from Radio to X-Rays." In: *ApJS* 196, 2, p. 2. doi: [10.1088/0067-0049/196/1/2](#). arXiv: [1107.1855 \[astro-ph.CO\]](#).
- Shen, Y. (2013). "The mass of quasars." In: *Bulletin of the Astronomical Society of India* 41, pp. 61–115.
- (2016). "Rest-Frame Optical Properties of Luminous $1.5 < z < 3.5$ Quasars: The H β -[O III] Region." In: *ApJ* in press. doi: [10.1088/0004-6256/141/5/167](#). arXiv: [1512.00005](#).
- Shen, Y. and L. C. Ho (2014). "The diversity of quasars unified by accretion and orientation." In: *Nature* 513, pp. 210–213.

- Shen, Y. and X. Liu (2012). "Comparing Single-epoch Virial Black Hole Mass Estimators for Luminous Quasars." In: *ApJ* 753, p. 125.
- Shen, Y., J. E. Greene, M. A. Strauss, G. T. Richards, and D. P. Schneider (2008). "Biases in Virial Black Hole Masses: An SDSS Perspective." In: *ApJ* 680, pp. 169–190.
- Shen, Y. et al. (2011). "A Catalog of Quasar Properties from Sloan Digital Sky Survey Data Release 7." In: *ApJS* 194, p. 45.
- Shen, Y. et al. (2015). "The Sloan Digital Sky Survey Reverberation Mapping Project: Technical Overview." In: *ApJS* 216, p. 4.
- Shen, Y. et al. (2016). "The Sloan Digital Sky Survey Reverberation Mapping Project: Velocity Shifts of Quasar Emission Lines." In: *ArXiv e-prints*. arXiv: [1602.03894](#).
- Silk, J. and M. J. Rees (1998). "Quasars and galaxy formation." In: *A&A* 331, pp. L1–L4. eprint: [astro-ph/9801013](#).
- Simcoe, R. A. et al. (2010). "The FIRE infrared spectrometer at Magellan: construction and commissioning." In: *Ground-based and Airborne Instrumentation for Astronomy III*. Vol. 7735. Proc. SPIE, p. 773514. DOI: [10.1117/12.856088](#).
- Skrutskie, M. F. et al. (2006). "The Two Micron All Sky Survey (2MASS)." In: *AJ* 131, pp. 1163–1183. DOI: [10.1086/498708](#).
- Sulentic, J. W., P. Marziani, and D. Dultzin-Hacyan (2000). "Phenomenology of Broad Emission Lines in Active Galactic Nuclei." In: *ARA&A* 38, pp. 521–571.
- Sulentic, J. W., T. Zwitter, P. Marziani, and D. Dultzin-Hacyan (2000). "Eigenvector 1: An Optimal Correlation Space for Active Galactic Nuclei." In: *ApJ* 536, pp. L5–L9.
- Sulentic, J. W., G. M. Stirpe, P. Marziani, R. Zamanov, M. Calvani, and V. Braito (2004). "VLT/ISAAC spectra of the H β region in intermediate redshift quasars." In: *A&A* 423, pp. 121–132. DOI: [10.1051/0004-6361:20035912](#). eprint: [astro-ph/0405279](#).
- Sulentic, J. W., P. Repetto, G. M. Stirpe, P. Marziani, D. Dultzin-Hacyan, and M. Calvani (2006). "VLT/ISAAC spectra of the H β region in intermediate-redshift quasars. II. Black hole mass and Eddington ratio." In: *A&A* 456, pp. 929–939. DOI: [10.1051/0004-6361:20054153](#). eprint: [astro-ph/0606309](#).
- Sulentic, J. W., R. Bachev, P. Marziani, C. A. Negrete, and D. Dultzin (2007). "C IV λ 1549 as an Eigenvector 1 Parameter for Active Galactic Nuclei." In: *ApJ* 666, pp. 757–777. DOI: [10.1086/519916](#). arXiv: [0705.1895](#).
- Sunyaev, R. A. and L. G. Titarchuk (1980). "Comptonization of X-rays in plasma clouds - Typical radiation spectra." In: *A&A* 86, pp. 121–138.
- Tilton, E. M. and J. M. Shull (2013). "Ultraviolet Emission-line Correlations in HST/COS Spectra of Active Galactic Nuclei: Single-epoch Black Hole Masses." In: *ApJ* 774, p. 67.

- Trakhtenbrot, B. and H. Netzer (2012). "Black hole growth to $z = 2$ - I. Improved virial methods for measuring M_{BH} and L/L_{Edd} ." In: *MNRAS* 427, pp. 3081–3102. doi: [10.1111/j.1365-2966.2012.22056.x](https://doi.org/10.1111/j.1365-2966.2012.22056.x). arXiv: [1209.1096](https://arxiv.org/abs/1209.1096).
- Treister, E., K. Schawinski, C. M. Urry, and B. D. Simmons (2012). "Major Galaxy Mergers Only Trigger the Most Luminous Active Galactic Nuclei." In: *ApJ* 758, L39, p. L39. doi: [10.1088/2041-8205/758/2/L39](https://doi.org/10.1088/2041-8205/758/2/L39). arXiv: [1209.5393 \[astro-ph.CO\]](https://arxiv.org/abs/1209.5393).
- Trichas, M. et al. (2012). "The Chandra Multi-wavelength Project: Optical Spectroscopy and the Broadband Spectral Energy Distributions of X-Ray-selected AGNs." In: *ApJS* 200, 17, p. 17. doi: [10.1088/0067-0049/200/2/17](https://doi.org/10.1088/0067-0049/200/2/17). arXiv: [1204.5148 \[astro-ph.CO\]](https://arxiv.org/abs/1204.5148).
- Tytler, D. and X.-M. Fan (1992). "Systematic QSO emission-line velocity shifts and new unbiased redshifts." In: *ApJS* 79, pp. 1–36. doi: [10.1086/191642](https://doi.org/10.1086/191642).
- Urrutia, T., R. H. Becker, R. L. White, E. Glikman, M. Lacy, J. Hodge, and M. D. Gregg (2009). "The FIRST-2MASS Red Quasar Survey. II. An Anomalously High Fraction of LoBALs in Searches for Dust-Reddened Quasars." In: *ApJ* 698, pp. 1095–1109. doi: [10.1088/0004-637X/698/2/1095](https://doi.org/10.1088/0004-637X/698/2/1095). arXiv: [0808.3668](https://arxiv.org/abs/0808.3668).
- Urry, C. M. and P. Padovani (1995). "Unified Schemes for Radio-Loud Active Galactic Nuclei." In: *PASP* 107, p. 803. doi: [10.1086/133630](https://doi.org/10.1086/133630). eprint: [astro-ph/9506063](https://arxiv.org/abs/astro-ph/9506063).
- Venemans, B. P., F. Walter, L. Zschaechner, R. Decarli, G. De Rosa, J. R. Findlay, R. G. McMahon, and W. J. Sutherland (2016). "Bright [C ii] and Dust Emission in Three $z > 6.6$ Quasar Host Galaxies Observed by ALMA." In: *ApJ* 816, 37, p. 37. doi: [10.3847/0004-637X/816/1/37](https://doi.org/10.3847/0004-637X/816/1/37). arXiv: [1511.07432](https://arxiv.org/abs/1511.07432).
- Vernet, J. et al. (2011). "X-shooter, the new wide band intermediate resolution spectrograph at the ESO Very Large Telescope." In: *A&A* 536, A105, A105. doi: [10.1051/0004-6361/201117752](https://doi.org/10.1051/0004-6361/201117752). arXiv: [1110.1944 \[astro-ph.IM\]](https://arxiv.org/abs/1110.1944).
- Véron, P., A. C. Gonçalves, and M.-P. Véron-Cetty (2002). "The "red shelf" of the $H\beta$ line in the Seyfert 1 galaxies RXS J01177+3637 and HS 0328+05." In: *A&A* 384. doi: [10.1051/0004-6361:20020072](https://doi.org/10.1051/0004-6361:20020072). eprint: [astro-ph/0201240](https://arxiv.org/abs/astro-ph/0201240).
- Vestergaard, M. (2002). "Determining Central Black Hole Masses in Distant Active Galaxies." In: *ApJ* 571, pp. 733–752.
- (2004). "Early Growth and Efficient Accretion of Massive Black Holes at High Redshift." In: *ApJ* 601, pp. 676–691.
- Vestergaard, M. and P. S. Osmer (2009). "Mass Functions of the Active Black Holes in Distant Quasars from the Large Bright Quasar Survey, the Bright Quasar Survey, and the Color-selected Sample of the SDSS Fall Equatorial Stripe." In: *ApJ* 699, pp. 800–816.
- Vestergaard, M. and B. M. Peterson (2006). "Determining Central Black Hole Masses in Distant Active Galaxies and Quasars. II.

- Improved Optical and UV Scaling Relationships." In: *ApJ* 641, pp. 689–709.
- Vestergaard, M., X. Fan, C. A. Tremonti, P. S. Osmer, and G. T. Richards (2008). "Mass Functions of the Active Black Holes in Distant Quasars from the Sloan Digital Sky Survey Data Release 3." In: *ApJ* 674, pp. L1–L4.
- Vogt, S. S. et al. (1994). "HIRES: the high-resolution echelle spectrometer on the Keck 10-m Telescope." In: *Instrumentation in Astronomy VIII*. Ed. by D. L. Crawford and E. R. Craine. Vol. 2198. Proc. SPIE, p. 362.
- Volonteri, M., M. Sikora, and J.-P. Lasota (2007). "Black Hole Spin and Galactic Morphology." In: *ApJ* 667, pp. 704–713. doi: [10.1086/521186](https://doi.org/10.1086/521186). arXiv: [0706.3900](https://arxiv.org/abs/0706.3900).
- Wall, J. V., C. A. Jackson, P. A. Shaver, I. M. Hook, and K. I. Kellermann (2005). "The Parkes quarter-Jansky flat-spectrum sample. III. Space density and evolution of QSOs." In: *A&A* 434, pp. 133–148. doi: [10.1051/0004-6361:20041786](https://doi.org/10.1051/0004-6361:20041786). eprint: [astro-ph/0408122](https://arxiv.org/abs/astro-ph/0408122).
- Wang, H., F. Xing, K. Zhang, T. Wang, H. Zhou, and S. Zhang (2013). "Outflow and Hot Dust Emission in High-redshift Quasars." In: *ApJ* 776, p. L15.
- Wang, J.-G., X.-B. Dong, T.-G. Wang, L. C. Ho, W. Yuan, H. Wang, K. Zhang, S. Zhang, and H. Zhou (2009). "Estimating Black Hole Masses in Active Galactic Nuclei Using the Mg II $\lambda 2800$ Emission Line." In: *ApJ* 707, pp. 1334–1346. doi: [10.1088/0004-637X/707/2/1334](https://doi.org/10.1088/0004-637X/707/2/1334). arXiv: [0910.2848](https://arxiv.org/abs/0910.2848).
- Weymann, R. J., S. L. Morris, C. B. Foltz, and P. C. Hewett (1991). "Comparisons of the emission-line and continuum properties of broad absorption line and normal quasi-stellar objects." In: *ApJ* 373, pp. 23–53. doi: [10.1086/170020](https://doi.org/10.1086/170020).
- White, R. L., R. H. Becker, D. J. Helfand, and M. D. Gregg (1997). "A Catalog of 1.4 GHz Radio Sources from the FIRST Survey." In: *ApJ* 475, pp. 479–493.
- Williams, R. J., R. Maiolino, Y. Krongold, S. Carniani, G. Cresci, F. Mannucci, and A. Marconi (2016). "An ultra-dense fast outflow in a quasar at $z=2.4$." In: *ArXiv e-prints*. arXiv: [1605.08046](https://arxiv.org/abs/1605.08046).
- Wilson, J. C. et al. (2004). "Mass producing an efficient NIR spectrograph." In: *Ground-based Instrumentation for Astronomy*. Ed. by A. F. M. Moorwood and M. Iye. Vol. 5492. Proc. SPIE, pp. 1295–1305. doi: [10.1117/12.550925](https://doi.org/10.1117/12.550925).
- Wisotzki, L., N. Christlieb, N. Bade, V. Beckmann, T. Köhler, C. Vanelle, and D. Reimers (2000). "The Hamburg/ESO survey for bright QSOs. III. A large flux-limited sample of QSOs." In: *A&A* 358, pp. 77–87. eprint: [astro-ph/0004162](https://arxiv.org/abs/astro-ph/0004162).
- Wright, E. L. et al. (2010). "The Wide-field Infrared Survey Explorer (WISE): Mission Description and Initial On-orbit Performance."

- In: *AJ* 140, 1868, pp. 1868–1881. doi: [10.1088/0004-6256/140/6/1868](https://doi.org/10.1088/0004-6256/140/6/1868). arXiv: [1008.0031 \[astro-ph.IM\]](https://arxiv.org/abs/1008.0031).
- Wu, X.-B., R. Wang, M. Z. Kong, F. K. Liu, and J. L. Han (2004). “Black hole mass estimation using a relation between the BLR size and emission line luminosity of AGN.” In: *A&A* 424, pp. 793–798.
- York, D. G. et al. (2000). “The Sloan Digital Sky Survey: Technical Summary.” In: *AJ* 120, pp. 1579–1587.
- Yuan, S., M. A. Strauss, and N. L. Zakamska (2016). “Spectroscopic identification of type 2 quasars at $z < 1$ in SDSS-III/BOSS.” In: *MNRAS* 462, pp. 1603–1615. doi: [10.1093/mnras/stw1747](https://doi.org/10.1093/mnras/stw1747). arXiv: [1606.04976](https://arxiv.org/abs/1606.04976).
- Zakamska, N. L. and J. E. Greene (2014). “Quasar feedback and the origin of radio emission in radio-quiet quasars.” In: *MNRAS* 442, pp. 784–804. doi: [10.1093/mnras/stu842](https://doi.org/10.1093/mnras/stu842). arXiv: [1402.6736](https://arxiv.org/abs/1402.6736).
- Zakamska, N. L., F. Hamann, I. Pâris, W. N. Brandt, J. E. Greene, M. A. Strauss, C. Villforth, D. Wylezalek, R. M. Alexandroff, and N. P. Ross (2016). “Discovery of extreme [O III] $\lambda 5007 \text{ \AA}$ outflows in high-redshift red quasars.” In: *MNRAS* 459, pp. 3144–3160. doi: [10.1093/mnras/stw718](https://doi.org/10.1093/mnras/stw718). arXiv: [1512.02642](https://arxiv.org/abs/1512.02642).
- Zamanov, R., P. Marziani, J. W. Sulentic, M. Calvani, D. Dultzin-Hacyan, and R. Bachev (2002). “Kinematic Linkage between the Broad- and Narrow-Line-emitting Gas in Active Galactic Nuclei.” In: *ApJ* 576, pp. L9–L13. doi: [10.1086/342783](https://doi.org/10.1086/342783). eprint: [astro-ph/0207387](https://arxiv.org/abs/astro-ph/0207387).
- Zamfir, S., J. W. Sulentic, P. Marziani, and D. Dultzin (2010). “Detailed characterization of H β emission line profile in low- z SDSS quasars.” In: *MNRAS* 403, pp. 1759–1786. doi: [10.1111/j.1365-2966.2009.16236.x](https://doi.org/10.1111/j.1365-2966.2009.16236.x). arXiv: [0912.4306](https://arxiv.org/abs/0912.4306).
- Zhang, S., H. Wang, T. Wang, F. Xing, K. Zhang, H. Zhou, and P. Jiang (2014). “Outflow and Hot Dust Emission in Broad Absorption Line Quasars.” In: *ApJ* 786, p. 42.
- van der Marel, R. P. and M. Franx (1993). “A new method for the identification of non-Gaussian line profiles in elliptical galaxies.” In: *ApJ* 407, pp. 525–539.

DECLARATION

Put your declaration here.

Saarbrücken, September 2015

Liam Coatman